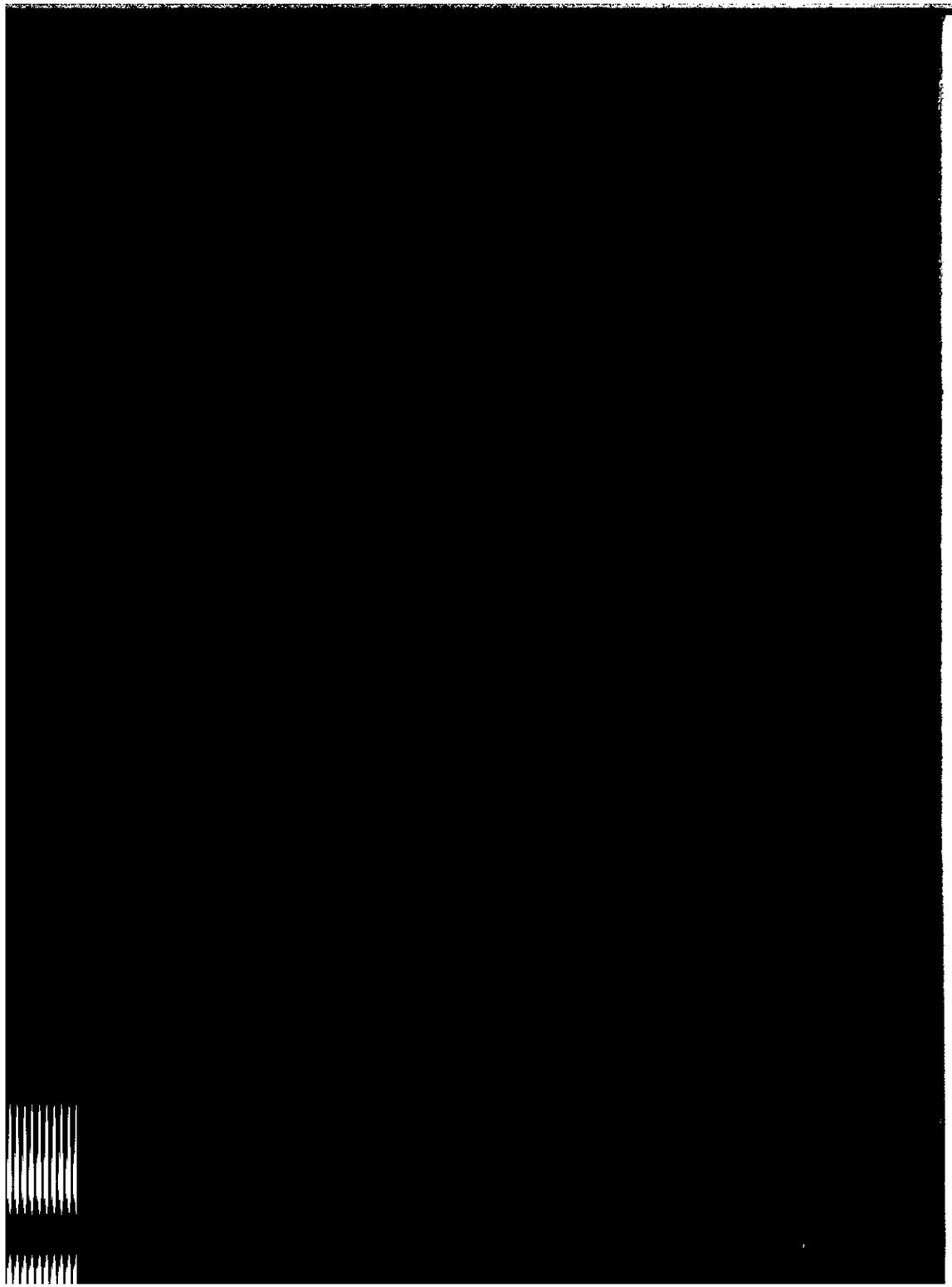

COMSAT
Technical Review

Volume 13 Number 1, Spring 1983

COMSAT TECHNICAL REVIEW is published twice a year by Communications Satellite Corporation (COMSAT). Subscriptions, which include the two issues published within a calendar year, are: one year, $10 U.S.; two years, $15; three years, $20; single copies, $7; article reprints, $1.50. Air mail delivery is available at an additional cost of $10 per year. Make checks payable to COMSAT and address to Treasurer's Office, Communications Satellite Corporation, 950 L'Enfant Plaza, S.W., Washington, D.C. 20024, U.S.A.

COMSAT TECHNICAL REVIEW

Volume 13 Number 1, Spring 1983

1 DEVELOPMENT OF A 60-CHANNEL FDM-TDM TRANSMULTIPLEXER **E. S. Yam** and **M. D. Redman**

57 LIMITATIONS ON SOLAR CELL OPEN-CIRCUIT VOLTAGE AND EFFICIENCY **A. Meulenberg, Jr.** and **R. A. Arndt**

71 MATCHING NETWORKS IN LINEAR PHASED ARRAYS **A. I. Zaghloul**

87 CAPACITY ALLOCATION SCHEME FOR TRANSMISSION OF PACKETS OVER SATELLITE LINKS **D. M. Chitre**

107 THIRD-ORDER DISTORTION OF TELEVISION AND SOUND MULTIPLEXED SIGNALS IN SATELLITE FM SYSTEMS **A. Hammer** AND **D. J. Schaefer**

123 MARITIME COMMUNICATIONS SATELLITE IN-ORBIT MEASUREMENTS **M. Barrett** and **K. Fullett**

143 EFFICIENT APPROACHES TO ERLANG LOSS FUNCTION COMPUTATIONS **T. N. Shimi** and **Y. L. Park**

157 CTR NOTES

SIMPLE METHOD FOR ESTIMATING ATMOSPHERIC ABSORPTION AT 1 TO 15 GHz **D. V. Rogers** 157

SUBJECTIVE EQUIVALENCE OF SPEECH-CORRELATED AND STATIONARY NOISE **V. Gupta, H. Suyderhoud, K. Virupaksha,** and **M. Onufry** 165

COMMUNICATIONS PERFORMANCE SPECIFICATIONS OF THE INTELSAT V WITH MARITIME COMMUNICATIONS SUBSYSTEM **J. Martin, D. Arnstein,** and **C. Adams** 173

COMMUNICATIONS PERFORMANCE SPECIFICATIONS OF THE INTELSAT V-A **J. Martin, D. Arnstein,** and **C. Adams** 181

GEOSYNCHRONOUS SATELLITE LOG **C. H. Schmitt** 193

205 TRANSLATIONS OF ABSTRACTS
FRENCH 205 SPANISH 209

213 AUTHOR INDEX, CTR 1982

215 INDEX OF 1982 PRESENTATIONS AND PUBLICATIONS BY COMSAT AUTHORS

Development of a 60-channel FDM-TDM transmultiplexer

E. S. YAM AND M. D. REDMAN

(Manuscript received August 20, 1982)

Abstract

A 60-channel supergroup FDM-TDM transmultiplexer developed for satellite TDMA application is described. The mathematical principles of digital single-sideband (SSB) modulation-demodulation are reviewed and fast computation algorithms for digital signal processing in the two directions are formulated. The approach uses an all-real, one-stage, bandpass filtering scheme and fast discrete cosine transforms for achieving computational efficiency. The algorithms were applied in the hardware implementation of a prototype supergroup transmultiplexer. The design employs a flexible PROM-based microcodable concept and features hardware simplicity. The design problem for the FIR prototype low-pass filter is outlined, and the system design considerations for satellite TDMA applications are discussed. The supergroup transmultiplexer hardware has been developed and tested, and its performance meets the desired CCITT standards.

Introduction

A transmultiplexer converts multiple telephone channels from the frequency-division multiplex (FDM) format to the time-division multiplex (TDM) format, and vice versa. The need for bilateral FDM-TDM conversion has arisen because of the emergence and growth of digital communications systems. Conventional long-haul telephone

transmission has been accomplished by using analog frequency-division multiplex and single-sideband, suppressed-carrier modulation techniques (FDM/SSB-SC). In digital systems, multiple telephone channels are represented in the time-division multiplex/pulse-code modulation (TDM/PCM) format. Because a major portion of long-haul circuits will continue to use analog facilities in the foreseeable future, the interconnection of the coexisting analog and digital systems requires that an efficient means for FDM-TDM conversion be available.

A transmultiplexer performs the required FDM-TDM conversion directly, eliminating the need for a back-to-back connection of conventional FDM and TDM channel banks. Using advanced digital signal processing techniques, a transmultiplexer can accomplish the bilateral FDM-TDM conversion with high efficiency and without the need for reduction to individual analog voice channels. Obvious advantages of a transmultiplexer are small size and low cost.

In a projected application of transmultiplexers in the planned INTELSAT TDMA/DSI system, the terrestrial interface to the earth stations is in analog FDM form, whereas the satellite transmission is in digital TDMA form. On the transmit side, transmultiplexers at the earth station will convert standard FDM assemblies, *e.g.*, the 60-channel supergroups, into appropriate TDM/PCM bit streams. The bit streams will then be supplied to the digital speech interpolation (DSI) units for compression, and, subsequently, transmitted via satellite. The transmultiplexers on the receive side will perform the opposite function.

In another possible application in the INTELSAT system, optical cable restoration would be performed with transmultiplexers used in a reversed mode. It is then assumed that the terrestrial interface to the earth stations via optical cables would be in digital TDM/PCM form, *e.g.*, 24-channel, 1.544-Mbit/s T1 carriers, and the satellite transmission would be analog FDMA.

Transmultiplexers can also find applications in terrestrial telecommunications systems, *e.g.*, as interfaces between analog facilities and digital switches, and between analog and digital transmission networks.

This paper describes a 60-channel transmultiplexer developed at COMSAT Laboratories. The objectives were low cost, small size, and suitability for satellite TDMA applications. The transmultiplexer provides conversion between an FDM 60-channel basic supergroup (312–552 kHz) and two 30-channel CEPT 2.048-Mbit/s TDM/PCM data streams. The underlying mathematical principles for the digital FDM-TDM processing will first be discussed, followed by the derivation of several fast computational algorithms and a comparison of their respective computational complexities. Finally, the system and hardware design considerations for the implementation of the 60-channel supergroup transmultiplexer will be described.

Background

The bilateral FDM-TDM conversion process can be divided into two parts. The first part corresponds to an FDM/SSB modulation-demodulation process, in which an FDM signal is converted into a collection of individual digital voice signals, each linearly encoded at an 8-kHz sampling rate, and vice versa. The second part corresponds to a time-division multiplex-demultiplex process, in which the collection of individual digital voice channels are converted into a standard serial PCM/TDM format, compressed according to a given companding law, and vice versa. Because the second part can be accomplished by straightforward digital processing, the first part is the key process of a transmultiplexer, and will be the main subject of this paper.

Three conventional schemes in the analog domain for SSB modulation-demodulation are the bandpass, Weaver, and Hartley schemes.

Figure 1 depicts the bandpass scheme for a single voice channel. The 4-kHz voice signal is first translated to a desired high frequency, f_c, by the modulation of a sinusoidal carrier at f_c. Then, a 4-kHz bandpass filter is used to extract the desired (upper or lower) sideband. For multiple channel implementation, a bank of similar configurations corresponding to different modulation frequencies is used in parallel. The desired FDM/SSB signal is obtained as the summation of the resulting signals. The SSB demodulation follows the exact inverse process.

Figure 2 depicts the Weaver scheme [1] for a single voice channel. The voiceband signal first modulates two midband sinusoidal carriers which are 90° apart in phase, *e.g.*, 2-kHz cosine and sine waves. The resulting two signals are then low-pass filtered to remove the energy above 2 kHz, and treated with a second quadrature modulation operation. The final SSB modulated signal is obtained by adding the two signals, whereby the unwanted sideband cancels out.

Figure 3 depicts the Hartley scheme for a single voice channel, which employs a balancing technique. The input signal is first fed through an all-pass 90° phase difference network. The two output signals then modulate two carriers in quadrature at the desired high frequency, f_c. Finally, a subtraction (addition) will yield the upper (lower) sideband, when the unwanted sideband cancels out. In Figure

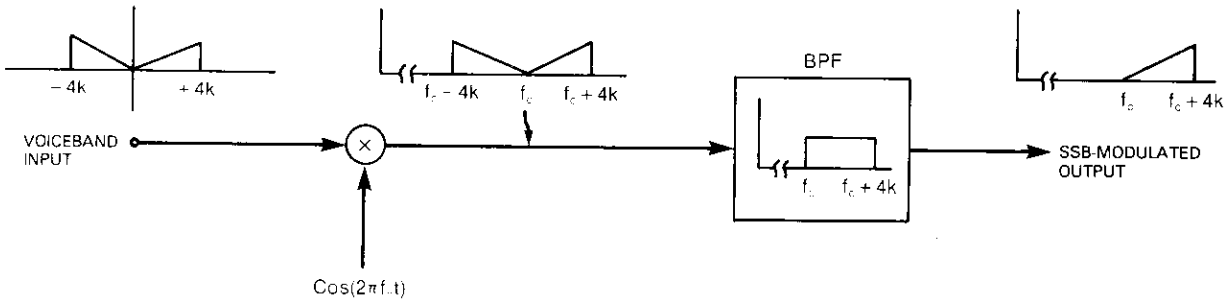

Figure 1. *Analog Bandpass SSB Modulation Scheme (per channel)*

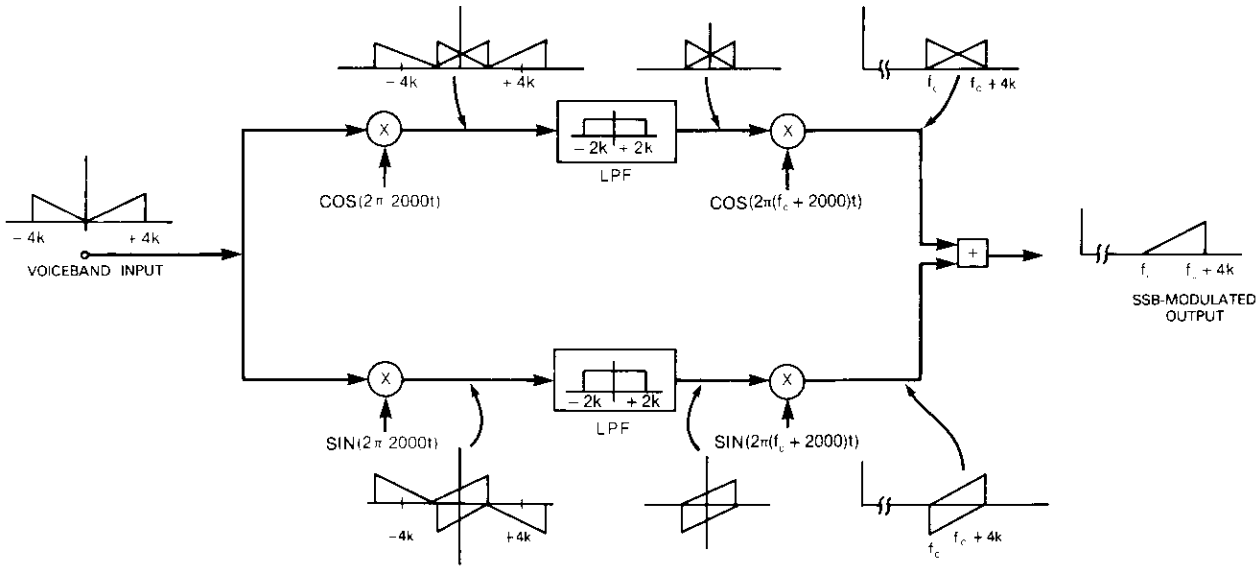

Figure 2. *Analog Weaver SSB Modulation Scheme (per channel)*

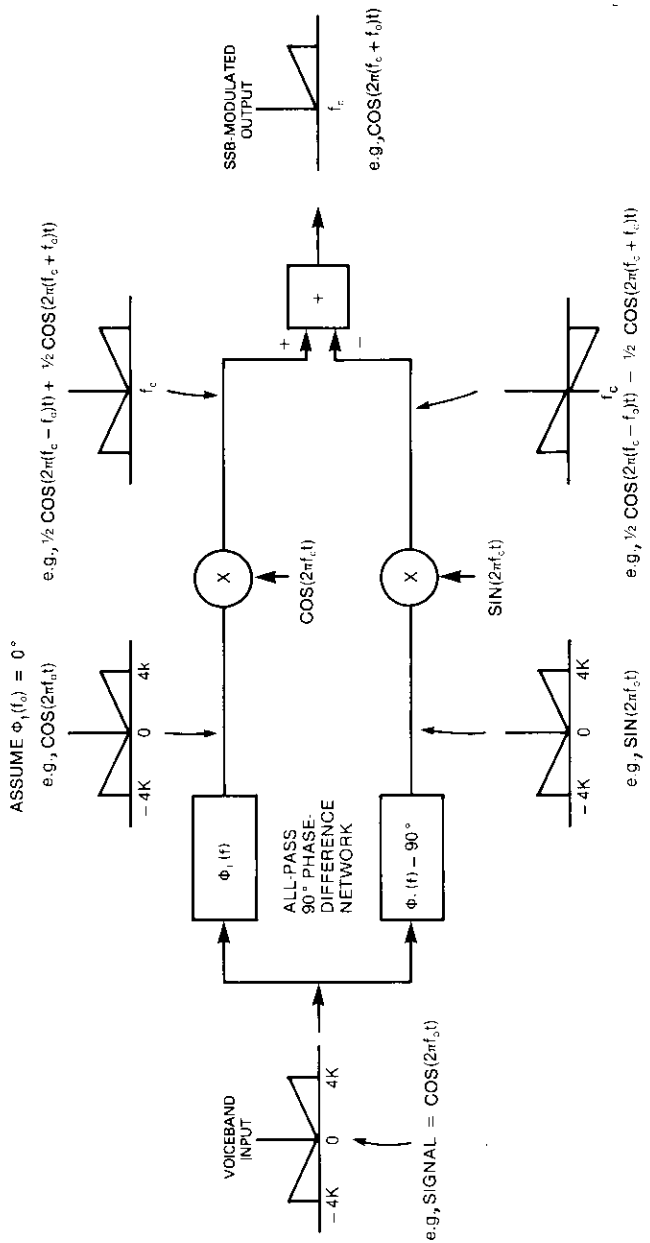

Figure 3. *Analog Hartley SSB Modulation Scheme (per channel)*

3, an example for an input signal $\cos(2\pi f_c t)$ illustrates the phase change and sideband cancelling relations.

In comparison, the bandpass scheme involves a simple per channel configuration, but more demanding filtering requirements. The dual paths for both the Weaver and the Hartley schemes result in more complex configurations. The Hartley scheme needs no amplitude filtering, but requires careful control of amplitudes and phases along the two paths. The Weaver scheme represents a compromise of the two other schemes.

For digital implementation, the analog signals will be replaced by digital sample streams, and the analog filters by digital filters. However, the relationship between an analog scheme and its digital counterpart does not constitute an exact duality. Specifically,

a. The time-sampling of a signal creates repeating spectral images with respect to the sampling frequency, and hence is equivalent to a "built-in" modulation process. By using the interpolation and decimation techniques, the sinusoidal modulation steps in the analog schemes can be eliminated.

b. A bank of digital bandpass filters can be very efficiently realized as a bank of up-shifted digital low-pass filters.

The concepts of digitally implementing an SSB modulation process based on the Weaver and Hartley schemes were first introduced by Darlington [2]. The concept based on the Weaver scheme was later developed into a more concrete algorithmic form using the fast Fourier transform (FFT) by Freeney *et al.* [3], [4]. A previous transmultiplexer design at COMSAT Laboratories essentially followed this approach [5]. Bellanger *et al.* developed an SSB modulation scheme using the polyphase network and FFT [6]–[8]. Somewhat different approaches were developed by Maruta *et al.* [9]–[11], and Takahata *et al.* [12], [13]. These schemes employ complex (real and imaginary) configurations involving IIR filtering or two-stage FIR/IIR filtering. The designs have resulted in hardware implementations as 24-channel (NEC, KDD), 60-channel (TRT, NEC, KDD) and 120-channel (NEC) transmultiplexers. More recently, Narasimha and Peterson pointed out that a digital bandpass filter bank with real input and real output can be realized using an all-real scheme [14]. The concept was later applied in a 24-channel transmultiplexer implementation (Granger Associates) [15]. The subject of digital SSB modulation techniques has generated a high level of interest in both the industrial and academic fields [16]–[20]. A review of more recent work is given in Reference 21.

The digital SSB modulation-demodulation scheme adopted for the implementation of the supergroup transmultiplexer corresponds to an all-real bandpass approach, using a one-step FIR (transversal) filter and the discrete cosine transform. Compared with the other approaches, the principal attractiveness of this approach is hardware simplicity, achieved in the following:

a. It uses an all-real, instead of a duplicating real-and-imaginary, operation.

b. It uses a one-step, instead of a two-step, filtering operation.

c. The FIR, instead of the IIR, filter requires a shorter internal word length, which allows less hardware, and the flexibility of using commercially available LSI components, such as the TRW 16-bit fast multipliers, as the principal computation elements.

Frequency domain interpretation of digital SSB demodulation

For the purpose of illustration, assume that the number of channels in the FDM/SSB signal is $N = 4$, and that the sampling frequency is $f_s = N \cdot f_s' = N \cdot 8$ kHz. Figure 4a shows the pictorial representation of the spectrum of such a time-sampled FDM signal $X(r)$. Assume that the channels in the frequency range of $0 \rightarrow f_s/2$ correspond to inverted sidebands, and those in $f_s/2 \rightarrow f_s$ correspond to erect sidebands. Figure 4d shows the spectra of the desired output demodulated signals sampled at 8 kHz. The objective of SSB demodulation is to start with Figure 4a and arrive at Figure 4d.

Figure 4b shows a bank of N digital bandpass filters, each operating at the FDM signal sampling frequency f_s. Each bandpass filter is 4 kHz wide and centered at $f_n = (2n + 1)(2 \text{ kHz})$. Passing the sampled FDM signal, $X(r)$, through each filter generates N output sampled signals $\{Y_0(r), Y_1(r), \ldots, Y_{N-1}(r)\}$. The spectra of the resulting signals are shown in Figure 4b.

Let an N:1 sampling rate reduction be performed on each signal; this operation is termed "decimation" [22]. In the time domain, the N:1 decimation operation corresponds to retaining only every N-th sample of the signal and discarding all samples in between. Denote the resulting signals as $\{Y_0(Nr), Y_1(Nr), \ldots, Y_{N-1}(Nr)\}$. The sampling rate of each of the decimated signals is now $f_s' = f_s/N = 8$ kHz. Figure 4c shows the resulting spectra.

Note that in Figure 4c the spectrum for $Y_n(Nr)$, n = odd, corresponds to that of a desired demultiplexed signal, but for n = even, the sidebands are inverted. The desired signals

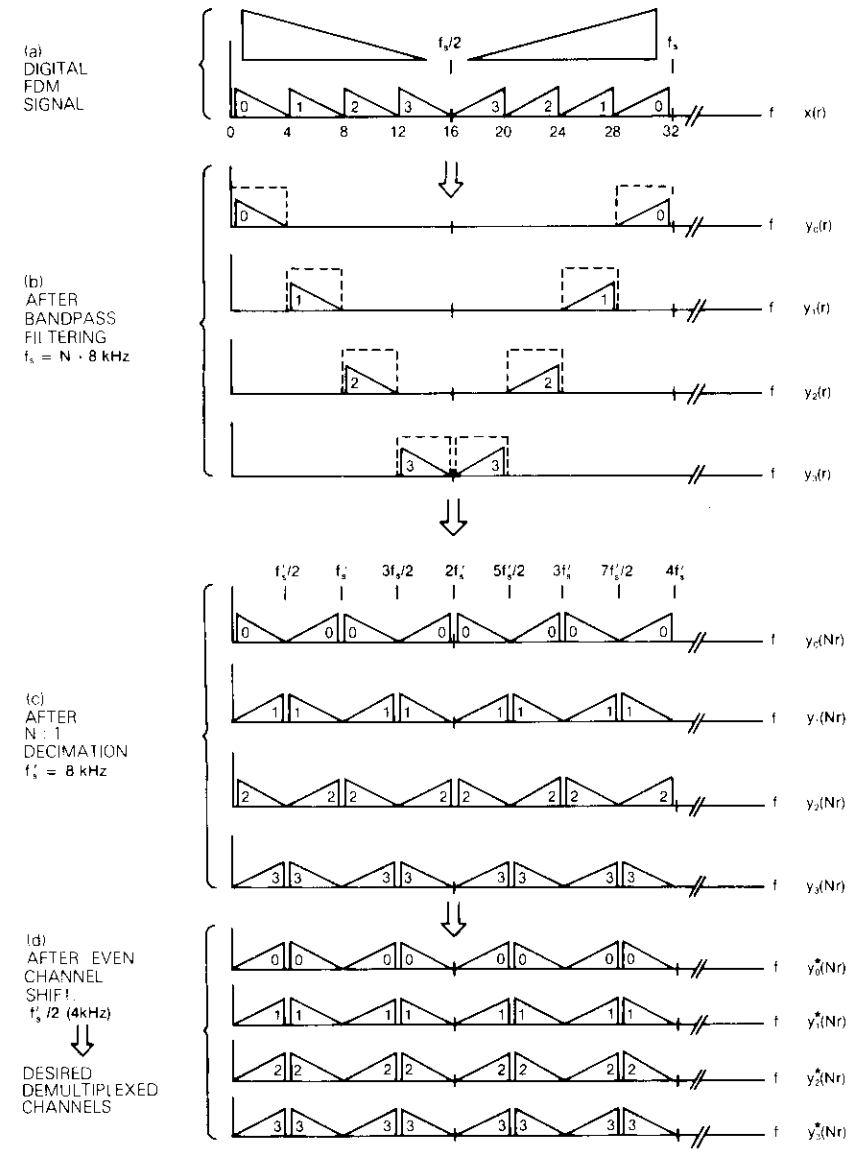

Figure 4. *Digital SSB Demodulation Process in the Frequency Domain (N = 4)*

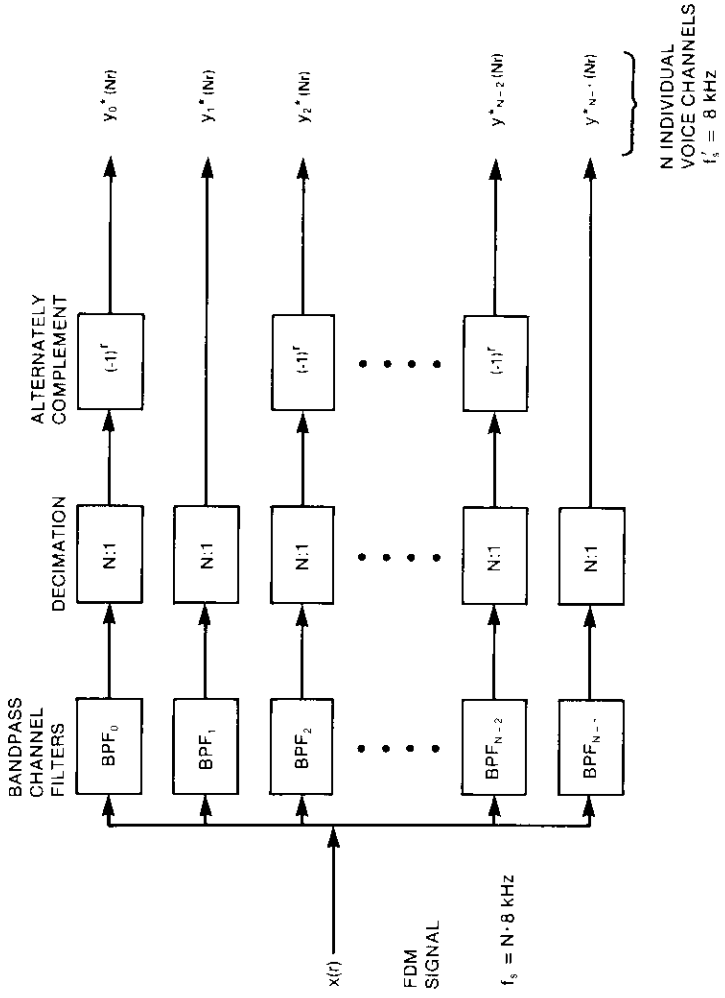

Figure 5. *Basic Digital SSB Demodulation Process in the Time Domain*

can be obtained by frequency translating the even channels by $f_s'/2 = 4$ kHz. The spectra of the resulting signals $\{Y_0^*(Nr), Y_1^*(Nr), \ldots, Y_{n-1}^*(Nr)\}$ are shown in Figure 4d.

Time-domain interpretation of digital SSB demodulation

Figure 5 depicts the digital SSB demodulation process in the time domain. The required channel filters can be acquired by frequency-translating the transfer function of a prototype low-pass filter of 2-kHz bandwidth. Let $H(f)$ be the transfer function of the prototype low-pass filter; then the transfer function of the desired n-th channel bandpass filter $H_n(f)$ is

$$H_n(f) = H\left[f - (2n + 1)\frac{f_s}{4N}\right] \quad .$$

Figure 6 shows the relationship between the low-pass and bandpass filters.

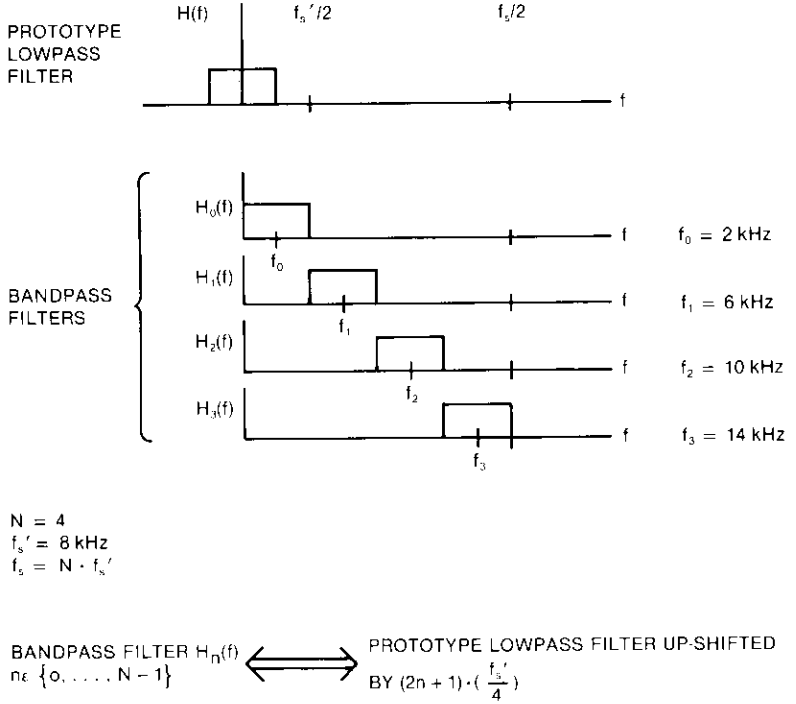

Figure 6. *Digital Filter Bank*

Assume the unit impulse response of the prototype low-pass filter is of finite duration $M + 1$,

$$\{h(m)\},\ m = 0, 1, \ldots, M \quad .$$

Then the corresponding unit impulse response of the n-th bandpass filter for real input and real output signals is

$$h_n(m) = h(m) \cdot \cos\left[\frac{\pi(2n + 1) \cdot m}{2N}\right], \quad \begin{matrix} m = 0, \ldots, M \\ n = 0, \ldots, N - 1 \end{matrix} \quad .$$

Let

$X(r)$ = wideband FDM signal at sampling rate f_s
$Y_n(r)$ = wideband signal for channel n after extraction by n-th bandpass filter, at sampling rate f_s
$Y_n(Nr)$ = narrowband signal for channel n obtained by N:1 decimation of $Y_n(r)$, at sampling rate $f_s' = f_s/N = 8$ kHz.

Then,

$$Y_n(r) = \sum_{m=0}^{M} X(r - m) \cdot h(m) \cdot \cos\left[\frac{\pi(2n + 1)m}{2N}\right]$$

$$n = 0, \ldots, N - 1 \qquad (1)$$

$$Y_n(Nr) = \sum_{m=0}^{M} X(Nr - m) \cdot h(m) \cdot \cos\left[\frac{\pi(2n + 1)m}{2N}\right]$$

$$n = 0, \ldots, N - 1 \quad . \qquad (2)$$

Equation (2) is a time-domain representation of the SSB demodulation process. Subsequently, $Y_n(Nr)$, n = even, must be translated by 4 kHz by complementing every other sample.

If equation (2) is implemented directly, the coefficients $h_n(m) = h(m) \cdot \cos[\pi(2n + 1)m/2N]$ can be precomputed, and the computation requirement per "frame" $\{Y_0(Nr), \ldots, Y_{N-1}(Nr)\}$ is

number of multiplications:	$(M + 1) \cdot N$
number of additions:	$M \cdot N$
memory (RAM):	$(M + 1)$
memory (PROM):	$(M + 1) \cdot N$

Fast algorithm for FDM-TDM direction

The demultiplexed signals represented in equation (2) can be formulated as the outputs of an N-th order discrete inverse cosine transform (DCT) of the form

$$Y_n = \sum_{m=0}^{N-1} U_m \cos\left[\frac{\pi(2n + 1)m}{2N}\right], n = 0, \ldots, N - 1 \qquad (3)$$

where the transform inputs, U_m, are some weighting function of the input FDM signal $X(r)$. As a result, the fast DCT algorithm can be exploited to achieve tremendous savings in computation. The step-by-step derivation of a fast computational algorithm following this approach is presented in Appendix A.

The fast algorithm for SSB demodulation (FDM-TDM direction) is depicted in Figure 7 and is summarized as follows:

FDM-TDM fast algorithm

Given:

a. FIR filter with length $M + 1$, where $M = 2KN$, K is an even integer and N is the number of channels within $(0 \rightarrow f_s/2)$, and coefficients $\{h(m)\}$, $m = 0, \ldots, M$, which are symmetric with respect to $m = M/2$.

b. $X(r)$ = time-sampled FDM signal.

1. Compute:

$$U(Nr, 0) = \sum_{p=0}^{K} X(Nr - 2Np) \cdot (-1)^p \cdot h(2Np)$$

$$U(Nr, q) = \sum_{p=0}^{K-1} [X(Nr - 2Np - q) + X(Nr - 2NK + 2Np + q)] \cdot (-1)^p \cdot h(2Np + q), \qquad q \in \{1, \ldots, N - 1\} \quad .$$

2. Take the inverse discrete cosine transform:

$$Y_n(Nr) = \sum_{q=0}^{N-1} U(Nr, q) \cdot \cos\frac{\pi(2n + 1)q}{2N} \qquad n = 0, \ldots, N - 1 \quad .$$

3. Complement alternate samples for the even channels, i.e., $Y_n^*(Nr) = (-1)^{(n+1)r} Y_n(Nr)$. Now, $Y_n^*(Nr)$ is the desired output sample for the n-th demultiplexed channel.

4. Shift down the data stream, $X(r)$, by a block of N samples and repeat (1)–(3).

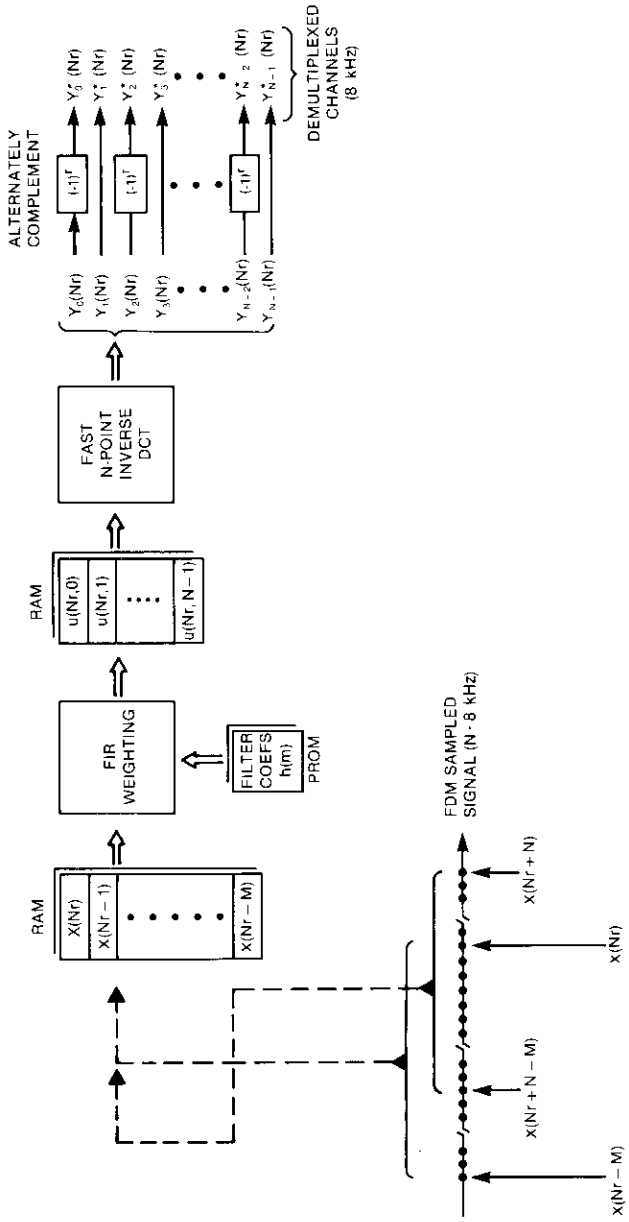

Figure 7. *FDM-TDM Fast Algorithm*

Frequency domain interpretation of digital SSB modulation

The SSB modulation process is depicted in Figure 8 for the case of four channels ($N = 4$). Figure 8a shows pictorial representations of the spectra of the input digital voice channels, each at the sampling rate $f_s' = 8$ kHz. Figure 8e shows the spectrum of the output FDM signal at a sampling frequency of $f_s = N \times 8$ kHz.

In Figure 8a, for the same sidebands to be extracted by the subsequent bandpass filtering, either the odd or even channels (depending on the sideband desired) have to be frequency-shifted by 4 kHz. Figure 8b shows where the even channels (0 and 2) are shifted.

Performing a 1:N interpolation by inserting $N - 1$ zeroes between pairs of adjacent samples [22]–[24] generates N interpolated signals, each at the sampling rate $f_s = N \times 8$ kHz. Figure 8c shows the resulting spectra.

The N interpolated signals are then filtered by a bank of N digital bandpass filters, each operating at frequency f_s. Figure 8d shows the filter characteristic and the signal spectra after filtering. Finally, a summation of the N filtered signals yields the desired FDM SSB signal (Figure 8e).

Time-domain interpretation of digital SSB modulation

Let

$s_n^*(p)$ = the p^{th} sample of the n^{th} voice channels at the sampling rate of $f_s' = 8$ kHz, $n \in \{0, \ldots, N - 1\}$

$X(r)$ = r^{th} sample of the output FDM signal at the sampling rate of $f_s = N \times 8$ kHz.

The process of forming the FDM signal, $X(r)$, from the collection of N individual voice signals $\{s_p^*(p), n = 0, \ldots, n - 1\}$ is conceptually depicted in Figure 9.

The signals for the even channels are first frequency shifted by 4 kHz, yielding

$$s_n(p) = s_n^*(p) \cdot (-1)^{(n+1)\cdot p}, \qquad n = 0, \ldots, N - 1 \quad .$$

A 1:N interpolation is performed on each of the N signals by inserting

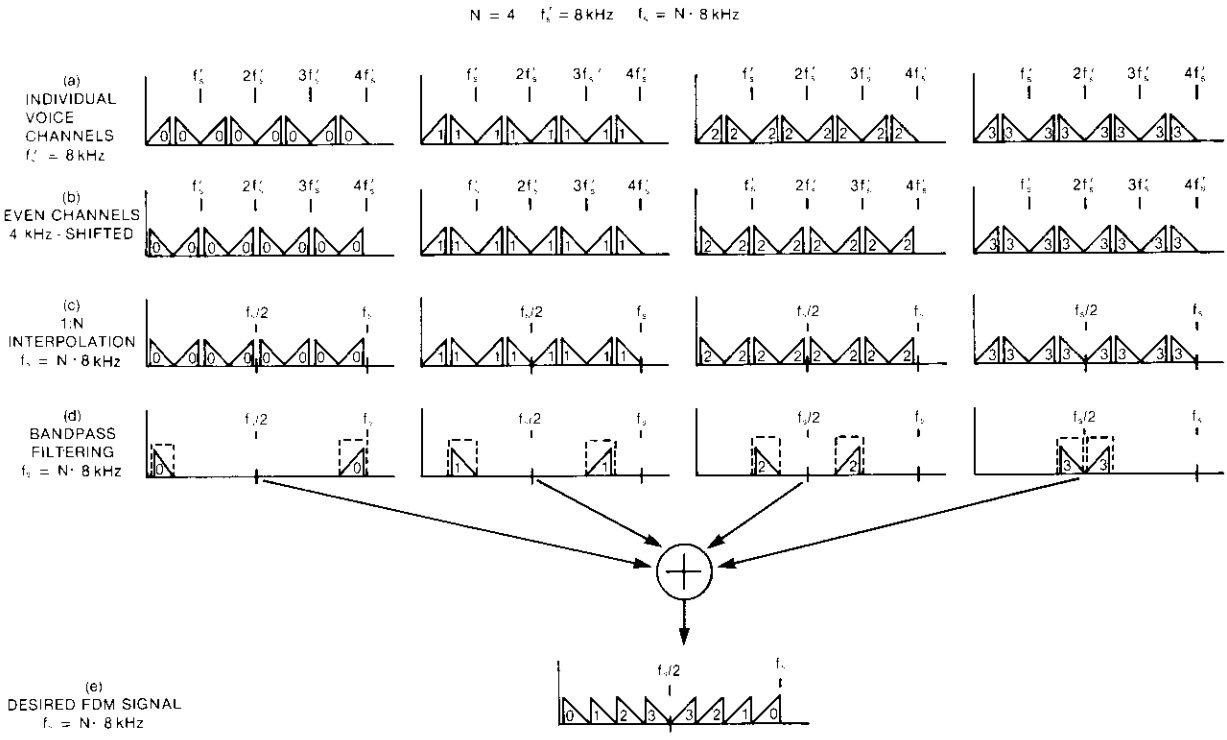

Figure 8. *Digital SSB Modulation in the Frequency Domain (N = 4)*

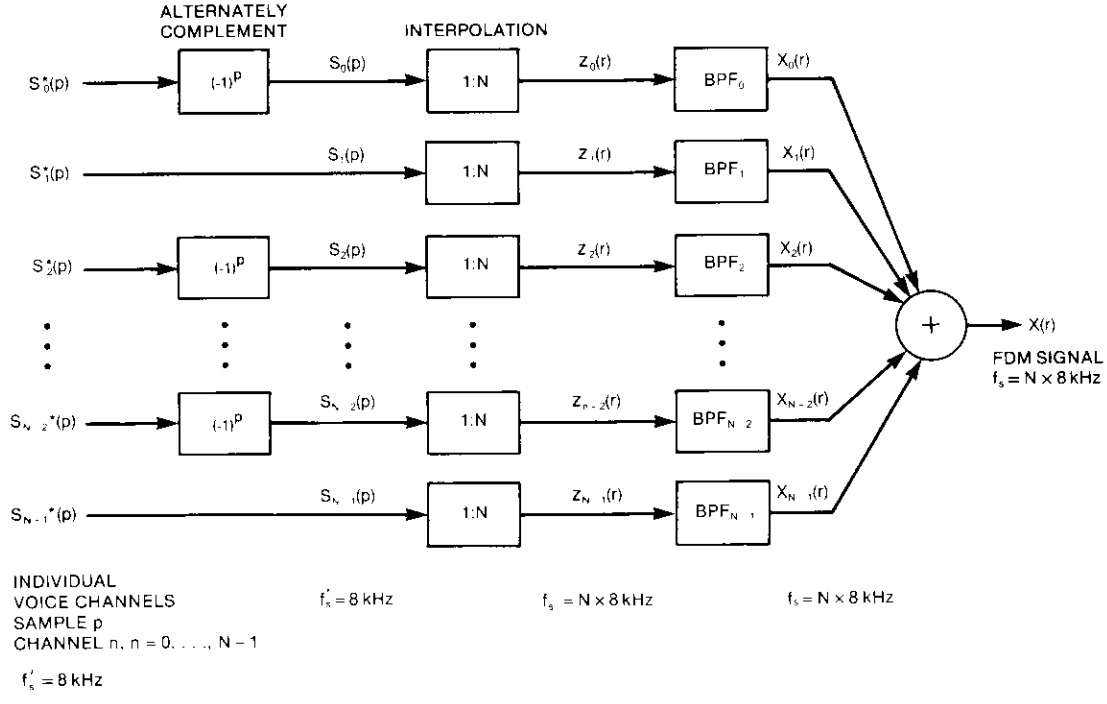

Figure 9. *Basic Digital SSB Modulation Process in the Time Domain*

$(N - 1)$ zeros between samples. Let

$$r = pN + q, \qquad q \in \{0, 1, \ldots, N - 1\} \quad . \tag{4}$$

The interpolated data streams can be expressed as

$$Z_n(r) = \begin{cases} s_n(p) & \text{for } r = pN \\ 0 & \text{for } r \neq pN \end{cases} \qquad n \in \{0, 1, \ldots, N - 1\} \quad . \tag{5}$$

The interpolated signals are then filtered by the appropriate bandpass channel filters, each operating at f_s. This yields

$$X_n(r) = \sum_{m=0}^{M} Z_n(r - m) \cdot h(m) \cdot \cos\left(\frac{\pi(2n + 1) \cdot m}{2N}\right) \qquad n \in \{0, 1, \ldots, N - 1\} \quad . \tag{6}$$

The desired FDM signal, $X(r)$, is finally obtained as the sum of the N filtered signals.

$$X(r) = \sum_{n=0}^{N-1} \sum_{m=0}^{M} Z_n(r - m) \cdot h(m) \cdot \cos\left(\frac{\pi(2n + 1) \cdot m}{2N}\right) \qquad r \in \{pN, pN + 1, \ldots, pN + N - 1\} \quad . \tag{7}$$

Equation (7) represents the essence of the digital processing in the TDM-FDM direction of the transmultiplexer. Given one "frame" of N sample for the N voice channels, a block of N consecutive samples of the FDM signal are generated.

If equation (7) is implemented, the filter coefficients and the cosine terms can be premultiplied, and the computation requirement per "frame" (by properly skipping the zero terms) is

number of multiplications: $N \cdot (M + 1)$
number of additions: $M \cdot N + (N - 1)$
memory (RAM) [for $Z_n(r - m)$]: $(M/N + 1) \cdot N$
memory (PROM) [for $h_n(m)$]: $(M + 1) \cdot N$.

Fast algorithms for TDM-FDM direction

The computation of $X(r)$ in equation (7) can be reformulated as a weighted sum of the outputs of an N^{th} order discrete cosine transform

(DCT) of the input voice samples. This will allow use of the fast DCT algorithms. A further 2:1 reduction in computation can be achieved by using an iterative scheme. To study the different computation alternatives, step-by-step derivation of three fast algorithms starting with the basic formulation (and without relying on the "transpose" relation with the opposite direction) is presented in Appendix B.

The final fast algorithm (Algorithm C) obtained is depicted in Figure 10 and is summarized as follows:

TDM-FDM fast algorithm (Algorithm C)

a. Given the input individual voice channel samples $s_n^*(p)$ where

n = channel index = $0, \ldots, N - 1$
p = frame index
N = number of channels .

and FIR filter coefficients $\{h(m)\}$, $m = 0, \ldots, M$, where $M = 2KN$ and K is an even integer. Complement alternate samples for the even channels

$$s_n(p) = s_n^*(p) \cdot (-1)^{(n+1)\cdot p} \quad .$$

b. Take the DCT of each incoming $s_n(p)$ frame

$$S_p(q) = \sum_{n=0}^{N-1} s_n(p) \cdot \cos\left(\frac{\pi(2n + 1) \cdot q}{2N}\right) \qquad q = 0, 1, \ldots, N - 1$$

and store the DCT outputs S.

c. For each DCT output frame $S_p(q)$, $q \in \{0, \ldots, N - 1\}$ compute

$$U_p(q, \ell) = h(q + 2\ell N)(-1)^{\ell} \cdot S_p(q), \qquad \ell \in \{0, \ldots, K - 1\}, \quad q \in \{0, \ldots, N - 1\} \quad .$$

d. Compute partial sums

$$\begin{aligned} Y_p(0, 2\ell) &= U_p(0, \ell) + Y_{p-1}(0, 2\ell + 1), && \ell \in \{0, \ldots, K - 1\} \\ Y_p(0, 2K - 1 - 2\ell) &= Y_{p-1}(0, 2K - 2\ell), && \ell \in \{0, \ldots, K - 1\} \\ Y_p(0, 2K) &= U_p(0, 0), && \ell = 0 \\ Y_p(q, 2\ell) &= U_p(q, \ell) + Y_{p-1}(q, 2\ell + 1), && \ell \in \{0, \ldots, K - 1\} \end{aligned}$$

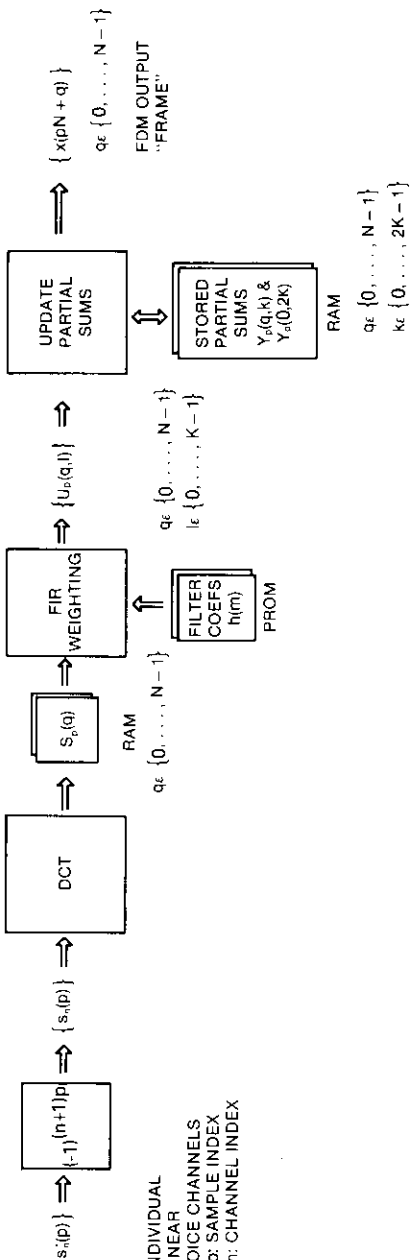

Figure 10. *TDM-FDM Fast Algorithm (Algorithm C)*

$$Y_p(q, 2K-1-2\ell) = U_p(N-q, \ell) + Y_{p-1}(q, 2K-2\ell), \quad \ell \in \{1, \ldots, K-1\}$$

$$Y_p(q, 2K-1) = U_p(N-q, 0), \quad \ell = 0$$

$$q \in \{1, \ldots, N-1\} \quad .$$

e. Store $\{Y_p(q, 1), Y_p(q, 2), \ldots, Y_p(q, 2K-1)\}$, $q \in \{0, \ldots, N-1\}$, and $Y_p(0, 2K)$

f. Output current FDM "frame"

$$X(pN + q) = Y_p(q, 0), \quad q \in \{0, \ldots, N-1\} \quad .$$

g. For the next input "frame," repeat steps *a* through *f*.

Supergroup transmultiplexer

The supergroup transmultiplexer being considered provides translation between a basic FDM supergroup and two 30-channel CEPT, 2.048-Mbit/s TDM/PCM data streams [25]. The basic FDM supergroup signal (BSG) consists of 60 voice channels with upper sidebands in the 312- to 552-kHz frequency band as shown in Figure 11. To apply the above digital processing technique to supergroup multiplex-demultiplex, the FDM spectrum must first be reduced to a form similar to that shown in Figure 4a. This requires the judicious selection of the sampling frequency for the supergroup signal and possibly some form of frequency translation. There are two feasible schemes: frequency translation and bandpass sampling.

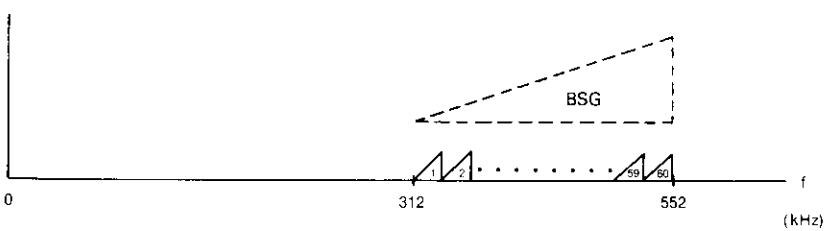

Figure 11. *Analog Basic Supergroup Spectrum*

The frequency translation scheme is illustrated in Figure 12, where the analog supergroup signal is first band limited (315–552 kHz). Then an analog modulation of a 560-kHz carrier is performed, which

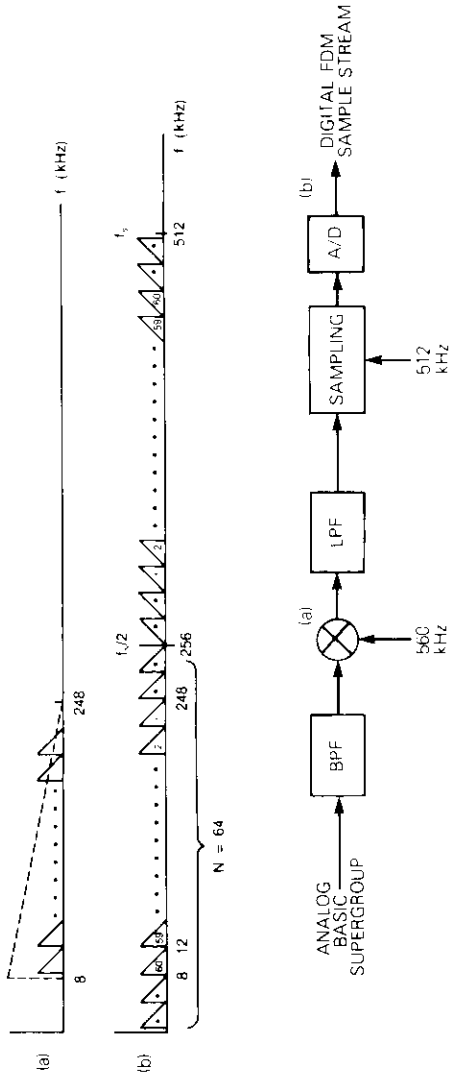

Figure 12. *Frequency Translation*

results in a collection of 60 inverted channels at 8–248 kHz. Subsequent analog low-pass filtering can be performed if needed. Then the signal is sampled at a sampling rate of f_s = 512 kHz. A total of 64 4-kHz frequency slots now occupy the frequency band 0–f_s/2, with two dummy slots on each side of the 60 voice channels. As $N = 64 = 2^6$, FFT algorithms for power-of-two orders, such as the Cooley-Tukey algorithm [26], can be used to construct the 64th order DCT algorithm.

The bandpass sampling scheme is illustrated in Figure 13, where the analog supergroup signal is first band limited (312–552 kHz). Then the signal is directly sampled at a rate f_s = 576 kHz. A total of 72 inverted 4-kHz channels now occupy the frequency band $0 \rightarrow f_s/2$, with six dummy channels residing on each side of the 60 voice channels. No analog frequency translation is involved here, and since $N = 72$, which is not a power of two, more advanced algorithms must be used for the DCT computation.

The bandpass sampling scheme has been adopted for implementation because the extra frequency modulation step can be eliminated, and the presence of six dummy slots on each side provides a wider guard band, therefore requiring less stringent supergroup bandpass filtering.

Figure 14 depicts the overall configuration of the supergroup transmultiplexer. In the TDM-FDM direction, the interface buffer at TDM interface performs the required interface and synchronization functions as well as the serial-to-parallel conversion for the two 2.048-Mbit/s PCM bit streams. The expander transforms the 8-bit A-law compressed codes into the 13-bit linear codes, which are required by the subsequent arithmetic operations. The combination of the 72-point forward DCT and the FIR weighting network corresponds to the fast digital SSB modulation algorithm which has been developed above. Algorithm C using the iterative approach is employed for the weighting network. Finally, the output digital FDM sample stream at a 576-kHz sampling rate is converted into a standard analog supergroup signal (312–552 kHz) by the digital-to-analog (D/A) converter and the analog supergroup filter, using the bandpass sampling scheme described above.

The processing in the FDM-TDM direction essentially represents an inverse operation as compared to the TDM-FDM direction. The FDM basic supergroup signal is first band limited (312–552 kHz) and then directly sampled at 576 kHz. An A/D converter transforms the time samples into digital form. The resulting digital supergroup data stream is then treated by the fast digital SSB demodulation processor, which consists of a combination of the FIR weighting network and the

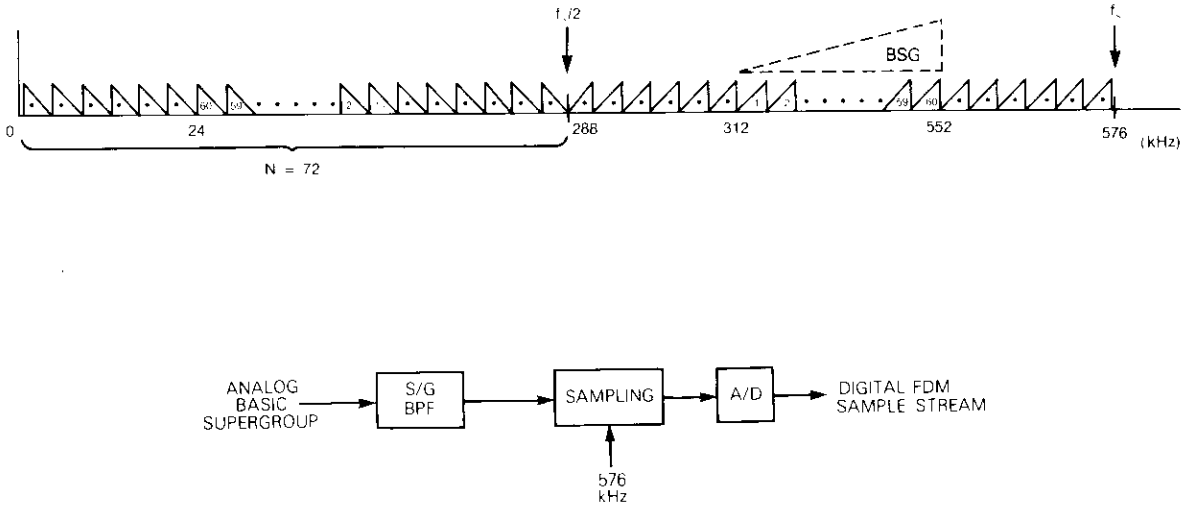

Figure 13. *Bandpass Sampling*

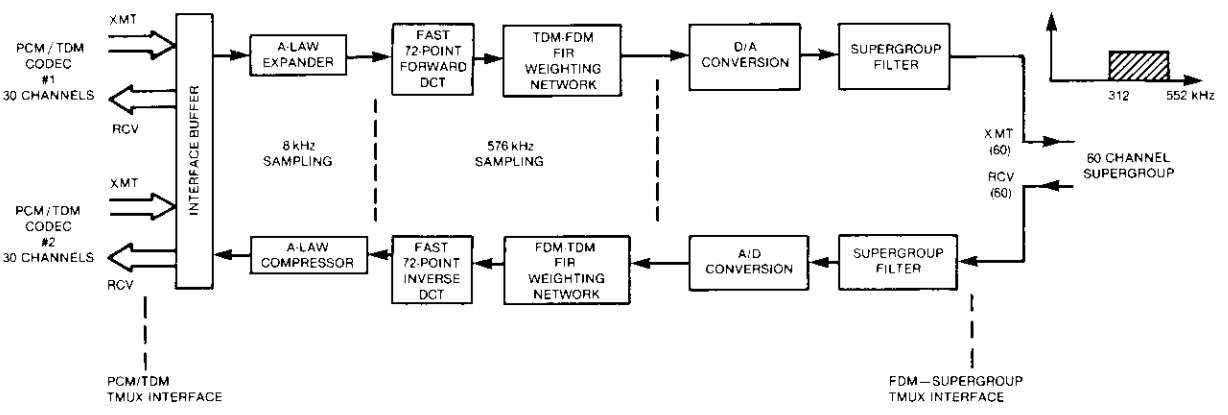

Figure 14. *60-Channel Supergroup Transmultiplexer*

72-point inverse discrete cosine transform (DCT) discussed earlier. The output of the processor is a frame of 60 samples for the 60-voice channel, each linearly encoded with 13-bit and at 8-kHz rate. The parallel voice samples are then compressed into 8-bit codes by the A-law compressor, and converted by the interface buffer into two 2.048-Mbit/s 30-channel serial bit streams.

Discrete cosine transform

The forward and inverse DCT are defined as follows.

a. Forward DCT: given inputs $f(0), \ldots, f(71)$,

$$F(r) = \sum_{k=0}^{71} f(k) \cos\left(\frac{\pi(2k+1)r}{144}\right) \quad , \qquad r = 0, \ldots, 71 \quad .$$

b. Inversed DCT: given inputs $G(0), \ldots, G(71)$,

$$g(k) = \sum_{r=0}^{71} G(r) \cos\left(\frac{\pi(2k+1)r}{144}\right) \quad , \qquad k = 0, \ldots, 71 \quad .$$

Compared to the conventional fast Fourier transforms (FFTs), such as the well-known Cooley-Tukey algorithms, the above defined DCTs are unique in several respects;

a. they are real-input/real-output transforms containing one "odd" index;
b. the required order of the DCTs, 72, corresponds to a relatively large and yet nonpower-of-two number;
c. the pair of "forward" and "inverse" DCTs defined above are not truly inverse of each other (that is, taking the inverse DCT on the outputs of the forward DCT will not recover the inputs of the forward DCT); and
d. the transforms previously defined do not exactly possess the orthogonal property.

The forward DCT can be represented as a standard DFT of the same order plus an exponential post-multiplication operation and proper index mappings [27]. Similarly, the inverse DCT can be represented as a standard DFT plus an exponential premultiplication operation and proper index mapping. Based on this, any fast algorithm for the standard DFT can be utilized to reduce the computational complexity.

However, the relatively large and nonpower-of-two order of the transforms, 72, calls for more sophisticated DFT algorithms when compared to the conventional butterfly-type algorithms. The required 72-point DFT can be constructed using multiples of 8-point and 9-point DFT algorithms as building blocks, plus proper exponential (twiddle factor) multiplication and index mapping. Further, the efficient Winograd-type small-N algorithms [28],[29] can be applied for the 8-point and 9-point DFTs. These algorithms evolved through the use of algebraic field theory (principally the Chinese Remainder Theorem) for reducing the computational complexity (especially the number of multiplications), and they normally do not possess the well-formed structures inherent in the butterfly-type FFT algorithms. Figures 15 and 16 show block diagrams of the resulting forward and inverse DCT algorithms. The forward DCT fast algorithm following this scheme requires 664 real multiplications and 911 real additions. The inverse DCT requires 696 real multiplications and 862 real additions. For comparison, the straightforward computation, according the basic DCT or IDCT formula, would each require 5,184 real multiplications and 5,112 real additions. Description of the detailed fast DCT algorithm development is complicated and beyond the scope of this paper.

Prototype FIR filter design

The performance of the transmultiplexer is crucially dependent on that of the prototype FIR low-pass filter, because the bandpass filters performing the channel-extraction function are simply the up-translated versions of the prototype filter. For the same reason, the voice-channel frequency response is symmetrical with respect to 2 kHz. The CCITT Recommendation G.792 [30] for the transmultiplexer has been used as the performance criterion. The essential performance parameters related to the channel filter include the following:

a. voice channel frequency response (specified mask, ±0.6 dB midband ripple),
b. intelligible crosstalk (65 dB),
c. unintelligible crosstalk (−60 dBm0p),
d. idle-channel noise, with all channels loaded except the one being measured (−62.5 dBm0p).
e. group delay distortion (specified mask, 0.5-ms midband distortion), and
f. absolute delay (3 ms).

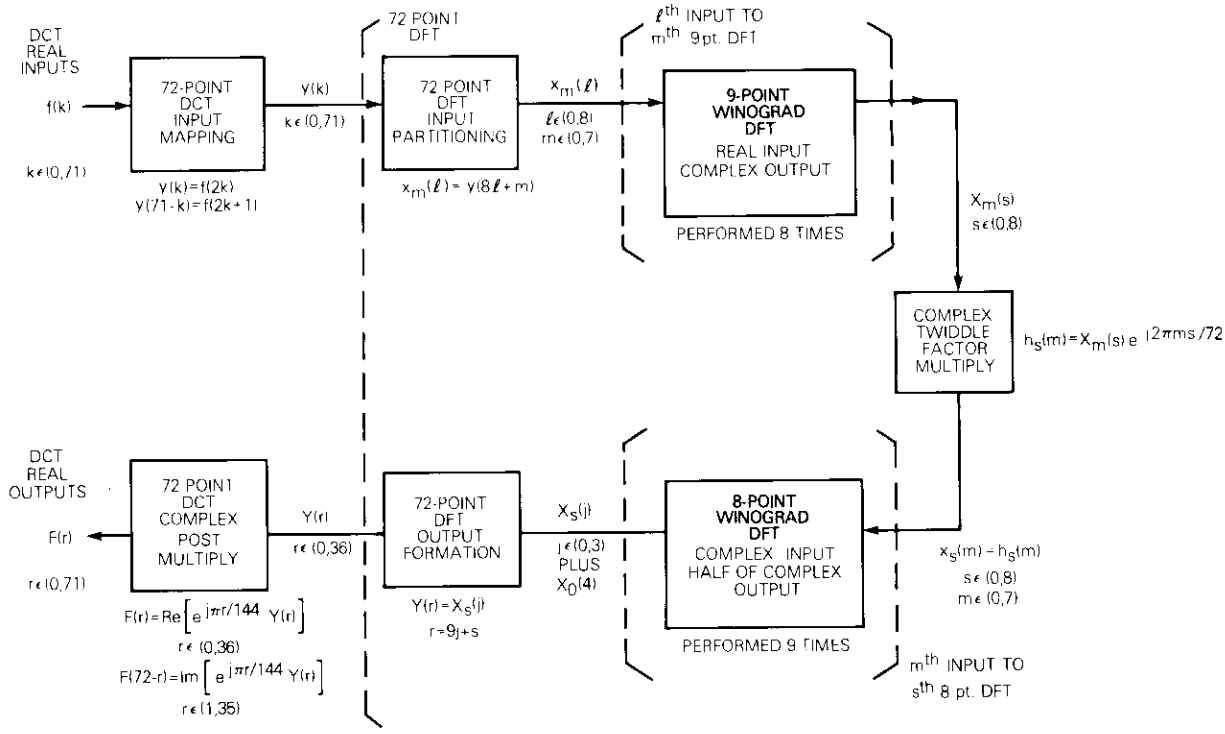

Figure 15. *Fast 72-Point Forward DCT Algorithm*

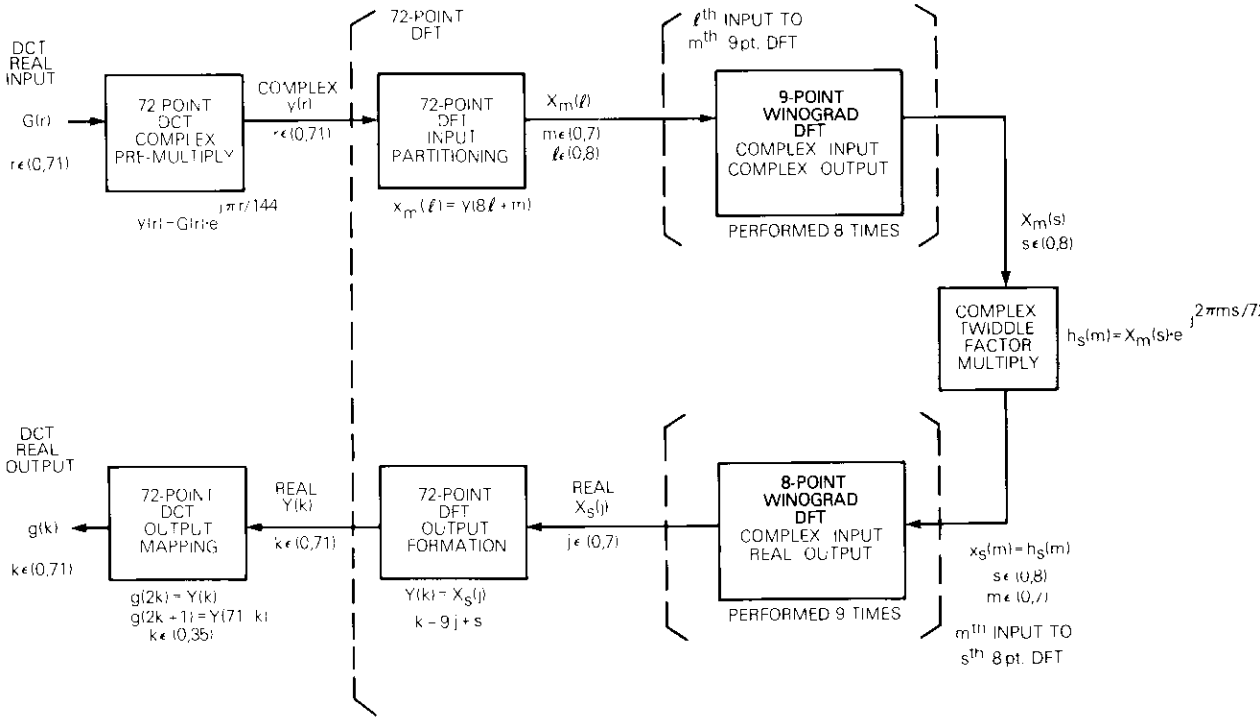

Figure 16. *Fast 72-Point Inverse DCT Algorithm*

The last two performance parameters are intrinsically related to the system design using an FIR filter, but are not dependent on the detailed filter characteristics. The first four performance parameters are used to define the design specification for the prototype low-pass filter. The specification is very stringent by normal filter design standards;

a. passband width equal to 0.00295 of the normalized frequency,
b. transition width equal to 0.00096 of the normalized frequency,
c. in-band ripple within ±0.3 dB,
d. stopband rejection greater than 82 dB, and
e. roll-off effect conforming to the CCITT mask (piecewise linear).

This specification allows margins for the finite word-length effect and system loopback effect, and requires a filter length of 3,169 taps ($K = 22$).

The digital filter design has been accomplished using the constrained ripple technique [31], in which the digital filter design problem is transformed into a numerical polynomial interpolation problem. Briefly, the frequency response of a real (even response) low-pass filter of odd length can be expressed as a cosine polynomial of the order equal to half the filter length. For a 3,169-tap filter, the frequency response is

$$G(f) = h(1584) + \sum_{k=1}^{1584} 2h(1584 - k)\cos(2\pi kf)$$

where $h(k)$ is half of the symmetric FIR filter coefficient. Given a frequency response specification, expressed as a mask of upper and lower bounds in the $G(f)$ versus f plane, the filter design problem is equivalent to finding a set of coefficients, $h(k)$, such that the cosine polynomial $G(f)$ is always within the given bounds along the entire f-axis. By substituting $x = \cos(2\pi f)$ and repeated use of the identity $\cos[(m + 1)\theta] \equiv 2\cos(\theta)\cos(m\theta) - \cos[(m - 1)\theta]$, the cosine polynomial can be transformed into a regular power polynomial of the same order as

$$Z(x) = \sum_{k=0}^{1584} b_k \cdot x^k \quad .$$

In the x-domain, any known numerical technique for solving the power polynomial interpolation problem can now be applied. For

computation convenience, the power polynomial can be expressed in the barycentric Lagrangian form [32], as

$$y(x) = \frac{\sum_{k=0}^{1584} \frac{C_k Y_k}{(x - x_k)}}{\sum_{k=0}^{1584} \frac{C_k}{(x - x_k)}}$$

where $\{[x(0), y(0)], \ldots, [x(1584), y(1584)]\}$ are a set of known "interpolation points," and

$$C_k = \frac{1}{(x_k - x_0)(x_k - x_1)\ldots(x_k - x_{k-1})(x_k - x_{k+1})\ldots(x_k - x_{1584})}$$

are the Lagrangian interpolating coefficients. The polynomial interpolation problem can be solved with a digital computer by employing an iterative optimization algorithm based on the local search and divided-difference concepts.

The numerical computation for the optimization with the given order and input specification has imposed extremely severe requirements in terms of computer time, memory, numerical precision, and dynamic range. The dynamic range has exceeded the normal capability of even a large computer such as an IBM 3032. To surmount these problems, special numerical schemes have been devised.

A 3,169-tap FIR filter has been designed which fulfills the specification. With a 16-bit arithmetic word length, the filter performance fully meets or surpasses the first four CCITT criteria listed above (the ones directly determined by the filter spectral characteristics). Moreover, a second prototype filter which has midband ripple complementary with respect to the first filter, has been designed to further improve the overall ripple response, when the pair is used in the opposite directions.

The group delay distortion should theoretically be zero for a system using an FIR filter with symmetric coefficients. This is true because such a filter is a linear-phase filter and the group delay response (the derivative of phase with respect to frequency) is absolutely constant with frequency, independent of the detailed filter design. This performance will be particularly attractive for voiceband data transmission through the transmultiplexer.

The absolute delay is principally determined by the half-length of the filter's impulse response; therefore, it is also intrinsic to the basic

system design. With the given filter length and sampling rate, a total loopback (two-way) delay of 6 ms has resulted. This exceeds the CCITT specified value of 3 ms. For geostationary orbit satellite applications that have an inherent delay of 240 ms, this delay is insignificant. With this understanding, the 6-ms delay was accepted to achieve a substantially more attractive system design.

Comparison of computation requirements

Table 1 summarizes rough estimates (based on mathematical expressions) of the computation requirements in the FDM-TDM direction in terms of number of multiplications, number of additions, RAM memory size and PROM memory size, for the fast algorithm and for direct computation. It is assumed that $N = 72$ and $K = 22$ (filter length = 3,169). The comparison shows that up to 100:1 savings in computation can be gained by the fast algorithm. A similar saving can be gained in the TDM-FDM direction as summarized in Table 2.

Synchronization and interface

Because of the nature of digital signal processing, the frequency accuracy of the FDM carrier being generated is dictated by the frequency accuracy of the clock source (master oscillator) for the hardware circuitry in the transmultiplexer. The frequency accuracy of a standard FDM supergroup carrier is specified by CCITT Recommendation G.225

TABLE 1. COMPUTATION REQUIREMENT PER FRAME FOR FDM-TDM DIRECTION (K = 22)

ALGORITHM	NUMBER OF MULTIPLICATIONS	NUMBER OF ADDITIONS	MEMORY (RAM)	MEMORY (PROM)
Fast Algorithm FIR Weighting	1,585	3,075	3,241	1,585
Inverse DCT	696	862	144	20
Total	2,281	3,937	3,385	1,605
Direct Computation	228,168	228,096	3,169	228,168
Percentage (fast algorithm/ direct computation)	1%	1.36%	107%	0.7%

TABLE 2. COMPUTATION REQUIREMENT PER FRAME FOR TDM-FDM DIRECTION (K = 22)

ALGORITHM	NUMBER OF MULTIPLICATIONS	NUMBER OF ADDITIONS	MEMORY (RAM)	MEMORY (PROM)
Fast Algorithm C FIR Weighting	1,584	3,124	3,241	1,585
Forward DCT	664	911	144	20
Total	2,248	4,035	3,385	1,605
Direct Computation (properly skipping zero terms)	228,168	228,240	3,240	228,168
Percentage (fast algorithm/ direct computation)	1%	1.7%	104%	0.7%

to be $\pm 10^{-7}$ [33]. Therefore, if the transmultiplexer is internally synchronized, a free-running master oscillator with accuracy of $\pm 10^{-7}$ or better must be provided. If it is synchronized to the external world by phase-lock technique, the external timing reference must meet the same accuracy requirement. Note that the frequency accuracy of the standard PCM bit streams is specified by CCITT to only within ± 50 parts per million (ppm) [25], which does not meet the requirement on the FDM side.

For satellite TDMA applications, it has been proposed that cesium beam oscillators of 1×10^{-11} accuracy be used in the reference station. In such a system, the major contribution to the frequency variation is due to the Doppler effect arising from satellite drift in the geostationary orbit [34]. The drift in the form of a daily excursion causes a variation in the transmission path length between an earth station and the satellite. For the INTELSAT V satellite, the nominal stationkeeping specification is $\pm 0.1°$ in latitude and longitude, but the stationkeeping may be relaxed to $\pm 0.5°$ in latitude in a portion of the satellite lifetime. For this worst case, the maximum peak-to-peak variation in station-to-station transmission time has been determined to be 1.1 ms and the maximum rate of change to be 40 ns/s.

The above phenomenon affects the transmultiplexer in two ways. First, the worst-moment frequency accuracy of the TDMA clock in the presence of Doppler effect is on the order of 10^{-8}. Therefore, from

the FDM side standpoint, it is possible to use the TDMA clock as an external synchronization signal for the transmultiplexer. Secondly, the Doppler effect causes the TDMA transmit and receive clock rates at a given earth station to be different. Frame slipping will occur if the transmultiplexer is synchronized to only one of the two clocks. To be completely immune to the Doppler effect, independent of the satellite stationkeeping performance, the transmultiplexer should be so implemented that its transmit and receive sides can operate according to independent timing references. A less direct solution would be to provide a Doppler compensation buffer on one side of the digital interface, with capacity being able to "absorb" the worst-case variation. For INTELSAT V, a buffer capacity equivalent to 2.2 ms would be required, assuming the buffer has no knowledge of the satellite position during its startup.

The supergroup transmultiplexer under consideration has been designed with completely separate transmit and receive processing sections, with identical but independent timing circuitries. On each side, a 55.296-MHz master VCXO is used and is phase locked to an external 8-kHz frame reference via a phase-locked loop (PLL) circuit. For direct interface with the DSI unit, the digital interface conforms to the standard CEPT data format but without the A-law even-bit inversion and the HDB3 encoding. This allows direct interface using the external timing references and eliminates frame-word detection.

Hardware design

The four fast digital signal processing algorithms within the supergroup transmultiplexer (the two FIR weighting networks, and the 72-point forward and inverse fast DCTs) have a common characteristic in that they require relatively flexible control for arithmetic operations. For example, the 72-point forward DCT requires a controlled repetition of 9-point and 8-point DFTs, in addition to the exponential multiplications. Each 9-point Winograd DFT algorithm in turn requires 51 steps of unique arithmetic operations and each 8-point DFT requires 42 steps. A second requirement for the digital processing is the real-time speed requirement that each algorithm must be completed within 125 μs (8-kHz period).

To best accommodate the flexibility and real-time speed requirements, the design of the digital signal processing units has been based on a microcodable, PROM-based, computer-like architecture. Three different high-speed hardware processors have been custom-designed, one for the FDM-TDM weighting, one for the TDM-FDM weighting, and

one for the DCT (both forward and inverse). Each processor is composed of arithmetic units (*e.g.*, multipliers, adders, and accumulators), memory segments, input/output ports, and a network of data and address buses. The architecture of each processor has been designed to intimately fit the basic computation requirements of the respective algorithm. The hardware structures are then "programmed" to perform the desired sequences of arithmetic operations, with the program steps (firmware) being stored in PROMs. A microcode generation (compiling and assembling) software package has been specially developed to allow firmware coding using a high-level human-interpretable language and to effectively implement pipelining operations to optimize the computation throughput. The programmability feature of the design permits not only rapid modification of program steps resulting in a shortened system development time; it also allows the hardware to be "reprogrammed" in the future for other system applications, such as for other basic FDM assemblies, without the need to redesign the major digital signal processing hardware, provided the future requirement is within the processor's capability (*e.g.*, speed and memory size).

Figure 17 illustrates the PROM-based control concept for the processors. A 55.296-MHz VCXO is first divided down to generate the 13.824-MHz system master clock. The master clock then drives a divide-by-1,728 master counter to partition each 125-μs (8 kHz) frame interval into 1,728 program steps, which corresponds to the maximum program length. The master counter is then used to sequentially address a set of PROMs whose outputs are the micro-instruction for each clock interval for the digital signal processors.

The prototype supergroup transmultiplexer uses a 13-bit D/A converter and a 12-bit A/D converter. The internal arithmetic is fixed point with a 16-bit word length. Multiplication is achieved using the TRW 16-bit LSI fixed-point parallel multipliers (MPY-16HJ) and multiplier-accumulator (MAC, TDC1010J).

The hardware design was implemented with TTL logic because that was perceived to offer the best compromise of speed and LSI/MSI component selection. Efforts to reduce the total power requirement have resulted in the use of a mixture of LS, S, and FAST logic families; that is, extensive use of LS components has been made in those areas permitting the larger propagation delay associated with this logic family. FAST components were employed wherever the speed required mandated its use and finally, S components were used where, in addition to a speed requirement, there was a significant output drive requirement which the FAST component would not satisfy.

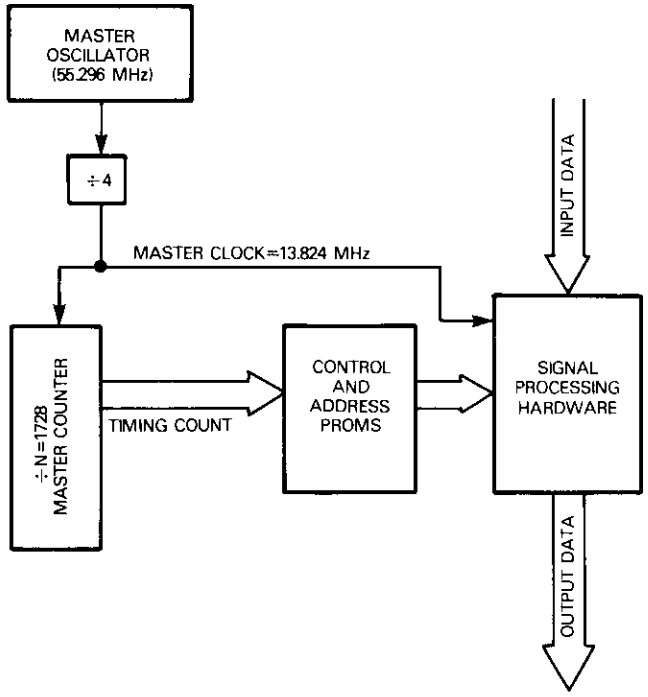

Figure 17. *PROM-Based Control Concept*

Figure 18 illustrates, in block diagram form, the actual hardware partitioning of the implemented prototype supergroup transmultiplexer. Each block in the diagram corresponds to a single Augat 6 section card of wire-wrapped electronics. The four major signal processor cards are completely populated and the remaining six cards are approximately one-third utilized. Figure 19 is a photograph of the prototype supergroup transmultiplexer. To refabricate the unit using printed circuit cards, the overall size can be reduced by a ratio of almost 2:1, and therefore a 120-channel system can be housed in a bucket of similar size.

Performance evaluation

The prototype supergroup transmultiplexer has been developed and tested. The objective test results have verified that its performance satisfies the relevant CCITT recommendations. Subjective evaluation

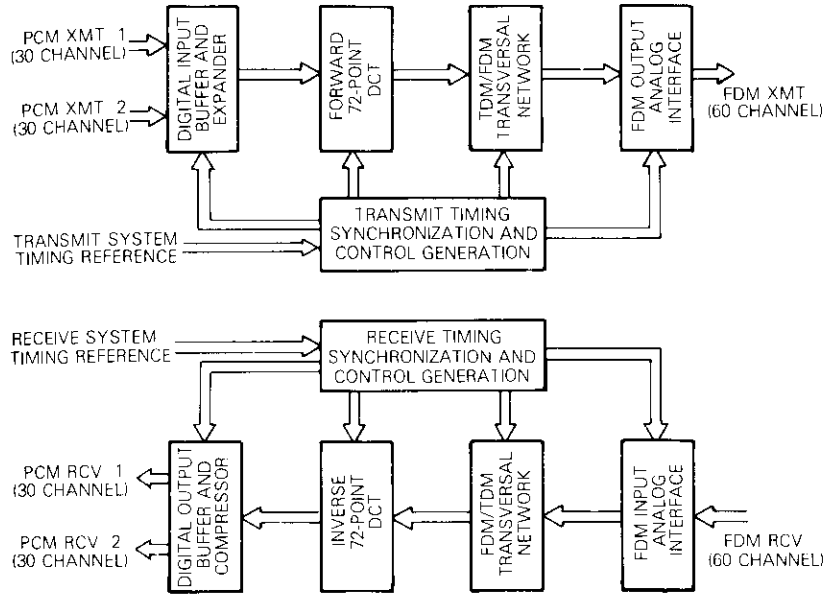

Figure 18. *Transmultiplexer Hardware Block Diagram*

under the full 60-channel actual voice loading condition has shown that the voice through the channels is of high subjective quality. The power consumption for the present prototype unit is 200 W. For a second-generation design, a reduction of the power consumption to 150 W appears achievable.

Signaling and pilots

Signaling or pilot processing has not been implemented in the prototype transmultiplexer. For the planned INTELSAT TDMA/DIS application, CCITT signaling system No. 5 will be used. The signaling information, represented by tones within the audio band, will be processed and transmitted in the same way as the speech signals. The transmultiplexer thus becomes transparent to the signaling system and no special processing for signaling is required.

The processing of signaling and pilots corresponds to the mapping of information between the respective representation formats in the FDM and PCM domains. The major problem involves the detection and

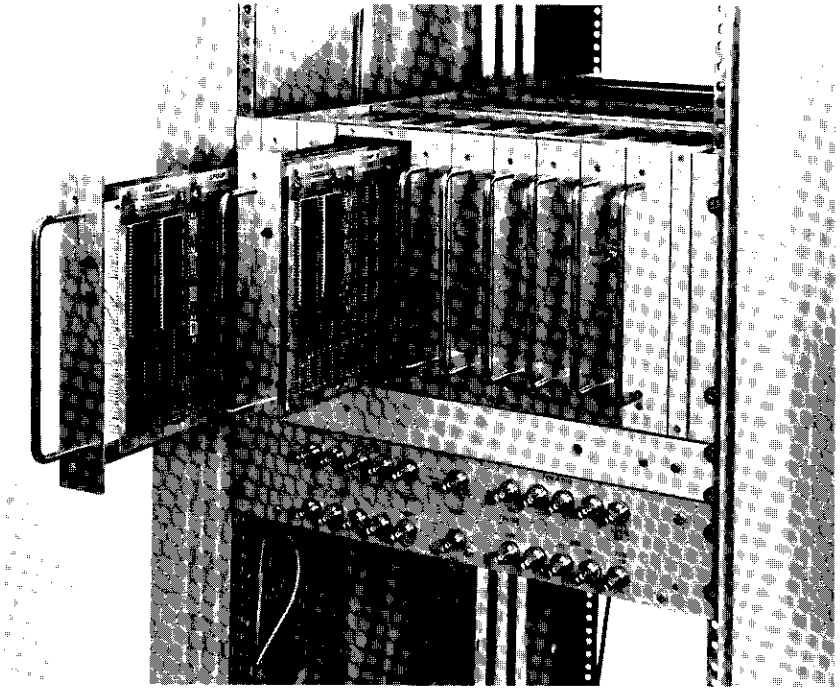

Figure 19. *Transmultiplexer*

insertion of slowly varying tones at fixed frequency locations. Commonly used signaling frequencies include 2,600 Hz (in-band signaling) and 3,825 Hz (out-of-band signaling). The common pilot frequencies correspond to 3,920 Hz within a voice channel. The desired task can be accomplished by digital signal processing techniques.

Conclusion

After a review of fundamentals, fast computational algorithms were obtained and applied to the hardware implementation of a prototype 60-channel supergroup transmultiplexer. Custom-designed, high-speed processors were developed for the major digital signal processing tasks including the fast DCT and FIR weighting algorithms. The design adopted a PROM-based microprogrammable concept, which offers flexibility in arithmetic control and for possible future system modification. The transmultiplexer was designed with independent timing controls for its two directions, ensuring its normal operation in a satellite TDMA network. The design of a 3,169-tap FIR prototype filter to meet the performance objectives was accomplished. The prototype supergroup transmultiplexer hardware has been developed and tested. Objective and subjective evaluations have verified that its performance meets the desired CCITT recommended standards and offers high voice quality under the full-load condition.

The implemented transmultiplexer has also manifested its merit of hardware simplicity. For example, compared with a previous transmultiplexer design at COMSAT Laboratories, which used a complex Weaver approach with 2-stage FIR-IIR filtering, an almost 2:1 reduction in hardware complexity was obtained. The improvement resulted from the elimination of hardware redundancy in the real-imaginary and 2-stage processing. More significantly, without the limit cycle effect of the IIR filtering, a 16-bit internal arithmetic word length has been verified to be sufficient to achieve the required signal-to-noise performance.

Acknowledgment

The authors wish to acknowledge the significant involvement of A. G. Gatfield in this project. They would also like to thank D. McAuliffe for his assistance in hardware implementation. Encouragement from S. J. Campanella and R. K. Garlow is appreciated.

References

[1] D. K. Weaver, "The Third Method of Generation and Detection of SSB Signals," *Proc. IRE,* December 1956, pp. 1703–1705.

[2] S. Darlington, "On Digital SSB Modulators," *IEEE Transactions on Circuit Theory,* Vol. CT-12, August 1970, pp. 409–414.

[3] S. L. Freeny et al., "Design of Digital Filters for an All-Digital FDM-TDM Translator," *IEEE Transactions on Circuit Theory,* Vol. CT-13, No. 4, November 1971, pp. 702–711.

[4] S. L. Freeny et al., "System Analysis of a TDM-FDM Translator A-Type Channel Bank," *IEEE Transactions on Communications Technology,* Vol. COM-19, December 1971, pp. 1050–1059.

[5] Z. M. Ali, "Fixed-Point, Parallel Arithmetic Digital Signal Processor," *COMSAT Technical Review,* Vol. 8, No. 2, Fall 1978, pp. 273–330.

[6] M. A. Bellanger and J. L. Daquet, "TDM-FDM Transmultiplexer: Digital Polyphase and FFT," *IEEE Transactions on Communication,* Vol. COM-22, September 1974, pp. 1199–1205.

[7] M. A. Bellanger, A. Bonnerot, and M. Coudreuse, "Digital Filtering by Polyphase Network: Application to Sample-Rate Alteration and Filter Banks," *IEEE Transactions on Acoustic, Speech, and Signal Processing*, Vol. ASSP-24, April 1976, pp. 109–114.

[8] G. Bonnerot, M. Coudreuse, and M. G. Bellanger, "Digital Processing Techniques in the 60-Channel Transmultiplexer," *IEEE Transactions on Communication*, Vol. COM-26, May 1978, pp. 698–706.

[9] R. Maruta and A. Tomozawa, "An Improved Method for Digital SSB-FDM Modulation and Demodulation," *IEEE Transactions on Communication*, Vol. COM-26, No. 5, May 1978, pp. 720–725.

[10] F. Mano et al., "TDM-FDM Transmultiplexer Development," *Proc. of ICC '80*, June 1980, pp. 47.4.1–47.4.5.

[11] T. Aoyama et al., "120-Channel Transmultiplexer Design and Performance," *IEEE Transactions on Communication*, Vol. COM-28, No. 9, September 1980.

[12] F. Takahata et al., "Development of a TDM/FDM Transmultiplexer," *IEEE Transactions on Communication*, Vol. COM-26, No. 5, May 1978, pp. 726–733.

[13] F. Takahata, K. Inagaki, and A. Ogawa, "Design of Digital Signal Processor in a TDM/FDM Transmultiplexer," *Proc. ICC*, 1980.

[14] M. J. Narasimha and A. M. Peterson, "Design and Applications of Uniform Digital Bandpass Filter Banks," *Proc.*, IEEE International Conference on Acoustic, Speech and Signal Processing (1978), pp. 499–503.

[15] M. J. Narasimha and A. M. Peterson, "Design of a 24-Channel Transmultiplexer," *IEEE Transactions on Acoustic, Speech, and Signal Processing*, Vol. ASSP-27, No. 6, December 1979, pp. 752–761.

[16] A. Peled and S. Winograd, "TDM-FDM Conversion Requiring Reduced Computation Complexity," *IEEE Transactions on Communications*, Vol. COM-26, May 1978, pp. 707–719.

[17] T. Tsuda, S. Morita, and Y. Fujii, "Digital TDM-FDM Translator with Multistage Structure," *IEEE Transactions on Communications*, Vol. COM-26, May 1978, pp. 734–741.

[18] T. Claasen and M. Mecklenbräuker, "A Generalized Scheme for an All-Digital TDM-FDM Translator," *IEEE Transactions on Circuits and Systems*, Vol. CAS-25, May 1978, pp. 252–259.

[19] C. R. Williams and B. J. Leon, "The Design of Digital SSB Modulators Using a Multirate Digital Filter," Purdue University, West Lafayette, IN, Rep. TR-EE, 77–29, May 1977.

[20] S. L. Freeny, "TDM/FDM Translation as an Application of Digital Signal Processing," *IEEE Communications Magazine*, January 1980, pp. 5–15.

[21] Special issue on Transmultiplexer, *IEEE Transactions on Communications*, July 1982, Vol. COM-30, Number 7.

[22] R. W. Schafer and L. R. Rabiner, "A Digital Signal Processing Approach to Interpolation," *Proc. IEEE*, Vol. 61, No. 6, June 1973, pp. 692–702.

[23] R. E. Crochiere and C. R. Rabiner, "Optimum FIR Filter Implementations for Decimation, Interpolation, and Narrowband Filtering," *IEEE Transactions on Acoustic, Speech, and Signal Processing*, Vol. ASSP-23, Ocober 1975, pp. 444–456.

[24] A. Peled and B. Liu, *Digital Signal Processing*, New York, Wiley, 1976.

[25] "Characteristics of Primary PCM Multiplex Equipment Operating at 2048 kbit/s," CCITT Recommendation G.732, *Orange Book*, Vol. II-2, pp. 425–437.

[26] L. R Rabiner and B. Gold, *Theory and Applications of Digital Signal Processing*, Prentice-Hall, Englewood Cliffs, N.J., 1975.

[27] M. J. Narasimha and A. M. Peterson, "On the Computation of Discrete Cosine Transform," *IEEE Transactions on Communications*, Vol. COM-26, No. 6, June 1978, pp. 934–936.

[28] S. Winograd, "On Computing the Discrete Fourier Transform," *Mathematics of Computation*, Vol. 32, No. 141, January 1978, pp. 175–199.

[29] H. F. Silverman, "An Introduction to Programming the Winograd Fourier Transform Algorithm (WTFA)," *IEEE Transactions on Acoustic, Speech and Signal Processing*, Vol. ASSP-25, No. 2, April 1977, pp. 152–165.

[30] "Characteristics Common to All Transmultiplexing Equipment," CCITT Recommendation G.792, *Orange Book*.

[31] M. T. McCallig, "Design of Nonrecursive Digital Filters to Meet Maximum and Minimum Frequency Response Constraints," Technical Report, TR-EE 75–43, Purdue University, West Lafayette, Indiana, December 1975.

[32] R. W. Hamming, *Numerical Methods for Scientists and Engineers*, New York: McGraw-Hill, 1973.

[33] "Recommendation Relating to the Accuracy of Carrier Frequency," CCITT Recommendation G.225, *Yellow Book*, Vol III-2, pp. 32–33.

[34] A. G. Gatfield, "Satellite Links in the Integrated Services Digital Network," *Proc.*, Fifth International Conference on Digital Satellite Communications, Genoa, Italy, May 1981, pp. 235–239.

Appendix A. Derivation of fast algorithm for the FDM-TDM direction

Assume the following:

a. The FIR filter is of length $M + 1$, where $M = 2KN$, K: integer.

b. The filter coefficients are symmetric with respect to the midpoint (linear phase). Now, partitioning the summation in equation (1) into three parts (writing $m' = M - m$ in the last summation),

$$Y_n(r) = \sum_{m=0}^{M/2-1} \left\{ X(r-m) \cdot h(m) \cdot \cos\left[\frac{\pi(2n+1)\cdot m}{2N}\right]\right\} + X\left(r-\frac{M}{2}\right)\cdot h\left(\frac{M}{2}\right)\cdot \cos\left[\frac{\pi(2n+1)\cdot M/2}{2N}\right] + \sum_{m'=0}^{M/2-1}\left\{X(r-M+m')\cdot h(M-m') \cdot \cos\left[\frac{\pi(2n+1)\cdot(M-m')}{2N}\right]\right\} \quad . \tag{A-1}$$

Utilizing the filter coefficient symmetry and trigonometric transformations, equation (A-1) can be rewritten as

$$Y_n(r) = \sum_{m=0}^{M/2-1}\left\{[X(r-m)+X(r-M+m)\cdot(-1)^K] \cdot h(m)\cdot\cos\left[\frac{\pi(2n+1)\cdot m}{2N}\right]\right\} + X\left(r-\frac{M}{2}\right)h\left(\frac{M}{2}\right)\cdot(-1)^{K/2} \quad . \tag{A-2}$$

The above rearrangement corresponds to a "fold over" of the filter coefficients about the midpoint.

Proceed further by partitioning the filter half-length $M/2$ into $K/2$ blocks of length $2N$ each. This operation places the restriction that K be even. Let $m = 2N\cdot p + q$ and using trigonometric transformations, equation (A-2) becomes

$$Y_n(r) = \sum_{q=0}^{2N-1}\sum_{p=0}^{K/2-1}\left\{[X(r-2Np-q)+X(r-M-2Np+q)] \cdot h(2Np+q)\cdot(-1)^p\cdot\cos\left[\frac{\pi(2n+1)q}{2N}\right] + X(r-M/2)\cdot h(M/2)\cdot(-1)^{K/2} \quad . \tag{A-3}$$

Define

$$v(r,q) = \sum_{p=0}^{K/2-1}\{[X(r-2Np-q)+X(r-M+2Np+q)] \cdot h(2Np+q)\cdot(-1)^p\} \quad . \tag{A-4}$$

With proper substituting, partitioning, and changing index,

$$Y_n(r) = \sum_{q=0}^{N-1} V(r,q)\cdot\cos\left[\frac{\pi(2n+1)q}{2N}\right] + \sum_{q'=1}^{N} V(r,2N-q')\cdot\cos\left[\frac{\pi(2n+1)(2N-q')}{2N}\right] + X\left(r-\frac{M}{2}\right)\cdot h\left(\frac{M}{2}\right)(-1)^{K/2} \quad . \tag{A-5}$$

Further utilizing trigonometric transformations and rearranging,

$$Y_n(r) = \left[V(r,0)+X\left(r-\frac{M}{2}\right)\cdot h\left(\frac{M}{2}\right)\cdot(-1)^{K/2}\right]\cdot(1) + \sum_{q=1}^{N-1}\left\{[V(r,q)-V(r,2N-q)] \cdot\cos\left[\frac{\pi(2n+1)q}{2N}\right]\right\} \quad . \tag{A-6}$$

Define

$$U(r,0) = V(r,0) + X\left(r-\frac{M}{2}\right)\cdot h\left(\frac{M}{2}\right)\cdot(-1)^{K/2}$$

$$U(r,q) = [V(r,q)-v(r,2N-q)], \qquad q\in\{1,\ldots,M-1\} \quad . \tag{A-7}$$

Now equation (A-6) can be written into the standard inverse DCT form as

$$Y_n(r) = \sum_{q=0}^{N-1} U(r,q)\cdot\cos\left[\frac{\pi(2n+1)q}{2N}\right] \quad . \tag{A-8}$$

Next, consider the operation of N:1 sampling rate reduction, which means that $Y_n(r)$ must only be computed at every r which is a multiple of N:

$$Y_n(Nr) = \sum_{q=0}^{N-1} U(Nr,q)\cdot\cos\left[\frac{\pi(2n+1)q}{2N}\right] \qquad n\in\{0,\ldots,N-1\} \tag{A-9}$$

where

$$U(Nr, 0) = v(Nr, 0) + X\left(Nr - \frac{M}{2}\right) \cdot h\left(\frac{M}{2}\right) \cdot (-1)^{K/2}$$

$$= \sum_{p=0}^{K} X(Nr - 2Np)(-1)^p h(2Np) \qquad \text{(A-10)}$$

and

$$U(Nr, q) = V(Nr, q) - V(Nr, 2N - q)$$

$$= \sum_{p=0}^{K/2-1} \{[X(Nr - 2Np - q) + X(Nr - M + 2Np + q)](-1)^p$$

$$\cdot h(2Np + q)\}.$$

$$- \sum_{p=0}^{K/2-1} \{[X(Nr - 2Np - 2N + q) + X(Nr - M + 2Np + 2N - q)]$$

$$\cdot (-1)^p \cdot h(2Np + 2N - q)\} \qquad q \in \{1, \ldots, N - 1\} \quad . \qquad \text{(A-11)}$$

By utilizing the coefficient symmetry for the second summation, equation (A-11) can be rewritten as

$$U(Nr, q) = \sum_{p=0}^{K-1} [X(Nr - 2Np - q) + X(Nr - 2NK + 2Np + q)]$$

$$\cdot (-1)^p \cdot h(2Np + q) \quad . \qquad \text{(A-12)}$$

To this point it has been shown that the SSB demodulation process is equivalent to first performing an "FIR weighting" operation on a block of FDM signal samples $X(r)$ equal to the FIR filter length [equations (A-10) and (A-12)], and then performing an inverse discrete cosine transform (DCT) on the weighting results [equation (A-9)]. For the DCT computation, any "fast" algorithm can be utilized to reduce the arithmetic requirement.

The computation requirement for the FIR weighting operation per "frame" is

number of multiplications:	$K + 1 + K(N - 1)$
number of additions:	$K + (2K - 1)(N - 1)$
memory (RAM):	$(2KN + 1) + N$
memory (PROM):	$KN + 1$

Appendix B. Derivation of fast algorithm for the TDM-FDM direction

Assume that the FIR filter is of length $M + 1$, where $M = 2KN$, K = integer and has symmetric coefficients.

Derivation of algorithm A

Starting with equation (7) and considering that the $Z_n(r)$ are interpolated sequences [equations (4) and (5)],

$$X(pN + q) = \sum_{n=0}^{N-1} \sum_{m=0}^{2KN} Z_n(pN + q - m) \cdot h(m)$$

$$\cdot \cos\left[\frac{\pi(2n + 1)m}{2N}\right] \quad . \qquad \text{(B-1)}$$

To identify the terms which are nonzero, consider the cases $q \neq 0$ and $q = 0$ separately.

a. $q \neq 0$ case: $q \in \{1, 2, \ldots, N - 1\}$. Observe that

$$Z_n(pN + q - m) = \begin{cases} s_n(p - k), & m = q + kN, k\text{: integer} \\ 0, & \text{otherwise} \end{cases} \quad . \qquad \text{(B-2)}$$

Substituting $m = q + kN$, rewriting the summation limits, and separating the even and odd terms, equation (B-2) becomes

$$X(pN + q) = \sum_{n=0}^{N-1} \sum_{k'=0}^{K-1} \left\{ s_n(p - 2k') \cdot h(q + 2k'N) \right.$$

$$\cdot \cos\left(\frac{\pi(2n + 1)(q + 2k'N)}{2N}\right) + s_n(p - 2k' - 1)$$

$$\cdot h(q + 2k'N + N)$$

$$\left. \cdot \cos\left(\frac{\pi(2n + 1)(q + 2k'N + N)}{2N}\right) \right\} \quad . \qquad \text{(B-3)}$$

Utilizing trigonometric transformations and exchanging summations,

$$X(pN+q)=\sum_{k=0}^{K-1}\left\{h(q+2kN)\cdot(-1)^k\cdot\left[\sum_{n=0}^{N-1}s_n(p-2k)\cdot\cos\left(\frac{\pi(2n+1)q}{2N}\right)\right]-h(q+2kN+N)\cdot(-1)^k\cdot\left[\sum_{n=0}^{N-1}s_n(p-2k-1)\cdot\cos\left(\frac{\pi(2n+1)(N-q)}{2N}\right)\right]\right\} \quad . \tag{B-4}$$

The expressions enclosed in [ ] above are in the form of a standard discrete cosine transform (DCT) of the input voice channel samples $s_n(\cdot)$ contained in the summations. The second term indicates that the DCT outputs are used in a reversed order of q.

Denoting the q^{th} output of the DCT of the p^{th} input frame $s_n(p)$ as

$$S_p(q)=\sum_{n=0}^{N-1}s_n(p)\cdot\cos\left(\frac{\pi(2n+1)\cdot q}{2N}\right) \qquad q\in\{0,\ldots,N-1\} \tag{B-5}$$

then equation (B-4) becomes, for the $q\neq 0$ case,

$$X(pN+q)=\sum_{k=0}^{K-1}\{h(q+2kN)(-1)^k\cdot S_{p-2k}(q)-h(q+2kN+N)\cdot(-1)^k\cdot S_{p-2k}(N-q)\} \qquad q\in\{1,\ldots,N-1\} \quad . \tag{B-6}$$

b. $q=0$ case.

Considering that $Z_n(pN-m)$ is interpolated,

$$Z_n(pN-m)=\begin{cases}s_n(p-k), & \text{for } m=kN,\ k=\text{integer}\\ 0, & \text{otherwise}\end{cases} \quad . \tag{B-7}$$

Equation (B-1) becomes

$$X(pN)=\sum_{n=0}^{N-1}\sum_{k=0}^{2K}s_n(p-k)\cdot h(kN)\cdot\cos\left(\frac{\pi(2n+1)(kN)}{2N}\right) \quad . \tag{B-8}$$

Separating the even terms, odd terms, and last term, and changing index notations, equation (B-8) becomes

$$X(pN)=\sum_{n=0}^{N-1}\sum_{k=0}^{K-1}\left\{s_n(p-2k)\cdot h(2kN)\cos\left(\frac{\pi(2n+1)\cdot(2kN)}{2N}\right)+\sum_{k=0}^{K-1}s_n(p-2k-1)\cdot h(2kN+N)\cos\left(\frac{\pi(2n+1)\cdot(2kN+N)}{2N}\right)+s_n(p-2K)\cdot h(2KN)\cos\left(\frac{\pi(2n+1)\cdot(2KN)}{2N}\right)\right\} \quad . \tag{B-9}$$

Utilizing properties of the cosine terms, assuming K is even, and exchanging summations,

$$X(pN)=\sum_{k=0}^{K-1}\left\{h(2kN)(-1)^k\cdot\left[\sum_{n=0}^{N-1}s_n(p-2k)\cos\left(\frac{\pi(2n+1)\cdot 0}{2N}\right)\right]\right\}+h(2KN)\left[\sum_{n=0}^{N-1}s_n(p-2K)\cdot\cos\left(\frac{\pi(2n+1)\cdot 0}{2N}\right)\right] \quad . \tag{B-10}$$

The expressions enclosed within [ ] above are the zeroth outputs of the DCT of the voice channel samples $s_n(\cdot)$ contained in the summation. In terms of the DCT notation defined in equation (B-5),

$$X(pN)=\sum_{k=0}^{K}(-1)^k\cdot h(2kN)\cdot S_{p-2k}(0) \quad . \tag{B-11}$$

Utilizing equations (B-6) and (B-11), a fast algorithm (Algorithm A) can be formulated as follows.

a. Given the input individual voice channel samples $s_n^*(p)$, complement alternate samples for even channels

$$s_n(p)=s_n^*(p)\cdot(-1)^{(n+1)\cdot p} \quad .$$

b. Take the DCT of $s_n(p)$

$$S_p(q)=\sum_{n=0}^{N-1}s_n(p)\cdot\cos\left(\frac{\pi(2n+1)\cdot q}{2N}\right) \qquad q=0,1,\ldots,N-1$$

and store the DCT outputs.

c. Take weighted sums of the stored $S_p(q)$ and form FDM output samples $\{X(pN), X(pN+1),\ldots, X(pN+N-1)\}$ according to equations (B-6) and (B-11).

d. Repeat steps *a* through *c* for the next "frame" of input voice samples.

Figure B-1 shows a block diagram of algorithm A. The computation requirement for the weighting operation per frame is as follows:

number of multiplications:	$2K(N-1)+K$
number of additions:	$(2K-1)(N-1)+K$
memory (RAM):	$2KN+1$
memory (PROM):	$KN+1$.

Derivation of algorithm B

It will be shown that by taking advantage of the filter coefficient's symmetry, the number of multiplications can be reduced to about one-half at the expense of memory requirements. In algorithm A, observe that the group of products of

$$\{h(q+jN)\cdot S_p(q)\}, \qquad q\in\{1,\ldots,N-1\},\quad j\in\{0,\ldots,K-1\}$$

is used twice in the computation cycle. During the second time, the products are used in a reversed order of q.

To derive this relationship, rewrite equation (B-6) for $q\neq 0$ as

$$X(pN+q)=\sum_{k=0}^{K-1}h(q+2kN)(-1)^k\cdot S_{p-2k}(q)-\sum_{k=0}^{K-1}h(q+2kN+N)(-1)^k\cdot S_{p\ 2k-1}(N-q)\quad . \qquad \text{(B-12)}$$

Reversing the k index with respect to $K-1$ and utilizing the coefficient symmetry property for the second summation,

$$X(pN+q)=\sum_{k=0}^{K-1}\{h(q-2kN)(-1)^k\cdot S_{p-2k}(q)+h(N-(q-2kN))(-1)^k\cdot S_{p\ 2K+2k+1}(N-q)\} \qquad \text{(B-13)}$$

$$q\in\{1,\ldots,N-1\}\quad .$$

Define the "product" variable as

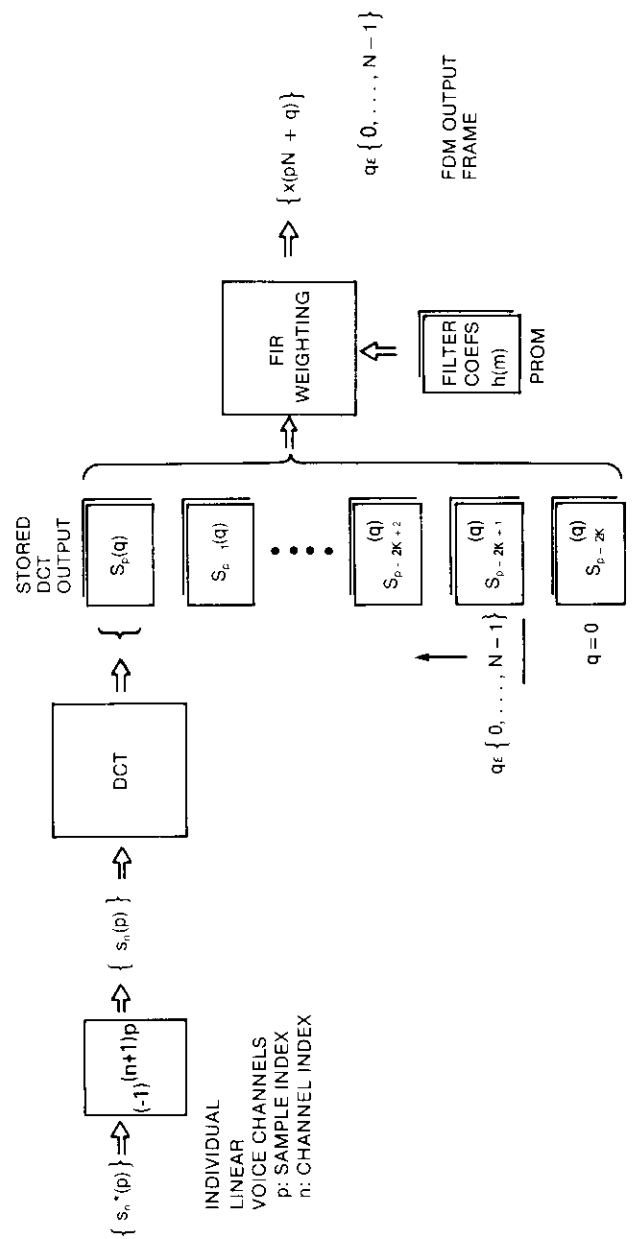

Figure B-1. *TDM-FDM Algorithm A*

$$U_p(q,k) \equiv \begin{cases} h(q+2kN)\cdot(-1)^k \cdot S_p(q) \\ \qquad\qquad q \in \{0,\ldots,N-1\} \\ \qquad\qquad k \in \{0,\ldots,K-1\} \\ h(2KN)\cdot S_p(0), q=0, k=K \quad . \end{cases} \tag{B-14}$$

That is, given each current frame of DCT outputs, multiply the frame by K blocks of coefficients of $2N$ each in length, utilizing only the first half of each coefficient block. For $k = K$, only the $q = 0$ term is required. Hence,

$$X(pN+q) = \sum_{k=0}^{K-1} [U_{p-2k}(q,k) + U_{p-2K+2k+1}(N-q,k)] \qquad q \in \{1,\ldots,N-1\} \tag{B-15}$$

$$X(pN) = \sum_{k=0}^{K} U_{p-2k}(0,k) \quad . \tag{B-16}$$

Algorithm B can now be formulated as follows.
Steps *a* and *b* are the same as those for algorithm A.

c. For each upcoming DCT output frame compute and store

$$U_p(q,k) = h(q+2kN)(-1)^k \cdot S_p(q)$$
$$q \in \{0,\ldots,N-1\}$$
$$k \in \{0,\ldots,K-1\}$$
$$U_p(0,K) = h(2KN)\cdot S_p(0) \quad .$$

d. Generate the FDM output frame by summation according to equations (B-15) and (B-16).
e. For the next input frame, repeat steps *a* through *d*.

Figure B-2 shows a block diagram of algorithm B. The computation requirement for the weighting and summation operations per frame is

number of multiplications:	KN
number of additions:	$(K-1)+(2K-1)(N-1)$
memory (RAM):	$N+N(K)(2K)+1$
memory (PROM):	$KN+1$.

Compared with algorithm A, the number of multiplications is reduced by about one-half. However, the high RAM requirement makes the algorithm unattractive.

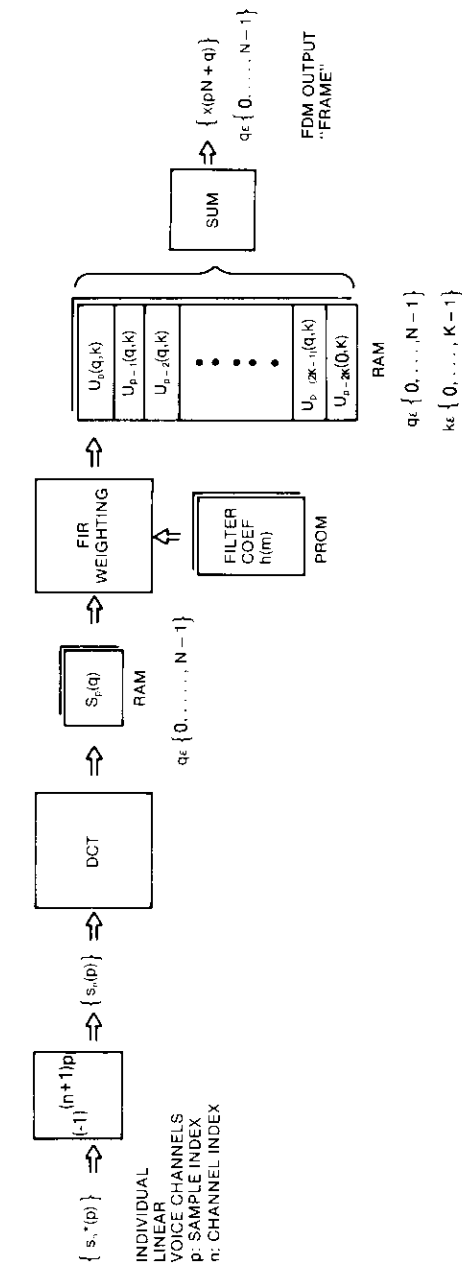

Figure B-2. *TDM-FDM Algorithm B*

Development of algorithm C

It will be shown that the RAM requirement can be reduced by exploiting the relationship between indices k (for blocks) and p (output frame), and using an iterative scheme. Consider the cases for $q \neq 0$ and $q = 0$, separately.

a. $q \neq 0$ case. Define for $q \in \{1, \ldots, N-1\}$.

$$V_p(q,j) \equiv \begin{cases} U_{p-j}\left(q, \dfrac{j}{2}\right), & \text{for } j \text{ even} \\ U_{p-j}\left(N-q, K-1-\dfrac{j-1}{2}\right), & \text{for } j \text{ odd} \end{cases} \quad . \tag{B-17}$$

The current output, equation (B-16), can be expressed as

$$X(pN+q) = \sum_{j=0}^{2K-1} V_p(q,j), \qquad q \in \{1, \ldots, N-1\} \quad . \tag{B-18}$$

Consequently,

$$X(pN+q) = V_p(q,0) + \sum_{j=1}^{2K-1} V_p(q,j) \tag{B-19a}$$

$$= U_p(q,0) + \sum_{j=1}^{2K-1} V_p(q,j) \quad . \tag{B-19b}$$

Define partial sums

$$Y_p(q,k) = \sum_{j=k}^{2K-1} V_{p+k}(q,j) \qquad k \in \{0, \ldots, 2K-1\} \quad . \tag{B-20}$$

The desired output is

$$X(pN+q) = Y_p(q,0) \quad . \tag{B-21}$$

Equation (B-20) can be rewritten as

$$Y_p(q,k) = \begin{cases} V_{p+k}(q,k) + \displaystyle\sum_{j=k+1}^{2K-1} V_{p+k}(q,j), & k \in \{0, \ldots, 2K-2\} \\ V_{p+k}(q,k), & k = 2K-1 \end{cases} \quad . \tag{B-22}$$

Now note that

$$Y_{p-1}(q,k+1) = \sum_{j=k-1}^{2K-1} V_{p+k}(q,j) \quad . \tag{B-23}$$

Substituting,

$$Y_p(q,k) = \begin{cases} V_{p+k}(q,k) + Y_{p-1}(q,k+1), & k \in \{0, \ldots, 2K-2\} \\ V_{p-k}(q,k), & k = 2K-1 \end{cases} \quad . \tag{B-24}$$

The even terms (in forward order) and odd terms (in reversed order) can be written as follows:

(1) *For $k = 2\ell$, $\ell \in \{0, \ldots, K-1\}$.*

$$Y_p(q,2\ell) = V_{p-2\ell}(q,2\ell) + Y_{p-1}(q,2\ell+1) \tag{B-25a}$$

$$= U_p(q,\ell) + Y_{p-1}(q,2\ell+1) \quad . \tag{B-25b}$$

(2) *For $k = 2K-1-2\ell$, $\ell \in \{0, \ldots, K-1\}$.*

$Y_p(q, 2K-1-2\ell)$

$$= \begin{cases} V_{p+2K-1-2\ell}(q, 2K-1-2\ell) + Y_{p-1}(q, 2K-2\ell), & \\ & \ell \in \{1, \ldots, K-1\} \\ V_{p+2K-1-2\ell}(q, 2K-1) & \ell = 0 \end{cases} \tag{B-26a}$$

$$= \begin{cases} U_p(N-q,\ell) + Y_{p-1}(q, 2K-2\ell), & \ell \in \{1, \ldots, K-1\} \\ U_p(N-q,0), & \ell = 0 \end{cases} \quad . \tag{B-26b}$$

b. $q = 0$ case. Define

$$V_p(0,j) \equiv \begin{cases} U_{p-j}(0, j/2) & \text{for } j \text{ even} \\ 0 & \text{for } j \text{ odd} \end{cases} \quad . \tag{B-27}$$

The partial sum is

$$Y_p(0,k) = \sum_{j=k}^{2K} V_{p-k}(0,j) \quad . \tag{B-28}$$

The desired output, equation (B-16), becomes

$$X(pN) = \sum_{j=0}^{2K} V_p(0, j) = Y_p(0, 0) \quad . \tag{B-29}$$

Rewriting the partial sums

$$Y_p(0, k) = \begin{cases} V_{p-k}(0, k) + \sum_{j=k+1}^{2K} V_{p+k}(0, j), & k \in \{0, \ldots, 2K-1\} \\ V_{p+k}(0, k), & k = 2K \end{cases} \tag{B-30a}$$

$$= \begin{cases} V_{p+k}(0, k) + Y_{p-1}(0, k+1), & k \in (0, \ldots, 2K-1) \\ V_{p-k}(0, k), & k = 2K \quad . \end{cases} \tag{B-30b}$$

The even terms (in forward order) and odd terms (in reversed order) can be written as follows:

(1) *For* $k = 2\ell$, $\ell \in \{0, \ldots, K\}$.

$$Y_p(0, 2\ell) = \begin{cases} V_{p-2\ell}(0, 2\ell) + Y_{p-1}(0, 2\ell+1), & \ell \in \{0, \ldots, K-1\} \\ V_{p+2\ell}(0, 2\ell), & \ell = K \end{cases} \tag{B-31a}$$

$$= \begin{cases} U_p(0, \ell) + Y_{p-1}(0, 2\ell+1), & \ell \in \{0, \ldots, K-1\} \\ U_p(0, K) = U_p(0, 0), & \ell = K \quad . \end{cases} \tag{B-31b}$$

(2) *For* $k = 2K - 1 - 2\ell$, $\ell \in \{0, \ldots, K-1\}$.

$$\begin{aligned} Y_p(0, 2K-1-2\ell) &= V_{p+2K-1-2\ell}(0, 2K-1-2\ell) \\ &\quad + Y_{p-1}(0, 2K-1-2\ell+1) \\ &= 0 + Y_{p-1}(0, 2K-2\ell) \quad . \end{aligned} \tag{B-32}$$

A computation algorithm (algorithm C) can be formulated as follows. Steps *a* and *b* are the same as those for algorithm A.

c. For each DCT output frame compute

$$U_p(q, \ell) = h(q + 2\ell N)(-1)^{\ell} \cdot S_p(q), \qquad \begin{matrix} \ell \in \{0, \ldots, K-1\} \\ q \in \{0, \ldots, N-1\} \end{matrix} \quad .$$

d. Compute partial sums according to equations (B-25), (B-26), (B-31), and (B-32).

e. Store $\{Y_p(q, 1), Y_p(q, 2), \ldots, Y_p(q, 2K-1)\}$, $q \in \{0, \ldots, N-1\}$, and $Y_p(0, 2K)$

f. Output current FDM frame

$$X(pN + q) = Y_p(q, 0), \qquad q \in \{0, \ldots, N-1\} \quad .$$

g. For the next input frame, repeat steps *a* through *f*.

The computation complexity for the weighting and summation operations per frame is

number of multiplications: KN
number of additions: $(K-1) + (2K-1)(N-1)$
memory (RAM): $N + 2KN + 1$
memory (PROM): $KN + 1$

The above RAM estimate assumes an "in-place" minimum memory scheme, by which each partial sum is always used before it is updated. Compared to algorithm A, the requirement for multiplications is one-half and that for memory is comparable. Compared to algorithm B, the requirement for multiplications is the same, and that for memory is reduced by a factor of K. Algorithm C is therefore selected for implementation. A block diagram of the algorithm is shown in Figure 10.

Eric S. Yam received a B.E.E. and an M.S.E.E. from the University of Minnesota in 1969 and 1971, and a Ph.D. from Purdue University in 1976. From 1967 to 1968, he participated in the development of the ARTIC computer at the University of Minnesota. From 1973 to 1974, he worked at the Laboratory for Applications of Remote Sensing at Purdue University, where he was responsible for research and development for machine processing of earth resources data collected via the LANDSAT satellite. From 1974 to 1976, he was engaged in research on artificial intelligence and robotic visual perception at the Laboratory for Advanced Automation at Purdue.

He joined COMSAT Laboratories in 1976, where he is currently a Member of the Technical Staff of the Image Processing Department of the Communications Technology Division. His R&D work at COMSAT has included bit rate compression coding, TV image processing, transmultiplexer TV energy dispersal and enhancement, interference reduction, direct broadcast TV, and advanced digital processing techniques. Dr. Yam is a member of Tau Beta Pi and Eta Kappa Nu.

Mark Redman received his B.E. (electrical) and M.E. (electrical) degrees from McGill University in 1973 and 1976. After 2 years at Bell Northern Research in the department of Fiber Optic Systems, he joined COMSAT in the Image Processing Department of the Communications Technology Division. His responsibilities have primarily involved the design and implementation of digital signal processing systems for error control in DPCM television transmission systems and for the supergroup transmultiplexer. He is currently participating in the design and development of the NMAC digital video processor for STC.

Index: radiation, solar cells

*Limitations on solar cell open-circuit voltage and efficiency**

A. MEULENBERG, JR. AND R. A. ARNDT

(Manuscript received December 22, 1982)

Abstract

Open-circuit voltages (V_{oc}) in 0.1 Ω-cm, n^+/p type, planar surface silicon solar cells produced by diffusion techniques are presently ≤654 mV, with corresponding conversion efficiencies of about 15 percent. This is lower than has been theoretically predicted. Experimental evidence is presented to demonstrate that the emitter is the largest source of the dark current that limits the attainment of higher V_{oc} values and, hence, reduces conversion efficiency. It is also shown that junction recombination current contributes to reduced V_{oc}. Because there is a lower limit on dark current from the base, even if the emitter and junction recombination currents are reduced to zero, a maximum V_{oc} of 695 mV is predicted, with a related conversion efficiency of 16.4 percent.

Introduction

Solar cells are the primary source of power for communications satellites. The power output of a cell is equal to the product of cell voltage and current, and it reaches a maximum at a voltage less than

* This paper is based on work performed at COMSAT Laboratories under the sponsorship of the Communications Satellite Corporation and supported in part by NASA-LeRC under Contract NAS3-21227.

at open-circuit. Characteristically, when the voltage at open-circuit increases, voltage at the maximum power point, power output, and conversion efficiency also increase. Because increases in solar cell efficiency will provide additional communications capacity without incurring higher fabrication costs or additional weight of solar cell arrays, there is significant incentive to obtain cells that exhibit values of open-circuit voltage higher than those presently in use. Further, investigations of open-circuit voltage (V_{oc}) limitations may lend insight to methods of preserving high values of V_{oc} for cells that are subjected to radiation from the space environment.

Research efforts to improve the output characteristics of solar cells require knowledge of the parameters that control these characteristics. As the cell output approaches the theoretical maximum (an early estimate for efficiency was ~22 percent [1]), it becomes increasingly difficult to identify and assign values to the parameters that are limiting further progress. Until a few years ago, a large discrepancy existed between theoretical values (700 mV) and practically realizable values (~620 mV) of open-circuit voltage, corresponding to efficiencies of 16.6 and 14.3 percent, respectively, in silicon solar cells [2]. During the past 10 years, better silicon material has become available and more precise techniques for measuring solar cell characteristics have been developed. These and other advances have led to increases in experimental values of V_{oc}, and, therefore, to a reduction of the discrepancy between theory and practice; for example, the highest V_{oc} reported for a conventional, diffused junction, silicon solar cell of the n^+/p type is 654 mV, with an efficiency of 14.8 percent [3]. Theories, which include more material parameters, have been proposed in an effort to obtain better predictions of V_{oc}. These include the effects of bandgap narrowing which take place as a result of very high doping concentrations [4]. Although the predicted V_{oc} for an optimized cell remained at 700 mV, a step toward improving theory and understanding material limitations was taken.

Because the V_{oc} discrepancy still exists, although it is less than that of 10 years ago, the problem of determining the reasons for it remains. Two recent studies have presented detailed analyses of possible causes. Both theories, which were proposed before the achievement of the 654 mV value of V_{oc}, discussed many parameters. One [5], included such features as bandgap narrowing, surface recombination velocity, and doping profiles. Predicted values of V_{oc} for $n^+ - p$ type cells were as high as 675 mV. The second paper [6], in addition to investigating the same parameters as those in Reference 5, also examined the effects taking place in the junction region, particularly

in the internal electric fields, and surface recombination at the metal contacts.

A result of these studies was that the major limitation to increased V_{oc} is the dark current from the emitter region. Further, high-surface recombination velocity at the emitter/metal contact interface was identified as the largest contributor to this dark current. In addition, a result of Reference 6 was that junction region recombination current could reduce the maximum power output and V_{oc}. However, both studies indicated that the computed values of the dark current from the base of the cell was quite small.

Use of improved silicon material and processing in the present work has resulted in cells having long minority carrier diffusion lengths. It will be shown that these values lead to nominal agreement between experimental and theoretical values for the dark current from the base and, further, that the base dark current is small compared to the total dark current in 0.1 Ω-cm cells. Evidence will also be presented to show that recombination current in the junction region can be important in determining V_{oc}.

Background

An approximate, general relationship for the current-voltage characteristic of a solar cell can be written as

$$J = J_{do}\left(\exp\left[\frac{qV}{kT}\right] - 1\right) + J_{ro}\left(\exp\left[\frac{qV}{2kT}\right] - 1\right) - J_\ell \qquad (1)$$

where
J = output current density
$J_{do} = J_{dN} + J_{dP}$
J_{dN} = dark current density from the emitter (n^+/p cell)
J_{dP} = dark current density from the base
J_{ro} = recombination dark current density in the junction
J_ℓ = photo-generated short-circuit current density
V = cell voltage, and the other symbols have their usual meaning.

It is apparent that, to achieve high open-circuit voltage (obtained when $J = 0$), the values of J_{dN}, J_{dP}, and J_{ro} should be as small as possible.

High values of V_{oc} have been obtained in conventional junction cells having a shallow (~0.15 μm), phosphorus diffused emitter on a p-type base of 0.1 Ω-cm resistivity (see Figure 1). This configuration results

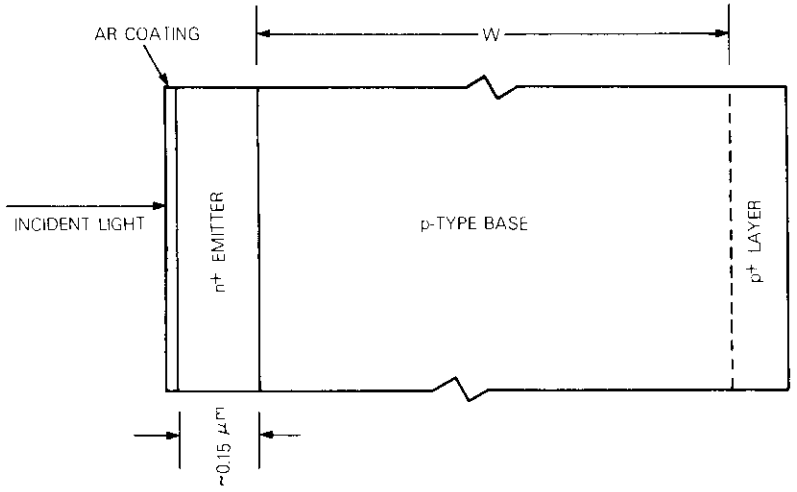

Figure 1. *Schematic Cross Section of a Conventional Junction Solar Cell*

in conditions, particularly in the emitter, that are not easily described by theory; for instance, it should be possible to compute values for J_{dN}, J_{dP}, and J_{ro}, and to determine which of these factors is the most significant in controlling the output characteristic (see for example Reference 7). However, as the various regions of a cell become more nonuniform, the mathematics involved in determining these factors become exceedingly complex, and some of the parameters may not be determinable in a finished solar cell. The ability to use experimental techniques for determining the values of these factors is therefore desirable.

The base region of a solar cell, unless the thickness is made very small, can be considered to be uniform and the theory can be used to write an expression for J_{dP} [6]:

$$J_{dP} = \frac{qn_i^2 D}{LN_A} \left\{ \frac{\frac{SL}{D}\cosh\left(\frac{W}{L}\right) + \sinh\left(\frac{W}{L}\right)}{\cosh\left(\frac{W}{L}\right) + \frac{SL}{D}\sinh\left(\frac{W}{L}\right)} \right\} \qquad (2)$$

where q = electronic charge
n_i = intrinsic carrier concentration
D = minority carrier diffusion constant

L = minority carrier diffusion length
W = base region thickness
N_A = doping concentration
S = surface recombination velocity.

Several terms in equation (2) must be known to compute a value for J_{dP}; these are D, N_A, n_i, S, and L. Actually, only the quantity qn_i^2D/N_A is needed and, as will be shown later, this can be measured. Even though qn_i^2D/N_A was measured in irradiated cells, the resultant value was very close to that which would be computed using published values of the individual quantities. This means the values of these individual quantities are not significantly altered by cell processing or moderate doses of radiation. The remaining terms, S and L, usually cannot be determined separately. There are two limiting cases, however, for which a determination of L can be made: when the base has an ohmic contact ($S = \infty$)* and when the base contact is a perfect, minority carrier reflector ($S = 0$), such as an ideal p/p^+ barrier. The conditions existing at the base contact of a real cell must place the value of S between these limits.

It will be shown later that J_{ro} cannot be neglected in equation (1). However, it will also be shown that the contribution of J_{dN} to J_{do}, because J_{dP} is smaller than J_{dN}, is not strongly dependent on J_{ro}. As a result, a good approximation to the ratio J_{dN}/J_{do} can be made by simply letting J_{ro} go to zero and computing the maximum value of J_{do} from

$$J_{do}(\max) = J_\ell \exp\left[-\frac{qV_{oc}}{kT}\right] . \qquad (3)$$

A description of the method used for measuring L in the above limiting cases is presented below.

Diffusion length measurement

COMSAT Laboratories has long used the ^{60}Co gamma cell to generate a uniform concentration of carriers within the base of a solar cell and to provide the basis for determining a range of minority carrier diffusion

* Actually, S is limited by the rate of arrival of carriers, and the upper value of S is 4×10^6 cm/s. Results using higher values of S are indistinguishable from those using this value.

lengths for most cells. In an earlier paper [8], the relationship between current collected from the solar cell under γ irradiation (I_γ) and the solar cell diffusion length L was established for two back surface conditions. These conditions were an ohmic base contact ($S = \infty$) and a perfectly reflecting base contact ($S = 0$). These relationships are

$$I_\gamma = \frac{L}{K}\left[\frac{\cosh\left(\frac{W}{L}\right) - 1}{\sinh\left(\frac{W}{L}\right)}\right] \qquad \text{for } S = \infty \tag{4}$$

and

$$I_\gamma = \frac{L}{K}\left[\frac{\cosh\left(\frac{2W}{L}\right) - 1}{\sinh\left(\frac{2W}{L}\right)}\right] \qquad \text{for } S = 0 \tag{5}$$

where K is a proportionality constant that depends on the geometry of the source and on the type, energy, and flux of the ionizing radiation. A plot of KI_γ versus L is shown in Figure 2.

The value of K is determined by calibrating the gamma cell with a solar cell having known W and L such that $W \gg 2L$, and where L was measured by another method [8].

An interesting feature of equations (4) and (5) is the dependence on W. More insight can be gained if these equations are rewritten using two trigonometric identities.* Equations (4) and (5) become

$$I_\gamma = \frac{L}{K}\tanh\left(\frac{W}{2L}\right) \qquad \text{for } S = \infty \tag{6}$$

and

$$I_\gamma = \frac{L}{K}\tanh\left(\frac{W}{L}\right) \qquad \text{for } S = 0 \tag{7}$$

* Use $\cosh(2W/L) = 1 + 2\sinh^2 W/L$ and $\sinh(2W/L) = 2\sinh(W/L)\cosh(W/L)$.

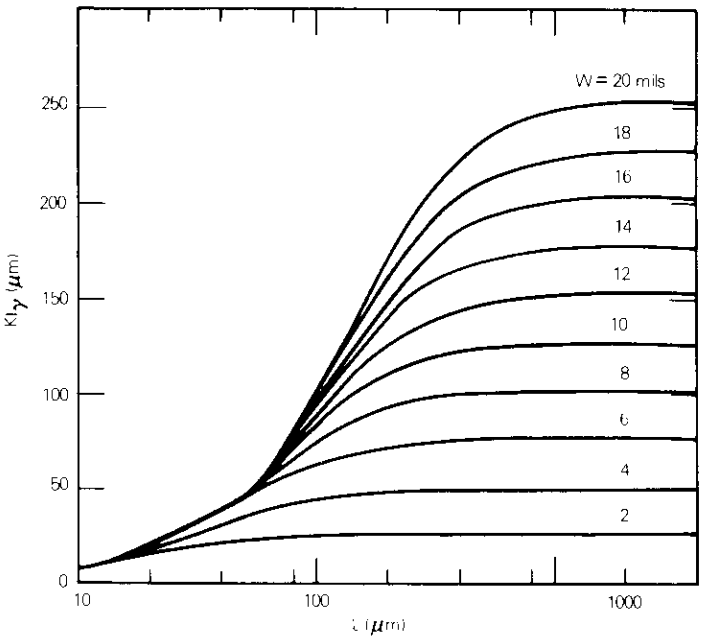

Figure 2. *Normalized Gamma Cell Current vs Solar Cell Diffusion Length for $S = \infty$ and Different Cell Thicknesses W (for $S = 0$ use the curves corresponding to 2W)*

Equation (7) is similar to that for the dark current equations of a diode of thickness W with a perfectly reflecting back $p - p^+$ contact [see equation (8)]. The $W/2$ in equation (6) now indicates that the $n^+ - p$ junction only collects current from the front half of the cell and the carriers in the back half of the cell all migrate to the ohmic back contact. For small values of the argument, the value of tanh approaches the value of the argument and the exact value of L becomes indeterminate. This is generally the case found in high-quality cells. When the argument becomes large, the value of tanh approaches unity and the value of L can be determined exactly. The value of L can be reduced by irradiating the cell; this procedure results in conditions that yield an exact determination of L. Although a photocurrent from the emitter is also present, it is too small to be measured under uniform generation of carriers because of the very small depth of the emitter compared to the base thickness.

Experimental procedure and results

As previously mentioned, an unambiguous value of L in the base can be obtained if W/L is of the order of unity or greater. Even in cells of ~0.1 Ω-cm resistivity, the diffusion length can be long enough so that this condition is not fulfilled. However, as stated above, the value of L can be reduced by irradiating the cell. (Irradiation doses sufficient to alter L in the base are not likely to affect J_{dN} because diffusion lengths in the heavily doped emitter are usually so short that only a very high radiation dose will alter them.)

Two cells (0.1 and 0.2 Ω-cm) were illuminated, and V_{oc} and J_ℓ were measured. In addition, the diffusion length was determined (within limits) by the method described earlier. Calibration of the gamma ray source resulted in a value for K of 6,400 cm³/A. These cells were then irradiated to several dose levels and remeasured (see the appendix for data). The value of J_{do} (maximum) was computed for each dose level, using equation (3), and the results were plotted versus $1/L$. This plot is shown in Figure 3 for the 0.1 Ω-cm cell for the cases $S = 0$ and $S = \infty$, and it can be seen that the data for both cases fit a common straight line as L becomes small. This result is expected when the following limiting cases of equation (2) are used. Rewriting equation (2) yields

$$J_{dP} = \frac{qn_i^2 D}{LN_A} \tanh \frac{W}{L} \qquad \text{for } S = 0 \tag{8}$$

or

$$J_{dP} = \frac{qn_i^2 D}{LN_A} \coth \frac{W}{L} \qquad \text{for } S = \infty \tag{9}$$

As L approaches zero, both tanh and coth approach unity and the slope approaches $qn_i^2 D/N_A$. If J_{dN} is constant with radiation dose, the slope of J_{do} (maximum) is the same as for J_{dP}. Since J_{do} (maximum) and J_{dP} are now known, a value for J_{dN} can be computed. This same procedure was also applied to the 0.2 Ω-cm cell. Results of these measurements are shown in Table 1 for the two cells before irradiation.

The values for J_{dN} in Table 1 (and marked on the ordinate of Figure 3) are those obtained by computing J_{dP} (before irradiation conditions) and subtracting this from J_{do} (maximum). It can be seen that, in each

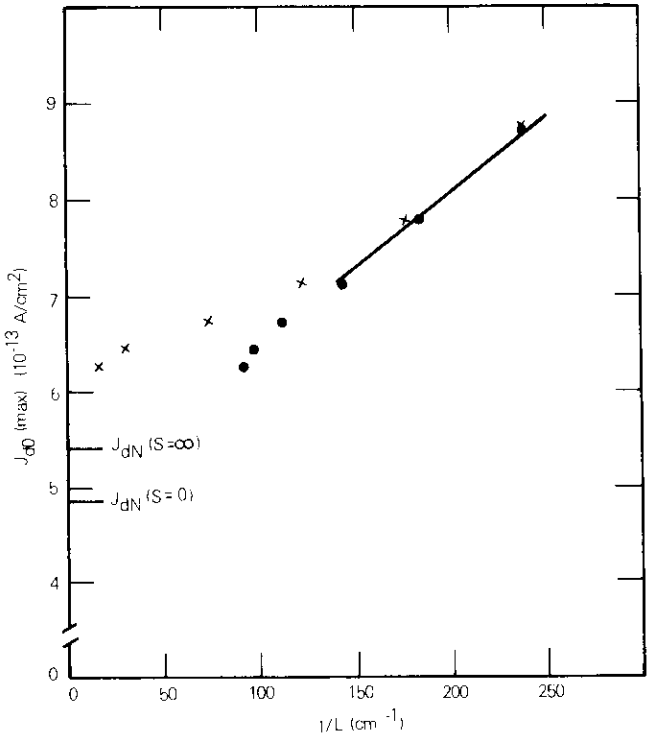

Figure 3. *Plot of J_{do} (maximum) vs 1/L for a 0.1 Ω-cm cell (the dots apply to $S = 0$ and the crosses to $S = \infty$)*

TABLE 1. DARK CURRENTS FOR LOW RESISTIVITY CELLS WITH PLANAR SURFACES

	0.1 Ω-cm		0.2 Ω-cm	
	$S = 0$	$S = \infty$	$S = 0$	$S = \infty$
J_{do} (max)(A/cm²)	6.15×10^{-13}	6.15×10^{-13}	7.73×10^{-13}	7.73×10^{-13}
$qn_i^2 D/N_A$ (A/cm)	1.52×10^{-15}	1.52×10^{-15}	5.00×10^{-15}	5.00×10^{-15}
J_{dP} (A/cm²)	1.32×10^{-13}	7.55×10^{-14}	2.95×10^{-13}	2.04×10^{-13}
J_{dN} (A/cm²)	4.83×10^{-13}	5.39×10^{-13}	4.77×10^{-13}	5.69×10^{-13}
J_{dN}/J_{do} (max)	0.785	0.876	0.618	0.736

column of Table 1, the dark current from the emitter is greater than that from the base and the values of J_{dP} agree with those computed in Reference 6. Two other features in Table 1 should be noted: the

values of J_{dN} are close for the same values of S, (which is to be expected because the emitters were formed identically) and the values of qn_i^2D/N_A are about a factor of three different (this factor reflects the differences in D and N_A for the two base resistivities).

In obtaining these results, it was assumed that the J_{ro} of equation (1) was negligible. If a value for J_{ro} is included, the ratio J_{dN}/J_{do} should not be significantly altered. The reason is that increases in J_{ro} must be accompanied by decreases in J_{do} because, for a given cell, the values of V_{oc} and J_ℓ do not change. The magnitude of the decrease in J_{do} can be found by using equation (1) for V_{oc} = 635 mV and an increase in J_{ro} of 1×10^{-8} A/cm^2; the decrease in J_{do} is less than 10 percent of the values reported in Table 1.

It was reported in earlier work [9] that the J_{ro} term cannot be neglected for high-voltage cells. It has also been shown that as the junction depth decreased in 0.12 Ω-cm cells, the value of J_{ro} increased [6]. This was attributed to bandgap narrowing in the junction caused by the presence of very high electric fields. The magnitude of the electric field decreases with increasing junction depth. In cells with textured surfaces, the junction follows the surface contour; and larger junction areas, as well as high, localized fields in the junction region, result. Therefore, a more sensitive measurement of the effects described in References 6 and 9 is made possible by using such cells.

Emitters were diffused into a set of 1.2 Ω-cm, textured surface cells for a fixed time (15 minutes) at various temperatures. The higher the diffusion temperature, the deeper the junction. Values of J_{ro} were obtained by computer fitting I–V curves of illuminated cells to equation (1) (as was done in Reference 5) and are displayed in Table 2.

TABLE 2. DARK CURRENTS OF 1.2 Ω-cm TEXTURED SURFACE CELLS

DIFFUSION TEMPERATURE (°C)	J_{do} (10^{-12} A/cm²)	J_{ro} (10^{-8} A/cm²)	J_ℓ (A/cm²)	V_{oc} (mV)
760	12 ± 1	17.2 ± 1	0.0425	558
790	5.0 ± 0.15	6.4 ± 1	0.0425	583
820	4.3 ± 0.60	4.5 ± 3	0.0425	588
850	3.4 ± 0.40	2.5 ± 2	0.0418	595

Several features in Table 2 should be noted. The values of J_{do} are higher than those reported in Table 1, because of the higher base resistivity and the increased area of the textured surface. The decrease in V_{oc} with reduced diffusion temperature is attributed to the large

diffusion current generated by surface recombination at the metal contacts [6]. The important point is the decrease in J_{ro} with increased diffusion temperature, an effect that is pronounced even in 1.2 Ω-cm cells. At higher temperatures, the junction depth will be greater and, consequently, the electric field will be smaller.

Discussion and conclusions

It has been experimentally determined that, in low resistivity (~0.1 Ω-cm), planar surface cells, the dark current from the emitter, J_{dN}, is the largest contributor to the limitation on increased V_{oc}. This situation is contrary to what would have been found by applying equation (2) to an emitter with an abrupt doping profile and using values for the parameters deduced from measurements on bulk samples. Without considering bandgap narrowing, such a procedure yields a value of J_{dN} of about 5.2×10^{-14} A/cm^2. It is concluded that bandgap narrowing and other effects, such as surface recombination velocity, can increase J_{dN} by at least an order of magnitude over this computed value.

Although the emitter dark current is less when $S = 0$ at the base contact than when $S = \infty$, the latter condition is more likely to occur in 0.1 Ω-cm cells. This is because of the difficulty in reducing the surface recombination velocity at the base contact by the addition of a minority carrier reflector. The quality of such a contact depends on the magnitude of the potential barrier that is set up when a heavily diffused (p^+) layer is applied. Since the doping concentration in 0.1 Ω-cm silicon is high, the height of the barrier will not be as great as with lower doping levels in the base.

It was also demonstrated that junction recombination current, J_{ro}, cannot be neglected. Although this current is usually not the major factor in limiting V_{oc}, it can affect the cell maximum power and, therefore, conversion efficiency. For example, the efficiency of a cell having $J_\ell = 0.040$ A/cm² and $J_{do} = 6.15 \times 10^{-13}$ A/cm² would drop by about 10 percent if J_{ro} increased from zero to 4×10^{-8} A/cm². If J_{do} were lowered signficantly, this level of J_{ro} could affect V_{oc}.

Although some of the limits to solar cell voltage and efficiency have been identified, it is desirable to know the ultimate values presently predicted for planar surface cells. For instance, consider the 0.1 Ω-cm, 208-μm thick cell reported in this paper. Because $S = \infty$ at the base contact is the likely value for this cell, J_{dP} has a lower limit. This can be realized by letting L become very large in equation (7). For this example J_{dP} approaches $qn_i^2D/WN_A = 7.3 \times 10^{-14}$ A/cm². If both

J_{dN} and J_{ro} were zero, the resulting V_{oc} for J_ℓ = 0.040 A/cm² would be 695 mV, with a corresponding efficiency of 16.4 percent. This should be compared to the present values of 654 mV and 14.8 percent [3]. Such conditions on J_{dN} and J_{ro} are not probable, although improvement is possible. The contribution to J_{dN} from the metal contact to the emitter has already been reduced significantly [6], [10]. The value of S at the emitter/AR coating interface for a Ta_2O_5 AR coating is about 5×10^3 cm/s [6]. The use of charged oxides, metal-insulator-semiconductor (MIS) technology, and thicker substrates has resulted in values of V_{oc} in excess of 690 mV [11]. This improvement leaves the emitter bulk itself as the main area for improvement in J_{dN}. To achieve increases in V_{oc} and efficiency the doping levels and profile must be altered to minimize the combined effects of bandgap narrowing, junction recombination current, and diffusion length of the emitter region. At values of V_{oc} as high as 690 mV, the base dark current becomes the factor controlling further increases, and the use of thicker cells could result in higher V_{oc}.

Acknowledgment

The authors thank Dr. E. S. Rittner for many helpful discussions regarding this work.

References

[1] E. S. Rittner, "Use of p-n Junctions for Solar Energy Conversion," *Physical Review*, December 1954, Vol. 96, pp. 1708–1709.

[2] H. W. Brandhorst, Jr., "Silicon Solar Cell Efficiency—Practice and Promise," 9th IEEE Photovoltaic Specialists Conference, *Proc.*, 1972, pp. 37–43.

[3] R. A. Arndt et al., "Advances in High Output Voltage Silicon Solar Cells," 15th IEEE Photovoltaic Specialists Conference, *Proc.*, 1981, pp. 92–96.

[4] M. P. Godlewski, H. W. Brandhorst, Jr., and C. R. Baraona, "Effects of High Doping Levels on Silicon Solar Cell Performance," 11th IEEE Photovoltaic Specialists Conference, *Proc.*, 1975, pp. 32–35.

[5] J. G. Fossum, F. A. Lindholm, and M. A. Shibib, "The Importance of Surface Recombination and Energy Bandgap Narrowing in p-n Junction Silicon Solar Cells," *IEEE Transactions on Electron Devices*, Vol. 26, 1979, pp. 1294–1298.

[6] E. S. Rittner, A. Meulenberg, and J. F. Allison, "Dependence of Efficiency of Shallow Junction Silicon Solar Cells on Substrate Doping," *AIAA Journal of Energy*, Vol. 5, 1981, pp. 9–14.

[7] See for example, H. J. Hovel, *Semiconductors and Semimetals*, Solar Cells, Academic Press, N.Y., 1975, Vol. 11, ch. 2.

[8] J. H. Reynolds and A. Meulenberg, Jr., "Measurement of Diffusion Length in Solar Cells," *Journal of Applied Physics*, Vol. 45, 1974, p. 2582.

[9] E. S. Rittner, "An Improved Theory of the Silicon p-n Junction Solar Cell," *Journal of Energy*, January–February 1977, Vol. 1, pp. 9–17.

[10] M. A. Green et al., "The MINP Solar Cell—A New High Voltage, High Efficiency Silicon Solar Cell," 15th IEEE Photovoltaic Specialists Conference, *Proc.*, 1981, pp. 1405–1408.

[11] M. A. Green et al., "Towards a 700 mV Silicon Solar Cell," 16th IEEE Photovoltaic Specialists Conference, San Diego, California, 1982 (in press).

Appendix. Experimental values for irradiated 0.1 and 0.2 Ω-cm solar cells

Two cells (0.1 and 0.2 Ω-cm) were illuminated, and the values of V_{oc} and J_ℓ were determined. Diffusion lengths were also measured by the method described in the section entitled "Diffusion Length Measurement." These cells were then irradiated to reduce the diffusion length and remeasured (total of six measurement points). Measured values of V_{oc}, J_ℓ, and I_γ are presented along with computed values for J_{do} (maximum) and L in Tables A-1 and A-2. When using Figure 2 to determine L, L_γ is in μA/4 cm² and K is 16 μm/μA/4 cm².

TABLE A-1. 0.1 Ω-cm (208 μm)

V_{oc} (mV)	J_ℓ (A/cm²)	I_γ (μA/4 cm²)	J_{do} (max) (10^{-13} A/cm²)	L (μm)	
				$S = 0$	$S = \infty$
635	0.0350	6.5	6.20	110	650
634	0.0350	6.3	6.38	104	345
632	0.0340	5.5	6.70	90	139
630	0.0333	4.4	7.10	71	83
627	0.0323	3.4	7.73	55	57
623	0.0310	2.6	8.68	42	42

TABLE A-2. 0.2 Ω-cm (250 μm)

V_{oc} (mV)	J_ℓ (A/cm²)	I_γ (μA/4 cm²)	J_{do} (max) (10^{-13} A/cm²)	L (μm)	
				$S = 0$	$S = \infty$
630	0.0363	9.0	7.73	156	*
622	0.0348	6.4	10.13	104	150
619	0.0340	5.6	11.13	90	110
614	0.0330	4.2	13.13	67	71
608	0.0320	3.4	16.10	55	55
603	0.0308	2.4	18.80	39	39

* The value for I_γ was actually greater than that which can be achieved for this thickness of cell and $S = \infty$; therefore, the contact must be partially reflecting for minority carriers.

Andrew Meulenberg received his B.A. from the University of the South in 1962 and his Ph.D. in physics from Vanderbilt University in 1968. Since joining COMSAT in 1968, he has been involved in defining and simulating the space environment encountered by synchronous satellites, studying the effects of this environment on spacecraft components, and investigating material parameters and radiation defects in silicon solar cells. He is currently a Staff Scientist in the Solid State Physics Department.

Richard A. Arndt received his Ph.D. from Northwestern University in 1961. From 1961 to 1969 he was a staff scientist at the Brookhaven National Laboratory. Since he joined COMSAT Laboratories in 1969, he has been with the Applied Sciences Laboratory, where he is now Manager of the Solid State Physics Department.

Index: antennas, earth stations, radiation, small terminals

Matching networks in linear phased arrays

A. I. ZAGHLOUL

(Manuscript received January 3, 1983)

Abstract

A linear phased array has properties that are different from those of the planar phased array. General relationships for linear array element gain are derived in this paper. The effects of interconnecting and matching networks on linear array performance are studied to show how the network parameters can be optimized to produce near flat response over a wide scan angle. Arrays of λ/2 dipoles or slots are analyzed, with the result that the realized element gains may be designed to be about 0 dB above isotropic for all scan angles in marked improvement over the ideal cos θ variation of planar arrays.

Introduction

Large planar arrays inherently require a large number of phase shifters (thousands or tens of thousands); the cost of building such arrays can become excessively high. Attention has thus been directed toward using the less expensive linear array [1]–[3] as a substitute and achieving two-dimensional scanning by other means, when necessary. Wasylkiwsky and Kahn [4] have given results for ideal element patterns for infinite linear arrays and have shown how these patterns depend on the array element. They show some analytic results for arrays of elementary dipoles, but do not indicate the effect of a practical matching network.

The present work is concerned with both finite and infinite linear arrays of elementary and half-wave dipoles, taking into account the effect of matching networks. An interesting special case appears when the array is matched near endfire. The realized gain is almost constant as a function of scan, in marked contrast with the well-known cos θ behavior for the fully matched planar array.

Element pattern

The power radiated per element in a large planar array in the *x*-*y* plane is given by [5]

$$P = \frac{|V_s|^2\lambda^2}{\eta_0 bd}\frac{|\vec{E}_1(u_0, v_0)|^2}{\cos\theta_0}, \; b, d \leq \lambda/2 \tag{1}$$

where d and b are the periodic separation between the elements in the x and y directions, η_0 and λ are the free space characteristic impedance and wavelength, V_s is the generator voltage for every element, $E_1(u, v)$ is the far-zone electric field per unit voltage of the generator of a singly excited element in the actual array environment, and u_0 and v_0 are the x and y direction cosines in the main beam direction (θ_0, ϕ_0). Also, (u, v) and (θ, ϕ) are interchangeable angular parameters for the same direction. Throughout this paper, the choice of such parameters is made only for convenience. Element functions are in terms of (θ, ϕ), and array functions are in terms of (u, v). This is especially convenient for linear arrays where the array parameters are functions of u only. The physical interpretation of equation (1) is that, for the ideal case of constant P during scanning, $|E_1|^2$ must be proportional to $\cos\theta_0$, the projection of the aperture in the direction of scan.

For a linear array of periodic spacing d, shown in Figure 1, the power radiated per element in the array environment can be shown to be (Appendix):

$$P = \frac{|V_s|^2\lambda}{\eta_0 d}\int_{-\sqrt{1-u_0^2}}^{\sqrt{1-u_0^2}} \frac{|\vec{E}_1(u_0, v)|^2}{\sqrt{1-u_0^2-v^2}}\,dv, \; d \leq \lambda/2 \quad . \tag{2}$$

A comparison of equations (1) and (2) reveals that the difference in the radiated power per element leads to a difference in the relationship between the element gain and the reflection coefficient, and thus in the expression for the ideal element pattern. Specifically, the simple relationship between the cos θ factor and the optical aperture can no

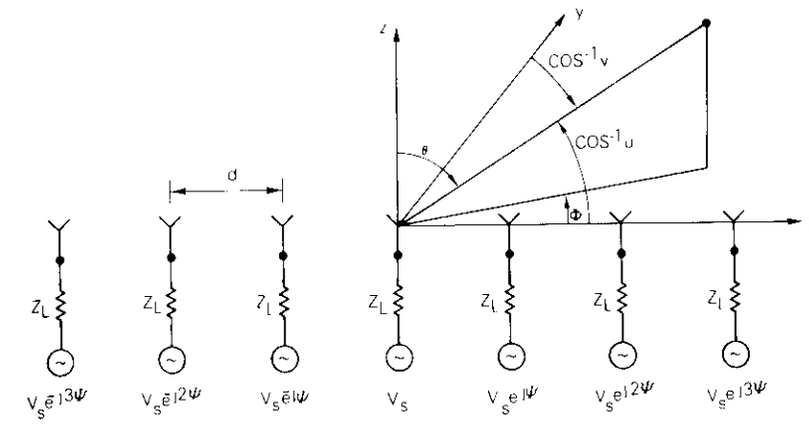

Figure 1. *Linear Phased Array*

longer be applied; this is not surprising because the array now is electrically large in only one direction.

The element pattern $G_e(\theta, \phi)$ in a planar array, defined as the radiation pattern when only one element is excited and all other elements terminated in their generator impedances, can be related to the active reflection coefficient $\rho_a(u, v)$ as [5], [6]

$$G_e(\theta, \phi) = \frac{4\pi bd}{\lambda^2}\cos\theta\,(1 - |\rho_a(u, v)|^2) \tag{3}$$

for $b < \lambda/2$ and $d < \lambda/2$. This shows that for the ideal situation, perfectly matching the array at all angles (ρ_a is zero), the element gain will have the form of cos θ, which can then be defined as the ideal element gain for the planar array, independent of the element type.

For linear arrays, the element pattern can be proven to have the following relation with the active reflection coefficient (Appendix):

$$G_e(\theta, \phi) = \frac{4\pi d}{\lambda}F(\theta, \phi)[1 - |\rho_a(u)|^2] \tag{4}$$

where

$$F(\theta, \phi) = |\vec{E}_1(\theta, \phi)|^2\left\{\int_{-\sqrt{1-u^2}}^{\sqrt{1-u^2}} \frac{|\vec{E}_1(u, v_1)|^2}{\sqrt{1-u^2-v_1^2}}\,dv_1\right\}^{-1}$$

for $d \leq \lambda/2$. The function $F(\theta, \phi)$ is called the ideal element pattern and is the maximum directivity obtainable when the array is matched at all angles. Here $F(\theta, \phi)$ is defined in terms of the element pattern $E_1(\theta, \phi)$ in the terminated environment. In Reference 4, a similar function is shown to be invariant to changes in loads. Thus, it appears that $F(\theta, \phi)$ may also be found by means of a simple integration over element patterns in the open-circuited environment.

Because the main interest in this paper is matching networks and the effect on finite linear arrays, alternative ways of finding $F(\theta, \phi)$ will be presented below. However, one special case, although unphysical, may be treated directly. A finite (or infinite) array of isotropic elements spaced by $\lambda/2$ has purely reactive mutual impedances, which can be matched by a simple interconnecting network [7]. Thus, $\rho_a = 0$, and the integration in equation (4) gives $F = 1/\pi$, leading to $G_e = 2$ independent of scan.

The ideal element pattern obtained by matching the array is equivalent to adjusting the phase velocity in traveling wave antennas. It is known through the Hansen-Woodyard condition that adjusting the phase velocity produces optimum gain at endfire. For a large array of isotropic elements of total length L, the maximum endfire gain obtainable by adjusting the phase velocity to the Hansen-Woodyard condition is $4L/\lambda$. In other directions, the directivity drops to $2L/\lambda$ under the same condition. Equation (4) shows that the ideal element pattern of $G_e = 2$ or of array directivity $2N = 4L/\lambda$ is achievable in all directions, including endfire, if the array is completely matched for all directions. This shows that this optimum directivity is theoretically achievable in all directions, if the array is matched in those directions, or equivalently, if the phase velocity is adjusted to produce the optimum gain.

A more practical case is shown in Figure 2, which gives $F(\theta, \phi)$ for an array of parallel half-wavelength dipoles; the cosine function is also shown. A variation of only 3.5 dB over the complete scanning range is theoretically possible. More important are the obtainable absolute gain values.

Large array of elementary dipoles

The element gain $G_e(\theta, \phi)$ can also be written in terms of the element pattern in the open-circuited array environment $G_{e1}(\theta, \phi)$ as [8]

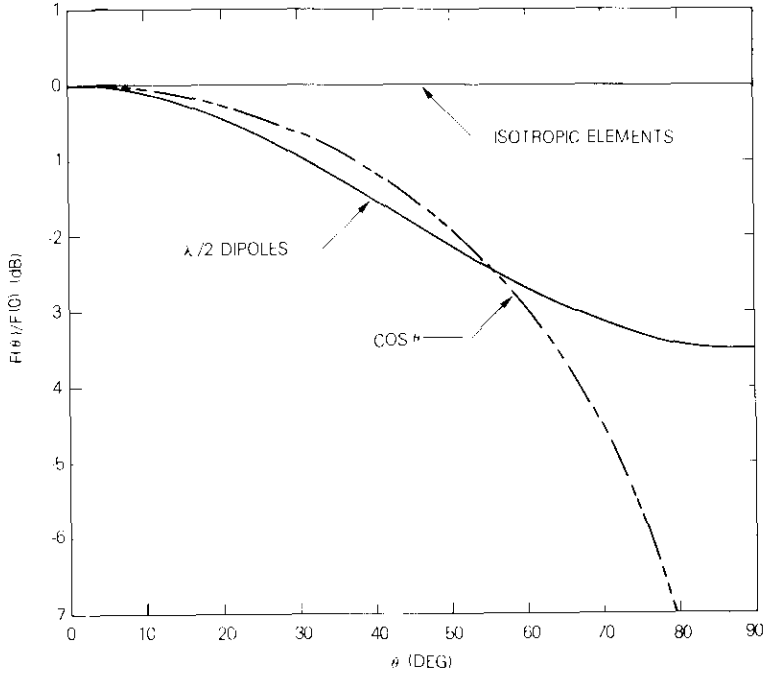

Figure 2. *Function $F(\theta)$ for Infinite Array of Isotropic Elements and Infinite Array of Parallel Half-Wavelength Dipoles*

$$G_e(\theta, \phi) = \frac{4Z_L R_0 G_{e1}(\theta, \phi)}{|Z_L + Z_{in}(\theta)|^2} \tag{5}$$

where Z_L is a resistive load impedance, Figure 1, and $Z_{in}(\theta)$ is the input impedance when the array is scanned to radiate a main beam in direction θ. For a large $(2M + 1)$ element array, the input impedance of the central element Z_{in} can be shown to be

$$Z_{in} = jX + Z_0 + 2 \sum_{m=1}^{M} Z_m \cos(md k_0 \sin\theta) \tag{6}$$

where X is a reactance inserted on the output side of the element, Z_0 is its self impedance, Z_m is the mutual impedance between this element and the element spaced a distance of md, and k_0 is the free-space wave

number. The term R_0 is the real part of Z_0. The array can be matched at one angle by choosing X to eliminate the imaginary part of Z_{in} and Z_L to be equal to the real part of Z_{in}.

From the definition of the active reflection coefficient ρ_a and from equations (4) and (5), the ideal-element gain function $F(\theta, \phi)$ can be related to the input impedance by

$$F(\theta, \phi) = \frac{\lambda}{4\pi d} \frac{R_0 G_{e1}(\theta, \phi)}{\mathrm{Re}(z_{in})} \quad . \tag{7}$$

Equation (7) illustrates the remark on invariance following equation (4). The real part of Z_{in}, and thus, the function $F(\theta, \phi)$ is invariant to changes in loads (as shown in Reference 4).

For an infinitely large array of parallel dipoles, the real part of $Z_{in}^{\infty}(\theta)$ is given by

$$\mathrm{Re}\,[Z_{in}^{\infty}(\theta)] = \frac{3\pi}{4kd}(1 + \sin^2\theta), \theta < \pi/2 \quad . \tag{8}$$

Based on equation (8), it would not be difficult to match the array near endfire, in contrast to the planar array which would have $\mathrm{Re}[Z_{in}(\pi/2)]$ either infinite or zero. However, the reactive part is more detrimental, which is easily seen when the relationship for the normalized mutual impedance is used:

$$Z_m = j\tfrac{3}{2}\left[\frac{1}{mk_0d} - \frac{1}{(mk_0d)^3} - \frac{j}{(mk_0d)^2}\right] e^{-jmk_0d}, m > 0 \quad . \tag{9}$$

Substituting equation (9) into (6), the input reactance of the central element in a $(2M + 1)$ element array is

$$X_{in}(\theta) = X + X_0 + 3\sum_{m=1}^{M}\left[\left(\frac{1}{mk_0d} - \frac{1}{(mk_0d)^3}\right)\cos mk_0d - \frac{\sin mk_0d}{(mk_0d)^2}\right]\cos(mk_0d\sin\theta) \quad . \tag{10}$$

Except for $\theta = \pi/2$, the series converges quickly, but for $\theta = \pi/2$ and $k_0d = \pi$, the series takes the form

$$\sum_{m=1}^{M}\left[\frac{1}{m\pi} - \frac{1}{(m\pi)^3}\right] \tag{11}$$

which diverges. It is important to note though, that the sum increases only logarithmically with M, so that even for M of the order of 100–1000, the mismatch of a central element is not large, when X is chosen properly. In practice, $\theta = \pi/2$ would be avoided when $k_0d = \pi$ because of the grating lobe emergence at this angle.

The optimum choice of Z_L and X can play the main role in obtaining the desired element gain pattern as dictated by equation (5). Consider the problem of a large array of parallel small dipoles, spaced half-a-wavelength, $k_0d = \pi$ with a scanning range of $\pm 80°$ from broadside. The question is how to choose the loading Z_L and X such that the minimum gain over the scanning range is maximized. It is further assumed that each element is self-resonant when isolated, so that X only takes care of the mutual effects. The impedance values at $\theta = 0°$ and $\theta = 80°$ for $M = 100$ are

$$Z_{in}(0°) = 0.75 - j0.57 + jX$$

$$Z_{in}(80°) = 1.477 + j2.6 + jX$$

where the reactive part corresponds to the sum in equation (10). The optimum loading can be found graphically as shown in Figure 3 in the domain of Z_L and X. The circles of equal gain at $\theta = 0°$ and at $\theta = 80°$ are drawn, determining the straight line that defines the locus of equal gain at those two angles. The maximum value of this equal gain is found to be -2.05 dB over the isolated element gain; that is, the minimum realized gain per element is -0.30 over isotropic. This occurs when $Z_L = 1.935$ and $X = -1.710$. It should be noted that this value of load impedance does not correspond to an impedance match at any angle. The curve showing the values of Z_L and X resulting in matching at specific angles is given in the same figure for reference. The element gain pattern is shown in Figure 4, together with the case when the scanning range is extended to endfire, $\theta = 90°$.

Because equations (6), (9)–(11) are valid only for the central element of a $(2M + 1)$ element array, the results of Figures 3 and 4 are strictly correct for that element only. For large arrays, this is valid for elements in the central region of the array, representing the majority of the elements. The edge elements can be treated similarly after replacing equation (6) with the proper expression for Z_{in}.

Interconnecting network

Bach Andersen and Rasmussen [7] showed that a class of lossless

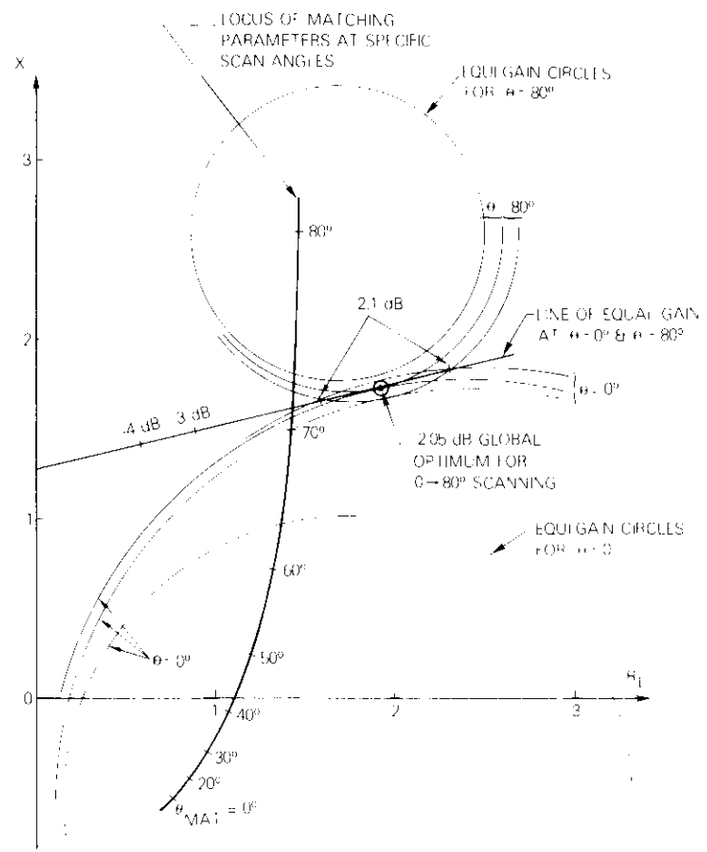

Figure 3. *Optimization of the Matching Parameters for 0°–80° Scanning*

decoupling and descattering networks can have the effect of nullifying the reactive part of the mutual impedances between elements in the array by connecting those elements by lossless transmission lines of proper lengths and characteristic impedances. Complete decoupling occurs when the resistive components of the mutual impedances are zero, thus obtaining the ideal element pattern as in the hypothetical case of an array of isotropic elements with spacing λ/2. For practical situations, however, the mutual resistances between the elements are not all zero and the improvement due to the network depends on the type of element and the spacing in the array.

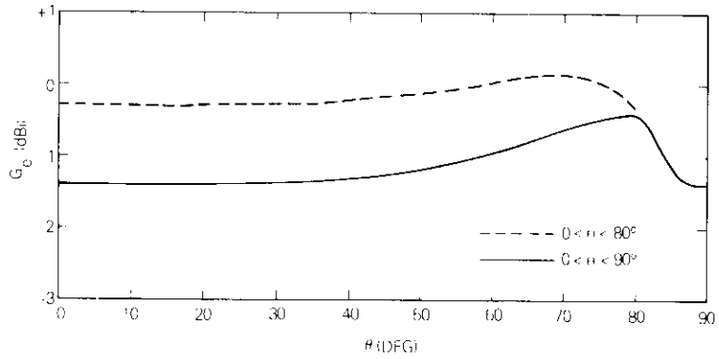

Figure 4. *Element Gain in dBi for Parallel, Small Dipoles with Optimum Loading as a Function of Scan Angle. M = 100.*

More complicated networks are theoretically possible [9], but as will be shown, the element patterns approach the ideal element patterns closely (within 0.5 dB) when this type of network is used. The simplicity of these and other interconnecting networks is only theoretical, because in practice it is impossible to connect each element with all other elements.

The example in Figure 5 illustrates the effect of this kind of network on the normalized element gain function of an array of resonant λ/2 dipoles with 25 elements and periodic spacing of 0.5λ. The curve is computed by exciting the center element and loading the other elements passively. Standard mutual impedances for thin wires have been used, and the interconnecting networks are simulated by nulling mutual reactances. The load impedance Z_L is chosen as the self resistance of the antenna element. The element pattern without the network is shown along with the pattern when a complete decoupling network is used. The element pattern gain for the unconnected array as a result of introducing the network is far above the ideal planar array pattern gain for most of the scanning range, and at endfire, there is a drop in gain of only 3.5 dB.

From a practical point of view, it is always desirable to reduce the size of the decoupling network, especially for large arrays. The effect of network size is studied in Figure 6, where the element pattern levels at two angles, 70° and 90°, are shown for the same example discussed above as the complexity of the network is increased from merely connecting every two neighboring elements to interconnecting all the elements in the array. The early saturation of the curves is to be noted.

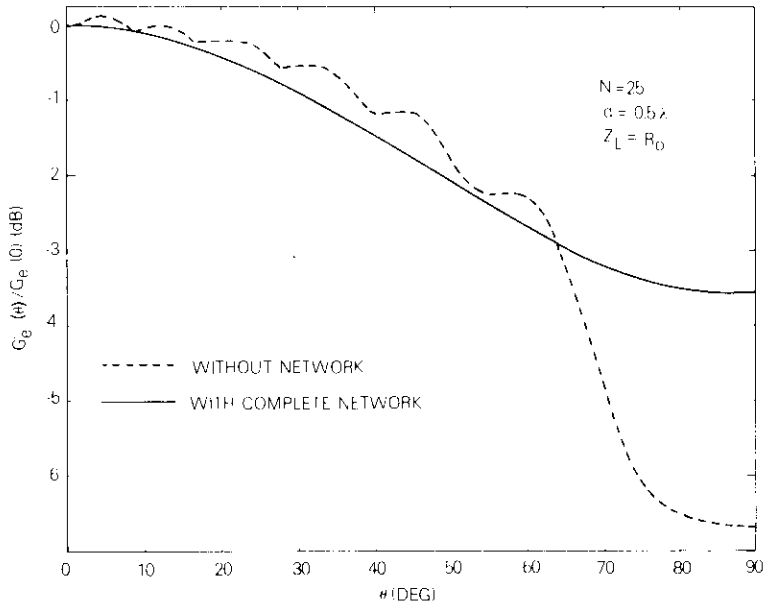

Figure 5. *Normalized Element Gains for a 25-Element Array of Half-Wavelength Dipoles*

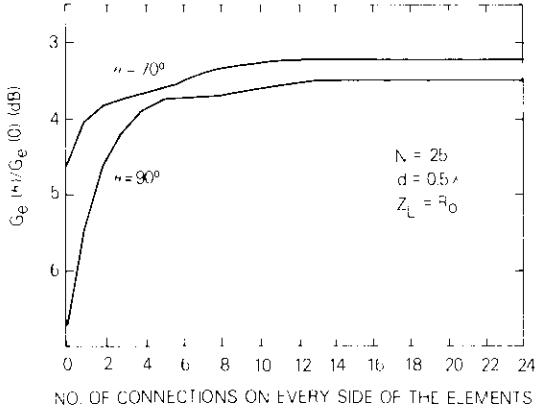

Figure 6. *Relative Element Gain Level of a 25-Element Array at θ = 70° and 90° for Different Network Sizes*

Further increases in the network size have little effect on the overall performance of the network.

The decoupling network can also be used in conjunction with the "ordinary matching" networks. Ordinary matching is matching the array at one angle without changing the nature of mutual impedances through interconnecting network or otherwise. To illustrate this principle, consider a 25-element array of parallel half-wavelength dipoles separated by λ/2. The ordinary matching at $\theta_{mat} = 70°$ is found to produce the maximum "minimum gain" in comparison with matching at other angles. This also produces the minimum variation of the element gain, and thus a nearly constant array gain over the full scanning range of ±90°. This is not the global optimum matching of Figure 3 that does not correspond to matching at a specific angle. Introducing an interconnecting network increases the average element gain and smooths the gain variation over the scanning range. Figure 7 shows the element patterns for the two matching angles of 70° and broadside (0°), with and without the complete decoupling network.

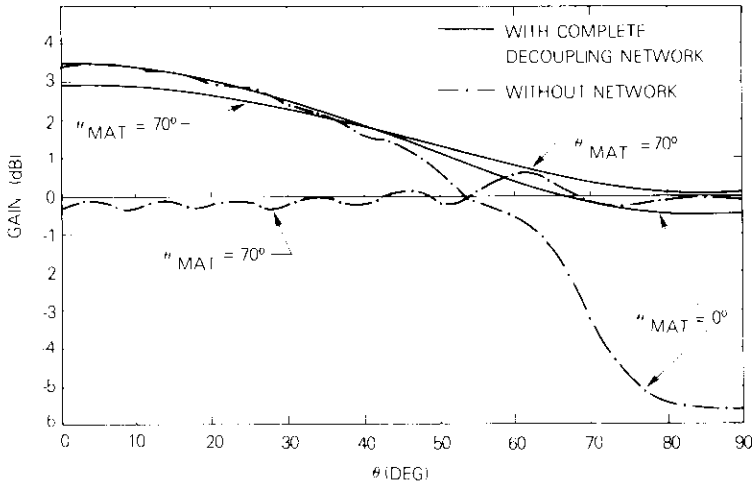

Figure 7. *Element Pattern for Different Matching Angles for Arrays With and Without Decoupling Networks*

The improvement in element gain patterns is a result of reducing the reflection coefficient over the scanning range as predicted in equation (4). Figure 8 depicts the variation of active reflection coefficients for the 25-element dipole array, with and without the intercon-

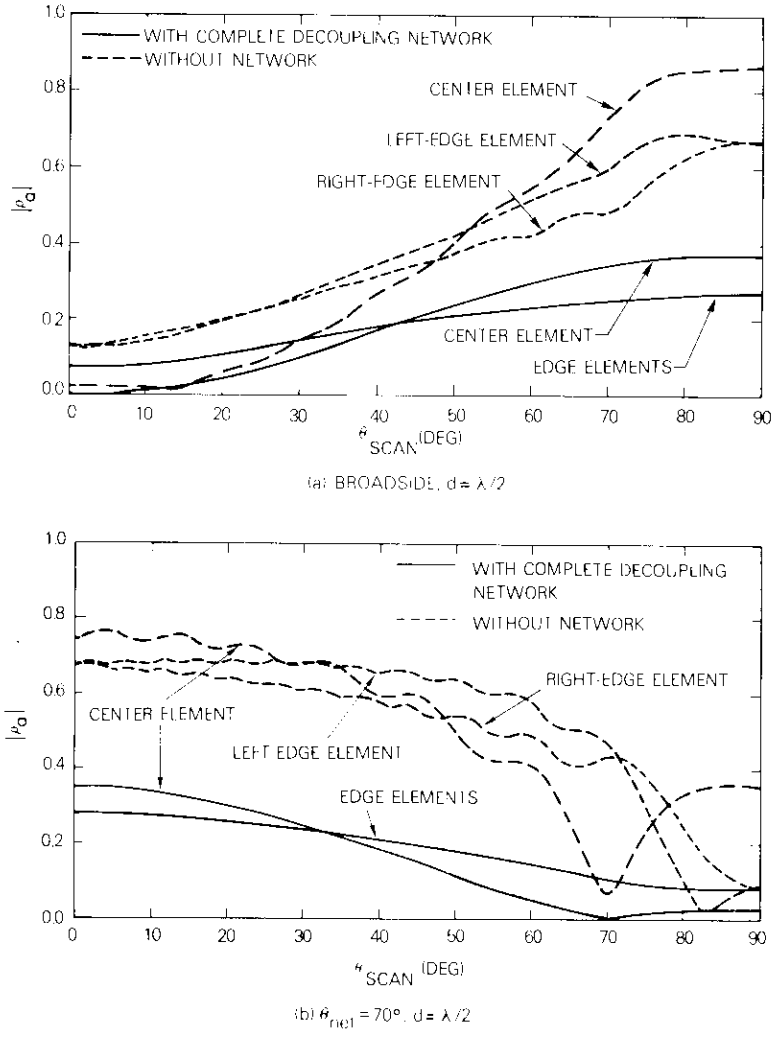

Figure 8. *Magnitude of Active Reflection Coefficient for a 25-Element Array Matched at Broadside, $d = \lambda/2$ and $\theta_{net} = 70°$, $d = \lambda/2$*

necting network. Figure 8a shows the case when the array is ordinary-matched at broadside and Figure 8b when the array is matched at $\theta_{mat} = 70°$.

Conclusions

The linear phased arrays are not merely a special case of the general planar arrays; they have unique fundamental features. For planar arrays, the ideal element pattern is the cos θ factor; for linear arrays the ideal element pattern depends on the type of element.

Parallel Hertzian and half-wave dipoles have been used in this work. Narrow slots are also amenable to the same argument.

Special interconnecting networks can be used to reduce the reactive coupling between the elements in the array, and thus improve the element pattern. The ordinary matching scheme can also be used to produce a complete match in one direction. This has been shown to give an almost constant gain with scan over the complete scanning range with about 0-dB gain per element.

Acknowledgments

Many ideas presented in this paper were initiated during the author's stay at Aalborg University Centre in Denmark. Thanks are due to J. Bach Andersen of that institution, who contributed immensely to this work. Thanks are also due to D. F. DiFonzo and G. Hyde of COMSAT *Laboratories, who showed interest in this work and with whom the author had many fruitful discussions, especially in connection with comparing the results in this paper with the Hansen-Woodyard endfire condition.*

References

[1] W. H. von Aulock, "Properties of Phased Arrays," *Proceedings of the IRE*, Vol. 48, October 1960, pp. 1715–1727.

[2] R. S. Elliott, "Beamwidth and Directivity of Large Scanning Arrays," *Microwave Journal*, Part 1, Vol. 6, December 1963, pp. 53–60, and Part 2, Vol. 7, January 1964, pp. 74–82.

[3] W. Wasylkiwsky and W. Kahn, "Mutual Coupling and Element Efficiency for Infinite Linear Arrays," *Proceedings of the IEEE*, Vol. 56, November 1968, pp. 1901–1907.

[4] W. Wasylkiwsky and W. Kahn, "Element Pattern Bounds in Uniform Phased Arrays," *IEEE Transactions on Antennas and Propagation*, Vol. AP-25, September 1977, pp. 597–604.

[5] N. Amitay, V. Galindo, and C. P. Wu, *Theory and Analysis of Phased Array Antennas*, Wiley-Interscience, Chapter 1, 1972.

[6] P. W. Hannan, "The Element Gain Paradox for Phased-Array Antennas," *IEEE Transactions on Antennas and Propagation*, Vol. AP-12, July 1964, pp. 423–433.

[7] J. Bach Andersen and H. Rasmussen, "Decoupling and Descattering Networks for Antennas," *IEEE Transactions on Antennas and Propagation*, Vol. AP-24, November 1976, pp. 841–846.

[8] J. L. Allen, "Gain and Impedance Variation in Scanned Dipole Arrays," *IEEE Transactions on Antennas and Propagation*, Vol. AP-10, September 1962, pp. 566–572.

[9] P. W. Hannan, "Proof That a Phased-Array Antenna Can Be Impedance Matched for All Scan Angles," *Radio Science*, Vol. 2, March 1967, pp. 361–369.

Appendix

The total power radiated by an array into space is given by

$$P_t = \frac{1}{\eta_0}\int_0^{\pi}\int_0^{2\pi} |\vec{E}_t(\theta, \phi)|^2 \sin\theta \, d\theta \, d\phi \tag{A-1}$$

where η_0 is the free space characteristic impedance, and $\vec{E}_t(\theta, \phi)$ is the electric field in direction (θ, ϕ) when the elements in the array are excited with a voltage V_s and progressive phase so that the main beam of the array pattern is in direction (u_0, v). In this case $\vec{E}_t(\theta, \phi)$ is given by

$$\vec{E}_t(\theta, \phi) = V_s \vec{E}_1(\theta, \phi)\, S_a(u - u_0) \tag{A-2}$$

where $\vec{E}_1(\theta, \phi)$ is the farfield per unit voltage of a singly excited element in the actual array environment, and S_a is the array factor:

$$S_a(u - u_0) = \frac{\sin[(N\pi d/\lambda)(u - u_0)]}{\sin[(\pi d/\lambda)(u - u_0)]} \quad . \tag{A-3}$$

Equation (A-1) can be written in terms of the directional cosines as

$$P_t = \frac{1}{\eta_0}\iint_{u^2+v^2\le 1} \frac{|\vec{E}_t(u, v)|^2}{\sqrt{1 - u^2 - v^2}}\, du\, dv \quad . \tag{A-4}$$

When equations (A-2) through (A-4) are combined, P_t is given as

$$P_t = \frac{|V_s|^2}{\eta_0}\int_{u=-1}^{1} S_a(u - u_0) \int_{-\sqrt{1-u^2}}^{\sqrt{1-u^2}} \frac{|\vec{E}_1(u, v)|^2}{\sqrt{1 - u^2 - v^2}}\, dv\, du \quad . \tag{A-5}$$

For a large array, the array factor takes the form of a Dirac-delta function and equation (A-5) can be reduced to the single integration

$$P_t = \frac{|V_s|^2 N\lambda}{\eta_0 d}\int_{-\sqrt{1-u_0^2}}^{\sqrt{1-u_0^2}} \frac{|\vec{E}_1(u_0, v)|^2}{\sqrt{1 - u_0^2 - v^2}}\, dv \tag{A-6}$$

for arrays with $d \le \lambda/2$. The average power radiated per element, $\bar{P}$, is thus given by

$$\bar{P} = \frac{|V_s|^2\lambda}{\eta_0 d}\int_{-\sqrt{1-u_0^2}}^{\sqrt{1-u_0^2}} \frac{|\vec{E}_1(u_0, v)|^2}{\sqrt{1 - u_0^2 - v^2}}\, dv \quad . \tag{A-7}$$

In active arrays (arrays where all elements are excited), the "active" radiated power per element, P_a, is related to the active reflection coefficient $\rho_a(u_0)$ through

$$P_a = \frac{|V_s|^2}{4Z_L}[1 - |\rho_a(u_0)|^2] \tag{A-8}$$

where $|V_s|^2/4Z_L$ represents the available power from each generator that is loaded with a load impedance of Z_L. The element pattern is defined as the radiation pattern when only one element in the array is excited and all other elements are terminated with their generator impedances. This type of operation produces a "passive" reflection coefficient $\rho_p(\theta, \phi)$ at the terminals of the excited element, and the element pattern will have a power gain of

$$G_e(u, v) = \text{directivity} \times [1 - |\rho_p(\theta, \phi)|^2] \tag{A-9}$$

which, from the definition of directivity, is given by

$$G_e(\theta, \phi) = \frac{4\pi|\vec{E}_1(\theta, \phi)|^2}{\int_0^{\pi/2}\int_0^{2\pi} |\vec{E}_1(\theta, \phi)|^2 \sin\theta \, d\theta \, d\phi}[1 - |\rho_p(\theta, \phi)|^2] \quad . \tag{A-10}$$

Since the radiated power in this case is given by

$$\begin{aligned} P_p &= \frac{|V_s|^2}{4Z_L}[1 - |\rho_p(\theta, \phi)|^2] \\ &= \frac{|V_s|^2}{\eta_0}\int_0^{\pi/2}\int_0^{2\pi} |\vec{E}_1(\theta, \phi)|^2 \sin\theta \, d\theta \, d\phi \end{aligned} \tag{A-11}$$

the element pattern will have the gain

$$G_e(\theta, \phi) = \frac{16\pi Z_L}{\eta_0}|\vec{E}_1(\theta, \phi)|^2 \quad . \tag{A-12}$$

To establish a relationship between the element gain and the active reflection coefficient, use equations (A-7), (A-8), and (A-12) to arrive at the following expression:

$$G_e(\theta, \phi) = \frac{4\pi d}{\lambda} \frac{|\dot{E}_1(\theta, \phi)|^2 [1 - |\rho_a(u)|^2]}{\int_{-\sqrt{1-u^2}}^{\sqrt{1-u^2}} \frac{|\vec{E}_1(u, v_1)|^2}{\sqrt{1 - u^2 - v_1^2}} dv_1} \qquad \text{(A-13)}$$

which can be rewritten as

$$G_e(\theta, \phi) = \frac{4\pi d}{\lambda} F(\theta, \phi)[1 - |\rho_a(u)|^2] \qquad \text{(A-14)}$$

where

$$F(\theta, \phi) = |\dot{E}_1(\theta, \phi)|^2 \left[\int_{-\sqrt{1-u^2}}^{\sqrt{1-u^2}} \frac{|\vec{E}_1(u, v_1)|^2}{\sqrt{1 - u^2 - v_1^2}} dv_1 \right]^{-1} .$$

Equation (A-14) relates two conditions of operating the array: passive operation from which the element gain in direction (θ, ϕ) is calculated, and active operation from which the reflection coefficient in direction u is calculated.

Amir I. Zaghloul received a B.Sc. from Cairo University, Egypt, in 1965 and an M.A.Sc. and a Ph.D. from the University of Waterloo, Canada, in 1970 and 1973, all in electrical engineering. Before joining COMSAT Laboratories in 1978 he held research and teaching faculty positions at the Universities of Waterloo and Toronto, in Canada; Aalborg University Centre, in Denmark; and Al-Azhar University in Egypt. At COMSAT Laboratories he has been a Member of the Technical Staff in the Microwave Systems Department and later in the Satellite Antennas Department. His responsibilities included design and development of microwave integrated circuits; microwave switch matrix for SS-TDMA systems; and phased array, slot array, and reflector antenna systems.

Dr. Zaghloul has been also involved in study and support efforts for several satellite programs, including INTELSAT IV, ARABSAT and SATCOL. He is a senior member of the IEEE.

Index: computer communications, multiplexing (multiplexers), networks, TDMA

Capacity allocation scheme for transmission of packets over satellite links

D. M. CHITRE

(Manuscript received October 22, 1981)

Abstract

A baseband capacity allocation algorithm, which is simple to implement and provides high throughput with low average queueing delay, has been developed for transmission of data packets over satellite links. Consideration is given to the processing capability of the receiving station. Packets arriving at a station for transmission to different destinations are placed either in a single-destinational queue or a multidestinational queue, depending upon the current status of the queue. A Markov model is used to determine the average queueing delay. The incoming traffic is monitored and capacities are allocated to service single and multidestinational queues according to the specified grade of service performance.

Introduction

The capacity allocation for transmission of packets over satellite links can be divided into two parts: first, the baseband capacity requirement for a transmitting station must be defined, and, second, the specific procedure for accessing the satellite channel to support

the required baseband capacity needs to be determined. Various demand-assigned multiple-access (DAMA) schemes address the second issue, and a considerable body of work [1]–[3] deals with methods for sharing satellite broadcast channels. The issue of the baseband capacity required for transmission of packets arriving over various terrestrial input lines at an earth station is considered here.

In contrast to teletraffic for which the required number of channels depends on the number of terrestrial input lines, for packet traffic, a baseband channel can support a multitude of users through the use of statistical multiplexing and/or packet switching. A local measure is described in this paper which, with the use of simple look-up tables, can determine the baseband capacity requirement. The baseband capacity allocation algorithm that has been developed is based on the statistical average of the incoming traffic over terrestrial lines and a required acceptable queueing delay before transmission over the satellite link. The algorithm is described in two phases.

In the first phase, the limitation on the processing capability of the receiving nodes is not taken into account. All the packets arriving over various terrestrial input lines at a given earth station and addressed to different earth station destinations are statistically multiplexed and placed in a common output queue for transmission. Through the use of the suitable local measure to determine the baseband capacity requirement, this scheme leads to the best baseband channel utilization, because it uses statistical multiplexing in the most effective manner.

The above scheme works well as long as no receiving station becomes overloaded. As an example, consider a simple case of a network of N earth stations within a global beam, each assigned a satellite channel of capacity C. Each station then receives data that could be addressed to it at the rate of $(N - 1) \times C$ bit/s. Thus, for a network consisting of several nodes, it may not be practical for every earth station to be able to scan the packet headers (to find the packets addressed to it) at the rate at which they are being received. This condition of overloading would make the system unstable.

A second capacity allocation algorithm is described which takes into account the above processing limitation. It is shown that by the proper use of a single multidestinational channel, the performance of the second algorithm can closely approximate that of the first algorithm.

The proposed algorithms are simple to implement and permit high channel utilization (better than 90 percent) with low queueing delays of the order of 10 to 15 ms. This is a considerable improvement in performance, as can be seen from Figure 1, which gives the performance

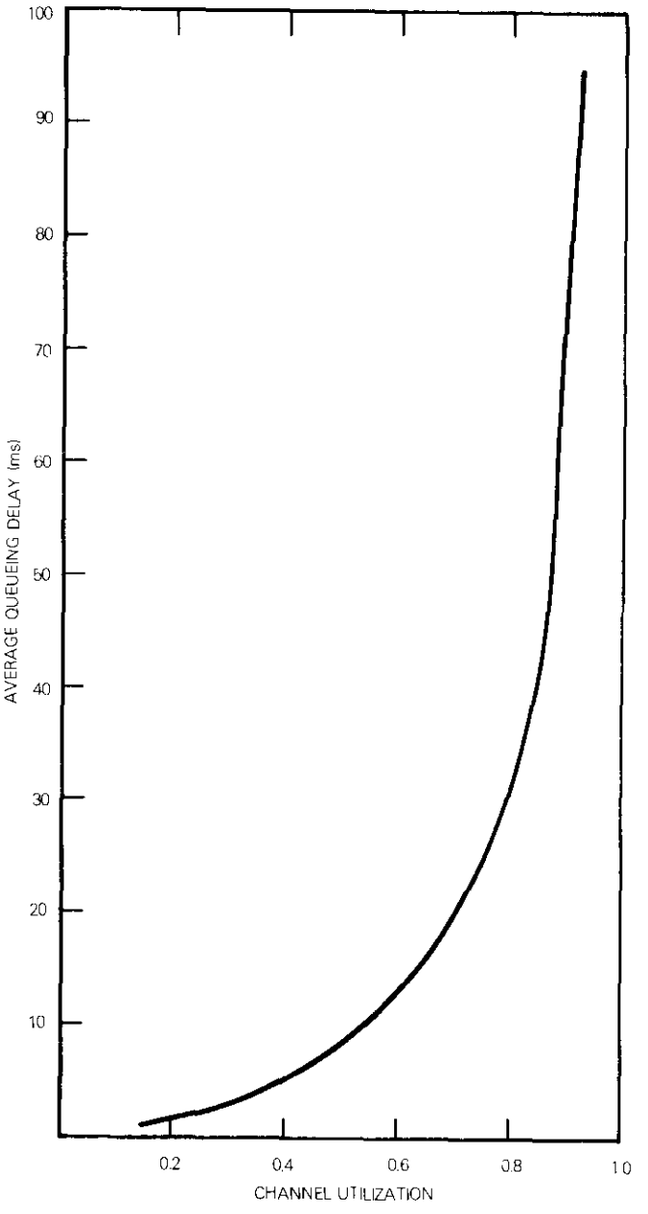

Figure 1. *Average Queueing Delay* vs *Channel Utilization for the Packet Traffic Served by a Channel of Capacity 64 kbit/s*

curve without using those algorithms. The next section describes their structures. Then, the mathematical modeling and analysis are carried out. The last section gives the tables to be used to implement these algorithms and presents the performance curves for different system parameters.

Capacity allocation algorithm

A packet-switching network with internodal links provided by satellite channels is considered. Baseband data streams are assembled as satellite packets with the source and destination encoded in the packet header, and then placed in transmit queues. Baseband channel capacity associated with a transmit queue is defined as the server capacity servicing that transmit queue.

First, a capacity allocation scheme is described in which all the packet traffic at one node (addressed to different destinations) is statistically multiplexed and placed in a common transmit queue. The incoming traffic activity is constantly monitored. The average number of packets placed in the transmit queue is computed by counting the number of packets going to that queue in a given time interval. The baseband capacity required to serve the packet traffic at that node is then computed for the acceptable queueing delay. Because the packets from different users are interleaved, the total input of packet traffic tends to be uniformly distributed as the number of sources increases; this occurs despite the bursty nature of each user's traffic. The maximum possible usage of statistical multiplexing in this scheme leads to high baseband channel utilization. The expression for queueing delay as a function of incoming average traffic and the baseband channel capacity are given in the following section. A table of capacity allocation for a particular value of queueing delay is presented next.

Statistical multiplexing of all packet traffic addressed to different destinations may not always be feasible. As stated earlier, a packet node may not find it practical to scan the headers to find packets addressed to it at a rate at which it is receiving packets. Also, in a mixed multibeam and global beam environment, packets transmitted on a narrow beam must be single destinational (or restricted to destinations covered by a narrow beam), unless there is a processor on board to scan the addresses. A new algorithm for capacity allocation is presented that takes into account the above considerations and is applicable whenever there is a provision of at least one multidestinational channel.

The general architecture at each node consists of several single-destinational transmit queues and one multidestinational queue. Each single-destinational transmit queue is restricted to only a specified maximum number of packets awaiting service. Any additional packets are routed to the multidestinational queue. A Markov model is used to compute the average queueing delay for this system. The traffic is monitored at each queue, and the number of packets arriving and the number of packets transferred from each queue to the multidestinational queue are counted over a predetermined time interval. The Markov model is solved, with the given grade of service delay requirement and 100-percent throughput on all single-destinational channels, to compute the baseband capacity required to serve the incoming packet traffic. The throughput for each single-destinational channel is defined as the number of packets arriving for that destination during the service time of a packet on that channel.

The system architecture is stable against variations in traffic (subject to total traffic being accommodated in the total baseband capacity allocated to that transmitting station) as the sum of the overflow of traffic from single-destinational queues is diverted to the multidestinational queue, thus smearing out individual single-destinational traffic changes. Hence, the system essentially moves from one Markov description of a certain set of values for capacities (and maximum queue lengths) for different transmit queues to another set of values, depending upon the traffic pattern. Whenever the average number of packets routed to the multidestinational channel from a single-destinational queue is not within a predetermined range, either more capacity for that destination is requested or a certain amount of capacity allocated to it is relinquished; while the total baseband capacity assigned to that station remains fixed. Capacity channels to serve the single-destinational queue are redistributed to assure the grade of service delay requirement, and at the same time, high utilization of baseband capacity is maintained.

The baseband reallocation scheme described above works on two levels. First, when the traffic pattern for single-destinational channels changes without the total traffic changing beyond certain levels, then the capacity is redistributed and other nodes are informed of it via a multidestinational channel. In essence, this procedure of the second algorithm mimics the advantage of the total statistical multiplexing of packets (to different destinations) of the first algorithm, within the constraints of the limitation of the processing capability of the receiving nodes.

On the second level, the traffic pattern could change such that the baseband capacity requirement given by the algorithm could indicate either an increase or decrease in the overall satellite capacity assigned to that node. That information would be relayed to whichever DAMA scheme is being used. In the second algorithm, more information is available (through the monitoring of traffic to each destination) regarding the changes in the traffic pattern. For moderate traffic changes, the increase in incoming traffic for a particular destination that warrants more capacity would not increase the queueing delay significantly because the increase in the overflow would be handled by the multidestinational channel. On the other hand, if the decrease in the traffic warrants relinquishing some capacity, it would not cause significant underutilization of the channel, because the fluctuations are around the values set at 100-percent throughput (resulting in high utilization). The above arguments are valid for moderate traffic changes; when drastic changes occur, the performance degradation in either of the algorithms described above would be comparable.

Delay analysis

The baseband capacity allocation algorithms described above are quite general. They are independent of any multiple-access method and can be adapted to an FDMA or TDMA scheme. They can be embedded in either a distributed or a centrally controlled way of acquiring and releasing satellite channel capacities. For mathematical analysis, the algorithms are applied to certain specific systems.

For the first algorithm, in which the packets of data (coming over all the input lines) are placed in a common queue, it is assumed that they follow a Poisson arrival distribution and are served by a baseband channel of capacity C. Then, the queueing delay, d, can be obtained from an $M/D/1$ model as [4]

$$d = \frac{\lambda\tau^2}{2(1 - \lambda\tau)} \tag{1}$$

where λ is the average number of packets arriving per second, and $\tau = b/C$ is the transmission time with b as the packet size and C as the server capacity. By monitoring the incoming traffic and determining the average traffic level, the baseband capacity required for an acceptable value of the queueing delay can be computed from equation (1). As the average traffic changes by a certain amount, so does the allocation of the baseband capacity. In the next section, a numerical

example is discussed, giving a table for capacity allocation for different ranges of incoming traffic and for different grades of service queueing delays.

The second algorithm, in which different transmit queues are formed for different destinations along with a multidestination queue, is applied to a TDMA system. In TDMA, each earth station transmits a burst of bits for a specified time, depending upon its allocated satellite capacity. The transmission times of the bursts are carefully controlled so that no two bursts from different earth stations will overlap. Each earth station accesses the satellite channel every F seconds, which is called the frame period. The frame format of this system is illustrated in Figure 2.

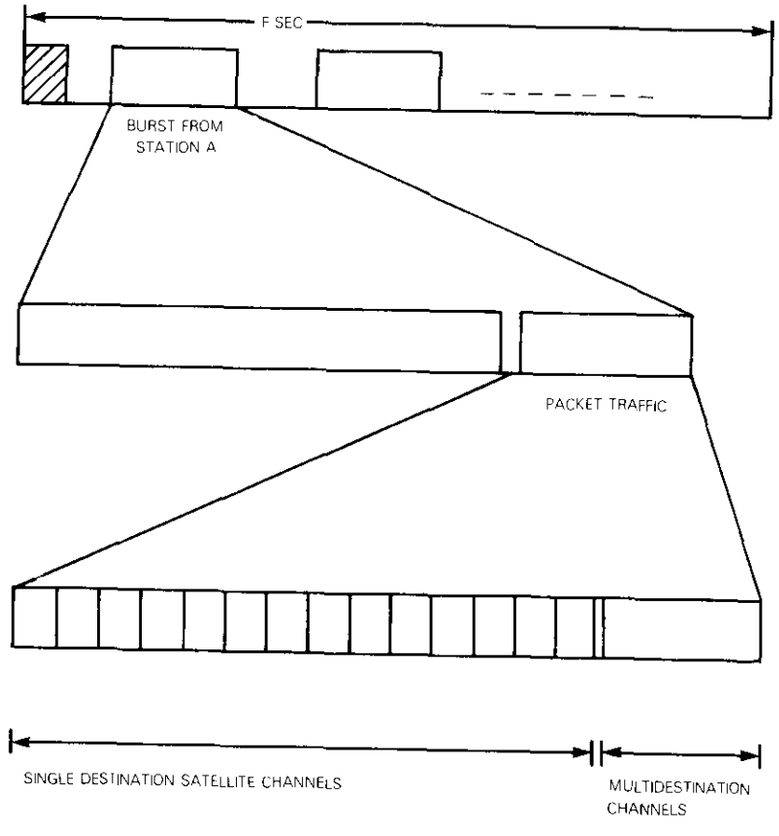

Figure 2. *TDMA Frame Format*

At each station, the incoming data streams are assembled as satellite packets with the source and destination encoded in the packet header and are placed in different transmit queues according to their destinations, provided that the number of packets in the transmit queue is less than a certain predetermined value. Otherwise, the packet is placed in the transmit queue of the multidestinational channel. Let C_I be the baseband capacity serving the transmit queue for destination I, and C_M the capacity allocated for the multidestinational queue. Let b_I be the packet size and λ_I the average number of packets for destination I, arriving per second at the earth station. It is assumed that the packets for each destination arrive with a Poisson distribution. Packets, or portions of them, are transmitted from each queue during a traffic burst every F seconds. Let the packet of size b_I be divided into n_I number of units, such that one unit is transmitted every F seconds, where n_I is given by

$$b_I = C_I \cdot F \cdot n_I \quad . \tag{2}$$

The packet size b_I can be adjusted to give integral values to n_I. The number of units in each transmit queue at the beginning of the frame, just after transmission, represents the state of the discrete time Markov chain. The stationary probability distribution for this system exists and can be computed by solving the following sets of equations:

$$\Pi_j^I = \sum_{i=0}^{\ell_I} \Pi_i^I P_{ij}^I \tag{3}$$

where Π_i^I = probability of having i units waiting in the transmit queue for destination I at the beginning of a frame (just after transmission)

ℓ_I = maximum possible number of units in the queue at that time

P_{ij}^I = transition probability of finding j units in the transmit queue at the beginning of a frame when there were i units at the beginning of the previous frame.

A newly arrived packet is placed in the multidestinational queue whenever it finds m_I, or more units waiting in its destinational queue. The terms ℓ_I and m_I are related by the following equation:

$$\ell_I = n_I + (m_I - 1) - 1 \quad . \tag{4}$$

The transition probability matrix P_{ij}^I is a function of m_I, n_I, and the arrival distribution of the packet traffic for the destination I. P_{ij}^I is first calculated and then substituted in equation (3), which is then solved for Π_j^I, $0 \le j \le \ell_I$. The average number of packets arriving at the multidestinational queue is computed by adding the average number of packets routed from each of the single-destinational transmit queues.

Because packets for each destination arrive with a Poisson distribution, their arrival times are distributed uniformly. Thus, the probability of a packet arriving between time t and $t + dt$ during the frame period F is dt/F; and the probability of that packet finding n units waiting in the transmit queue for destination I is

$$a_n^I = \sum_{i=0}^{n} \Pi_i^I p_{n-i}^I(t) \tag{5}$$

where $p_{n-i}^I(t)$ is the probability of $(n - i)$ units arriving for destination i in time t. The probability that a newly arrived packet for destination I will be diverted to the multidestinational transmit queue is equal to

$$1 - \sum_{n=0}^{m_I - I} a_n^I \quad . \tag{6}$$

The average queueing delay is then given by

$$\bar{D}^I = \int_o^F \frac{dt}{F} \left\{ \sum_{n=0}^{m_I - 1} [(n + 1)F - t]\, a_n^I + \bar{D}_M \left[1 - \sum_{n=0}^{m_I - 1} a_n^I \right] \right\} \tag{7}$$

where $\bar{D}_M$ is the average queueing delay for a packet in the multidestinational queue, which will be computed by assuming that the sum of the overflow traffic from various single-destinational queues follows a Poisson distribution.

The above expressions for probability and delay are applicable when the baseband capacity serving the single-destinational queue is such that a packet or a portion of it can be transmitted during one frame period. When more than one packet can be serviced from a single-destinational transmit queue during a frame period, the above equations need to be suitably modified.

In the next section, the above analysis is applied to specific examples to show that proper choice of values for ℓ_I (the maximum number of units allowed to wait in each single-destinational transmit queue), C_I, and C_M, can produce low queueing delay and high throughput.

Numerical examples

The baseband capacity is assumed to be available in units of 64-kbit/s channels. For the permissible queueing delay of 10 ms, the required baseband capacity is obtained from equation (1) as

$$C_R = \left[\frac{\lambda b}{2} \cdot \frac{1}{64000}\left(1 + \sqrt{1 + \frac{200}{\lambda}}\right)\right]$$

where λ is the average packet traffic (in packets per second) input to the transmit queue and b is the packet size in bits. The expression in the brackets is rounded to the next higher integer. Table 1 shows the capacity requirements for ranges of input packet traffic for an acceptable average queueing delay of 10 ms.

TABLE 1. BASEBAND CAPACITY REQUIREMENTS FOR 10-MS AVERAGE QUEUEING DELAY
(Assuming 1-kbit packet size)

AVERAGE INPUT TRAFFIC RANGE (PACKETS/S)	NUMBER OF 64-KBIT/S CHANNELS REQUIRED
0–35	1
36–91	2
92–151	3
152–213	4
214–276	5
277–339	6
340–402	7
403–465	8
466–529	9
530–593	10
594–656	11
657–720	12
721–784	13
785–848	14
849–911	15
912–975	16

The second algorithm is applied to a network of earth stations accessing the satellite channels via TDMA. Let the frame period be 2 ms. Consider a particular earth station transmitting packets of data to destination I. Let C_I be the server capacity assigned to the transmit

queue for destination I. The allocation of capacity C_I is determined by the incoming traffic at this earth station for destination I. If λ_I is the average number of packets arriving per second for destination I, C_I is determined by demanding that the throughput, ρ_I, be 100 percent, where

$$\rho_I = \lambda_I \tau_I; \qquad \tau_I = \frac{b_I}{C_I} \tag{8}$$

and τ_I is the service time for a packet of size b_I bits.

Again, assume that the baseband capacity is available in units of 64 kbit/s. Table 2 gives the capacity requirement for ranges of input traffic around the values given by equation (8).

TABLE 2. BASEBAND CAPACITY REQUIREMENT USING A COMMON MULTIDESTINATIONAL CHANNEL
(Assuming 1024-bit packet size)

AVERAGE INPUT TRAFFIC RANGE (PACKETS/S)	NUMBER OF 64-KBIT/S CHANNELS REQUIRED
31–93	C
94–155	$2C$
156–217	$3C$
218–279	$4C$
280–331	$5C$
332–393	$6C$
394–455	$7C$
456–517	$8C$

The average queueing delay for each transmit queue is computed from equation (7). It depends upon the maximum number of packets allowed to wait in the transmit queue and the average queueing delay, $\bar{D}_M$, in the multidestinational queue. $\bar{D}_M$ can be approximated as

$$\bar{D}_M = \frac{\rho_M \tau_M}{2(1 - \rho_M)} + \frac{F}{2} \tag{9}$$

where τ_M is the service time for a packet on the multidestinational channel and ρ_M is the aggregate sum of the traffic intensity from overflow from single-destinational channels and various thin streams that do not warrant a separate channel (see Figure 3).

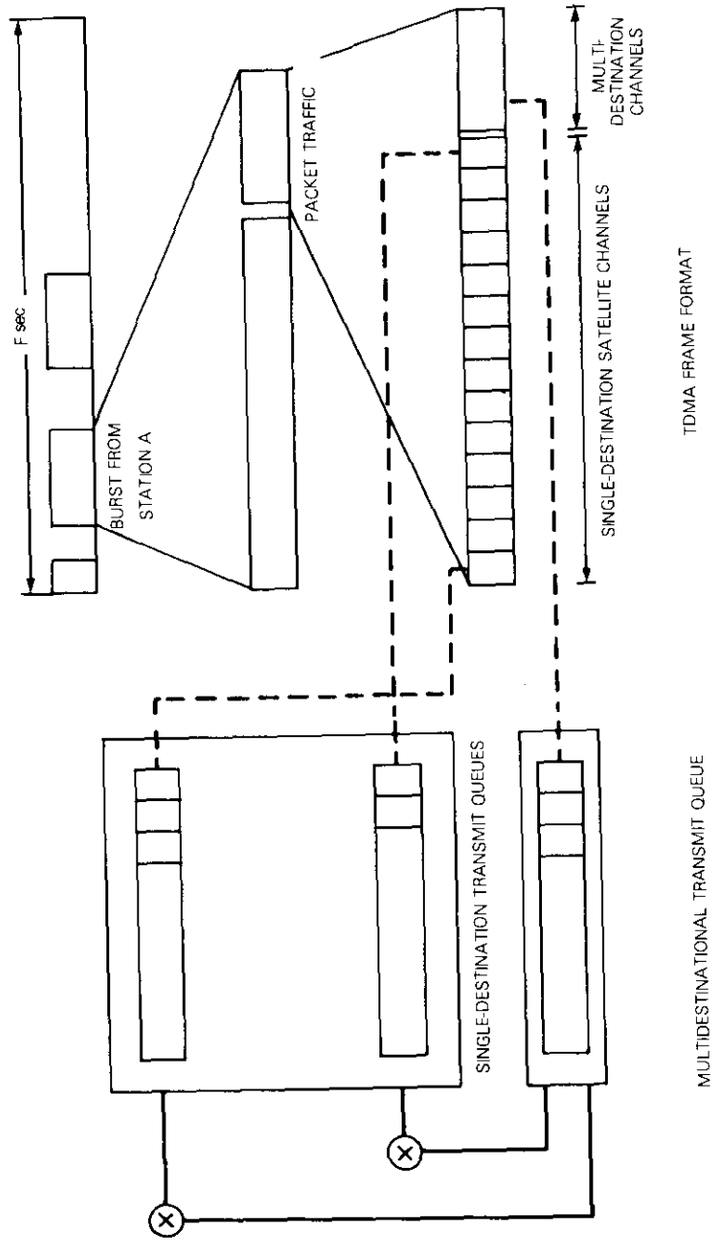

Figure 3. *Routing of Packets from Single-Destinational Transmit Queue to Multidestinational Queue*

The maximum number of packets allowed to wait in each transmit queue and the capacity needed for the multidestinational channel are determined by the requirement of the queueing delay for each destination.

As an example, the Markov analysis has been performed with the queueing delay requirement of 10 to 15 ms for each of the transmit queues served by capacity channels of various multiples of 64 kbit/s. The details of the calculation for one case are presented in Appendix A. Figures 4 and 5 give performance curves (of queueing delay versus channel utilization) for traffic served by baseband channels with capacities of 64 kbit/s and 128 kbit/s. The performance improves for higher capacity channels. Thus, while maintaining the queueing delay as low as 10 to 15 ms on all transmit queues (single and multidestinational), the above scheme yields a very high aggregate throughput ($\geq$95 percent) for a wide range of traffic scenarios. For example, consider the packet traffic originating from a node going to four different destinations. The algorithm computes the baseband capacity requirement depending upon the incoming traffic to each destination and concludes that the capacity requirement is C, $2C$, $4C$, and $8C$ (C = 64 kbit/s) for each of these destinations, when a multidestinational channel of capacity C is available for overflow traffic.

The curve identified as "Mixed" in Figure 6 shows the performance for the packet traffic to the destination served by the channel of capacity C, as computed using the formulas developed in Appendix A. This compares very favorably with the performance for the packet traffic on a channel of capacity C, when only single-destinational channels are available, as shown by the curve identified as "Single-D" in Figure 6. (Note that the Single-D curve in Figure 6 is identical to that in Figure 1.) If, however, there were no constraints on the limitation of the processing capability of the receiving nodes, the packet traffic to all destinations could be statistically multiplexed and the first capacity allocation algorithm would then give an even better performance, as shown by the curve labeled "Multi-D" in Figure 6.

Conclusion

It is thus concluded that by appropriately using a multidestinational channel, low delay and high throughput can be maintained for packet traffic despite processing limitations. This is accomplished by using the local measures computed by the capacity allocation algorithm described in this paper.

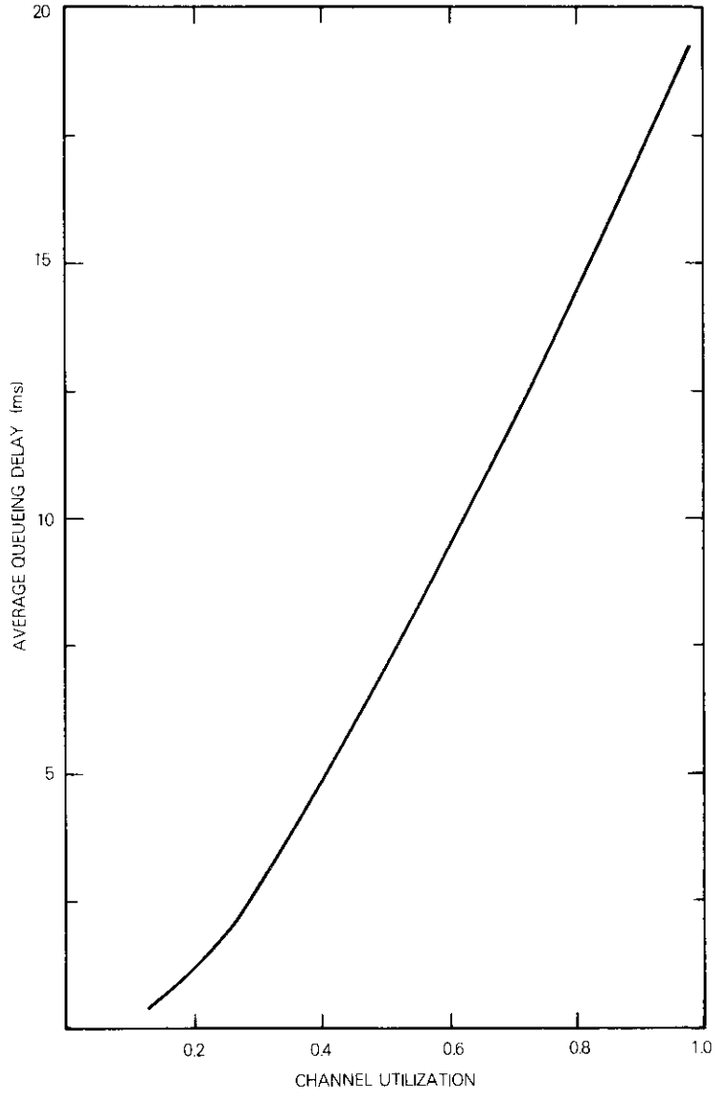

Figure 4. *Average Queueing Delay* vs *Baseband Channel Utilization for the Packet Traffic Served by a Baseband Channel of 64-kbit/s Capacity with the Overflow Packets Served by a Multidestinational Channel*

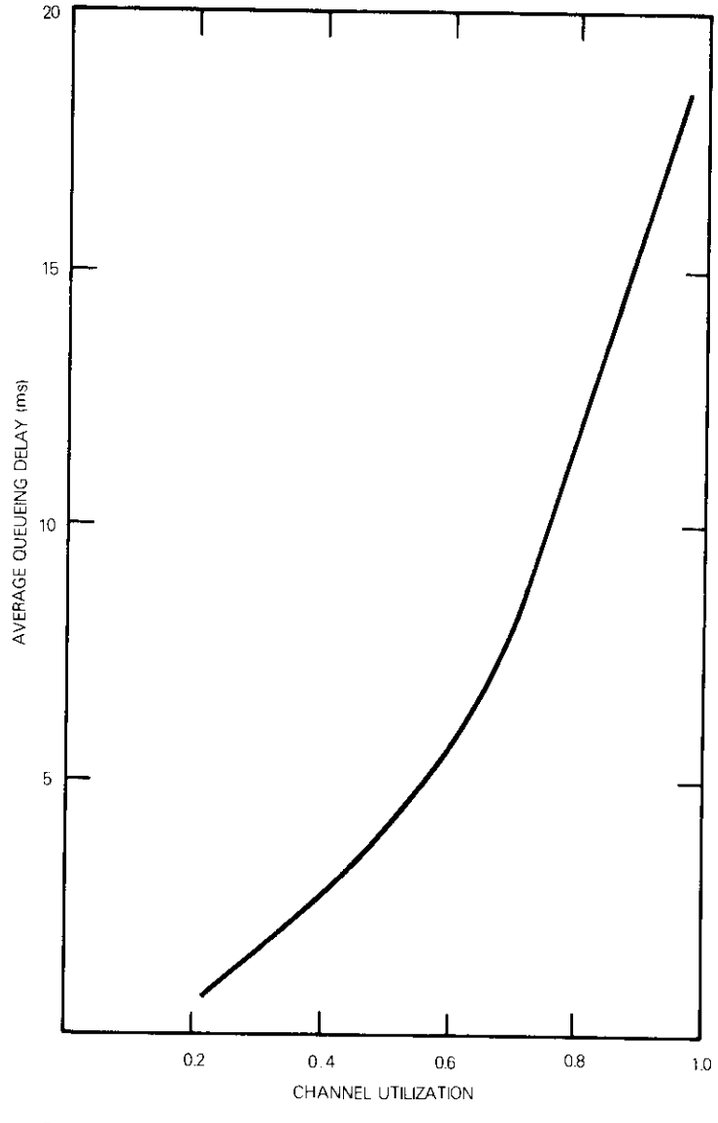

Figure 5. *Average Queueing Delay* vs *Baseband Channel Utilization for the Packet Traffic Served by a Baseband Channel of 128-kbit/s Capacity with the Overflow Packets Served by a Multidestinational Channel*

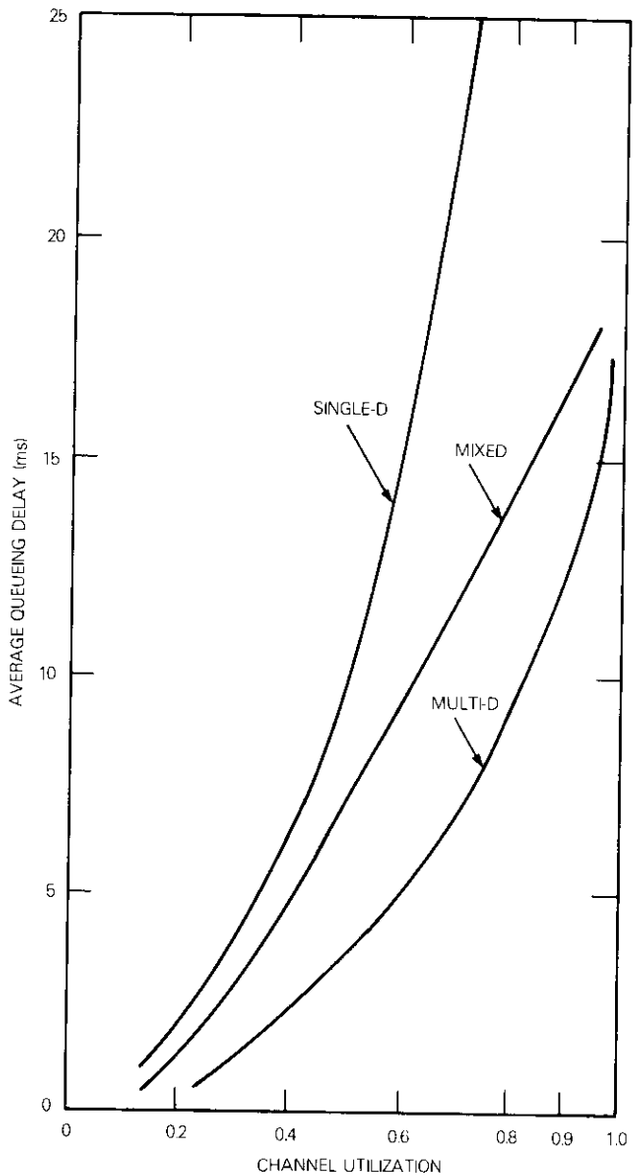

Figure 6. *Performance Comparison of Different Capacity Allocation Algorithms*

Acknowledgment

The author would like to thank Dr. A. K. Kaul for many useful discussions.

References

[1] L. G. Roberts, "Dynamic Allocation of Satellite Capacity Through Packet Reservation," *1973 AFIPS Conference Proceedings*, Vol. 42, pp. 711–716.

[2] R. Binder, "A Dynamic Packet-Switching System for Satellite Broadcast Channels," *1975 Proceedings International Communications Conference*, pp. 41-1–41-5.

[3] F. A. Tobagi, "Multiaccess Protocols in Packet Communication Systems," *IEEE Transactions on Communications*, Vol. COM-28, April 1980, pp. 468–488, (and exhaustive list of references cited therein).

[4] T. L. Saaty, *Elements of Queueing Theory*, New York: McGraw-Hill, 1961.

Appendix A. Derivation of queueing delay

Consider a packet communications network in which each node has access to the satellite every 2 ms. The calculation for queueing delay for different single-destinational transmit queues is illustrated by explicit computation for one case, namely, the single-destinational queue serviced by a baseband channel of capacity C, where C = 64 kbit/s. The computation for other server capacities can be carried out along similar lines.

Single-destinational queue serviced by a 64-kbit/s channel

Let the packets be of bit size 1024 arriving at a station for a particular destination I. Let P_i be the probability of i packets arriving during one 2-ms frame period. With the available server capacity of 64 kbit/s, the packet divides into eight units, such that one unit is transmitted every 2 ms. Further, let the algorithm specify that when a newly arriving packet finds two or more packets waiting in the transmit line for destination I, it is diverted to the multidestinational queue. The maximum number of units that can occupy the transmit queue just after transmission of one unit is given by equation (4) as

$$\ell_I = n_I + (m_I - 2) = 22 \quad . \tag{A-1}$$

By substituting the values for the transition probabilities in equation (3), the following sets of equations for stationary probabilities Π_i can be obtained:

$$\begin{aligned}
\Pi_0 &= \Pi_0 P_0 + \Pi_1 P_0 \\
\Pi_1 &= \Pi_2 P_0 \\
\Pi_2 &= \Pi_3 P_0 \\
\Pi_3 &= \Pi_4 P_0 \\
\Pi_4 &= \Pi_5 P_0 \\
\Pi_5 &= \Pi_6 P_0 \\
\Pi_6 &= \Pi_7 P_0 \\
\Pi_7 &= \Pi_8 P_0 + \Pi_0 P_1 \\
\Pi_8 &= \Pi_9 P_0 + \Pi_1 P_1 \\
\Pi_9 &= \Pi_{10} P_0 + \Pi_2 P_1 \\
\Pi_{10} &= \Pi_{11} P_0 + \Pi_3 P_1 \\
\Pi_{11} &= \Pi_{12} P_0 + \Pi_4 P_1 \\
\Pi_{12} &= \Pi_{13} P_0 + \Pi_5 P_1 \\
\Pi_{13} &= \Pi_{14} P_0 + \Pi_6 P_1 \\
\Pi_{14} &= \Pi_{15} P_0 + \Pi_7 P_1 \\
\Pi_{15} &= \Pi_{16} + \Pi_8(1 - P_0) + \Pi_0(1 - P_0 - P_1) \\
\Pi_{16} &= \Pi_{17} + \Pi_9(1 - P_0) + \Pi_1(1 - P_0 - P_1) \\
\Pi_{17} &= \Pi_{18} + \Pi_{10}(1 - P_0) + \Pi_2(1 - P_0 - P_1) \\
\Pi_{18} &= \Pi_{19} + \Pi_{11}(1 - P_0) + \Pi_3(1 - P_0 - P_1) \\
\Pi_{19} &= \Pi_{20} + \Pi_{12}(1 - P_0) + \Pi_4(1 - P_0 - P_1) \\
\Pi_{20} &= \Pi_{21} + \Pi_{13}(1 - P_0) + \Pi_5(1 - P_0 - P_1) \\
\Pi_{21} &= \Pi_{22} + \Pi_{14}(1 - P_0) + \Pi_6(1 - P_0 - P_1) \\
\Pi_{22} &= \Pi_{15}(1 - P_0) + \Pi_7(1 - P_0 - P_1)
\end{aligned} \tag{A-2}$$

The above sets of equations are solved to obtain Π_i's; e.g.,

$$\Pi_0 = \frac{P_0^{15}}{P_0^{16} + 8(1 - P_0)(1 + P_0^8) - 8P_1P_0^7(8 - 7P_0)} \quad . \tag{A-3}$$

The average number of packets transferred to the multidestinational queue from the above transmit queue during one frame period (F) is given by

$$\lambda_{MI}F = \lambda_I F - \frac{(1 - \Pi_0 P_0)}{8} \tag{A-4}$$

where λ_I is the average number of packets arriving per second. The average queueing delay is then obtained as a function of the incoming traffic and is given by substituting the values for Π_i's in equation (7).

Take the incoming traffic for destination I to be such that

$$\lambda_I \tau_I = 1 \tag{A-5}$$

where τ_I is the service time for a packet. From equation (7), average queueing delay is obtained as

$$\bar{D}^I = (5.4)F + D_M \cdot \frac{\lambda_{MI}}{\lambda_I} \tag{A-6}$$

where λ_{MI} as computed from equation (A-4) is given by

$$\lambda_{MI} = (0.18)\lambda_I \quad . \tag{A-7}$$

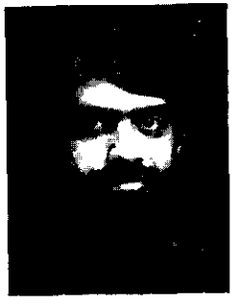

Dattakumar M. Chitre received a B.Sc. in mathematics from the University of Bombay, India, an M.A. in mathematics from Cambridge University, U.K., and a Ph.D. in physics from the University of Maryland. In 1980 he joined COMSAT Laboratories, where he is currently Manager of the Data Communications Systems Analysis Department of the Data Communications Laboratory, Systems Technology Division. His current responsibilities include research activities in data communications analysis and systems study of network architectures for data communications, teleconferencing, and ISDN satellite networks. Dr. Chitre is a member of the International Astronomical Union.

Index: distortion, modulation, multiplexing, television

Third-order distortion of television and sound multiplexed signals in satellite FM systems

A. HAMMER AND D. J. SCHAEFER

(Manuscript received November 18, 1981)

Abstract

An analysis of third-order distortion components arising when video and audio multiplexed signals frequency modulate an RF carrier in a satellite system is presented. Composite baseband signal and distortion spectra are derived, and the signal-to-distortion power ratio is evaluated. Preemphasis and delay equalization effects are shown to significantly enhance the signal-to-distortion ratio. Suggestions regarding preemphasis and filtering are offered, and numerical examples and computer results are given.

Introduction

The transmission of television and sound multiplexed signals in band-limited FM systems has been examined [1]–[4]. The evaluation of television and sound distortion in those systems was performed either experimentally or numerically in some cases. However, an analytical tool may be needed to assist in calculating the distortion as

This paper is based upon work performed at COMSAT Laboratories under the sponsorship of the International Telecommunications Satellite Organization (INTELSAT).

a function of frequency overdeviation, filter characteristics, and other parameters.

This paper discusses both the analysis and some synthesis aspects of band-limited FM systems in terms of distortion of the modulating television and sound multiplexed signals. This problem arises in satellite communications, where it may be desirable to transmit within half a transponder bandwidth a color TV signal and two high-quality sound channels (or several sound channels of overall equivalent bandwidth). The TV and sound signals are first frequency-division multiplexed, and these signals then frequency modulate a common RF carrier. The frequency deviation of this carrier should be as large as possible to maximize the signal-to-thermal-noise ratio for a given satellite transponder power. However, the distortion arising because of the band-limited frequency range poses an upper bound to the carrier frequency deviation.

Figure 1 is a block diagram of the system investigated. The transponder is assumed to operate in the linear region, and hence is represented by a filter (incorporating the earth station filters, if any). The total carrier frequency deviation is determined both by the TV signal amplitude, r_1, and by the audio subcarrier amplitude, r_2. In the figure, $x(t)$, $y(t)$, and $z(t)$ represent the TV chrominance waveform, the TV luminance waveform, and the FM audio waveform, respectively.

The following assumptions have been made:

a. The TV input is assumed to be a test signal, such as an NTSC color bar.

b. The audio subcarrier is modulated by a single tone whose frequency is identical to the overall audio bandwidth.

c. The composite baseband modulating signal is considered to be deterministic.

d. The FM modulators and demodulators have ideal characteristics.

e. The equivalent transmission link filter is considered to be linear and symmetrically conjugate.

f. The demodulated output is obtained as a Maclaurin series expansion [5], and only the third-order distortion component is computed.

g. The composite FM carrier modulation index is assumed to be relatively small, so that the Maclaurin series converges.

h. The input TV signal is expanded into a Fourier series, disregarding the TV half-field frequency spectral lines.

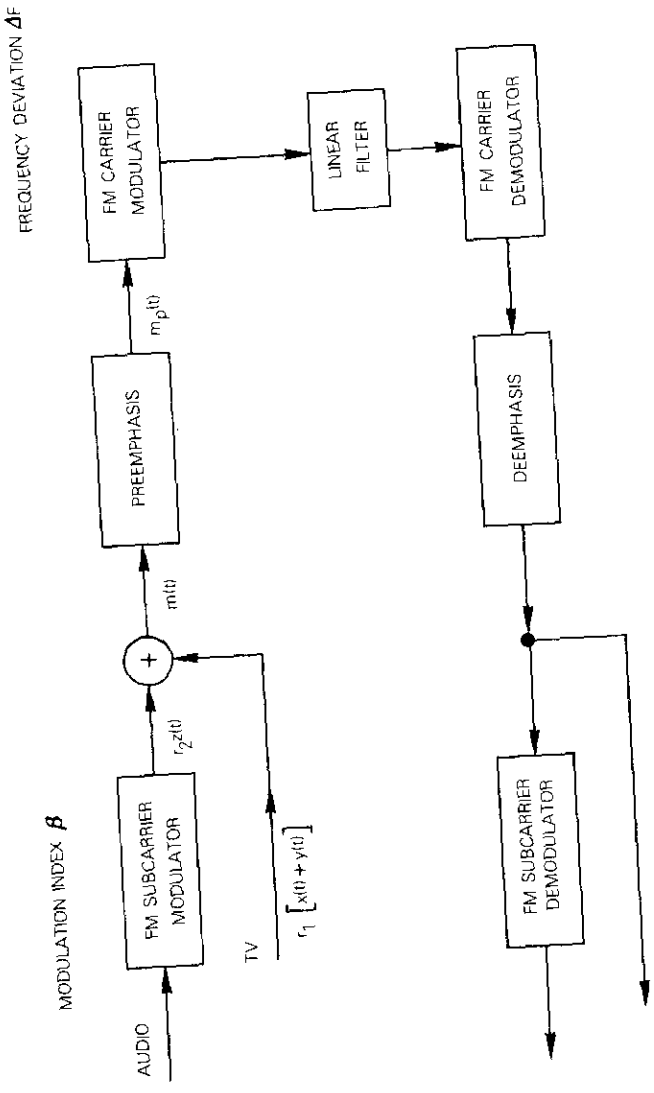

Figure 1. *Band-Limited FM System Modulated by TV and Audio Multiplexed Signals*

i. The distortion term is considered to be independent of the thermal noise. Thermal noise effects are not included in the analysis.

An appropriate composite baseband signal representation is given, and the third-order distortion spectrum and power are derived. Higher order distortion components are disregarded. The ratio of signal to third-order distortion power is chosen as a basis for performance criteria. Certain synthesis aspects of preemphasis networks and filter equalization are discussed. Finally, several numerical results, based on a relevant computer program, are presented.

Composite baseband signal representation

The composite baseband signal is assumed to be composed of three parts: TV luminance, TV chrominance, and a frequency-modulated audio subcarrier. To enable the calculation of distortion power, the TV luminance and chrominance components are expanded into a Fourier series, while the frequency-modulated audio subcarrier is represented by the appropriate Bessel function coefficients. The TV test signal, to be discussed, is assumed to be a color bar [6]. Other forms of repetitive, piecewise constant level test signals may be treated in a similar manner.

The luminance waveform $y(t)$ can be approximated by

$$y(t) \approx \sum_{k=-N}^{N} d_k \exp(jk\omega_L t) \tag{1}$$

where d_k, for $k = -N, -N+1, \ldots, N$, is the kth Fourier series coefficient, and ω_L is the TV line scanning frequency. The value of N is determined by the luminance bandwidth.

The Fourier series coefficients are

$$d_k = \frac{1}{T_L}\int_{-T_L/2}^{T_L/2} y(t)\exp(-jk\omega_L t)\,dt,$$
$$k = -N, -N+1, \ldots, N \quad . \tag{2}$$

Replacement of $y(t)$ in equation (2) by the piecewise constant level luminance waveform yields

$$d_k = \frac{1}{2\pi k}\sum_{\ell=1}^{P} C_\ell \{[\sin(k\omega_L\delta_\ell) - \sin(k\omega_L\gamma_\ell)]$$

$$+ j[\cos(k\omega_L\delta_\ell) - \cos(k\omega_L\gamma_\ell)]\},$$
$$k = -N, -N+1, \ldots, N \tag{3}$$

where C_ℓ, γ_ℓ, and δ_ℓ, for $\ell = 1, 2, \ldots, P$, are the luminance levels and their initial and final timing instants, respectively, as shown in Figure 2.

The chrominance waveform $x(t)$ is composed of Q piecewise constant amplitude phasors:

$$x(t) = \sum_{i=1}^{Q} S_i(t)\cos(\omega_{SI}t + \phi_i),$$
$$S_i(t) = \begin{cases} c_i\colon \gamma_i < t \le \delta_i \\ 0\colon \text{otherwise} \end{cases} \tag{4}$$

where ϕ_i, c_i, γ_i, and δ_i, for $i = 1, 2, \ldots, Q$, are the chrominance subcarrier phases, levels, and timing instants, respectively, as shown in Figure 2, and ω_{SI} is the chrominance subcarrier angular frequency. Thus, $S_i(t)$ is the envelope of the ith color phasor.

Equation (4) can be rewritten as

$$x(t) = \tfrac{1}{2}\sum_{k=-M}^{M} b_{k+}\exp[j(k\omega_L + \omega_{SI})t]$$
$$+ \tfrac{1}{2}\sum_{k=-M}^{M} b_{k-}\exp[j(k\omega_L - \omega_{SI})t] \tag{5}$$

where the value of M depends on the chrominance signal bandwidth, and the Fourier series coefficients b_{k+} and b_{k-} are derived from transformed chrominance waveforms by

$$b_{k+} = \frac{1}{T_L}\int_{-T_L/2}^{T_L/2}\left[\sum_{i=1}^{Q} S_i(t)\exp(j\phi_i)\right]\exp(-jk\omega_L t)\,dt$$

$$b_{k-} = \frac{1}{T_L}\int_{-T_L/2}^{T_L/2}\left[\sum_{i=1}^{Q} S_i(t)\exp(-j\phi_i)\right]\exp(-jk\omega_L t)\,dt$$
$$k = -M, -M+1, \ldots, M \quad . \tag{6}$$

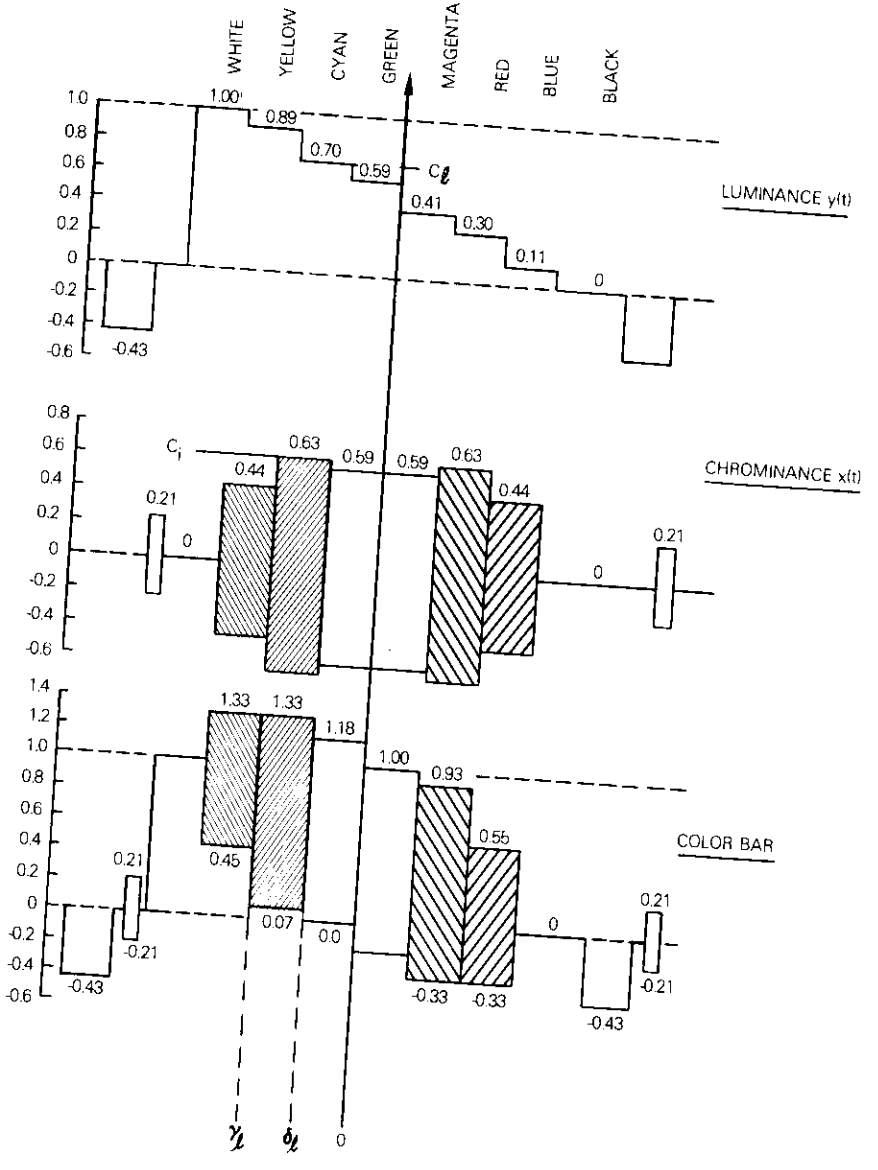

Figure 2. *NTSC Color Bar Signal Waveforms*

Inserting the expressions for $S_i(t)$, $i = 1, 2, \ldots, Q$, given in equation (4), into equation (6) yields

$$b_{k+} = \frac{1}{2\pi k} \sum_{i=1}^{Q} c_i \{[\sin(k\omega_L \delta_i - \phi_i) - \sin(k\omega_L \gamma_i - \phi_i)] + j[\cos(k\omega_L \delta_i - \phi_i) - \cos(k\omega_L \gamma_i - \phi_i)]\},$$
$$k = -M, -M+1, \ldots, M \quad . \tag{7}$$

Since the waveform $x(t)$, given in equation (5), is real, b_{k-} is the complex conjugate of b_{k+}.

The total composite baseband signal $m(t)$ is

$$m(t) = r_1 \left[\sum_{k=-N}^{N} d_k \exp(jk\omega_L t) + \tfrac{1}{2} \left\{ \sum_{k=-M}^{M} b_{k+} \exp[j(\omega_{S1} + k\omega_L)t] + \sum_{k=-M}^{M} b_{k+} \exp[j(-\omega_{S1} + k\omega_L)t] \right\} \right] + \frac{r_1}{2} \sum_{k=-(\beta+1)}^{\beta+1} J_k(\beta) \{\exp[j(\omega_{S2} + k\omega_m)t] + \exp[j(-\omega_{S2} + k\omega_m)t]\} \tag{8}$$

where $J_k(\beta)$, for $k = -(\beta + 1), -\beta, \ldots, \beta + 1$, is the Bessel function of the first kind and order k: β and ω_{S2} are the frequency modulation index and angular frequency, respectively, of the audio subcarrier; and ω_m is the ratio angular bandwidth.

The composite baseband signal $m(t)$, given in equation (10), may be rewritten more briefly as

$$m(t) = \sum_k a_k \exp(j\omega_k t) \tag{9}$$

where a_k, ω_k, and k are given in Table 1.

The preemphasis network transfer function $H_p(f)$ is approximated by

$$H_p(f) = \frac{1 + j(f/f_p)}{1 + j(f/f_u)} \tag{10}$$

where f_p and f_u are the lower and upper break point frequencies, respectively.

TABLE 1. PARAMETERS a_k, ω_k AND k IN COMPOSITE BASEBAND SIGNAL EXPRESSION

PARAMETER	LUMINANCE	CHROMINANCE	FM AUDIO SUBCARRIER
a_k	$r_1 d_k$	$\frac{1}{2} r_1 b_{k+}$, $\frac{1}{2} r_1 b_{k-}$	$\frac{1}{2} r_2 J_k(\beta)$
ω_k	$k\omega_L$	$\pm\omega_{S1} + k\omega_L$	$\pm\omega_{S2} + k\omega_m$
Range of k			
Upper Limit	N	M	$\beta + 1$
Lower Limit	$-N$	$-M$	$-(\beta + 1)$

The overdeviation V may be defined as

$$V \triangleq 20 \log \frac{\Delta F}{\Delta F_c} \tag{11}$$

where the carrier frequency deviation ΔF is determined by baseband signal and preemphasis parameters, and ΔF_c is the frequency deviation according to Carson's rule.

Third-order distortion components

The analysis of the filtering effect on the FM carrier signal is based on a convolution process and the subsequent Maclaurin series expansion of the demodulated signal. Since the linear filter is assumed to have a symmetrically conjugate transfer function, the resulting Maclaurin series contains only odd-order terms [5]. In this case, the first term of the Maclaurin series expansion represents the linearly filtered modulating signal, while the second term is the third-order distortion component.

The third-order distortion component $D_{i3}(t)$ of a linearly filtered angle modulated signal is [5]

$$D_{i3}(t) = -\frac{1}{3!}\frac{\partial}{\partial t}\left\{\int_0^\infty \gamma(\tau)[\phi(t-\tau) - \psi(t)]^3\, d\tau\right\} \tag{12}$$

where $\phi(t)$ is a phase-modulating signal, $\gamma(t)$ is the normalized (low-pass equivalent) filter impulse response, and

$$\psi(t) \triangleq \int_0^\infty \gamma(\tau)\,\phi(t-\tau)\, d\tau \quad . \tag{13}$$

The derivative of the phase-modulating signal $\partial\phi(t)/\partial t$ is assumed to be the preemphasized composite baseband signal $m_p(t)$, derived from equations (9) and (10) and Table 1 as

$$\frac{\partial\phi(t)}{\partial t} = m_p(t) = \sum_k a_k \frac{1 + j(f_k/f_p)}{1 + j(f_k/f_u)} \exp(j\omega_k t) \quad . \tag{14}$$

The summation in equation (14) is performed for all possible values of k, which are given in Table 1.

The term $D_{i3}(t)$, given in equation (14), is the third-order distortion component at the input to the deemphasis network, shown in Figure 1. Performing the partial differential in equation (12) and using the left-hand equality in equation (14) yield

$$\begin{aligned} -2D_{i3}(t) = &\int_0^\infty \gamma(\tau)\,\phi^2(t-\tau)\, m_p(t-\tau)\, d\tau \\ &- \frac{\partial\psi(t)}{\partial t}\int_0^\infty \gamma(\tau)\,\phi^2(t-\tau)\, d\tau \\ &- 2\psi(t)\int_0^\infty \gamma(\tau)\,\phi(t-\tau)\, m_p(t-\tau)\, d\tau \\ &+ 2\psi^2(t)\frac{\partial\psi(t)}{\partial t} \end{aligned} \tag{15}$$

where $\psi(t)$, determined from equations (13) and (14) by operating in the frequency domain, is

$$\psi(t) = \sum_k \frac{a_k}{j\omega_k}\frac{[1 + j(f_k/f_p)]}{[1 + j(f_k/f_u)]}\Gamma_{f_k}\exp(j\omega_k t) \quad . \tag{16}$$

The term $\partial\psi(t)/\partial t$ is the filtered preemphasized baseband signal (not containing any FM distortion), and Γ_{f_k} is the complex (low-pass equivalent) filter transfer function at frequency f_k, namely

$$\Gamma_{f_k} = |\Gamma_{f_k}| \exp\left[-2\pi j\left(\tau_0 f_k + \int_0^{fk} \tau_g(f)\, df\right)\right] \quad .$$

The variables τ_0 and $\tau_g(f)$ are the filter constant delay and group delay, respectively.

Substitution of equations (14) and (16) into equation (15) and repeated operations in the time and frequency domains yield the third-order distortion spectrum $G_{D_3}(f)$ at the output of the deemphasis network:

$$G_{D_3}(f) = \frac{1}{8\pi^2} \sum_k \sum_n \sum_i \frac{a_k a_n a_i}{f_n f_i} P \Gamma_\ell\, \delta(f - f_\Sigma) \tag{17}$$

where

$$P \triangleq \frac{\left(1 + j\frac{f_k}{f_p}\right)\left(1 + j\frac{f_n}{f_p}\right)\left(1 + j\frac{f_i}{f_p}\right)\left(1 + j\frac{f_\Sigma}{f_u}\right)}{\left(1 + j\frac{f_k}{f_u}\right)\left(1 + j\frac{f_n}{f_u}\right)\left(1 + j\frac{f_i}{f_u}\right)\left(1 + j\frac{f_\Sigma}{f_p}\right)} \tag{18}$$

$$\Gamma_\ell \triangleq \Gamma_{f_\Sigma} - \Gamma_{f_n+f_i}\Gamma_{f_k} + 2\Gamma_{f_k}\Gamma_{f_n}\Gamma_{f_i} - 2\Gamma_{f_k+f_n}\Gamma_{f_i} \tag{19}$$

and where $f_\Sigma = f_k + f_n + f_i$, with the range of n and i identical to that of k, given in Table 1. The triple sum in equation (17) is performed for all luminance, chrominance, and FM audio subcarrier components of the baseband signal. The parameters a_k, a_n, and a_i, are the Fourier series coefficients of the composite baseband signal, and P represents preemphasis and deemphasis effects. The term Γ_ℓ, defined by equation (19), depends solely on the filter characteristics, and its value would be zero if the filter were ideal. Thus, the discrete components of the third-order distortion spectrum are generated as additive combinations of baseband frequency terms.

In this analysis, the third-order distortion power at the output of the deemphasis network is chosen as the basis for a performance criterion. The distortion power $P_{D_3}(\Delta f_g)$ within a specified positive frequency range may be derived from equations (17) through (19) to obtain

$$P_{D_3}(\Delta f_g) = 3.2 \times 10^{-4} \sum_{f_\Sigma} \left| \underbrace{\sum_k \sum_n \sum_i}_{f_\Sigma = \text{const}} \frac{a_k a_n a_i}{f_n f_i} P \Gamma_\ell \right|^2 \tag{20}$$

with $f_\Sigma \in \Delta f_g$.

Thus, only combinations of k, n, and i resulting in f_Σ being in the frequency range contribute to the value of $P_{D_3}(\Delta f_g)$ in equation (20). The spectral components are added vectorially at a given frequency while scalar addition is performed over different frequencies.

The useful signal $s(t)$ at the receiver output is given by the first term in the Maclaurin series

$$s(t) = \int_0^\infty \gamma(\tau)\, m(t - \tau)\, d\tau = \sum_k a_k \Gamma f_k \exp(j\omega_k t) \quad . \tag{21}$$

If group delay equalization is introduced, $s(t)$ is undistorted.

The signal power $P_S(\Delta f_g)$ within the positive frequency range Δf_g obtained from equation (21) is

$$P_S(\Delta f_g) = 2 \sum_k |a_k|^2 |\Gamma_{f_k}|^2 \tag{22}$$

with $f_k \in \Delta f_g$.

The signal-to-distortion ratio within any frequency interval can thus be evaluated by means of equations (20) and (22).

Preemphasis and equalization effects

In equation (20) the third-order distortion power is composed of products of the form $A\, P\, \Gamma_\ell$, where P and Γ_ℓ are given in equations (18) and (19), respectively, and A is defined as

$$A \triangleq \frac{a_k a_n a_i}{f_n f_i} \quad . \tag{23}$$

The complex value of the product $A\, P\, \Gamma_\ell$ depends on the combination (k, n, i) as follows: Whenever some of the indices k, n, and i indicate luminance terms, the value of A is relatively large because of the smaller values of the frequencies in the denominator of equation (23). (Luminance component frequencies are usually much smaller than chrominance or FM audio subcarrier spectral frequencies). However, at those combinations of (k, n, i) and the related frequencies, the value of Γ_ℓ is relatively small. (The departure of filter characteristics from ideal ones is relatively small at those frequencies.) Whenever f_Σ is derived only from chrominance or audio terms, the value of A is

relatively small [involving larger values of f_n or f_i in equation (23)]. However, at those larger frequency combinations, the value of Γ_ℓ may be relatively large because of larger deviations from ideal filter characteristics.

The amount of distortion power arising from contributions by the luminance components can be decreased by increasing the preemphasis upper break point frequency f_u, with decreased luminance amplitude levels resulting. This increase in preemphasis amplitude range may also be desirable for purposes of chrominance signal to thermal noise improvement and convergence of the Maclaurin series [5] by achieving a smaller composite frequency modulation index.

Equations (17) and (19) show that improved group delay equalization within the equivalent baseband frequency range may considerably decrease the value of Γ_ℓ arising from luminance term contributions. Hence, whenever the luminance components contribute to the dominant distortion terms, it may be desirable to increase the preemphasis amplitude range or improve the filter delay equalization, as explained.

Numerical examples

The equations presented in the preceding sections have been implemented by means of a digital computer program. The TV test signal was chosen as an NTSC 75-percent color bar [6]. The TV line scanning frequency, f_L, and the chrominance subcarrier frequency, f_{S1}, assumed the values of 15.75 kHz and 3.58 MHz, respectively. The audio bandwidth, f_m, was 35 kHz, and the audio subcarrier frequency, f_{S2}, and modulation index β were assumed to be 6.6 MHz and 5, respectively. The preemphasis lower break point frequency, f_p, was 120 kHz.

Since the filter has been assumed to be symmetrically conjugate, group delay values for either positive or negative frequencies (or average values) were used in the computer runs.

Tables 2 through 4 show values of the signal-to-third-order distortion ratio $P_S(\Delta f_g)/P_{D3}(\Delta f_g)$ calculated by the computer program for various combinations of the following parameters:

a. overdeviation V,
b. ratio r_1/r_2 of TV and FM subcarrier signal amplitudes,
c. upper break point frequency f_u,
d. type of filter, and
e. type of group delays.

TABLE 2. SIGNAL-TO-DISTORTION RATIO WITHIN FM AUDIO SUBCARRIER RANGE: PREEMPHASIS AND EQUALIZATION EFFECTS (V = 6 dB, and r_1/r_2 = 20 dB)

f_u (MHz)	P_S/P_{D_3} (dB): 20-MHz Filter, Average-Frequency Delays	17.5-MHz Filter, Negative-Frequency Delays	17.5-MHz Filter, Positive-Frequency Delays
0.57	5.9	−10.9	15.8
2.5	21.3	8.3	18.7

TABLE 3. SIGNAL-TO-DISTORTION RATIO WITHIN FM AUDIO SUBCARRIER RANGE: OVERDEVIATION AND BASEBAND LEVEL EFFECTS (17.5-MHz filter, positive-frequency delays)

V (dB)	r_1/r_2 (dB)	f_u (MHz)	P_S/P_{D_3} (dB)
6	10	0.57	21.2
12.8	20	0.57	2.2
12.8	20	2.5	5.1

TABLE 4. SIGNAL-TO-DISTORTION RATIO WITHIN TV FREQUENCY RANGE (V = 6 dB)

Filter and Group Delay	r_1/r_2 (dB)	f_u (MHz)	P_S/P_{D_3} (dB)
20-MHz, Average Frequencies	20	0.57	34.5
20-MHz, Average Frequencies	20	2.5	53.1
17.5-MHz, Positive Frequencies	20	0.57	58.9
17.5-MHz, Positive Frequencies	10	0.57	45.1

The comparative values of signal-to-distortion ratio for the 17.5-MHz filter are 3–5 dB larger than those given in Tables 2 through 4 because

of a difference in frequency deviation scaling between the FM systems employing the two filters.

The numerical results indicate that a considerable increase in the signal-to-distortion ratio may be achieved either by reducing the group delay within the equivalent baseband frequency range, or by an increase in preemphasis amplitude range, or by a combination of both.

Conclusions

A third-order distortion analysis and certain synthesis aspects of satellite band-limited FM systems carrying television and sound multiplexed signals have been presented. Composite baseband signal and distortion frequency spectra were derived, and signal-to-distortion ratio expressions were obtained. Computer results indicated that, in some cases, a considerable improvement in signal-to-distortion ratio can be achieved by increasing the preemphasis amplitude range or improving filter group delay equalization (or by both methods).

This study has assumed that the third-order component in the Maclaurin series is the major distortion term and thus can adequately approximate the overall distortion. However, the theory presented here may also serve as a basis for evaluating a fifth-order distortion component.

References

[1] H. Mertens and G. Brun, "Distortion of Frequency-Modulated Television Signals Transmitted by Satellite," *E.B.U. Review*, No. 132, April 1972, pp. 52–61.

[2] M. Aigner, "Two Channel Sound Transmission in Television," *Rundfunktechnische Mitteilungen*, Vol. 22, No. 4, 1978, pp. 185–194.

[3] V. Rajic, "Transmission of Two-Sound Components in Frequency-Modulated Television," *E.B.U. Review*, No. 166, December 1977, pp. 300–305.

[4] K. G. Johannsen, F. L. Paulsen, and J. E. Morton, "Television Sound Subcarrier Transmission in Space Communication," *IEEE Transactions on Broadcasting*, BC-20, No. 3, September 1974, pp. 42–48.

[5] E. Bedrosian and S. O. Rice, "Distortion and Crosstalk of Linearly Filtered Angle-Modulated Signals," *Proc. IEEE*, Vol. 56, No. 1, January 1968, pp. 2–13.

[6] B. Townsend, *Pal Colour Television*, Cambridge: Cambridge University Press, 1970.

Amnon Hammer received a B.Sc. in electrical engineering from the Technion Israel Institute of Technology, Haifa, in 1958, and a Ph.D. in engineering from the University of Liverpool, England, in 1969.

From 1958 to 1961, he was with the Israeli army. From 1961 to 1964 he was with Disa Elektronik, Copenhagen, Denmark. Dr. Hammer joined the Ministry of Defence, Israel, in 1964. His current research interests are in communication, radar, control, and learning systems.

From 1979 to 1981, while on sabbatical leave, he was an INTELSAT assignee at COMSAT Laboratories.

Daniel J. Schaefer received a B.S.E.E. from Iowa State University in 1966, and M.S.E.E. and Ph.D. from Purdue University in 1969 and 1975, respectively. Until 1982, he was Manager of the Digital Applications Department at COMSAT Laboratories, where he was responsible for a variety of programs related to satellite communications and signal processing. Before joining COMSAT in 1975, he was with ITT, engaged in the development of UHF/VHF communications equipment. Currently, he is Director of Satellite Systems with M/A-COM LINKABIT Eastern Operations. Dr. Schaefer is a senior member of IEEE.

*Maritime communications satellite in-orbit measurements**

M. BARRETT AND K. FULLETT

(Manuscript received October 1, 1982)

Abstract

This paper describes the measurement equipment used to make in-orbit tests of the Maritime Communications Subsystem (MCS). The MCS is a communications package added to INTELSAT V satellites (F-5 through F-9) to provide maritime communications to INMARSAT. The measurement techniques and objectives are described.

The optimum operation of the equipment and performance of the in-orbit tests requires the use of a sophisticated computer control and monitoring system and of software developed for this purpose. A description of this computer system is however beyond the intended scope of this paper.

Introduction

In 1982, the first of a new series of maritime communications packages designated as the Maritime Communications Subsystem (MCS) was launched as part of the INTELSAT V satellite program. In-orbit testing of this additional satellite capability has been performed with

* This paper is based upon work performed at COMSAT Laboratories under the sponsorship of the International Telecommunications Satellite Organization (INTELSAT).

equipment developed and built by COMSAT Laboratories and installed at earth stations at Fucino, Italy, and Yamaguchi, Japan.

Test complexity and time constraints make it virtually essential that the in-orbit tests be carried out using computer controlled equipment. Accordingly, in parallel with the development of the RF and analog equipment described in this paper, a major program of software design and development was undertaken.

Maritime communications subsystem description

The MCS performs the same functions as the earlier MARISAT system [1], but is designed to handle the growing demand for maritime communications. Enhancements over the MARISAT system include increased bandwidth and improvements in G/T and e.i.r.p. for the satellite and shore stations.

Communications between the six existing INMARSAT shore stations and the ship terminals, which currently exceed 1,000, are carried in the 6-, 4-, 1.6-, and 1.5-GHz bands. The specific frequency capabilities required of the MCS system and thus, of the in-orbit test equipment, are

Shore-to-satellite up-link: 6,417.5–6,425.0 MHz
Satellite-to-ship down-link: 1,535.0–1,542.5 MHz
Ship-to-satellite up-link: 1,636.5–1,644.5 MHz
Satellite-to-shore down-link: 4,192.5–4,200.5 MHz

Other system parameters are:

Ship L-band G/T: −4 dB/K
Ship L-band e.i.r.p.: 36 dBW
Shore C-band G/T: 32 dB/K
Shore C-band e.i.r.p.: 70 dBW

The satellite parameters specified to the spacecraft contractor are

L-band G/T: −15 dB/K
L-band e.i.r.p.: 32.6 dBW (high-power mode)

C-band G/T: −17.6 dB/K
C-band e.i.r.p.: 20 dBW (saturated)

Test requirements—measured parameters

In-orbit tests are made as soon as practical after launch to determine how well the spacecraft has survived the stresses of launch and to compare spacecraft performance with prelaunch data. The nature and number of tests performed are limited by the technological limitations of in-orbit testing and the desire to place the satellite in commercial operation. However, high resolution and accuracy are required to detect any changes that may impact communications performance.

Measurement procedures developed over a number of years guarantee that all the needed parameters can be determined to the desired accuracy [2]–[5]. With the increasing complexity of satellites, the number of tests to be made would be overwhelming without the use of computer-automated measurements that permit greater in-orbit measurement speed.

The initial set of measurements to be made on the MCS consisted of the following:

C- to L-Band Transponder

- e.i.r.p. with a 10-carrier up-link
- G/T
- LO frequency
- NPR

L- to C-Band Transponder

- e.i.r.p.
- G/T
- LO frequency

For both L- to C- and C- to L-band transponders, the spacecraft is required to transmit a minimum e.i.r.p. at the edge of its coverage pattern for a given up-link flux density. For the C- to L-band transponder, the e.i.r.p. is the sum of 10 equal power carriers.

The G/T measurement determines the difference between the spacecraft receive antenna gain (in dB) and the effective spacecraft noise temperature, measured in dB relative to 1 K, for both L- to C- and C- to L-band transponders.

The LO frequency measurement determines the frequency of the spacecraft local oscillators. The NPR measurement, which is made only

on the C- to L-band transponder, is a measure of the linearity of the solid-state L-band transmitter.

Test set description

The maritime transponders can be tested in orbit from earth stations at Fucino, Italy, or Yamaguchi, Japan. Nominally identical sets of test equipment have been installed at both stations.

Figure 1 shows the equipment racks installed at Fucino. This equipment, when operated in conjunction with its associated C- and L-band antennas, low-noise receivers, and high-power transmitters (Figure 2), generates and transmits the required up-link signals, and receives and processes the resultant down-link signals.

The nominal levels and frequencies of these signals (for the e.i.r.p. compliance tests performed at the Fucino station) are shown in Figures 3 and 4 for the C- to L- and L- to C-band transponders, respectively.

Figure 5 is a block diagram showing the essential functions of the RF measurement equipment. These functions are provided for both C- and L- and L- to C-band transponder tests.

As shown in Figure 2, separate high-power transmitter amplifiers and low-noise receivers are provided for the C- and L-band frequencies. The two antennas, for C- and L-band, are both diplexed to provide transmit and receive functions. The rest of the test equipment, that is, the signal sources, processors, and measuring instruments, is used for both C to L or L to C tests, since only one transponder is tested at a time.

C- to L-band transponder test set

In Figure 5, source *A* represents three different signal sources that generate signals in a band at 6,421 ± 3.75 MHz. These signals may be a single carrier, up to 10 carriers, or a band of noise that can have a 3-kHz-wide notch inserted. These three signals may be digitally tuned across the 7.5-MHz-wide maritime communications band. Provision exists to measure and monitor the up-link power and spectrum, and to count the frequency.

The corresponding down-link signal (at 1.5 GHz), after low-noise amplification, is mixed with the up-link signal in mixer *M*. For a single-carrier up-link, the mixer output frequency is the spacecraft local oscillator (at about 4,882.5 MHz) and is counted.

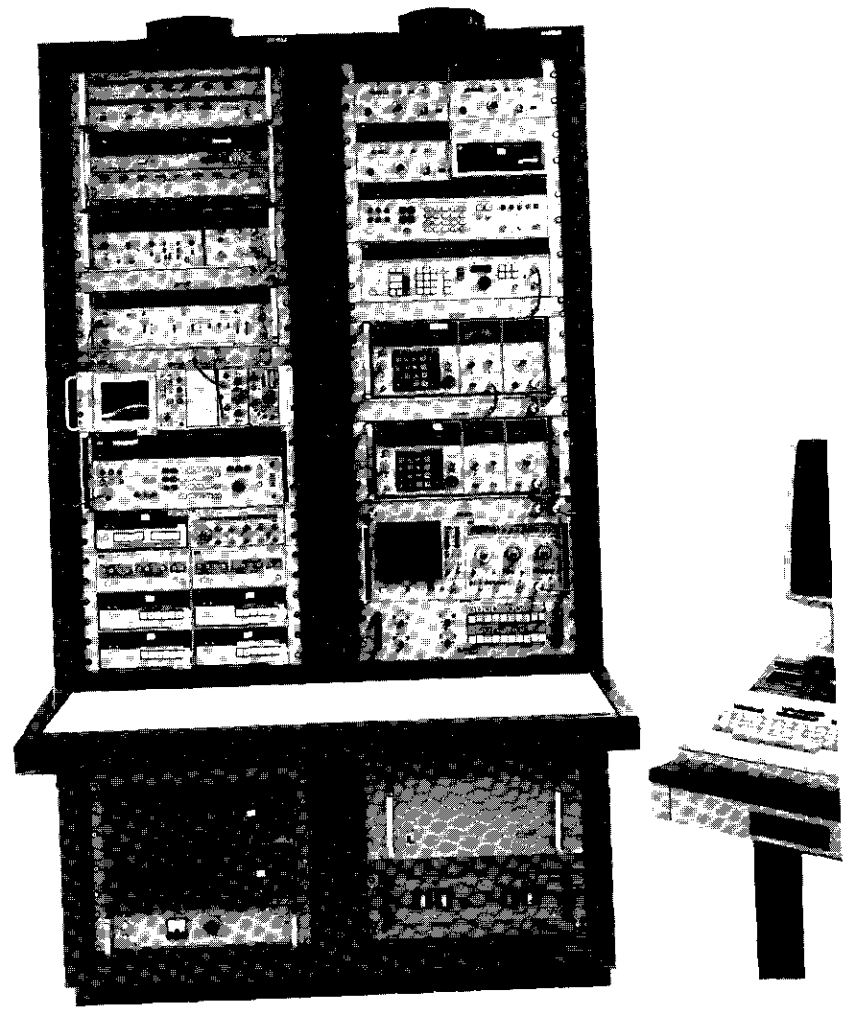

Figure 1. *MCS IOT Racks*

A signal from source *B* may be injected into the input of the low-noise amplifier. This signal is tuned to 27 kHz below the down-link signal. These two signals share an identical path through a frequency down-converter DC to the input of the 10.7-MHz processor, which is used to measure down-link power, and is discussed later. The down-link signal can also be measured and monitored on the selective level meter, spectrum analyzer, and counter.

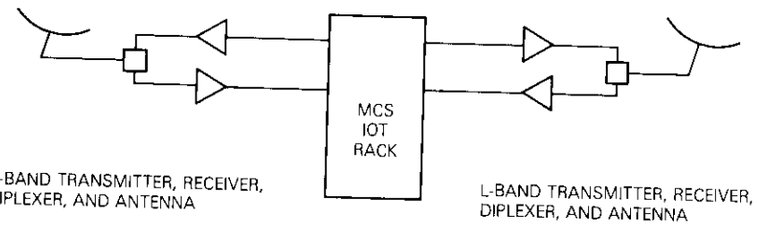

Figure 2. *MCS IOT Earth Station Equipment*

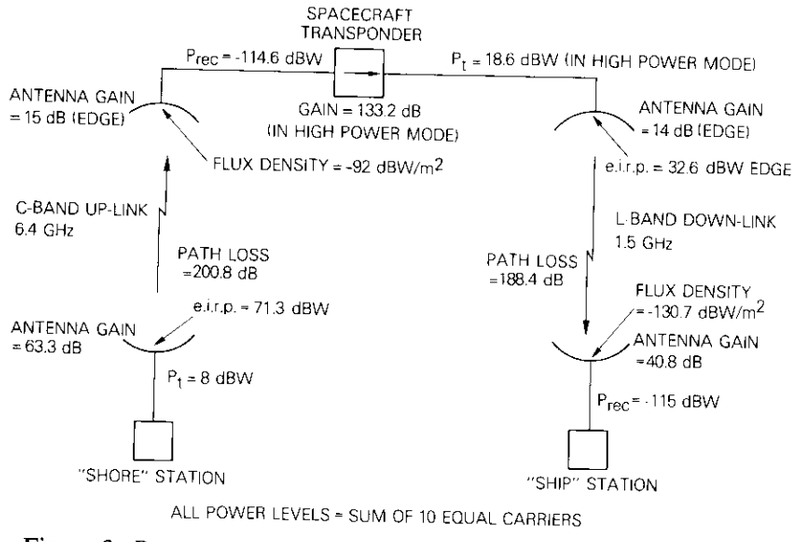

Figure 3. *Power Levels for C- to L-Band Transponder e.i.r.p. Test (10 Carriers)*

L- to C-band transponder test set

For the L- to C-band test set, source *A* in Figure 5 provides a single up-link carrier at 1,640.5 MHz. This signal may be digitally tuned across the 7.5-MHz-wide MCS bandwidth. Provision exists to measure and monitor the up-link power spectrum and frequency.

The corresponding down-link signal (at about 4.2 GHz) is mixed with the up-link signal in mixer *M*. The mixer output frequency, which is independent of the up-link frequency, is the spacecraft local oscillator frequency (at about 2,556 MHz) and is counted.

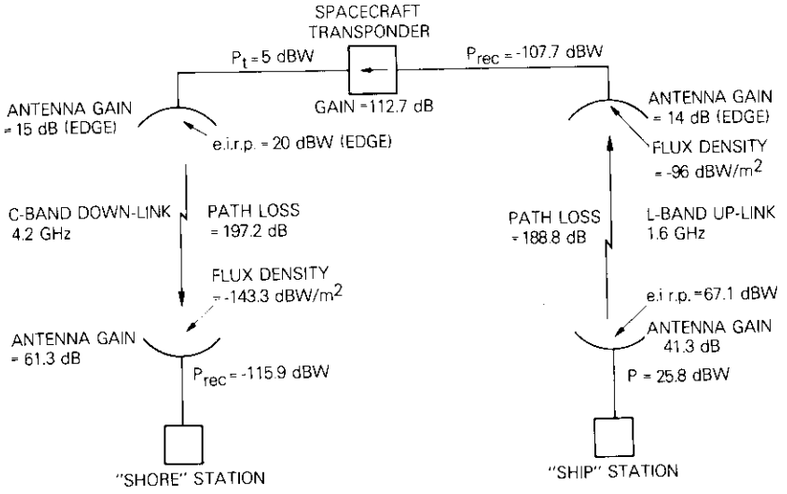

Figure 4. *Power Levels for L- to C-Band Transponder e.i.r.p. Test*

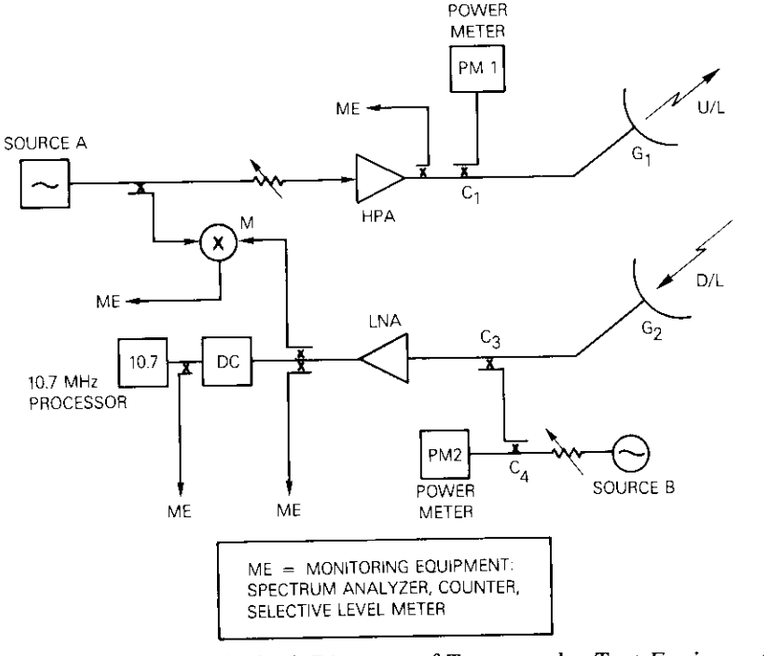

Figure 5. *Functional Block Diagram of Transponder Test Equipment*

A signal from source *B* may be injected into the input of the low-noise amplifier. This signal is tuned to 27 kHz below the down-link signal. These two signals share an identical path through a double-conversion frequency translation (in DC) to the input of the 10.7-MHz processor for down-link power measurement. The down-link signal can also be measured and monitored on the selective level meter, spectrum analyzer, and counter.

10.7-MHz processor

The 10.7-MHz processor is used in conjunction with other components to accurately measure down-link received power, and thus, by further calculation, spacecraft e.i.r.p.

The actual down-link power received from the spacecraft is about −115 dBW and is not directly measurable. The measurement principle used is illustrated in Figure 6.

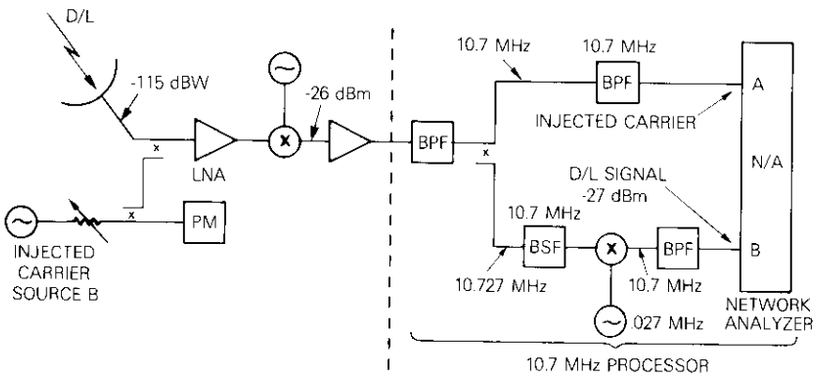

Figure 6. *Down-Link Power Measurement*

A CW signal, known as the injected carrier, from synthesizer source *B* is coupled into the down-link receiver chain at the antenna flange. Its frequency is set precisely to 27 kHz less than the down-link carrier frequency. Since the injected signal couplers can be accurately calibrated, the level of the injected signal can be determined from the power meter, PM.

The injected and down-link signals both pass through the low-noise amplifier, down-converting mixer, and subsequent filter. The two signals, now at 10.7 and 10.727 MHz, respectively, are then separated

by filters into two paths. The 10.727-MHz (down-link) signal is further down-converted to 10.7 MHz, and the two signals, P_{INJ} and $P_{D/L}$, now both at 10.7 MHz, are measured (in power) at the input ports *A* and *B*, respectively, of a dual channel network analyzer. The analyzer then determines the difference $P_{D/L} - P_{INJ}$ (in dB) of the two signals. This difference, designated as NA, taken in conjunction with the power meter reading PM and the network analyzer offset OS (to be discussed later), determines the down-link received power. The power level of the injected carrier into the LNA is made comparable to that of the down-link carrier, and both signals must be low enough to ensure that the LNA and mixers are operating linearly. Nominal power levels for down-link signals are shown in Figure 6.

The network analyzer offset OS allows for the insertion loss difference between the down-link and injected signal paths, from the injected signal coupler output to the two network analyzer inputs. This loss difference results primarily from the coupler, filters, and mixer in the 10.7-MHz processor. The offset is measured by turning off the up-link (and thus, the down-link) signal and tuning the injected carrier source at a constant power level first to the down-link frequency, and then to the "injected carrier" frequency, 27 kHz lower. At each frequency, one of the two network analyzer inputs *A* and *B* receives 10.7-MHz power, P_A and P_B, which is measured. The difference between the two measured powers is the desired offset, OS, which is defined by $OS = P_B - P_A$.

The 10.7-MHz processor is required to measure and compare signals separated by only 27 kHz. For this reason, and to ensure good signal-to-noise ratio, the measurement bandwidth is only 3 kHz. This imposes a tight tuning accuracy requirement on the down-link receive channel tuning.

Down-link receive channel tuning

The 10.7-Hz signal processor has a bandwidth of only 3 kHz, which is imposed by other MCS test requirements. Consequently, the down-link frequency must be known to within 1 kHz or less to select the correct local oscillator frequency for the down-link frequency down-converter.

Usually, the down-link frequency is not known to 1-kHz accuracy because even though the up-link frequency is known to high accuracy, the spacecraft LO frequency is only accurate to within ±49 kHz (for

C to L; ±25.6 kHz for L to C). The spacecraft LO frequency must, therefore, be measured to high accuracy before the down-link receive channel can be tuned. Measuring the spacecraft LO frequency is part of the MCS test requirement, and the same measurement technique and equipment are used before any down-link receiver tuning and power measurement is made.

Measurement procedures

The accurate in-orbit measurement of spacecraft RF power parameters depends on an accurate knowledge of the following:

a. up-link transmitted power,
b. down-link receiver power,
c. earth station transmit and receive antenna gains, and
d. injected signal coupling level at the earth station receive antenna flange.

These parameters are required at both C and L transmit and receive frequencies; there is a total of four frequencies. The spacecraft power measurement uncertainty will be the sum of at least the uncertainty of the relevant parameters listed above.

As discussed in the subsection entitled "L- to C-Band Transponder Test Set," before any down-link power measurement can be made using the 10.7-MHz processor, the down-link down-converter local oscillator must be precisely tuned; this requires knowledge of the spacecraft local oscillator frequency.

Spacecraft local oscillator frequency

Figure 5 shows that when the up-link signal is mixed (in mixer *M*) with its returned down-link, the mixer output is at the spacecraft LO frequency. To measure the LO frequency, the injected signal from source *B* is turned off, a single CW carrier is transmitted, and the mixer output is counted by the microwave counter. The computer printed output for this measurement will be typically as shown in Figure 7.

Whenever the spacecraft LO frequency is needed for down-link receive tuning for other measurements, it is automatically measured under computer control, and the measured value is then used to compute the appropriate earth station LO frequency.

LO Measurement

S/C:F1
E/S:FUCINO
Date:07/19/1982
Time:10:00:34 GMT
E/S is :3.42°E of S.S. point
E/S is :6.39°N of S.S. point
Configuration:C to L
Receiver:4, Gain NORMAL
U/L Calibration Factor : -81.0 dB
D/L Calibration Factor : 40.4 dB
Converter:1
Transmitter:A, Side 2&1
COMMENT:MARISAT F1

U/L Freq [MHz]	Nominal D/L Freq [MHz]	L.O. Freq [MHz]	TIME [GMT]
6421.2500	1538.2439	4883.0061	10:00:56
6421.2500	1538.2439	4883.0061	10:01:17

Figure 7. *Computer Printout of Typical Spacecraft LO Measurements*

Spacecraft e.i.r.p.

Before the e.i.r.p. is measured, the appropriate spacecraft LO frequency is measured, and the result is used to appropriately tune the down-link receive system. Spacecraft e.i.r.p. is measured with a known flux density, which is established at the spacecraft receive antenna.

The single-carrier flux density at the spacecraft and the up-link power meter reading on PM1 in Figure 5 are related by the following:

$$\begin{aligned} \text{FD} &= \text{e.i.r.p.}_{\text{up}} - \text{SF} \\ &= \text{PM1} + C_1 + G_1 - \text{SF} - 30 \end{aligned}$$

where
FD = flux density (dBW/m²)
$\text{e.i.r.p.}_{\text{up}}$ = up-link e.i.r.p. (dBW)
SF = spreading factor = 10 log $(4\pi D^2)$
PM1 = reading of *PM*1 (dBm)
C_1 = coupling level (dB), taken as a positive number
G_1 = earth station transmit antenna gain (dB)
D = distance to spacecraft (meters).

The single-carrier spacecraft e.i.r.p. and the instrument readings are related by

$$\text{e.i.r.p.}_{S/C} = P_{rec} - G_2 + \text{PL}$$
$$= \text{PM2} - C_2 + \text{PL} - G_2 + \text{NA} - \text{OS} - 30$$

where $\text{e.i.r.p.}_{S/C}$ = spacecraft e.i.r.p. (dBW)
P_{rec} = received power at earth station antenna flange (dBW)
G_2 = earth station receive antenna gain (dB)
PL = down-link path loss = $20 \log (\lambda/4\pi D)$ (dB)
PM2 = reading on PM2 (dBm)
C_2 = sum of coupling factors C_3, C_4 (dB) taken as a positive number
NA and OS are defined in a previous subsection
λ = wavelength of down-link (meters).

For the L to C measurement, a single CW up-link carrier power level is specified and established, and the down-link power is then measured as described earlier. When operated under computer control, the L to C e.i.r.p. data output is typically as shown in Figure 8.

Flux-Eirp Measurements

S/C:F1
E/S:FUCINO
Date:07/19/1982
Time:11:58:55 GMT
E/S is :3.42°E of S.S. point
E/S is :6.39°N of S.S. point
Configuration:L to C
Receiver:1
Attenuator:OUT
TWTA:A
COMMENT:MARISAT F 1 TEST

U/L Calibration Factor :-104.5 dB
D/L Calibration Factor : 35.0 dB

U/L Freq [MHz]	Pup [dBm]	Pinj [dBm]	N/A [dB]	F.D. [dBW/m²]	E.i.r.p. [dBW]	D/L Freq [MHz]	TIME [GMT]
1642.4100	-11.6	-9.5	-11.2	-116.0	+14.3	4198.9061	12:05:47
1642.4100	-11.6	-9.5	-11.0	-116.1	+14.5	4198.9061	12:05:55

Figure 8. *Computer Printout for Typical Spacecraft Flux-e.i.r.p. Measurement, L to C, 1 Carrier*

It is specified that the C to L e.i.r.p. be measured with 10 equal amplitude carriers passing through the transponder. The 10 carriers conform to an established frequency plan; therefore, after the appropriate 10 carrier up-link power is established, both the down-link receive chain and the injected carrier are tuned to place one down-link carrier and the injected carrier into the 10.7-MHz processor. The down-link power measurement permits calculation of the e.i.r.p. of the individual carrier. Then both the down-link receive chain and the injected carrier are step tuned to place the next down-link carrier and the injected carrier into the processor for measurement. After stepping through and measuring all 10 carriers under computer control, the summed e.i.r.p. is computed; a typical computer printout is shown in Figure 9.

More extensive measurements may be made as the up-link power and frequency, under operator control, may be changed, thereby enabling gain transfer characteristics and frequency response to be determined.

Ten Carrier Eirp Measurements

S/C:F1
E/S:FUCINO
Date:07/19/1982
Time:10:42:28 GMT
E/S is :3.42°E of S.S. point
E/S is :6.39°N of S.S. point
Configuration:C to L
Receiver:4, Gain NORMAL
Converter:?
Transmitter:?, Side ?
COMMENT:MARISAT F 1 TEST

U/L Calibration Factor : -81.0 dB
D/L Calibration Factor : 40.4 dB

Sig	U/L Freq [MHz]	Pup [dBm]	Pinj [dBm]	N/A [dB]	F.D. [dBW/m	Eirp. [dBW]	D/L Freq [MHz]	TIME [GMT]	Total Eirp [dBW]
1	6419.8750	-22.9	-8.8	-27.4	-103.9	+5.0	1536.0690	10:45:23	
2	6419.9250	-22.8	-8.8	-27.1	-103.8	+5.2	1536.9190	10:45:29	
3	6420.1750	-22.8	-8.8	-27.1	-103.8	+5.3	1537.1690	10:45:35	
4	6420.3750	-22.8	-8.8	-26.8	-103.8	+5.6	1537.3690	10:45:41	
5	6421.0500	-22.8	-8.1	-27.7	-103.8	+4.6	1538.0440	10:45:47	
6	6421.1750	-22.8	-8.1	-27.4	-103.8	+4.9	1538.1690	10:45:52	
7	6421.5749	-22.8	-8.1	-27.0	-103.8	+5.2	1538.5689	10:45:58	
8	6421.9250	-22.8	-8.1	-27.2	-103.8	+5.0	1538.9190	10:46:07	
9	6422.5250	-22.8	-8.2	-27.5	-103.8	+4.7	1539.5190	10:46:13	
10	6422.6250	-22.8	-8.2	-27.1	-103.8	+5.1	1539.6190	10:46:18	+15.1

Figure 9. *Computer Printout for Typical Spacecraft e.i.r.p. Measurement, C to L, 10 Carriers*

G/T

A figure of merit of signal reception capabilities of the spacecraft is the G/T ratio, which when expressed in dB, is given by

$$G/T \text{ (dB)} = G_a - T_a$$

where G_a is the spacecraft receive antenna gain in dB and T_a is the equivalent noise temperature at the spacecraft receive antenna flange in dB relative to 1 K. This noise temperature includes all contributions within the spacecraft, as well as noise sources in the antenna field of view. (In this case, the antenna sees the earth whose noise temperature is 300 K.) Figure 10 shows that if G_b is defined as $G_a + G_\ell$, and T_b is the equivalent noise temperature contribution at plane B because of the noise from the spacecraft alone, then since $G_b = G_a + G_\ell$ and $T_b = T_a + G_\ell$,

$$G_a - T_a = G_b - T_b \quad . \tag{1}$$

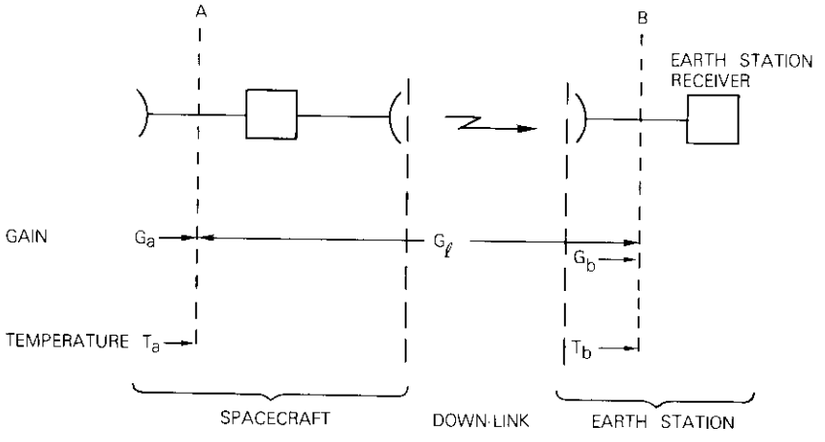

Figure 10. *Gains and Noise Temperatures in G/T Measurement*

This equation will be true only if the same G_ℓ applies for the experimental determination of both G_b and T_b. G_ℓ includes the active gain of the spacecraft, which is constant only in the linear region of the spacecraft gain characteristic, that is, for small input signals. The noise input signals are definitely in this linear range. Therefore, when G_b is determined, the up-link signal must be set at a sufficiently low level such that the spacecraft will exhibit the same small signal linear gain.

The method of measuring T_b, the required noise temperature, is now developed. If no up-link signal is transmitted to the spacecraft, then the transmitted down-link signal from the spacecraft is noise generated

entirely by the equivalent spacecraft temperature. However, the noise power into the earth station receiver consists of contributions resulting from the sky temperature (T_{sky}) and the earth station receiver temperature (T_{rec}), as well as that resulting from the spacecraft temperature.

Determination of T_b, the equivalent spacecraft noise temperature as measured at the earth station, requires separation of the spacecraft temperature contribution from the total noise temperature measured at the earth station.

The measurement procedure to separate these quantities consists of measuring the earth station received noise power with the earth station receiver connected to the following:

a. the antenna, while the antenna is pointed at
   (1) the sky away from the spacecraft, and at
   (2) the spacecraft;
b. a hot load at a known temperature T_h K; and
c. a cold load at a known temperature T_c K.

These four measurements yield P_{sky}, $P_{S/C}$, P_h, and P_c (watts), respectively. The four noise powers (at the earth station receiver input flange) are amplified, down-converted to a center frequency of 10 MHz, filtered to a 7.5-MHz bandwidth, and measured by a selective level meter. The gain between the receiver input flange and the measuring meter affects all four power measurements equally, and thus does not appear explicitly in the equations leading to T_b. Figure 11 shows the noise temperature contributions to each of the four measurements.

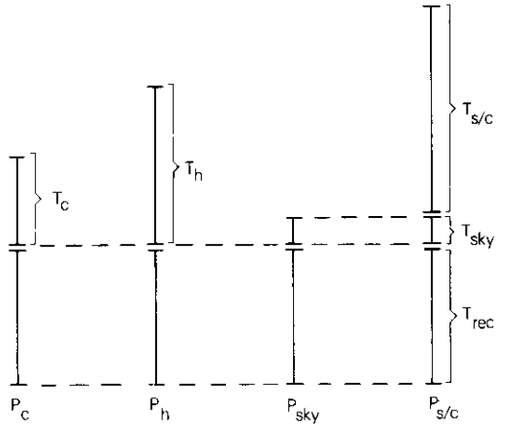

Figure 11. *G/T Measurement: Noise Powers Measured at Earth Station Receiver Output—Showing Noise Temperature Contributions*

The desired quantity $T_{S/C}$ is the temperature contribution (in Kelvin) of the spacecraft as measured at the earth station receiver flange. Because the equivalent noise temperatures at the receiver flange (in Kelvin) and the measured powers (in watts) are linearly related, it is found that

$$T_{S/C} = \frac{T_h - T_c}{P_h - P_c} \times (P_{S/C} - P_{sky}) \quad . \tag{2}$$

The desired temperature T_b (in dB with respect to 1 K) is given by

$$T_b = 10 \log T_{S/C} \quad . \tag{3}$$

Using the methods described to obtain the spacecraft e.i.r.p., G_b is determined. An up-link carrier is transmitted (at a sufficiently low level to ensure that the spacecraft is operated in the linear gain region) and the appropriate instruments are read. Then, using the notation given in the section discussing spacecraft e.i.r.p.,

$$\begin{aligned} G_b &= \text{e.i.r.p.}_{S/C} - \text{FD} - \text{SF} + G_2 \\ &= \text{PM2} - \text{PM1} - C_2 - C_1 - G_1 + \text{NA} - \text{OS} + \text{PL} \quad . \end{aligned}$$

Equations (1), (2), and (3) are used to determine the desired G/T ratio. A typical computer printout for this measurement is shown in Figure 12.

NPR testing

Noise power ratio (NPR) measurements are a method of characterizing the distortion and intermodulation properties of multichannel communications systems.

The test consists of loading the multichannel system with bandlimited white noise simulating all loaded channels and measuring first the resultant noise power in a single channel. A bandstop filter is then inserted at the input of the measurement channel, creating a single nominally "quiet" channel. The ratio of noise at the output of the quiet channel to the noise in the same channel when loaded is the noise power ratio. The method tests the system under realistic conditions, as the loading with noise closely simulates the condition of loading with many channels.

G/T Measurements

S/C:F1
E/S:FUCINO
Date:07/19/1982
Time:10:02:59 GMT
E/S is :3.42°E of S.S. point
E/S is :6.39°N of S.S. point
Configuration:C to L
Receiver:4, Gain NORMAL
U/L Calibration Factor : -81.0 dB
D/L Calibration Factor : 40.4 dB
Converter:1
Transmitter:A, Side 2&1
COMMENT:MARISAT F1

Item	Slms [dB]	Temp	Tes [K]	Tsc [dBK]	G/T [dB/K]	U/L Freq [MHz]	Pup [dBm]	Pinj [dBm]	N/A [dB]	TIME [GMT]
S/C	-25.2									10:04:41
S/C	-25.2									10:04:47
SKY	-33.2									10:05:49
SKY	-33.1									10:05:58
COLD	-29.9	293K								10:07:13
COLD	-29.9	293K								10:07:28
HOT	-29.3	100°C	253.0	31.1						10:07:45
HOT	-29.2	100°C	234.2	30.8						10:08:03
GRIN					-17.5	6423.90990	-21.9	-8.3	-14.0	10:11:56
GRIN					-17.4	6423.90990	-22.1	-8.2	-14.0	10:12:23

Figure 12. *G/T Printout*

NPR measurements are often used to measure the performance of frequency multiplexed microwave links, where the multichannel baseband frequency modulates the microwave carrier. In contrast, in this test, the simulated multichannel baseband is simply frequency translated to the microwave frequency before transmission and down-converted at reception. Therefore, the notch in the baseband is visible in the RF spectrum, thus differing from the frequency modulated case. It is believed that this is the first time that such an RF NPR technique has been used for satellite in-orbit testing.

For the C- to L-band transponder, an up-link signal consisting of a 7.5-MHz-wide band of noise is transmitted with and without a 3-kHz notch in it. The down-link receiver is tuned to place the 3-kHz-wide channel at the notch filter frequency into the selective level meter set (SLMS), which measures the power in the narrow channel, with and without the notch filter switched in. The receiver bandwidth of the SLMS is narrower than the notch bandwidth, so that the SLMS measures only power within the single channel bandwidth.

The test specification requires an NPR of 10 dB. To ensure that the NPR being measured is caused by the spacecraft transponder, provision is made to measure the NPR of the earth station HPA. An HPA NPR of

30 dB or greater will make a negligible contribution to the result measured through the spacecraft transponder. A typical computer printout for this measurement is shown in Figure 13.

NPR Measurements

S/C:F1
E/S:FUCINO
Date:07/20/1982
Time:09:37:01 GMT
E/S is :3.42°E of S.S. point
E/S is :6.39°N of S.S. point
Configuration:C to L
Receiver:?
Converter:?
Transmitter:?, Side ?
COMMENT:MARISAT F1 TEST

U/L Calibration Factor : -81.0 dB
D/L Calibration Factor : 40.4 dB

Item	Sims [dB]	NOTCH	NPR [dB]	Pwp [dBm]	TIME [GMT]
CHECK	-59.6	OUT			09:37:27
CHECK	-108.9	IN	49.3		09:37:32
U/L	-74.4	OUT		-22.0	09:37:56
U/L	-104.1	IN	29.7	-24.2	09:38:02
S/C	-54.2	OUT		-22.0	09:38:24
S/C	-58.2	IN	3.9	-24.3	09:38:29

Figure 13. *NPR Printout*

Computer-automated measurement methods

To describe how the computer controls the measurement test set and produces the desired data is beyond the intended scope of this paper. However, most of the test instruments used in the equipment described are coupled to an HP-9845B computer at the test site; and special software, developed by COMSAT Laboratories, is used to conduct the test procedure. The software has been designed to permit extreme flexibility in equipment operation, such that the tests may be conducted almost fully automatically or manually.

Computer control is a vital and essential part of the test equipment, since it would be virtually impossible to perform the tests without it. The number of adjustments, readings, and calculations that would be required would be too time consuming to be practical. The flexibility built into the software permits highly interactive operation, permitting operator intervention at any point to repeat, modify, or cancel any part(s) of the measurements.

In addition to the program that performs the initial satellite testing, a second program was developed for periodic performance testing while the satellite is in use, carrying traffic.

Conclusion

Techniques and equipment used to measure in-orbit performance of the MCS transponder have been described. These techniques are examples of the continual evolution and improvement that have occurred in in-orbit testing, particularly in the area of increased automation.

Relative to earlier partially automated methods of measuring *G/T* and determining the network analyzer offset, the methods described here are faster and more accurate. The multiple carrier e.i.r.p. test and the NPR measurements are both examples of measurements that could be performed only with extreme difficulty and with reduced accuracy by manual methods.

Acknowledgments

The test methods and equipment electrical design described here were developed in the Transponder Department at COMSAT *Laboratories. The basic equipment design was made primarily by C. Mahle, and other vital contributions were made by V. Riginos. Two sets of test equipment were mechanically designed, assembled, and installed by the Development Engineering Division* (DED) *of* COMSAT. *The substantial contribution of* DED *to this project is acknowledged. Finally, the installation could not have been completed without the excellent cooperation of the earth station staffs at Fucino and Yamaguchi.*

References

[1] D. W. Lipke et al., "MARISAT—A Maritime Satellite Communications System," COMSAT *Technical Review*, Vol. 7, No. 2, Fall 1977, pp. 351–391.

[2] I. Dostis et al., "In-Orbit Testing of Communications Satellites," COMSAT *Technical Review*, Vol. 7, No. 1, Spring 1977, pp. 197–226.

[3] V. Riginos, C. Mahle, and I. Atohoun, "In-Orbit Measurements of RF Subsystem of Communications Satellite," INFO II, 2nd International Conference on Information Sciences and Systems, Patras, Greece, July 9–14, 1979.

[4] V. Riginos, C. Mahle, and I. Atohoun, "ATE Checks Health of Orbiting Spacecraft," *Microwaves*, August 1980.

[5] E. Emmert, V. Riginos, and J. Potukuchi, "In-Orbit Measurement of the SBS Satellite," 9th AIAA Communications Satellite System Conference, San Diego, California, March 1982.

Michael J. Barrett received B.Sc. and Ph.D. degrees from London University, England. After coming to the United States in 1964, he was employed by Raytheon Company and by Sylvania Semiconductor Division, designing microwave components. As a Member of the Technical Staff of the Microwave Laboratory at COMSAT Laboratories since 1972, he has worked on the design and evaluation of present and future satellite components and systems. He developed and built hardware for the millimeter wave experiments flown on board the COMSTAR satellites. Recent responsibilities have included design and engineering of equipment for testing of orbiting satellites and participation in the in-orbit testing of INTELSAT spacecraft.

Kenneth D. Fullett received a B.S.E.E. and M.S.E.E. from the University of Illinois, Urbana-Champaign, in 1979 and 1981, respectively. He joined COMSAT Laboratories in 1981 as a member of the Transponders Department of the Microwave Communications Laboratory. He has been involved in various facets of in-orbit testing of communications satellites.

Index: networks, telephone transmission, traffic statistics, transmission systems

Efficient approaches to Erlang loss function computations

T. N. SHIMI AND Y. L. PARK

(Manuscript received July, 1, 1982)

Abstract

This paper presents a new approach for obtaining a first estimate of the maximum allowable traffic intensity for a given grade of service and channel size. The Erlang loss function, along with other mathematical tools, is utilized to produce a more direct and time-efficient method for obtaining an accurate estimate of the traffic intensity. Of particular interest are applications in which the trunk size is relatively large.

An integral representation of the Erlang loss function is used in developing theoretical bounds on traffic intensity that are taken as first estimates; further refinements are obtained by using asymptotic expansions and Newton's iterative method.

Introduction

The Erlang loss function, introduced by A. K. Erlang [1], is fundamental to the study of telephone trunking problems. This function relates the probability of an incoming call being rejected to the total number of circuits in the trunk group and the maximum traffic intensity to be served.

Traditionally, tables based on the Erlang loss function have been constructed to obtain the maximum allowable traffic intensity for a given grade of service and channel size. In many recent investigations, rapid and accurate approximations of traffic intensity for very large

trunk groups were needed. This requirement occurs frequently in the study of satellite communications systems.

Existing techniques either are not accurate enough or would require excessive processing time to handle large circuits. To overcome these shortcomings, this paper introduces a method which uses an integral representation of the Erlang loss function, ascribed to Fortet, to obtain an initial value of the maximum allowable traffic intensity, followed by a more accurate value obtained with Newton's method. This approach allows the direct calculation of traffic intensity from a single value of service grade and channel size, thus saving considerable processing time. Furthermore, the accuracy of the result is specified by the user to fit the application. Reference 2 gives a detailed description of Newton's method. A FORTRAN program is also included to illustrate the use of this method.

Mathematical representation of the Erlang loss function

The Erlang loss function is

$$B(C, A) = \frac{A^C/C!}{\sum_{k=0}^{C} A^k/k!} \qquad (1)$$

where $B(C, A)$ = probability of a call being rejected

A = traffic intensity (Erlangs)

C = total number of circuits in the trunk group.

This function describes an arrival stream satisfying a Poisson distribution and assumes that all calls receiving a busy signal are lost. Traffic intensity is defined as the product of the average number of incoming calls per hour (both served and rejected) and the average call length.

An integral representation of the Erlang loss function that utilizes the Eulerian integral is given in Reference 3:

$$\int_0^\infty e^{-Ay} y^C \, dy = \Gamma(C + 1)A^{-C-1}; \qquad C > -1 \quad .$$

With this representation, one can write

$$B^{-1}(C, A) = A \int_0^\infty e^{-Ay}(1 + y)^C \, dy \quad . \qquad (2)$$

As pointed out in Reference 2, the series representation of equation (1) has numerous drawbacks for numerical calculations of the Erlang function. In particular, this representation becomes unwieldy for large numbers of circuits in trunk groups for the following reasons:

a. For given B and C, it is difficult to obtain the corresponding value of A because of the high polynomial power of A in equation (1).

b. The series has many terms that are more significant for higher powers of A; this feature inhibits the accuracy of the calculation.

c. The powers and factorials in equation (1) can easily exceed the normal limits of expressing numbers by most computers.

The following sections describe methods that deal with these difficulties.

Fortet integral method

Given the service grade B and channel size C, the Fortet integral method employs two separate steps to calculate the corresponding maximum allowable traffic intensity A. First, the Fortet integral is used to obtain initial estimates of A. In the second step, this first estimate is used as a primer for Newton's iterative method. The accuracy of the final result is specified by the user.

Mathematical derivations

Introducing in equation (2) the transformation $z = 1 + y$ leads to

$$\begin{aligned} B^{-1} &= Ae^A \int_1^\infty e^{-Az} z^C \, dz \\ &= Ae^A \left(\int_0^\infty e^{-Az} z^C \, dz - \int_0^1 e^{-Az} z^C \, dz \right) \\ &= Ae^A (I_1 - I_2) \end{aligned} \qquad (3)$$

where

$$I_1 = \int_0^\infty e^{-Az} z^C \, dz = \frac{\Gamma(C+1)}{A^{C+1}}$$

$$I_2 = \int_0^1 e^{-Az} z^C \, dz \quad .$$

Since in I_2, $0 < z < 1$, it follows that

$$I_2 < \int_0^1 e^{-Az} \, dz = \frac{-1}{A} e^{-Az} \Big|_0^1 = \frac{1 - e^{-A}}{A} \quad .$$

That is,

$$0 < I_2 < \frac{1 - e^{-A}}{A} < \frac{1}{A} \quad .$$

Clearly, then, $I_2 \to 0$ as $A \to \infty$, and

$$B^{-1} < Ae^A(I_1 - 0) = Ae^A \frac{1}{A^{C+1}} \Gamma(C+1) = \frac{e^A}{A^C} \Gamma(C+1) \quad .$$

That is,

$$B^{-1} < \frac{e^A}{A^C} \Gamma(C+1) \quad . \tag{4}$$

Inequality (4) is used to calculate an initial value of A. However, for large values of C, the inequality in its present form is not suitable for computer use. Taking the logarithm of both sides eliminates the problem of overflow and underflow. Hence,

$$f(A) \equiv A - C \ln (A) + \ln \Gamma(C+1) - \ln (B^{-1}) \approx 0 \quad . \tag{5}$$

Note that

$$\Gamma(X) = X^X e^{-X} \sqrt{\frac{2\pi}{X}} \left(1 + \frac{1}{12X} + \frac{1}{288X^2} - \frac{139}{51{,}840X^3} + \cdots \right) \quad .$$

One of the roots of the function $f(A)$ will be taken as the initial value of A. To solve equation (5), a FORTRAN subroutine, ZREAL1, described in Reference 4, is used. However, it is still necessary to supply the subroutine with initial guesses of the roots. These estimations can be obtained from the following observations:

a. Differentiating $f(A)$ yields

$$\frac{df(A)}{dA} = 1 - \frac{C}{A} \quad .$$

Hence f attains its minimum at $A = C$, decreases for $A < C$, and increases for $A > C$.

b. From equation (2),

$$B^{-1} = A\,I$$

where

$$I = \int_0^\infty e^{-Ay}(1+y)^C \, dy > \int_0^\infty e^{-Ay}(1+y)^{C-1} \, dy$$

$$= \frac{1}{C} \left\{ [(1+y)^C e^{-Ay}] \Big|_0^\infty + A \int_0^\infty (1+y)^C e^{-Ay} \, dy \right\}$$

$$= \frac{1}{C}(-1 + AI) \quad .$$

That is,

$$\frac{B^{-1}}{A} > \frac{1}{C}(-1 + B^{-1}) \quad .$$

Hence,

$$A < \frac{C}{1 - B} \quad .$$

Observations *a* and *b* show that the two values C and $C/(1 - B)$ are good candidates for inputs to ZREAL1.

It should be noted that if $f(C) > 0$, equation (5) has no roots because

f attains its minimum at C, in which case, C is taken as the initial value of A.

Computer programs

Figures 1 and 2 display two FORTRAN programs for the calculation of traffic intensity. Each program employs two subroutines, ZREAL1

```
C T N SHIM1. A FORTRAN PROGRAM TO CALCULATE THE MAXIMUM ALLOWABLE
C TRAFFIC INTENSITY FOR A GIVEN GRADE OF SERVICE AND CHANNEL SIZE.
C
C INPUTS
C    B = PROBABILITY OF A CALL BEING REJECTED (GRADE OF SERVICE)
C    C = TOTAL NUMBER OF CIRCUITS IN THE TRUNK GROUP (CHANNEL SIZE)
C OUTPUT
C    A = MAXIMUM TRAFFIC INTENSITY(MAXIMUM LOAD IN ERLANG)
C
      IMPLICIT REAL*8 (A-H,O-Z)
      DOUBLE PRECISION X(2)
      COMMON C,XLGAMC,XLBINV,BINV
      EXTERNAL F
      INTEGER IYES/'Y'/
    5 CONTINUE
      WRITE (6,10)
   10 FORMAT(1X,'ENTER B AND C')
      READ (5,*) B,C
      BINV = 1.0D0/B
      XLGAMC = DLGAMA(C + 1.0D0)
      XLBINV = DLOG(BINV)
      EPS = 1.0D-6
      EPS2 = 1.0D-6
      ETA = 1.0D-6
      NSIG = 6
      ITMAX = 100
      N = 2
      X(1) = C
      X(2) = C / (1.0D0 - B)
      Y1 = X(1) - C * DLOG(X(1)) + XLGAMC - XLBINV
      Y2 = X(2) - C * DLOG(X(2)) + XLGAMC - XLBINV
      IF (Y1 .GT. 0.0D0)  GO TO 15
      CALL ZREAL1 (F,EPS,EPS2,ETA,NSIG,N,X,ITMAX,IER)
      Y1 = X(1) - C * DLOG(X(1)) + XLGAMC - XLBINV
      Y2 = X(2) - C * DLOG(X(2)) + XLGAMC - XLBINV
   15 CONTINUE
      IF (DABS(Y1) .LT. DABS(Y2)) GO TO 18
      CALL PRCISE (X(2))
      WRITE (6,17) X(2)
   17 FORMAT ('0','MAX. LOAD IN ERLANG  = ',F13.4/)
      GO TO 19
   18 CONTINUE
      CALL PRCISE (X(1))
      WRITE(6,17) X(1)
   19 WRITE (6,20)
   20 FORMAT(1X,'DO YOU WANT ANOTHER RUN ? YES OR NO')
      READ (6,30)JYES
   30 FORMAT(A1)
      IF (JYES .EQ. IYES) GO TO 5
      STOP
      END
```

Figure 1. *Monitor Conversational Program ERLANG*


```
      DOUBLE PRECISION FUNCTION F(A)
      IMPLICIT REAL*8 (A-H,O-Z)
      COMMON C,XLGAMC,XLBINV,BINV
      IF (A .LE. 0.0D0) GO TO 31
      F = A - C * DLOG(A) + XLGAMC - XLBINV
      GO TO 32
   31 F = A + C * 228.0D0 + XLGAMC - XLBINV
   32 RETURN
      END
```

```
      SUBROUTINE PRCISE (A)
C
C  THIS SUBROUTINE UTILIZES NEWTON'S ITERATIVE METHOD TO OBTAIN
C  THE FINAL VALUE OF A. THE PRECISION OF THIS VALUE IS A USER INPUT.
C  IN THE PRESENT APPLICATION THE ITERATIVE PROCESS IS TERMINATED
C  WHEN EITHER ONE OF THE FOLLOWING CONDITIONS IS SATISFIED:
C
C  1) THE VALUE OF TERM IS LESS THAN 1.E-12.
C  2) THE CHANGE IN THE VALUE OF A IS LESS THAN 1.E-10.

C  IF CONVERGENCE FAILS, A IS SET TO -666
C
      IMPLICIT REAL*8 (A-H,O-Z)
      COMMON C,XLGAMC,XLBINV,BINV
      IC = IFIX(SNGL(C))
      DO 30  J = 1,20
      F = 1.0D0 - BINV
      FP = 0.0D0
      TERM = 1.0D0
      DO 10 K = 1,IC
      XK = DFLOAT(K)
      TERM = TERM * (C-XK+1.0D0)/A
      F = F + TERM
      FP = FP + XK * TERM
      IF (TERM .LT. 1.0D-12) GO TO 20
   10 CONTINUE
   20 A = A * (1.0D0 + F/FP)
      IF (DABS(F/FP) .LT. 1.0D-10) GO TO 40
   30 CONTINUE
      A = -666.0D0
   40 CONTINUE
      RETURN
      END
```

Figure 1. *Monitor Conversational Program ERLANG (Continued)*

and PRCISE. Subroutine ZREAL1, from International Mathematical and Statistical Libraries, Inc., was implemented to find the real roots of a real function F. Given a user-supplied external function subprogram $F(A)$ and two initial guesses for these real roots, $X_1 = C$ and $X_2 = C/(1 - B)$, the subroutine uses Muller's method [5], [6] to locate two real roots of F. The routine has two convergence criteria:

a. Value of function—

$$|F(X_i^m)| < 10^{-7}; \qquad i = 1, 2$$

b. Value of root—

$$\left|\frac{X_i^{m+1} - X_i^m}{X_i^m}\right| < 10^{-6}; \qquad i = 1, 2$$

```
C T N SHIMI. A FORTRAN PROGRAM TO GENERATE A TABLE OF TRAFFIC
C LOADS, A, FOR GIVEN VALUES OF BLOCKING PROBABILITIES, B,
C AND CHANNEL SIZES, C.
C
      IMPLICIT REAL*8 (A-H,O-Z)
      DOUBLE PRECISION X(2),BSTOR(5),ROOT(5)
      COMMON C,XLGAMC,XLBINV,BINV
      EXTERNAL F
      WRITE(6,10)
   10 FORMAT (7X,'C',7X,'B=.001',7X,'B=.005',8X,'B=.01',8X,'B=.05',
     * 9X,'B=.1')
C
C  B = 0.001, 0.005, 0.01, 0.05, 0.1
C
      DATA BSTOR /1.0D-3,.5D-2,1.0D-2,.5D-1,1.0D-1/
      EPS = 1.0D-6
      EPS2 = 1.0D-6
      ETA = 1.0D-6
      NSIG = 6
      N = 2
C
C  C TAKES THE VALUES FROM 10000 TO 100000 WITH INCREMENTS OF 2000
C
      DO 30 I = 10000,100000,2000
      C = DFLOAT(I)
      XLGAMC = DLGAMA(C + 1.0D0)
      DO 20 K = 1,5
      ITMAX = 100
      B = BSTOR(K)
      BINV = 1.0D0/B
      XLBINV = DLOG(BINV)
      X(1) = C
      X(2) = C / (1.0D0 - B)
      Y1 = X(1) - C * DLOG(X(1)) + XLGAMC - XLBINV
      Y2 = X(2) - C * DLOG(X(2)) + XLGAMC - XLBINV
      IF (Y1 .GT. 0.0D0)  GO TO 15
      CALL ZREAL1 (F,EPS,EPS2,ETA,NSIG,N,X,ITMAX,IER)
      Y1 = X(1) - C * DLOG(X(1)) + XLGAMC - XLBINV
      Y2 = X(2) - C * DLOG(X(2)) + XLGAMC - XLBINV
   15 CONTINUE
      IF (DABS(Y1) .LT. DABS(Y2)) GO TO 18
      CALL PRCISE (X(2))
      ROOT(K) = X(2)
      GO TO 20
   18 CONTINUE
      CALL PRCISE (X(1))
      ROOT(K) = X(1)
   20 CONTINUE
      WRITE (6,25) I,ROOT
   25 FORMAT (' ',I7,5F13.4)
   30 CONTINUE
      STOP
      END
```

Figure 2. *Table Generation Program ERLTABLE*

The quantity X_i^m is the mth approximation of X_i. Convergence is taken to mean the satisfaction of either criterion.

Subroutine PRCISE, introduced in Reference 3, implements Newton's iterative method to find refinements of the roots obtained from ZREAL1. Convergence is achieved when variations in the successive refinements of the zeros are less than 10^{-12}. The subroutine limits the number of iterations to 20. If convergence is not attained, the value of A is set to -666. This contingency, however, never occurred in practice.

Program applications and execution

The first program, ERLANG (Figure 1), is a monitor conversational program. It prompts the user to supply, as input, both B, the grade of service, and C, the channel size, and returns the corresponding value of A, the maximum traffic intensity. The program then asks the user if another run for other values of B and C is desired. A sample run session is given in Figure 3. It was found that for values of C between 10 and 1,000, the average CPU time of processing per calculation is 0.013 s; for C between 1,000 and 10,000, the CPU time is 0.07 s; and for C between 10,000 and 100,000, the CPU time is 0.1 s. The increase in CPU time is due to the increase in the interval in which the roots are to be found.

The second program, ERLTABLE (Figure 2), generates a table of values of A for specified values of B and C. This program can be of value for applications in which fixed values of B are of interest to the user, and a certain range of C is to be considered. The present program generates a table of values of A for B = 0.001, 0.005, 0.01, 0.05, and 0.1, and C between 10,000 and 100,000 with channel increments of 2,000 (Figure 4).

This example demonstrates the flexibility afforded by the table building program:

a. The starting value of C (10,000 in this example) is chosen by the user to fit the application. (No computations of values of C less than 10,000 are required.)

b. The increment size for C is also a user option because no C step size is required by the building algorithm or the computational methodology.

```
CMS

->erlang
EXEC IMSLLIBS
GLOBAL TXTLIB FORTLIB FORTEEH IMSL81SP
LOAD ERLANG ( CLEAR START NODUP NOMAP
EXECUTION BEGINS...
WRITE B AND C
?
->.001 635.

MAX. LOAD IN ERLANG  =       577.5147

DO YOU WANT ANOTHER RUN ? YES OR NO
->yes
WRITE B AND C
?
->.1 433.

MAX. LOAD IN ERLANG  =       472.4085

DO YOU WANT ANOTHER RUN ? YES OR NO
->yes
WRITE B AND C
?
->.01 12345.

MAX. LOAD IN ERLANG  =     12397.1937

DO YOU WANT ANOTHER RUN ? YES OR NO
->yes
WRITE B AND C
?
->.012 33456.

MAX. LOAD IN ERLANG  =     33789.5501

DO YOU WANT ANOTHER RUN ? YES OR NO
->yes
WRITE B AND C
?
->.01 350400.

MAX. LOAD IN ERLANG  =    353841.9500

DO YOU WANT ANOTHER RUN ? YES OR NO
->yes
WRITE B AND C
?
->.034 650754.

MAX. LOAD IN ERLANG  =    673629.0109

DO YOU WANT ANOTHER RUN ? YES OR NO
->no
```

Figure 3. *Sample Run of Program ERLANG*

C	B=.001	B=.005	B=.01	B=.05	B=.1
10000	9831.6676	9948.6259	10031.2583	10506.9846	11101.1982
12000	11821.3146	11953.7296	12049.0741	12612.1470	13323.4063
14000	13812.1465	13959.5566	14067.3106	14717.3359	15545.6183
16000	15804.0512	15965.9261	16085.8546	16822.5420	17767.8329
18000	17796.8162	17972.7249	18104.6324	18927.7600	19990.0491
20000	19790.2390	19979.8634	20123.5933	21032.9865	22212.2665
22000	21784.3561	21987.2824	22142.7011	23138.2192	24434.4847
24000	23778.9306	23994.9359	24161.9289	25243.4568	26656.7036
26000	25773.9442	26002.7882	26181.2566	27348.6981	28878.9231
28000	27769.3422	28010.8113	28200.6683	29453.9424	31101.1429
30000	29765.0800	30018.9826	30220.1515	31559.1891	33323.3630
32000	31761.1206	32027.2837	32239.6964	33664.4378	35545.5834
34000	33757.4330	34035.6995	34259.2943	35769.6861	37767.8040
36000	35753.9912	36044.2172	36278.9399	37874.9398	39990.0248
38000	37750.7727	38052.8261	38298.6263	39980.1927	42212.2457
40000	39747.7581	40061.5170	40318.3492	42085.4465	44434.4668
42000	41744.9305	42070.2821	42338.1046	44190.7012	46656.6879
44000	43742.2754	44079.1146	44357.8892	46295.9567	48878.9092
46000	45739.7798	46088.0085	46377.7001	48401.2128	51101.1305
48000	47737.4320	48096.9567	48397.5346	50506.4695	53323.3520
50000	49735.2219	50105.9606	50417.3907	52611.7267	55545.5734
52000	51733.1403	52115.0101	52437.2664	54716.9843	57767.7950
54000	53731.1791	54124.1037	54457.1600	56822.2423	59990.0166
56000	55729.3307	56133.2381	56477.0700	58927.5007	62212.2382
58000	57727.5883	58142.4103	58496.9950	61032.7594	64434.4599
60000	59725.9460	60151.6179	60516.9339	63136.0184	66656.6816
62000	61724.3981	62160.8585	62536.8856	65243.2777	68878.9033
64000	63722.9395	64170.1299	64556.8492	67348.5372	71101.1251
66000	65721.5655	66179.4301	66576.8238	69453.7969	73323.3469
68000	67720.2717	68188.7576	68596.8086	71559.0568	75545.5687
70000	69719.0543	70198.1105	70616.8030	73664.3169	77767.7906
72000	71717.9095	72207.4874	72636.8063	75769.5771	79990.0124
74000	73716.8340	74216.8871	74656.8179	77874.8376	82212.2343
76000	75715.8245	76226.3081	76676.8372	79980.0981	84434.4562
78000	77714.8782	78235.7494	78696.8639	82085.3588	86656.6782
80000	79713.9922	80245.2099	80716.8974	84190.6196	88878.9001
82000	81713.1641	82254.6887	82736.9374	86295.8805	91101.1220
84000	83712.3913	84264.1847	84756.9835	88401.1416	93323.3440
86000	85711.6716	86273.6971	86777.0353	90506.4027	95545.5660
88000	87711.0034	88283.2252	88797.0925	92611.6639	97767.7880
90000	89710.3841	90292.7682	90817.1548	94716.9252	99990.0100
92000	91709.8120	92302.3255	92837.2220	96822.1866	102212.2320
94000	93709.2854	94311.8963	94857.2937	98927.4480	104434.4540
96000	95708.8027	96321.4800	96877.3698	101032.7096	106656.6760
98000	97708.3623	98331.0762	98897.4501	103137.9711	108878.8980
100000	99707.9626	100340.6842	100917.5342	105243.2328	111101.1201

Figure 4. *Sample Run of Program ERLTABLE*

From a practical viewpoint, if the application requires repetitive calculations of the allowable load, A, for a fixed blocking probability, B, it is more advantageous for the user to generate, prior to the application, a separate file containing a table of the offered loads corresponding to all numbers of circuits within a certain suitable target range (program ERLTABLE can be used here). Subsequently, this table, in conjunction with an efficient table search program, would be used to find the corresponding value of A for any number of circuits within this target range.

The table could be expanded into a multidimensional table encompassing a number of fixed blocking probabilities $B_1, B_2, \ldots, B_k$. The table search algorithm could be easily expanded to take into account these different blocking probabilities. Creating the offered load file, which is external to the application program, results in shorter running time, because the required values of offered load can be determined much more rapidly by repeatedly performing a file lookup than by repeatedly employing an iterative algorithm.

Conclusions

This paper introduced an interactive program that uses an algorithm for the direct calculation of Erlang load A, corresponding to any given grade B of service and channel size C. The following advantages are afforded by this program, compared to previous efforts in this area:

a. For given B and C, the program eliminates the need for calculation of A for smaller values of C. This feature is particularly helpful if the number of channels is large.

b. The program does not require prior building of tables for set values of B. This feature affords the user more flexibility and on-the-spot investigation of various options.

The paper also offers a program that generates a table of values of A for specified values of B and C. This program offers two advantages that contribute to its flexibility:

a. The table can be initiated from any arbitrary value of C, eliminating the need to start at $C = 1$.

b. The spacing of the desired successive values of C is a user choice that does not affect the algorithm used because no intermediate values of C are needed.

References

[1] A. K. Erlang, "Solution of Some Problems in the Theory of Probabilities of Significance in Automated Telephone Exchanges," *Post Office Electronics Engineers Journal*, No. 10, 1917, p. 189.

[2] G. D. Dill and G. D. Gordon, "Efficient Computation of Erlang Loss Functions," *COMSAT Technical Review*, Vol. 8, No. 2, Fall 1978, pp. 353–370.

[3] D. L. Jagerman, "Some Properties of the Erlang Loss Function," *Bell System Technical Journal*, Vol. 53, No. 3, March 1974, pp. 525–551.

[4] International Mathematical and Statistical Libraries, Inc., IMSL Library Reference Manual, Edition 8, Volume 3.

[5] B. Leavenworth, "Algorithm 25: Real Zeros of an Arbitrary Function," *Communications of the ACM*, Vol. 3, No. 11, 1960, p. 602.

[6] D. E. Muller, "A Method for Solving Algebraic Equations Using an Automatic Computer," *Mathematical Tables and Aids to Computations*, 10, 1956, pp. 208–215.

T. N. Shimi received a B.S. in 1966 and a Ph.D. in 1973 from the University of Iowa, both in mathematics. During a sabbatical leave from 1976 to 1977, he received an M.S. in operations research from Stanford University. In 1977, he was Senior Mathematical Consultant at General Electric Company, Nuclear Energy Division, where he worked on neutron flux, thermal transfer, and probabilistic fuel cycle problems. He joined the MITRE Corporation in 1979, where he worked on reliability and safety analysis of various air traffic control systems, as well as airspace and airport capacity and operations models. Since he joined COMSAT *in 1981, he has worked on statistical analysis and demand projections of DBS for Satellite Television Corporation. He has also participated in the development of the BEEFS1 (Bit Error Rate/Error Free Second) program applied to* INTELSAT *TDMA Links for use in data transmission networks. He has several publications in the areas of system reliability and fixed-point theory. Dr. Shimi is a member of the AMS and SSS.*

Young L. Park is the Manager of Analytic Software Systems, within Communication Services of World Systems Division. She is responsible for system design, analysis, development, and maintenance of software systems supporting various areas within World Systems Division. She received a B.S. degree in chemistry from Seoul National University, Seoul, Korea, in 1965 and a Ph.D. in theoretical chemistry from the University of Rochester, Rochester, New York, in 1969. Before joining COMSAT *in 1974, Dr. Park had worked for Martin Marietta Corporation in the development of software systems. She is a member of AMA and IEEE Computer Society.*

CTR Notes

Simple method for estimating atmospheric absorption at 1 to 15 GHz

D. V. ROGERS

(Manuscript received November 15, 1982)

Introduction

To obtain estimates of propagation impairments for system studies, it is often desirable to use simple, fast computational methods that require minimal site-specific meteorological data. Such a procedure has been developed for estimating atmospheric gaseous absorption at frequencies of 1 to 15 GHz and slant path elevation angles of 0° to 90°, using only frequency and elevation angle as input parameters. Analytic expressions are derived by curve fitting absorption data from the CCIR [1], assuming fixed values of surface water vapor concentration, ρ_s, and surface temperature, T_s. To illustrate the method, equations are obtained for values of ρ_s and T_s corresponding to two different standard atmospheric conditions.

Development of method

The method is based on the standard expression [1] for slant path attenuation by atmospheric gases:

$$A = \gamma_s r_a \,(\mathrm{dB}) \tag{1}$$

where γ_s is the specific attenuation (dB/km) at the earth surface and r_a the effective slant path length (km) for absorption by atmospheric water vapor and molecular oxygen, which account for essentially all of the observed

David Rogers is a Staff Scientist in the Propagation Studies Department at COMSAT Laboratories.

attenuation. In Figure 1, γ_s, as computed from CCIR expressions [1], is plotted versus frequency, f (GHz), for two standard sets of the relevant atmospheric parameters: surface water vapor concentration, ρ_s (g/m³), and surface temperature, T_s (°C). Curve A of Figure 1 represents global mean values of ρ_s and T_s: 11.1 g/m³ and 14.6°C, respectively. Curve B is based on values of ρ_s and T_s that are most often used for CCIR reference purposes: 7.5 g/m³ and 20°C, respectively. (This labeling convention will be used throughout this note.)

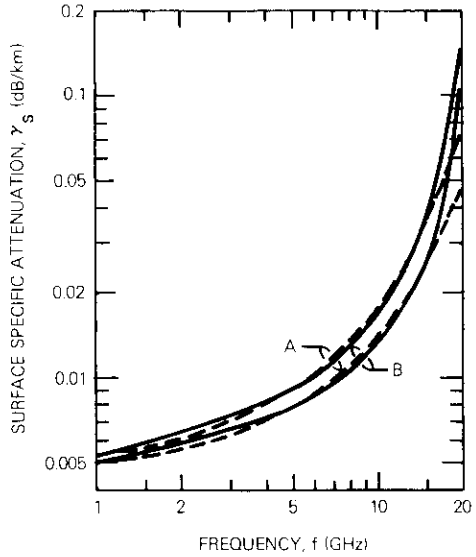

Figure 1. *Surface Specific Attenuation vs Frequency (solid lines) and Corresponding Curve Fits (dashed lines) for Global Mean Values of ρ_s and T_s (curves A) and for ρ_s = 7.5 g/m³, T_s = 20°C (curves B)*

Also shown in Figure 1 are the corresponding exponential curve fits obtained by fitting $\ln(\gamma_s)$ versus f for frequencies 4, 6, 12, and 15 GHz with the linear regression subroutines of a Texas Instruments TI-59 calculator. The fit for global mean surface conditions (curve A) is given by

$$\gamma_s = 0.00466e^{0.1362f} \tag{2a}$$

and for the other conditions (curve B) by

$$\gamma_s = 0.00442e^{0.1178f} \tag{2b}$$

Note that these regression fits agree acceptably with the CCIR curves over the frequency range $1 \leq f \leq 15$ GHz.

The expression used to compute the effective path length is [1]

$$r_a = \begin{cases} \dfrac{2H_a}{[\sin^2\theta + (2H_a/R)]^{1/2} + \sin\theta} & ,\theta \leq 10° \\ H_a/\sin\theta & ,\theta > 10° \end{cases} \tag{3}$$

with H_a being the "scale height" (km) of the atmosphere (*i.e.*, the equivalent height of an equally lossy atmosphere of uniform ρ_s and T_s), θ the path elevation angle, and R = 8500 km the effective earth radius after compensating for atmospheric refraction. The form of r_a for $\theta > 10°$ is an approximation, but the associated error is only about 0.5 percent even at the worst-case elevation angle (10°).

The scale height H_a is defined by the relationship

$$H_a = A_v/\gamma_s \text{ (km)} \tag{4}$$

where A_v is the total vertical (zenith) attenuation (dB) caused by gaseous absorption. Values of A_v obtained from the CCIR [1] are plotted versus frequency in Figure 2 for both sets (A and B) of atmospheric conditions. The corresponding

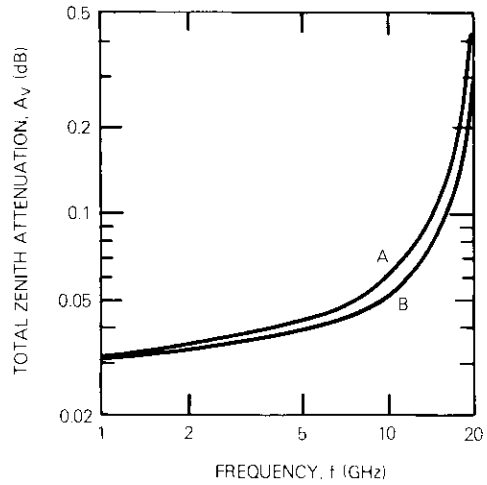

Figure 2. *Total Zenith Attenuation vs Frequency for Atmospheric Parameters A and B of Figure 1*

scale heights determined by combining the results of Figures 1 and 2 are presented in Figure 3. Also shown are the exponential curve fits to curve A:

$$H_a = 6.01e^{\,0.0485f} \tag{5a}$$

and to curve B:

$$H_a = 6.43e^{\,0.0487f} \tag{5b}$$

Again, these regressions appear acceptably accurate for $1 \leq f \leq 15$ GHz.

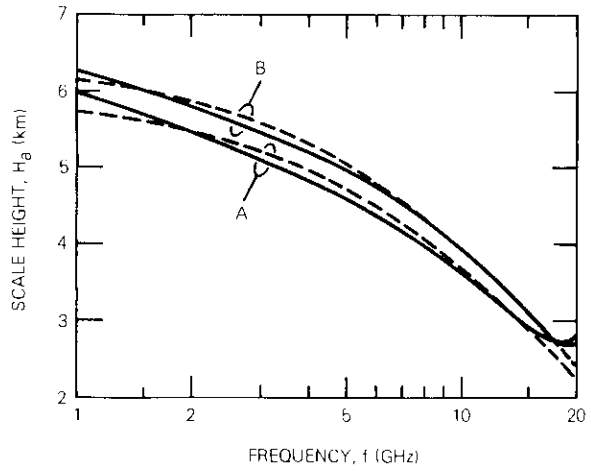

Figure 3. *Scale Height vs Frequency (solid lines) and Corresponding Curve Fits (dashed lines) for Atmospheric Parameters A and B*

By combining equations (1), (2a) or (2b), (3), and (5a) or (5b), the atmospheric attenuation caused by gaseous absorption can be estimated for either of the two sets of standard parameters. Estimates are presented and analyzed in the next section.

Results

To check the general behavior of the model, the atmospheric attenuation predicted for conditions given by $\rho_s = 7.5$ g/m^3 and $T_s = 20$°C are compared to CCIR results [1] for elevation angles of 0°, 5°, 10°, 20°, and 90° in Figure 4. Good agreement is obtained at all elevation angles over the 1- to 15-GHz frequency range, with the simple method underpredicting for $f \leq 5$ GHz, and overpredicting for $5 \leq f \leq 15$ GHz. Over the applicable range of the model,

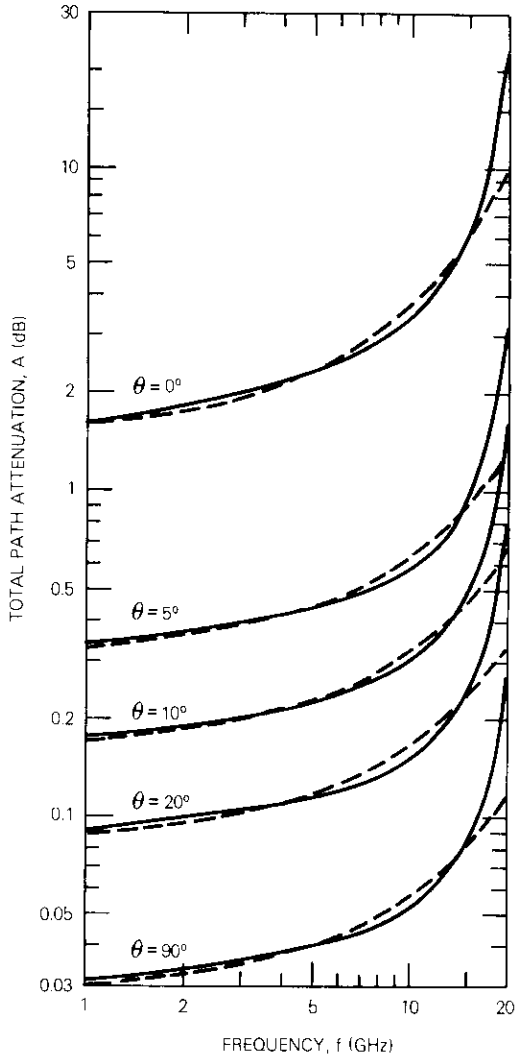

Figure 4. *Total Path Attenuation vs Frequency for Several Elevation Angles, with $\rho_s = 7.5$ g/m^3 and $T_s = 20$°C*

the largest deviations occur for $f \simeq 10$ GHz, being as large as 10 percent; however, the practical effects of these errors are small. As shown in Figure 4, above 15 GHz, the deviations become quite large because of the water vapor absorption line at 22.3 GHz.

A comparison of model estimates and measured data for 15 GHz is presented in Figure 5, mainly to verify the elevation angle behavior of the method. The data are based on measurements of Altshuler *et al.* [2], collected under various atmospheric conditions near Boston during 1975–1976. Also shown in Figure 5 are the attenuation estimates of the model for the parameter sets A and B. Curve A (global mean conditions) agrees well with the measurements made during cloudy conditions, while curve B agrees with the data for mixed conditions. Because the measured data are specific to a given location, the fact that the measurements agree with the model does not actually confirm the accuracy of the model (or of the CCIR data on which the model is based). The comparison does, however, reveal that the elevation angle behavior of the simple method, shown in equation (3), agrees well with at least one set of observations.

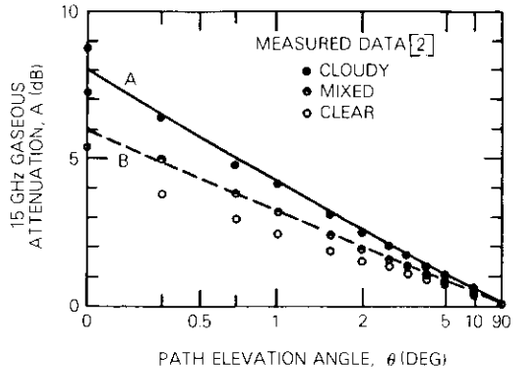

Figure 5. *Comparison Between Measured 15-GHz Gaseous Absorption and Predicted Attenuation for Atmospheric Parameters A and B*

Conclusion

A simple method for estimating attenuation by atmospheric gases has been developed, requiring as inputs only frequency (1–15 GHz) and path elevation angle (0°–90°). Equations were derived for two sets of standard atmospheric parameters, ρ_s and T_s. Over the quoted range of applicability of the model, the computed estimates are in good agreement with CCIR results. Furthermore, the elevation angle dependence of both the CCIR and simple methods is in excellent agreement with one set of measured data. The simple method appears quite useful for general systems calculations.

The simplicity of the model derives from curve fitting the quantities γ_s and H_a for fixed surface atmospheric conditions ρ_s and T_s. New regression fits will be required if ρ_s and T_s are changed. For applications in which actual ρ_s and T_s values are known or must be frequently varied, the more complicated CCIR approach [1] can be used.

References

[1] "Attenuation by Atmospheric Gases," *CCIR Report 719-1*, Recommendations and Report of the CCIR, Vol. V, Geneva, 1982, pp. 138–150.

[2] E. E. Altshuler, M. A. Gallop, Jr., and L. E. Telford, "Atmospheric Attenuation Statistics at 15 and 35 GHz for Very Low Elevation Angles," *Radio Science*, Vol. 13, 1978, pp. 839–852.

*Subjective equivalence of speech-correlated and stationary noise**

V. GUPTA, H. SUYDERHOUD, K. VIRUPAKSHA, AND M. ONUFRY

(Manuscript received December 2, 1982)

Introduction

The term S/N usually implies the independence of signal power S from continuously present stationary noise power N. However, the speech quality of a digital codec is characterized by the ratio of speech signal power to total quantizing distortion (noise) power, which in modern digital codecs depends on the signal level. Also, the perception of quantizing distortion is different from that of stationary noise at the same level. Since the ultimate success of a codec is determined by subjective quality perception by users, a subjective equivalent signal-to-noise ratio, $(S/N)_{eq}$, has been adopted by the CCITT [1].

In the past, considerable information has been reported on quality assessment in telephone communications, showing the effect of stationary noise on speech quality. By injecting noise into experimental voice circuits used for subjective evaluation, the familiar S/N ratio is obtained and expressed by the term dB(*I*).

V. Gupta is a Member of the Technical Staff of the Signal Processing Laboratory at COMSAT Laboratories.

H. Suyderhoud is Assistant to the Executive Director of Communications Technology, COMSAT Laboratories.

K. Virupaksha is a Member of the Technical Staff of the Signal Processing Laboratory at COMSAT Laboratories.

M. Onufry is Manager of Voice Band Processing in the Signal Processing Laboratory at COMSAT Laboratories.

This note describes the results of a laboratory experiment that subjectively relates the effect of speech-correlated noise expressed in dB(Q) to that of stationary noise, expressed in dB(I), when quality is judged to be equal. Similar results obtained by other laboratories in the United States and abroad confirm the importance of such data for assessing digital codecs.

The Youden Square experimental design was applied to determine the subjectively equivalent effect of speech perturbed by stationary noise and by noise correlated with the speech. Seven levels of stationary noise and six levels of speech-correlated noise were used to obtain a statistical relationship between the two types of noise. Both trained and untrained groups of listeners were used, and their test results were analyzed separately. Regression analysis revealed that the two regression curves for trained and untrained listeners can best be modeled by second-order polynomials, and that they both fall within the range of curves reported in the literature. It was also found that for a given level of stationary noise, trained listeners will tolerate a higher level of speech-correlated noise than untrained listeners.

Youden square

Details of the use of the Youden Square technique to assess the quality of processed speech samples can be found in Reference 2. The technique, as applied for the present purpose, is briefly described here for a 13 × 4 Youden Square (the choice of 13 and 4 is a necessary constraint resulting from the statistical requirements of balanced incomplete block designs) [3], [4].

Thirteen speech samples were selected; 7 had known amounts of stationary noise, and the remaining 6 had known amounts of speech-correlated noise. The mixture of 13 samples was randomized and recorded in groups of 4 as required by the Youden Square format. A group is referred to as a block, and 13 blocks were needed to form a 13 × 4 evaluation unit called a Youden Square.

The 13 4-sample blocks constitute a balanced set in that each of the 78 pairs of samples, 13 samples taken two at a time, appears an equal number of times, such as once per block in this case. Moreover, each of the 13 conditions appears as a first, second, third, and fourth sample in a block. The rectangular 13 × 4 array of blocks is one example of a Youden Square. It was derived by Youden from a full 13 × 13 (usually $N \times N$) array called a "Latin square" [5]; hence, it is known as a Youden Square.

Each of the 13 blocks of 4 prerecorded speech samples is evaluated subjectively by requiring subjects to rank order each sample within a block (1 for most preferred, to 4 for least). Each block, that is, a group of 4 speech samples, is played back twice to allow subjects to confirm their preferences. A subject is required to evaluate several blocks but generally not all.

The 13 samples are designated by the letters A to M; then after completion of a square, each letter will be scored 4 times with a rank, R, of 1, 2, 3 or 4 each time. The rank mean, $\overline{R}$, can be formally calculated by simply averaging scores. For a perfect rank order, the mean rank values would be scored

respectively, as 4/4, 5/4, . . ., 16/4, that is, in the range of 1 to 4 (the associated letters are not necessarily in alphabetical order). Alternatively, if no ranking were possible, all mean rank values would be nearly equal. A statistical variance ratio called the coefficient of concordance W, calculated for each completed Youden Square, determines whether the obtained ranking was meaningful (statistically significant). Because a meaningful ranking is expected, if not essential, the coefficient of concordance, W, is only a first measure to ensure that the experiment is functioning correctly. Three or 4 completed squares usually yield a highly significant ranking.

The mixture of conditions with stationary noise is chosen to span the perceived quality of conditions with speech-correlated noise. A least-squares curve is fitted through the obtained mean rank values $\overline{R}$ *vs* S/N dB(I) of the reference conditions. The $(S/N)_{eq}$ values of the dB(Q) conditions are then obtained by mapping their mean ranks on the curve as shown in Figure 1.

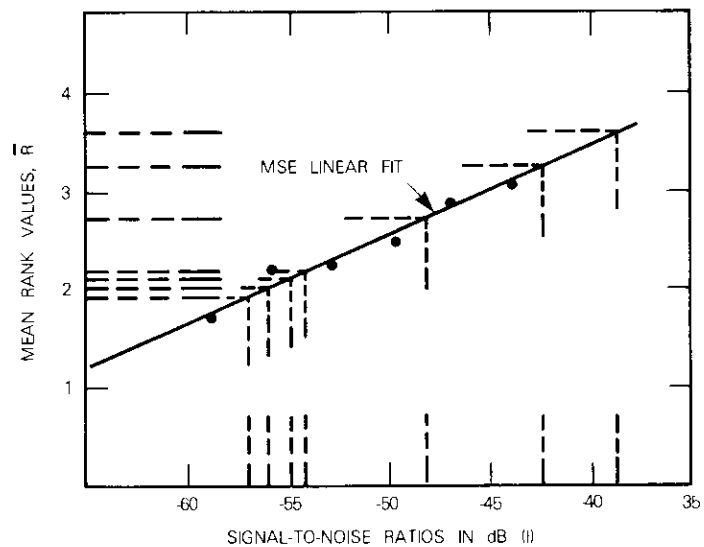

Figure 1. *Example of Results of Youden Square Rank Order Experiment*

The reliability of this procedure can be confirmed by its success in reproducing the same values under different combinations of conditions. Even though rank means do not qualify theoretically as statistical variates, the validity of the curve fitting can be statistically justified.

The success of the technique largely depends on the specific details of the test administration procedure briefly described below.

Selection of signal-to-noise ratio range for reference conditions

To select the range of reference noise conditions, expert listening tests are performed to determine the reference samples for the experiment. This necessity arises because the subjective results of the unknown conditions must be within those of the reference conditions to avoid the need for extrapolated results.

In the present study, the range of dB(Q) values was selected according to the CCITT recommendations and then several trial experiments were conducted to match the range of dB(I). The specific dB(Q) and dB(I) values chosen are described next.

Generation of source material

To hold the input source constant and thereby eliminate its contribution as a source of error, a source tape is prepared rather than using live talkers. The talker's voice is recorded using a 500-type telephone handset and the signal is passed through an artificial line to simulate a local loop. The tape is played into the computer and digitized at the appropriate sampling rate. The digitized source material is used to create the processed speech samples and the reference speech samples, all of which are stored on the computer.

In the present experiment, a sentence spoken by a female talker, "Add salt before you fry the egg," was bandlimited to the telephone bandwidth (*i.e.*, 300–3,400 Hz), digitized at a sampling rate of 8,000 Hz, and stored on the computer. A 13 × 4 Youden Square with seven known and six unknown conditions was used. For the known conditions, seven speech samples with speech-to-stationary noise ratios of 5, 12, 19, 26, 33, 40, and 47 dB(I) were used. These samples were created on the computer by adding appropriate levels of Gaussian noise to the test sentence digitized earlier. The 6 unknown conditions were represented by 6 samples having speech-to-speech correlated noise ratios of 6, 10, 14, 18, 22, and 26 dB(Q). Again, these samples were created on the computer by adding appropriate levels of speech-correlated noise to the test sentence. As described earlier, speech-correlated noise is nonstationary and proportional to the "short-term" speech power level.

Preparation of instructions

A data recording form with instructions was designed for the test subjects. Additional instructions were given to assure the subjects that they were not being tested and to explain the format of the speech samples they would be evaluating.

Test location

To increase the efficiency of data collection, subjects are required to participate in the experiment in groups of 4. A suitable environment is provided, including comfortable surroundings and elimination of hallway distractions. The test subjects are seated in separated but open booths.

Results of equivalence between speech-correlated noise and stationary noise

By creating the necessary speech samples for determining the equivalence between speech-correlated noise and stationary noise, 13 blocks of 4 speech samples chosen from the 13 conditions were created on the computer. An automated procedure was used to conduct the subjective listening experiment. Two sets of subjects, trained and untrained, were used for the subjective test.

The results of the experiment in Figure 2 show that both trained and untrained subjects rate speech-correlated noise [in dB(Q)] numerically less severe than injected stationary noise [in dB(I)] over the range of interest [dB(Q) > 10]. This is a universal result also found in comparable tests, as

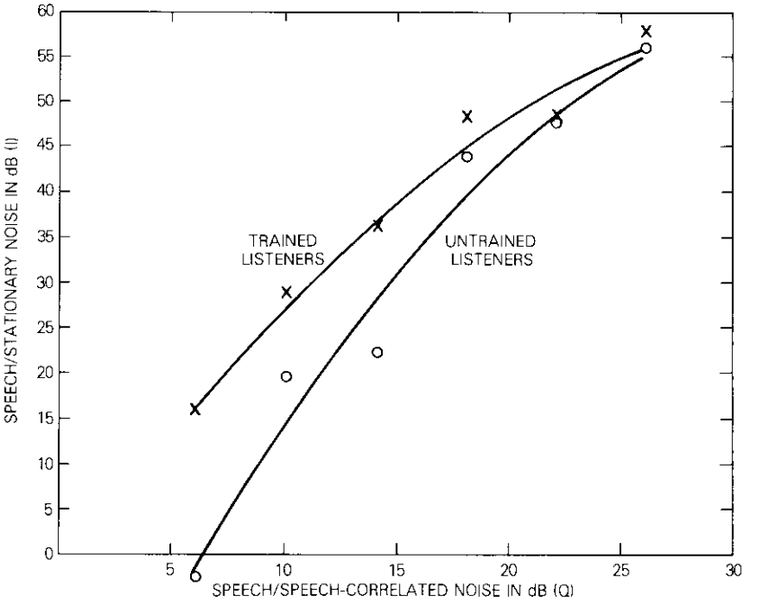

Figure 2. *dB(Q) vs dB(I)*

shown in both Figures 3 and 4. However, the trained listeners were more "generous" in this judgment than the untrained listeners. This difference was similarly experienced in tests conducted by NTT (Figure 3). Note that in the context of this paper, SNR_s represents speech-to-stationary noise ratio in dB(I), SNR_c represents speech-to-speech-correlated noise ratio in dB(Q).

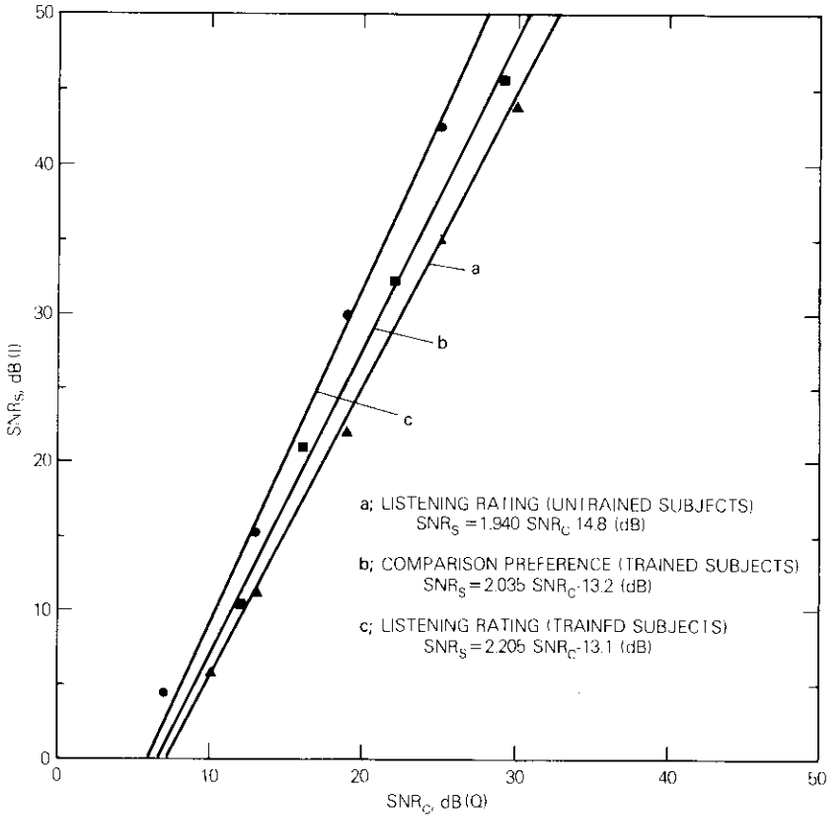

Figure 3. *SNR$_s$ vs SNR$_c$ [6]*

The curves relating dB(Q) to dB(I) values were best fitted by second-order polynomials, which are convex toward the dB(I) axis. For comparison, the results of COMSAT's untrained subjects were plotted with the family of similar data published in a CCITT contribution (in Study Group XII), and shown in Figure 4. Even though COMSAT's results fall within the boundaries of the entire population of curves, there are important differences. The most noted is in slope for the low dB(Q) range, where the COMSAT slope is significantly steeper. This may be caused by the evaluation technique of the Youden Square procedure, which confronts subjects with a direct comparison of test conditions. In contrast, other laboratories employ "absolute" judgment (excellent, good, fair, poor, etc.) for relating dB(Q) and dB(I) values. Further analysis would be required to substantiate this hypothesis.

Another difference is that the COMSAT curve tends toward a dB(I) asymptote (horizontal) for higher values of dB(Q). This is a logical consequence of hearing perception, that is a stationary noise at a given low level may not be perceptible

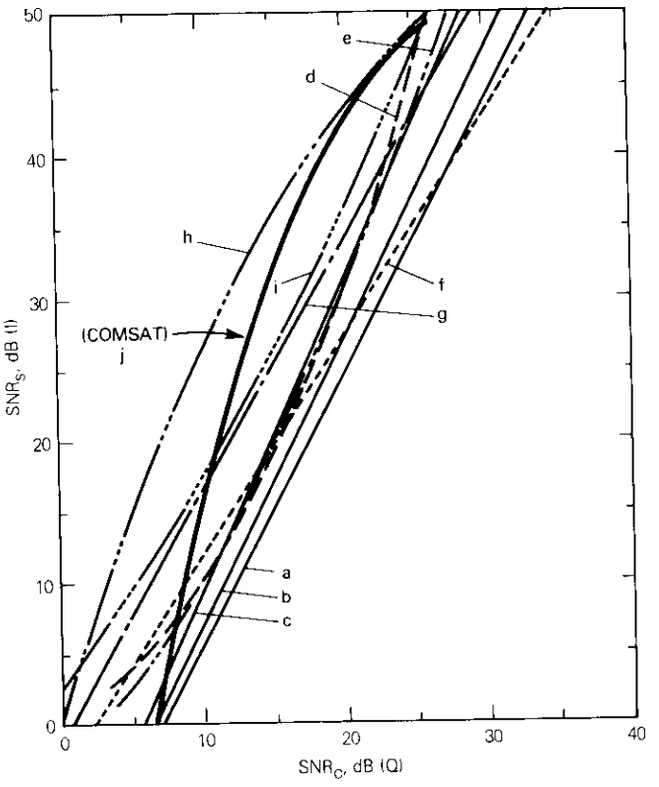

a; NTT, LISTENING RATING — SNR$_s$ = 1.940SNR$_c$ − 14.8 [dB(I)]

b; NTT, COMPARISON PREFERENCE (TRAINED SUBJECTS) — SNR$_s$ = 2.035SNR$_c$ − 13.2 [dB(I)]

c; NTT, LISTENING RATING (TRAINED SUBJECTS) — SNR$_s$ = 2.205SNR$_c$ − 13.1 [dB(I)]

d; BT, COMPARISON PREFERENCE — SNR$_s$ = 0.0602SNR$_c^2$ + 0.2850SNR$_c$ + 1.07 [dB(I)]

e; AT&T, COMPARISON PREFERENCE — SNR$_s$ = 0.0270SNR$_c^2$ + 1.2600SNR$_c$ − 5.08 [dB(I)]

f; NTA, COMPARISON PREFERENCE — SNR$_s$ = 1.623SNR$_c$ 4.70 [dB(I)]

g; NTA, LISTENING RATING — SNR$_s$ = 1.750SNR$_c$ − 1.10 [dB(I)]

h; BNR, COMPARISON PREFERENCE — SNR$_s$ = −0.044SNR$_c^2$ + 3.0066SNR$_c$ + 0.25 [dB(I)]

i; BNR, LISTENING RATING — SNR$_s$ = 0.0219SNR$_c^2$ + 1.2183SNR$_c$ + 2.97 [dB(I)]

j; COMSAT, RANK ORDERING (UNTRAINED SUBJECTS) — SNR$_s$ = .052SNR$_c^2$ + 3.645SNR$_c$ − 4.428 [dB(I)]

Figure 4. *SNR$_s$ vs SNR$_c$ by Various Organizations [6]*

and neither are increasing values of dB(Q). It is therefore somewhat questionable that only one other laboratory (h, BNR of Figure 4) exhibits this otherwise expected behavior in its results.

Conclusion

This study provides COMSAT with an important data base to allow assessment of digital codecs in terms of CCITT recommended dB(Q) standards. It also demonstrates that the Youden Square technique is a useful method for obtaining the quantitative data needed for comparison.

References

[1] CCITT Temporary Document No. 79, Meeting of Study Group XII, (Geneva), June 8–11, 1982.
[2] H. G. Suyderhoud, M. Onufry, and J. Sennott, "Subjective Performance Assessment of Delta Modulation in Terms of Equivalent Noise at 16, 24, 32, and 40 kbit/s," in *Proceedings 4th International Conference on Digital Satallite Communications,* October 23–25, 1978.
[3] D. R. Cox, *Planning of Experiment,* New York: John Wiley and Sons, 1958, Ch. 11.3.
[4] M. Kendall, *Rank Correlation Methods,* U.K.: J. W. Arrowsmith, Ltd, Bristol, 1975, Ch. 1–6.
[5] O. L. Davies, "Design and Analysis of Industrial Experiments," Oliver and Boyd, London, U.K., 1960, Ch. 15.
[6] CCITT Contribution COM XII, No. 24E.

Communications performance specifications of the INTELSAT V with maritime communications subsystem

J. MARTIN, D. ARNSTEIN, AND C. ADAMS

(Manuscript received December 27, 1982)

Introduction

Several important changes and additions to the communications performance specifications for flight models 5 through 9 of the INTELSAT V are being implemented. The modifications to the spacecraft include the provision of a Maritime Communications Subsystem (MCS) and a few changes in the international fixed services communications payload [1], [2].

This note summarizes the communications performance specifications for the MCS and modifications to the fixed international communications payload of flight models 5 through 9 of the INTELSAT V spacecraft.

The specifications for these modifications were prepared by the INTELSAT Executive Organ Staff and approved by the INTELSAT Board of Governors.

General characteristics of the MCS

The MCS is incorporated on board flight models 5 through 9 of the INTELSAT V spacecraft to provide a sufficient space segment allocation to INMARSAT for its maritime communications services. The MCS consists of two transponders. One, known as the L- to C-band transponder, receives signals from ship terminals at L-band and retransmits them to shore stations at C-

J. E. Martin is Spacecraft Consulting Engineer in World Systems Division, Communications Services.

D. Arnstein is Manager of Communications Systems in World Systems Division, Communications Services.

C. Adams is Systems Evaluation Analyst in World Systems Division, Communications Services.

band; the other, known as the C- to L-band transponder, receives signals at C-band from shore stations and transmits them to ship terminals at L-band.

The total dry mass of the INTELSAT V spacecraft must not be increased by more than 40 kg after incorporating an on-board MCS. In addition, the MCS-equipped spacecraft has been configured so that the satellite remains compatible for launch on the Ariane and Atlas-Centaur launch vehicles.

The MCS has enough redundancy to provide a total estimated probability of survival of 0.97 after 7 years. The MCS is incorporated into the spacecraft so that failure of the MCS or in the deployment of its antennas does not interfere with the successful operation of the remainder of the spacecraft.

Modes of operation of MCS-equipped INTELSAT V spacecraft

Any MCS-equipped INTELSAT V spacecraft is capable of operating in any of the following modes during its entire 7-year life, including periods of sun eclipse:

a. the L-band amplifier in a high-power mode with all 14/11-GHz equipment off,

b. the L-band amplifier in a low-power mode with channels (7–12) in the east and west spot beams off and either channels (1–2) or channels (5–6) in the east and west spot beams off,

c. all 14/11-GHz channels fully operational and the MCS off.

It is possible to switch from one mode to another by ground command. After switching, the chosen mode will be operational within 5 minutes and will meet all specification requirements within 30 minutes.

The power required to operate the MCS, including its thermal control equipment, in either of the first two modes does not exceed the DC power made available by switching off the allowable 14/11-GHz equipment.

MCS coverage and frequency bands

In all of its transmit and receive frequency bands, the MCS provides coverage of the full earth disk visible from synchronous orbit. These coverages are achieved in the presence of all spacecraft pointing errors in addition to an attitude control bias of $\pm 2.0°$ in pitch and $\pm 0.2°$ in roll.

The C- to L-band transponder operates over 7.5 MHz in each band, *i.e.*, over a receive band from 6,417.5 to 6,425.0 MHz and a transmit band from 1,535.0 to 1,542.5 MHz. The L- to C-band transponder operates over 8.0 MHz in each band, *i.e.*, over a receive band of 1,636.5 to 1,644.5 MHz and a transmit band from 4,192.5 to 4,200.5 MHz.

Overall MCS communications performance specifications

This section summarizes the link performance parameters, nonlinear channel performance specifications, filter requirements, and miscellaneous specifications of the MCS antennas, receivers, transmitters, and filters.

LINK PERFORMANCE PARAMETERS

Major performance parameters of the two transponders of the MCS are given in Table 1. In addition to these link performance parameters, the gain of the C- to L-band transponder is sufficient to provide a useful per-carrier e.i.r.p. of at least 17.8 dBW within the defined coverage area when the transponder is illuminated by 2 to 30 carriers in the high-power output mode or by 2 to 15 carriers in the low-power output mode, each carrier having a flux density of -105.8 dBW/m^2. A 7.5-dB gain step, switchable by ground command, permits a useful per-carrier e.i.r.p. of at least 17.8 dBW when the C- to L-band transponder is illuminated by 2 to 30 carriers in the high-output-power mode or by 2 to 15 carriers in the low-output-power mode, each carrier having a flux density of -98.3 dBW/m^2.

TABLE 1. POLARIZATION PERFORMANCE, RECEIVE G/T, TRANSMIT E.I.R.P., AND SATURATION FLUX DENSITIES FOR THE MCS

Polarization Performance (voltage axial ratio)	
C-Band Transmit (left-hand circularly polarized)	1.05
C-Band Receive (right-hand circularly polarized)	1.05
L-Band Transmit (right-hand circularly polarized)	1.6
L-Band Receive (right-hand circularly polarized)	1.6
Receive System G/T (dB/K)	
C-Band Receive	−17.6
L-Band Receive	−15.0
e.i.r.p. (dBW)	
C-Band Transmit[a]	20.0
L-Band Transmit[b]	
High-Power Mode	32.6
Low-Power Mode	29.6
Saturation Flux Density (dBW/m^2)	
L- to C-Band Transponder[c]	
High Gain Step	-98.0 ± 2
Low Gain Step	-94.0 ± 2

[a] Single-carrier saturated e.i.r.p.

[b] Useful carrier e.i.r.p. when transponder is transmitting 10 equal amplitude and unmodulated carriers.

[c] Single-carrier saturation flux density.

NONLINEAR CHANNEL PERFORMANCE SPECIFICATIONS

The specifications regarding phase linearity, AM/PM transfer characteristics, intelligible crosstalk ratio, and amplitude linearity for the L- to C-band transponder are shown in Table 2. Table 3 gives specifications for phase linearity, AM/PM transfer characteristics, and intelligible crosstalk ratio for the C- to L-band transponder. For this transponder, when the C-band receive

TABLE 2. NONLINEAR PERFORMANCE SPECIFICATIONS FOR THE MCS L- TO C-BAND TRANSPONDER

a. Phase Linearity

Relative Flux Density[a] (dB)	Output Transmission Phase Shift (deg)	AM/PM Transfer Coefficient (deg/dB)
0	46	8
−3	38	9
−6	28	9
−9	18	8
−12	12	5
−14	9	3
< −14	—	3

b. Intelligible Crosstalk Ratio (dB)

Relative Flux Density[a] (dB)	Location of Modulated Carrier Center Frequency[b]: Within Center 70% of Usable Bandwidth	Location of Modulated Carrier Center Frequency[b]: Over 100% of Usable Bandwidth
0 to −14	$-146 + 20 \log f_m$	$-136 + 20 \log f_m$
< −14	$-152 + 20 \log f_m$	$-142 + 20 \log f_m$

c. Amplitude Linearity

Relative Flux Density per Carrier[c] (dB)	Maximum Intermodulation-to-Carrier Ratio[d] (dB)
−3	−10
−10	−15
−17	−26

[a] Defined as flux density below that which produces single-carrier saturation.
[b] Modulation frequency, f_m, expressed in Hz.
[c] Flux density illuminating L-band receive antenna for each of two equal amplitude carriers, below the flux density which produces single-carrier saturation.
[d] Maximum level of third-order intermodulation products relative to the level of the RF carriers, measured at the output of the L- to C-band transmission channel.

antenna is illuminated by white noise extending over the 7.5-MHz receive band with an empty slot (at least 4 kHz but less than 100 kHz wide) at band center, and the noise-producing useful e.i.r.p. is less than or equal to those shown in Table 1, the ratio of the noise power density to the power density in the center slot exceeds 11.0 dB.

FILTER REQUIREMENTS

The out-of-band response specifications for both MCS transponders are given in Table 4. In addition, the total group delay measured between the input and output of each transponder does not vary more than 100 ns from the delay at the center of the respective bands.

TABLE 3. NONLINEAR PERFORMANCE SPECIFICATIONS FOR THE MCS C- TO L-BAND TRANSPONDER

a. Phase Linearity

Total Flux Density (dBW/m²): High Gain	Total Flux Density (dBW/m²): Low Gain	Output Transmission Phase Shift (deg)	AM/PM Transfer Coefficient (deg/dB)
−91	−83.5	46	10
−94	−86.5	38	9
−97	−89.5	28	9
−100	−92.5	18	8
−103	−95.5	12	5
−105	−97.5	9	3
< −105	< −97.5	—	3

b. Intelligible Crosstalk Ratio (dB)

Total Flux Density (dBW/m²): Low Gain	Total Flux Density (dBW/m²): High Gain	Location of Modulated Carrier Center Frequency*: Within Center 70% of Usable Bandwidth	Location of Modulated Carrier Center Frequency*: Over 100% of Usable Bandwidth
−83.5/−97.5	−91.0/105.0	$-146 + 20 \log f_m$	$-136 + 20 \log f_m$
97.5	105.0	$-152 + 20 \log f_m$	$-142 + 20 \log f_m$

* Modulation frequency, f_m, expressed in Hz.

TABLE 4. OUT-OF-BAND RESPONSE SPECIFICATIONS FOR THE MCS TRANSPONDERS

Transponder	Out-of-Band Response Parameter	Frequency from Band Center (MHz)	Maximum Out-of-Band Response (dB)
C- to L-Band	Receive	7.5	−24
		14.5	−40
	Transmit*	25.0	−17
		35.0	−34
L- to C-Band	Receive	7.5	−24
		14.5	−40
	Transmit*	25.0	−20
		35.0	−40

* Measured between the input of the final amplifier and the output of the channel.

MISCELLANEOUS SPECIFICATIONS

Several additional specifications that are important to the satisfactory performance of the MCS are given in Table 5.

TABLE 5. ADDITIONAL PERFORMANCE SPECIFICATIONS

	TRANSPONDER	
	L- TO C-BAND	C- TO L-BAND
Spurious Outputs[a]	−55 dBW	−45 dBW
Frequency Stability		
Over Lifetime Including Initial Tolerances and Eclipse Effects	±10 parts in 10^6	±10 parts in 10^6
Over One Month Excluding Eclipse Effects	±10 parts in 10^7	±10 parts in 10^7
Gain Flatness[b]		
Over 90% of Usable Bandwidth	1.0 dB	1.0 dB
Over 100% of Usable Bandwidth	1.3 dB	1.3 dB
Gain Slope[c]		
Over 90% of Usable Bandwidth	0.7 dB/MHz	0.7 dB/MHz
Over 100% of Usable Bandwidth	1.1 dB/MHz	1.1 dB/MHz
Overdrive Capability[d]	30 dB	30 dB

[a] In any 4-kHz band measured at the input to the transmit antenna.
[b] Down-link e.i.r.p. must not vary by an amount greater than that shown.
[c] Measured over the total transmission channel including antennas.
[d] Without subsequent degradation of performance or lifetime.

Modifications to INTELSAT V flight models 5 through 9

Flight models 5 through 9 of the INTELSAT V spacecraft have been designated to carry MCS packages. For these flight models, there have been a few important changes in the international communications payload that are not related to the incorporation of the MCS. On flight models 1 through 4, the up-link of channel (7–8) in the hemispheric beams is split into two channels, (7) and (8) [1]. On flight models 5 through 9, channels (7) and (8) in each hemispheric beam are combined into a single channel, channel (7–8), on both the up-link and down-link.

A second major change in flight models 5 through 9 is that the saturation flux densities for all 6-GHz up-link beams have been decreased by 2.6 dB, and all 6-GHz receive system G/T values have been increased by 2.6 dB relative to those for flight models 1 through 4. The saturation flux densities and receive system G/T values for flight models 5 through 9 are shown in Table 6.

It should be noted that two important changes in the communications performance specifications for INTELSAT V flight models 1 through 4 were adopted after Reference 1 was published. The voltage axial ratio for the global beam was improved from 1.09 to 1.05 (Table 3, Reference 1). Also, an extra high gain step of 7.5 dB was incorporated in all 6/4-GHz transponders (Table 4, Reference 1). All communications performance parameters for flight models

TABLE 6. SATURATION FLUX DENSITY AND RECEIVE SYSTEM G/T FOR INTELSAT V, FLIGHT MODELS 5 THROUGH 9

a. Saturation Flux Density (dBW/m²)

UP-LINK BEAM	EXTRA HIGH GAIN[a]	HIGH GAIN[b]	LOW GAIN
6 GHz, All Beams			
Channels (1–2), (3–4), (5–6), (7–8)	−82.1	−74.6	−67.1
Channels 9, 10, 11, 12	−85.1	−77.6	−70.1
14 GHz, East Spot			
Channels (1–2), (5–6), (7–8), (7–12)		−77.0	−72.0
14 GHz, West Spot			
Channels (1–2), (5–6), (7–8), (7–12)		−80.3	−75.3

b. Receive System G/T (dB/K)

6 GHz, Global	−16.0
6 GHz, Hemispheric	−9.0
6 GHz, Zone	−6.0
14 GHz, East Spot	0.0
14 GHz, West Spot	3.3

[a] The switch from the high gain to the extra high gain state can be accomplished on a beam-by-beam basis only.
[b] The switch from the low gain to the high gain state can be accomplished on a channel-by-channel basis.

5 through 9 of the INTELSAT V that are not detailed in this note remain unchanged from the values given in Reference 1.

References

[1] J. C. Fuenzalida, P. Rivalan, and H. J. Weiss, "Summary of the INTELSAT V Communications Performance Specifications," *COMSAT Technical Review*, Volume 7, No. 1, Spring 1977, pp. 311–326.

[2] N. J. Barberis and C. F. Hoeber, "Design of the Advanced INTELSAT V Spacecraft," AIAA 9th Communications Satellite Systems Conference, 1982.

Communications performance specifications of the INTELSAT V-A

J. MARTIN, D. ARNSTEIN, AND C. ADAMS

(Manuscript received December 27, 1982)

Introduction

The need for several INTELSAT V class spacecraft beyond flight model 9 led to a contract with FACC for the manufacture of INTELSAT V-A spacecraft. Although the INTELSAT V-A incorporates many of the major concepts and communications performance specifications of the INTELSAT V, there are several important differences between the two spacecraft. This note summarizes the differences between the INTELSAT V and V-A spacecraft and the performance specifications of the INTELSAT V-A communications payload.

The specifications for these modifications were prepared by the INTELSAT Executive Organ Staff and approved by the INTELSAT Board of Governors.

Major differences between the INTELSAT V and INTELSAT V-A spacecraft

There will be several important differences between the INTELSAT V and INTELSAT V-A spacecraft. The introduction and expansion of TDMA into the INTELSAT system will require that the communications subsystem of the INTELSAT V-A be fully compatible for use as a repeater of TDMA signals. This

---

J. E. Martin is Spacecraft Consulting Engineer in World Systems Division, Communications Services.

D. Arnstein is Manager of Communications Systems in World Systems Division, Communications Services.

C. Adams is Systems Evaluation Analyst in World Systems Division, Communications Services.

compatibility will require a change in the saturation flux density and gain step for those channels that may be used for TDMA traffic.

Another important difference between the INTELSAT V and V-A spacecraft will be the addition of a second global beam and two spot beams in the 6/4-GHz band of the INTELSAT V-A. The two new spot beams are intended to enhance the capabilities for providing domestic services through the INTELSAT system. Two changes in the zone beams for the INTELSAT V-A are also intended to enhance domestic service capability: channel (9) will be added to both zone beams, and the coverage configurability of the zone beams will be modified.

General characteristics of the INTELSAT V-A are presented in the following sections, along with communications subsystem performance specifications that differ from those for the INTELSAT V spacecraft.

General characteristics of the INTELSAT V-A spacecraft

The INTELSAT V-A spacecraft will be an active repeater, body-stabilized, communications satellite in geosynchronous orbit. It will be compatible with placement into transfer orbit by the Ariane 2 or Atlas-Centaur launch vehicle. This requirement will constrain the spacecraft mass, including in-orbit propellant, apogee motor, and spacecraft adapter assembly (less the apogee motor destruct unit), to 1,950 kg for launch by the Ariane 2 and to 2,141 kg for launch by the Atlas-Centaur.

The estimated probability of survival of the spacecraft with more than 65 percent of its RF channels operational in each coverage area must be at least 0.99 after two months and 0.74 after seven years, including eclipse periods.

All communications subsystem specifications must be met under the worst-case pointing error expected of the spacecraft or when the spacecraft is subjected to a worst-case combined pointing error of $\pm 0.2°$ in pitch, $\pm 0.2°$ in roll, and $\pm 0.4°$ in yaw.

Coverages, channelization, and connectivity requirements of the INTELSAT V-A

FREQUENCY BANDS AND BEAM COVERAGES

The INTELSAT V-A will operate in the 6/4- and 14/11-GHz bands. The up-link in the 6/4-GHz band will be from 5,925 to 6,425 MHz; the down-link will be from 3,700 to 4,200 MHz. The 14/11-GHz band will consist of 14,000 to 14,500 MHz on the up-link and 10,950 to 11,200 MHz and 11,450 to 11,700 MHz on the down-link. Fourfold frequency reuse in the 6/4-GHz band and twofold frequency reuse in the 14/11-GHz band will be accomplished by spatial and/or polarization isolation of beams.

The reuses in the 14/11-GHz band will be provided by two spot beams, steerable by ground command. The 6/4-GHz band will have two hemispheric beams and two zone beams, as well as two orthogonally polarized global beams on both the up-link and down-link and two orthogonally polarized spot beams on the down-link. Switching between the global or spot beams on the down-link will permit any two orthogonally polarized beams to be operational at the same time. The two 4-GHz down-link spot beams will be steerable so that the edge of coverage can be positioned anywhere on the visible earth disk. However, the coverage chosen for the 4-GHz down-link spot beams will depend on the coverage chosen for the 14/11-GHz spot beams. That is, the center of the 14/11-GHz east spot beam will be approximately 8.2° north and 1.1° east, in spacecraft coordinates, of the center of the 4-GHz east spot beam, while the center of the 14/11-GHz west spot beam will be approximately 8.0° north and 2.8° west, in spacecraft coordinates, of the center of the 4-GHz west spot beam. The coverage areas of the 4-GHz spot beams will be circular with diameters of 5° measured in spacecraft coordinates. Table 1 summarizes the beam coverages and their corresponding polarizations.

TABLE 1. INTELSAT V-A COVERAGE BEAMS

		POLARIZATION	
BAND	COVERAGE	UP-LINK	DOWN-LINK
6/4 GHz	Global A	LHC[a]	RHC[b]
	Global B	RHC	LHC
	West Hemispheric	LHC	RHC
	East Hemispheric	LHC	RHC
	Zone 1	RHC	LHC
	Zone 2	RHC	LHC
	Spot A[c]		RHC
	Spot B[c]		LHC
14/11 GHz	East Spot	Linear[d]	Linear
	West Spot	Linear	Linear

[a] Left-hand circular.
[b] Right-hand circular.
[c] Spot A and Spot B used on the down-link only.
[d] The polarization of the east spot beam will be orthogonal to the west spot beam.

The coverage areas required for the 6/4-GHz zone and hemispheric beams of the INTELSAT V-A spacecraft in each of the three ocean regions will be the same as those for INTELSAT V, as shown in Figure 1 [1]. The spacecraft is to be designed so that the configuration is switchable by ground command to meet coverage requirements for any of the three ocean regions. In addition, the zone beams must be reconfigurable by ground command so that the zone 1 coverage orientation as shown in Figures 1a and 1b can be used with the zone 2 coverage orientation as shown in Figure 1c. Figure 1d shows the range of steerability of the east 14/11-GHz and 4-GHz spot beams, and Figure 1e shows the range of steerability of the west 14/11-GHz and 4-GHz spot beams.

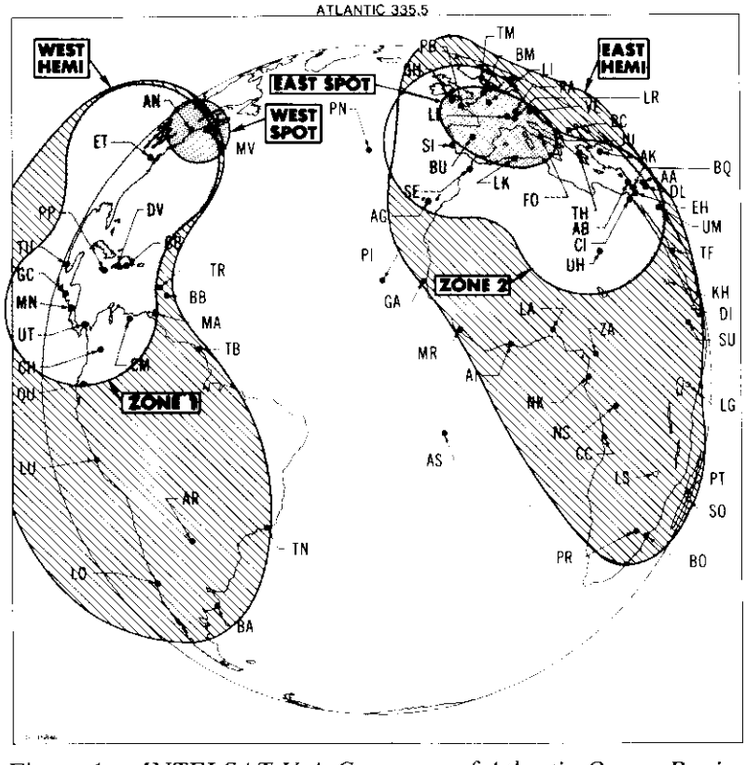

Figure 1a. *INTELSAT V-A Coverage of Atlantic Ocean Region*

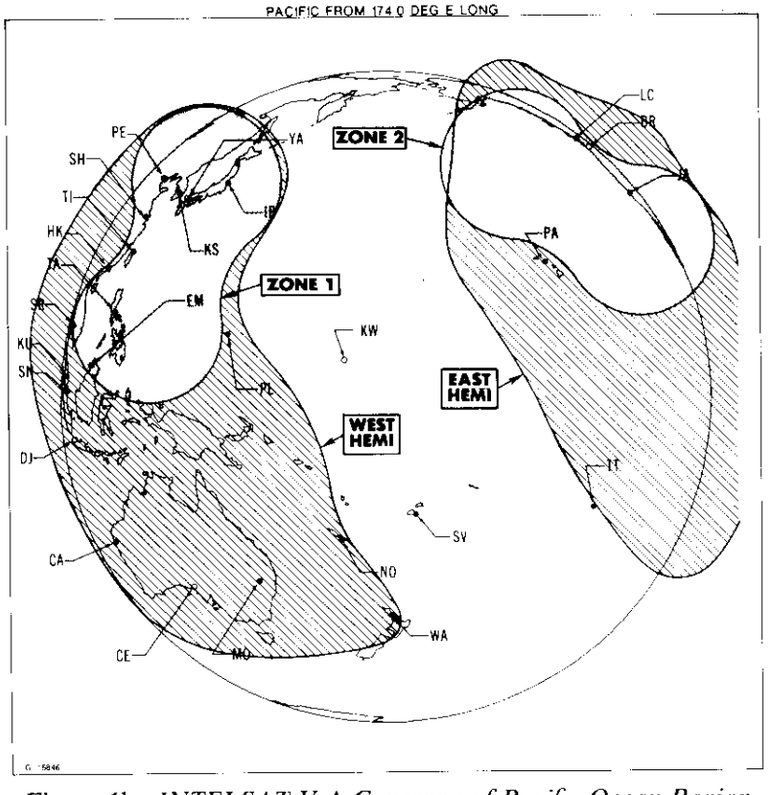

Figure 1b. *INTELSAT V-A Coverage of Pacific Ocean Region*

TRANSPONDER CHANNELIZATION PLAN

Figure 2 shows the transponder channelization plan for the INTELSAT V-A spacecraft. Each of the frequency bands to be used will be divided into nominal 40-MHz segments identified by a channel number. When more than one segment is allocated to a given transponder, the channel will be designated by a multiple channel number, *e.g.*, channel (1–2).

TRANSPONDER SWITCHING CAPABILITY

The communications subsystems will have the routing switches necessary to accomplish the interconnections shown in Table 2 by ground command. The switching will be on a channel-by-channel basis with the exception of the channels in the global and 4-GHz down-link spot beams, which will be switchable on a beam-by-beam basis. In all cases, a channel will interconnect only one receive coverage with one transmit coverage at a time.

Overall communications performance specifications for the INTELSAT V-A

LINK PERFORMANCE PARAMETERS

Polarization performance, beam isolation, receive G/T, and transmit e.i.r.p. requirements are given in Table 3. Table 4 gives the saturation flux densities and shows that an extra high gain step is to be incorporated in the 14/11-GHz zone beam transponders for flight models 13 through 15. This extra high gain step will allow new business services and domestic communications services to be provided using ground terminals with small antennas (3.5–8 meters in diameter).

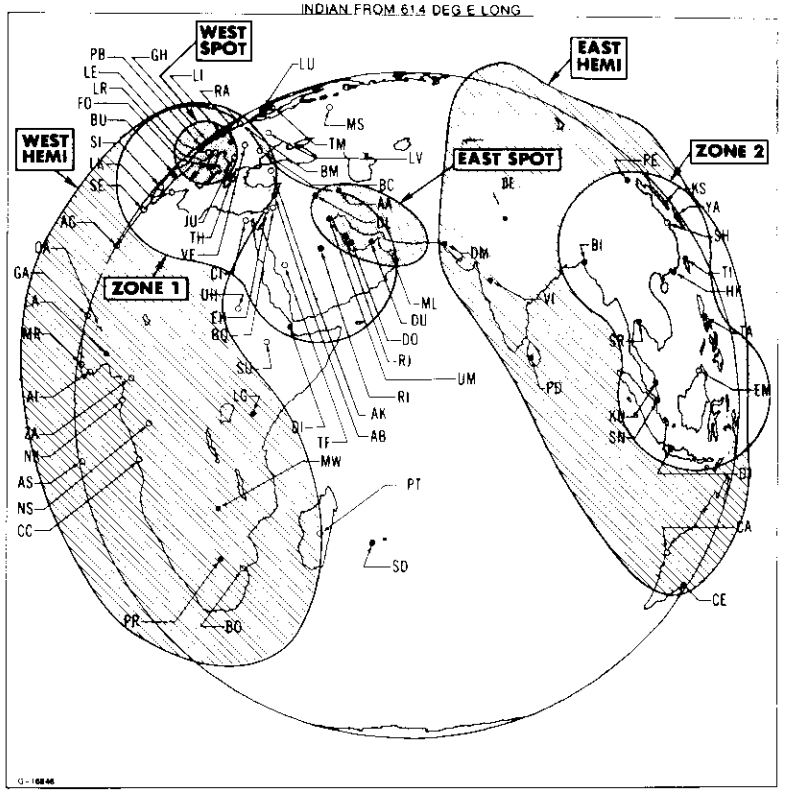

Figure 1c. *INTELSAT V-A Coverage of Indian Ocean Region*

NONLINEAR CHANNEL PERFORMANCE SPECIFICATIONS

Table 5 gives phase shift and intelligible crosstalk ratio specifications for single-carrier performance and minimum carrier-to-intermodulation power ratio specifications for 2-carrier operation (*i.e.*, nonlinear performance specifications for input sections common to more than one channel). Nonlinear performance specifications that are applicable to each transmission channel, such as phase and amplitude linearity, are the same for the INTELSAT V and V-A spacecraft, and can be found in Table 6 of Reference 1.

OTHER REQUIREMENTS

Other specifications, such as gain slope requirements and out-of-band response specifications, are important for satisfactory performance of the communications payload. Those that are the same for the INTELSAT V-A and INTELSAT V spacecraft can be found in Tables 7–9 of Reference 1.

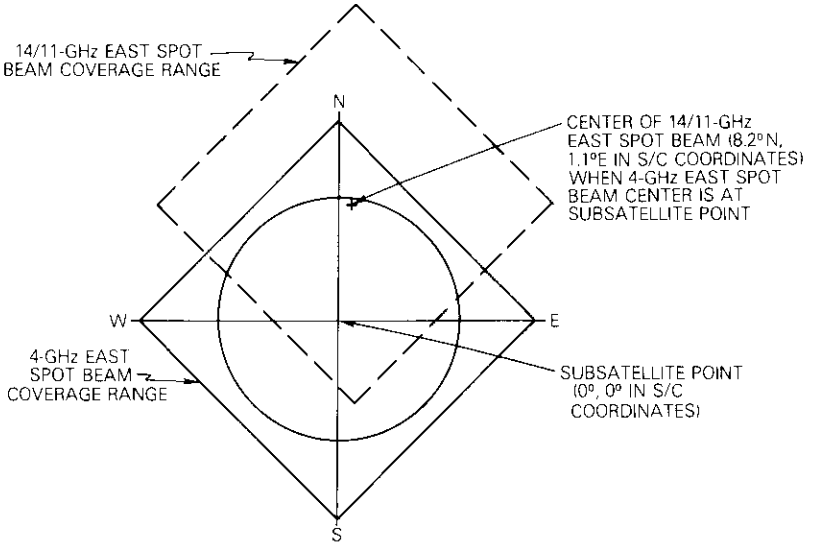

Figure 1d. *Range of Steerability for East Spot Beam*

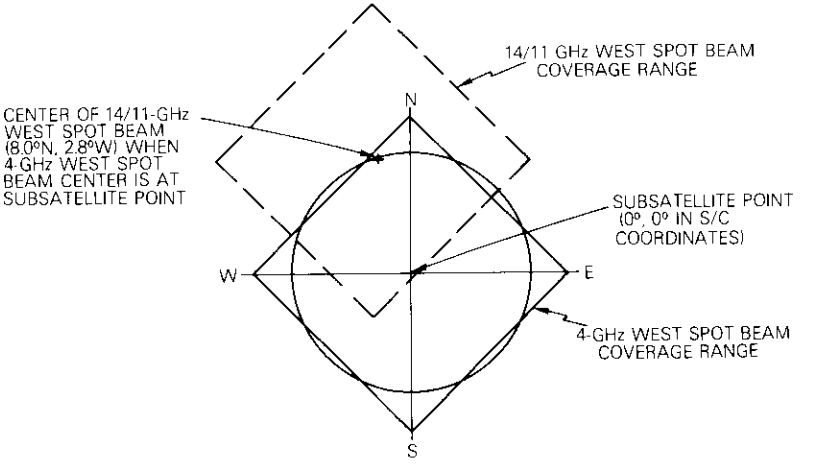

Figure 1e. *Range of Steerability for West Spot Beam*

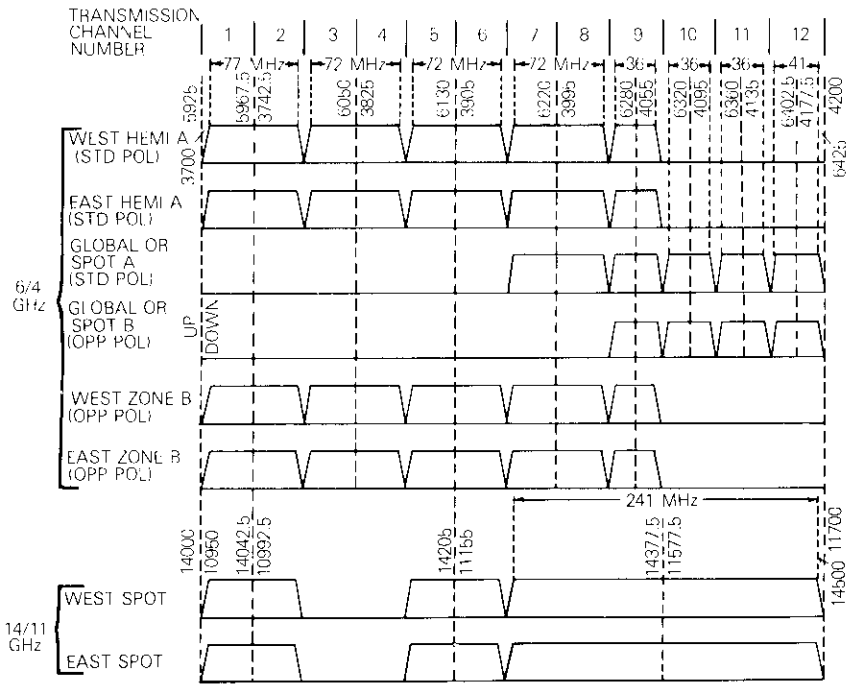

Figure 2. *INTELSAT V-A Transponder Plan*

References

[1] J. C. Fuenzalida, P. Rivalan, and H. J. Weiss, "Summary of the INTELSAT V Communications Performance Specifications," *COMSAT Technical Review*, Volume 7, Number 1, Spring 1977, pp. 311–326.

[2] N. J. Barberis and C. F. Hoeber, "Design of the Advanced INTELSAT V Spacecraft," AIAA 9th Communications Satellite Systems Conference, 1982.

TABLE 2. INTELSAT V-A TRANSPONDER INTERCONNECTION CAPABILITIES*

RECEIVE COVERAGE	TRANSMIT COVERAGE							
	WEST SPOT	EAST SPOT	WEST HEMI	EAST HEMI	ZONE 1	ZONE 2	GLOBAL A	GLOBAL B	SPOT A	SPOT B
West Spot	(1–2)	(1–2)	(1–2)	(1–2)	(7–8)	(7–8)				
	(5–6)	(5–6)	(5–6)	(5–6)						
	(7–12)	(7–12)								
East Spot	(1–2)	(1–2)	(1–2)	(1–2)	(7–8)	(7–8)				
	(5–6)	(5–6)	(5–6)	(5–6)						
	(7–12)	(7–12)								
West Hemi	(1–2)	(1–2)	(1–2)	(1–2)	(3–4)	(3–4)				
	(5–6)	(5–6)	(3–4)	(3–4)	(5–6)	(5–6)				
			(5–6)	(5–6)						
			(7–8)	(7–8)						
			(9)	(9)						
East Hemi	(1–2)	(1–2)	(1–2)	(1–2)	(3–4)	(3–4)				
	(5–6)	(5–6)	(3–4)	(3–4)	(5–6)	(5–6)				
			(5–6)	(5–6)						
			(7–8)	(7–8)						
			(9)	(9)						

TABLE 2. INTELSAT V-A TRANSPONDER INTERCONNECTION CAPABILITIES (Continued)*

RECEIVE COVERAGE	TRANSMIT COVERAGE								
	WEST SPOT	EAST SPOT	WEST HEMI	EAST HEMI	ZONE 1	ZONE 2	GLOBAL A	GLOBAL B	SPOT A	SPOT B
Zone 1	(7–8)	(7–8)	(3–4)	(3–4)	(1–2)	(1–2)	(9)	(9)	(9)	(9)
			(5–6)	(5–6)	(3–4)	(3–4)				
					(5–6)	(5–6)				
					(7–8)	(7–8)				
					(9)	(9)				
Zone 2	(7–8)	(7–8)	(3–4)	(3–4)	(1–2)	(1–2)	(9)	(9)	(9)	(9)
			(5–6)	(5–6)	(3–4)	(3–4)				
					(5–6)	(5–6)				
					(7–8)	(7–8)				
					(9)	(9)				
Global A							(7–8)		(7–8)	
							(9)		(9)	
							(10)		(10)	
							(11)		(11)	
							(12)		(12)	
Global B								(9)		(9)
								(10)		(10)
								(11)		(11)
								(12)		(12)

* Only Spot A or Global A and Spot B or Global B can be used at one time.

TABLE 3. BEAM ISOLATION, RECEIVE G/T, AND TRANSMIT E.I.R.P. FOR THE INTELSAT V-A

Polarization Performance[a]	
Global A[b]	1.05
Global B[b]	1.05
Hemispheric	1.09
Zone	1.09
4-GHz Spot[b]	
Antenna Isolation[c] (dB)	
Hemi to Hemi	27
Hemi to Zone	27
Zone to Zone	27
4-GHz Spot to 4-GHz Spot	27
14/11-GHz Spot to 14/11-GHz Spot	
8°E-W Separation	33
6.5° E-W Separation	27
Receive System G/T (dB/K)	
6-GHz Global	−16.0
6-GHz Hemispheric	−9.0
6-GHz Zone	−6.0
14-GHz East Spot	0.0
14-GHz West Spot	3.3
e.i.r.p. (dBW)	
4-GHz Global	
Channels (7–8)	26.5
Channels (9), (10), (11), (12)	23.5
4-GHz Hemi or Zone	
Channels (1–2), (3–4), (5–6), (7–8)	29.0
Channel (9)	26.0
4-GHz Spot	
Channels (7–8)	35.5
Channels (9), (10), (11), (12)	32.5
11-GHz East Spot	
Channels (1–2), (5–6), (7–12)	41.1
11-GHz West Spot	
Channels (1–2), (5–6), (7–12)	44.4

[a] Voltage axial ratio for transmit and receive beams.

[b] The 4-GHz spot beams will utilize the global receive antennas and the 14/11-GHz spot beam transmit antennas.

[c] Minimum beam isolation for transmit and receive beams

TABLE 4. SATURATION FLUX DENSITY FOR THE INTELSAT V-A

Up-Link	Saturation Flux Density (dBW/m²)		
	Extra High Gain[a]	High Gain[b]	Low Gain
6-GHz Hemi and Zone			
Channels (1–2), (3–4), (5–6), (7–8)	−84.1	−76.6	−67.1
Channel (9)	−85.1	−77.6	−70.1
6-GHz Global			
Channels (7–8)	−82.1	−74.6	−67.1
Channels (9), (10), (11), (12)	−85.1	−77.6	−70.1
14-GHz East Spot,			
Channels (1–2), (5–6), (7–8), (7–12)			
Flight Models 10–12		−77.0	−72.0
Flight Models 13–15	−84.0	−77.0	−72.0
14-GHz West Spot,			
Channels (1–2), (5–6), (7–8), (7–12)			
Flight Models 10–12		−80.3	−75.3
Flight Models 13–15	−87.3	−80.3	−75.3

[a] The switch from the extra high gain to the high gain state can be accomplished on a beam-by-beam basis only.

[b] The switch from the high gain to the low gain state can be accomplished on a channel-by-channel basis.

TABLE 5. NONLINEAR PERFORMANCE SPECIFICATIONS APPLICABLE TO INPUT SECTIONS COMMON TO MORE THAN ONE TRANSMISSION CHANNEL ON INTELSAT V-A

a. Single-Channel Performance

Flux Density Illuminating the Spacecraft (dBW/m²)		Total Phase Shift (deg)	Intelligible Crosstalk Ratio*
6 GHz	14 GHz		
−64.6	−67.5	1.5	$-175 + 20 \log f_m$
−73.6	−76.5	0.2	$-193 + 20 \log f_m$

b. Two-Carrier Performance

Flux Density Illuminating the Spacecraft for Each of Two Carriers (dBW/m²)		C/I (dB)
6 GHz	14 GHz	
−67.6	−70.5	26
−72.6	−75.5	36
−77.6	−80.5	46

* Modulation frequency f_m expressed in Hz

Geosynchronous satellite log

C. H. SCHMITT

(Manuscript received February 23, 1983)

This note provides lists of current (First Quarter 1983) and future geosynchronous satellites for the Fixed Satellite Service (FSS) and the Maritime Mobile Satellite Service (MMSS). Broadcasting Satellite Service (BSS) satellites are also listed where notifications to the International Frequency Registration Board (IFRB) have been made. The lists are ordered along increasing east longitude orbit position and update previously published material [1].

Table 1 lists the satellites that are operating now or satellites that may be capable of operating in orbit. Satellites being moved to new orbits are shown at their planned final positions; their current locations (First Quarter 1983) are given in the remarks column.

Table 2 lists newly proposed and replacement satellites and their currently planned orbit positions. Additional technical characteristics may be found in the IFRB circulars published weekly in the special sections [2].

A key to the frequency bands used in Tables 1 and 2 is included in Table 3, as are the service allocations and the applicable ITU region when the band is not allocated worldwide.

REFERENCES

[1] W. L. Morgan, "1980 Geosynchronous Satellite Log," *COMSAT Technical Review*, Vol. 10, No. 1, Spring 1980, pp. 233–262.

[2] *IFRB Circulars*, The International Telecommunications Union IFRB, CH 1211 Geneva 20, Switzerland.

Carl H. Schmitt is an Assistant to the Director for Communications on the Staff of the Division Director, Engineering and System Integration, System Technology Services, COMSAT General Corporation.

TABLE 1. FIXED, BROADCAST AND MARITIME MOBILE SERVICE SATELLITES IN GEOSTATIONARY ORBIT, FIRST QUARTER 1983

Subsatellite Longitude[1]	Launch Date	Satellite Designation	Country or Organization	Function	Up/Down-Link Frequency (GHz)	Remarks
4.2°E	11 May 1978	OTS-2	ESA	FSS	14/11	Experimental
4.6°E	23 Jan 1972	INTELSAT IV (F-4)	INTELSAT	FSS	6/4	Retired from operational service[2]
33.1°E	30 July 1981	RADUGA 9	USSR	FSS	6/4	
36.6°E	26 Nov 1982	RADUGA 11	USSR	FSS	6/4	
43.9°E	20 Feb 1980	RADUGA 6	USSR	FSS	6/4	
49.6°E	26 Dec 1980	EKRAN 6	USSR	BSS	6/UHF	
53.9°E	18 July 1981	RADUGA 4	USSR	FSS	6/4	
57°E	29 Jan 1976	INTELSAT IV-A (F-2)	INTELSAT	FSS	6/4	Indian Ocean spare
59.2°E	15 March 1982	GORIZONT-5	USSR	FSS	6,8/4,7	
60°E	23 May 1981	INTELSAT V (F-1)	INTELSAT	FSS	6,14/4,11	Indian Ocean Major Path
62.9°E	28 Sept 1982	INTELSAT V (F-5)	INTELSAT	FSS/MMSS	6,14/4,11 1.6,6/1.5,4	Indian Ocean Region coverage; contains Maritime Communications System package
72.5°E	10 June 1976	MARISAT 2	US-COMSAT General	MMSS	1.6,6/1.5,4	INMARSAT Indian Ocean spare
73.6°E	21 Feb 1979	EKRAN 3	USSR	BSS	6/UHF	
77°E	13 March 1977	PALAPA A-2	INDONESIA	FSS	6/4	

83.1°E	7 July 1976	PALAPA A-1	INDONESIA	FSS	6/4	
84.8°E	9 Oct 1981	RADUGA 10	USSR	FSS	6/4	
86°E	28 Dec 1979	GORIZONT 3	USSR	FSS	6,8/4,7	
87.9°E	26 June 1981	EKRAN 7	USSR	BSS	6/UHF	
89.6°E	6 July 1979	GORIZONT 2	USSR	FSS	6,8/4,7	
90.8°E	5 Feb 1982	EKRAN 5	USSR	BSS	6/UHF	
91.3°E	10 Oct 1982	GORIZONT 6	USSR	FSS	6,8/4,7	
93.6°E	21 Feb 1979	EKRAN 3	USSR	BSS	6/UHF	
98.5°E	16 Sept 1982	EKRAN 9	USSR	BSS	6/UHF	
132°E	4 Feb 1983	CS-2a	Japan	FSS	6,30/4,20	Drifting from 147°E at 0.4°W per day
135°E	15 Dec 1977	SAKURA (C.S.)	Japan-NTT and NASDA	FSS	6,30/4,20	Experimental
174°E	31 March 1978	INTELSAT IV-A (F-6)	INTELSAT	FSS	6/4	Pacific Ocean Region satellite
176.3°E	14 Oct 1976	MARISAT 3 (F-2)	US-COMSAT General	MMSS	1.6,6/1.5,4	Pacific Ocean Maritime satellite; also carries UHF capability
179°E	7 Jan 1978	INTELSAT IV-A (F-3)	INTELSAT	FSS	6/4	Pacific Ocean Region spare
217°E (143°W)	26 Oct 1982	SATCOM (F-5) AURORA	US-Alascom, Inc.	FSS	6/4	Alaskan coverage only On 2/17 drifting .64°E/day from 144.7°W
225°E (135°W)	13 Dec 1975	SATCOM 1 (F-1)	US-RCA	FSS	6/4	
229°E (131°W)	21 Nov 1981	SATCOM 3R (F-3R)	US-RCA	FSS	6/4	On 2/25 drifting 3.5°E/day from 128.6°W
233°E (127°W)	21 Feb 1981	COMSTAR 4	US-COMSAT General	FSS	6/4	
237°E (123°W)	9 June 1982	WESTAR 5	US-Western Union	FSS	6/4	

TABLE 1 (continued). FIXED, BROADCAST AND MARITIME MOBILE SERVICE SATELLITES IN GEOSTATIONARY ORBIT, FIRST QUARTER 1983

Subsatellite Longitude[1]	Launch Date	Satellite Designation	Country or Organization	Function	Up/Down-Link Frequency (GHz)	Remarks
241°E (119°W)	26 March 1976	SATCOM 2 (F-2)	US-RCA	FSS	6/4	
242.6°E (117.4°W)	12 Nov 1982	ANIK C3 (E)	Canada-TELESAT	FSS	14/12	
246°E (114°W)	7 May 1975	ANIK 3 (A-3)	Canada-TELESAT	FSS	6/4	
251°E (109°W)	16 Dec 1978	ANIK B1 (4)	Canada-TELESAT	FSS	6,14/4,12	
255.5°E (104.5°W)	26 Aug 1982	ANIK D1	Canada-TELESAT	FSS	6/4	
260°E (100°W)	15 Nov 1980	SBS 1	US-Satellite Business Systems	FSS	14/12	
261°E (99°W)	26 Feb 1982	WESTAR 4	US-Western Union	FSS	6/4	
263°E (97°W)	24 Sept 1981	SBS 2	US-Satellite Business Systems	FSS	14/12	
265°E (95°W)	13 May 1976	COMSTAR 1	US-COMSAT General	FSS	6/4	Colocated for operational reasons
265°E (95°W)	22 July 1976	COMSTAR 2	US-COMSAT General	FSS	6/4	Colocated for operational reasons
266°E (94°W)	11 Nov 1982	SBS 3	US-Satellite Business Systems	FSS	14/12	
269°E (91°W)	10 Aug 1979	WESTAR 3	US-Western Union	FSS	6/4	
273°E (87°W)	29 June 1978	COMSTAR 3	US-COMSAT General	FSS	6/4	
277°E (83°W)	16 Jan 1982	SATCOM 4	US-RCA	FSS	6/4	
281°E (79°W)	13 April 1974	WESTAR 1	US-Western Union	FSS	6/4	
281°E (79°W)	10 Oct 1974	WESTAR 2	US-Western Union	FSS	6/4	WESTAR 1 was taken out of service in December 1982 due to lack of fuel to maintain north-south stationkeeping
307°E (53°W)	22 May 1975	INTELSAT IV (F-1)	INTELSAT	FSS	6/4	Replaces F-7 in 1983
316.3°E (43.7°W)	23 Aug 1973	INTELSAT IV (F-7)	INTELSAT	FSS	6/4	Retired from operational service[2]
320.9°E (39.1°W)	20 Dec 1971	INTELSAT IV (F-3)	INTELSAT	FSS	6/4	Retired from operational service[2]
325.5°E (34.5°W)	6 Dec 1980	INTELSAT V (F-2)	INTELSAT	FSS	6,14/4,11	Atlantic Ocean Region Major Path 1
332.5°E (27.5°W)	4 March 1982	INTELSAT V (F-4)	INTELSAT	FSS	6,14/4,11	Atlantic Ocean spare
333.9°E (26.1°W)	20 Dec 1981	MARECS-A	INMARSAT	MMSS	1.6,6/1.5,4	Atlantic Ocean Region INMARSAT
335.5°E (24.5°W)	15 Dec 1981	INTELSAT V (F-3)	INTELSAT	FSS	6,14/4,11	Atlantic Ocean Primary Path satellite
338.5°E (21.5°W)	25 May 1977	INTELSAT IV-A (F-4)	INTELSAT	FSS	6/4	Atlantic Ocean Region contingency satellite
341.5°E (18.5°W)	26 Sept 1975	INTELSAT IV-A (F-1)	INTELSAT	FSS	6/4	Atlantic Ocean Region Major Path 2
345°E (15°W)	26 Aug 1977	SIRIO	Italy	--	17/12	Experimental[3]
345.0°E (15.0°W)	19 Feb 1976	MARISAT 1	US-COMSAT General	MMSS	1.6,6/1.5,4	Atlantic Ocean Region spare, leased to INMARSAT, also has UHF capability

TABLE 1 (continued). FIXED, BROADCAST AND MARITIME MOBILE SERVICE SATELLITES IN GEOSTATIONARY ORBIT, FIRST QUARTER 1983

Subsatellite Longitude[1]	Launch Date	Satellite Designation	Country or Organization	Function	Up/Down-Link Frequency (GHz)	Remarks
345.4°E (14.6°W)	14 June 1980	GORIZONT 4	USSR	FSS	6,8/4,7	
348.8°E (11.2°W)	19 Dec 1974	SYMPHONIE 1 (A)	France/ Germany	--	6/4	Experimental Colocated
348.5°E (11.5°W)	27 Aug 1975	SYMPHONIE 2 (B)	France/ Germany	--	6/4	Experimental Colocated
359°E (1°W)	21 Nov 1974	INTELSAT IV (F-8)	INTELSAT	FSS	6/4	Spare satellite

Note: 1. The list of satellite longitudes was compiled from the best information available for early 1983.

2. Retired INTELSAT satellites are located between 1° and 7°E or 316°-322°E. Operations are limited to Telemetry and Command.

3. Being moved to 65°E.

TABLE 2. PLANNED GEOSTATIONARY SATELLITES FOR FIXED, BROADCAST AND MARITIME MOBILE SERVICES

Subsatellite Longitude	Launch Date	Satellite Designation	Country or Organization	Function	Up/Down-Link Frequency (GHz)	IFRB Reference Circulars
3.5°E	1987	SICRAL 1A	Italy	MSS/FSS	UHF,8,14, 40/7,12,20	AR11/A/44
5°E	1985	TELE-X	Norway, Sweden, Finland	FSS/BSS	30,17/20,12	SPA-AA/27/1535, SPA-AA/29/1539
10°E	1983	EUTELSAT-1	France	FSS	14/11	SPA-AJ/327/1492
15°E	1986	AMS-1	Israel	FSS	6,14/4,11	AR11/A/39/1554
15°E	1986	AMS-2	Israel	FSS	6,14/4,11	AR11/A/39/1554
17°E	1984	SABS	Saudi Arabia	BSS	14/11	SPA-AA/267/1424
19°E	1984	ARABSAT I	Arab League	FSS/BSS	6/4,2.5	SPA-AJ/172/1388
22°E	1987	SICRAL 1B	Italy	MMSS/FSS	UHF,8,14, 40/7,12,20	AR11/A/45
23.5°E	1987	DFS-1	Germany	FSS	14,30/12,20	AR11/A/40/1556
26°E	1984	ARABSAT II	Arab League	FSS/BSS	6/4,2.5	SPA-AJ/173/1388
26°E	Unknown	ZOHREH-2	Iran	FSS	14/11,12	SPA-AJ/76/1303
28.5°E	1987	DFS-2	Germany	FSS	14,30/12,20	AR11/A/41/1556
34°E	Unknown	ZOHREH-1	Iran	FSS	14/11,12	SPA-AA/163/1278
45°E	Unknown	LOUTCH-P2	USSR	FSS	14/11	SPA-AJ/122/1340
47°E	Unknown	ZOHREH-3	Iran	FSS	6/4	SPA-AA/165/1278
53°E	Unknown	LOUTCH 2	USSR	FSS	14/11	SPA-AJ/85/1318
58°E	1983-1985	VOLNA-4	USSR	MMSS	1.6/1.5	SPA-AA/172/1286
64.5°E	Mid-1980s	MARECS-C	INMARSAT	MMSS	1.6,6/1.5,4	SPA-AJ/243/1432
70°E	Unknown	STW-1	China	FSS	6/4	SPA-AJ/239/1431

TABLE 2 (continued). PLANNED GEOSTATIONARY SATELLITES FOR FIXED, BROADCAST AND MARITIME MOBILE SERVICES

Subsatellite Longitude	Launch Date	Satellite Designation	Country or Organization	Function	Up/Down-Link Frequency (GHz)	IFRB Reference Circulars
70°E	1983/1984	STW-2	China	FSS	6/4	SPA-AA/142/1255
80°E	Unknown	STATSIONAR-13	USSR	FSS	6/4	SPA-AJ/305/1469
80°E	Unknown	POTOK-2	USSR	FSS	6/4	SPA-AA/345/1485
85°E	Unknown	LOUTCH-P3	USSR	FSS	14/11	SPA-AJ/1340
85°E	Unknown	VOLNA-5	USSR	MMSS	1.6/1.5	SPA-AA/173/1286
90°E	Unknown	LOUTCH-3	USSR	FSS	14/11	SPA-AJ/86/1318
90°E	Unknown	VOLNA-8	USSR	MMSS	1.6/1.5	SPA-AA/289/1445
94°E	1983	INSAT-1B	India	FSS/BSS	6/4	SPA-AJ/231/1429
95°E	Unknown	STATSIONAR-14	USSR	FSS	6/4	SPA-AJ/306/1469
108°E	1983	PALAPA-B1	Indonesia	FSS	6/4	SPA-AA/197/1319
110°E	1984	BS-2	Japan TCSJ	BSS	14/12	AR11/C/10
113°E	1983	PALAPA-B2	Indonesia	FSS	6/4	SPA-AA/198/1319
118°E	1983-1984	PALAPA-B3	Indonesia	FSS	6/4	SPA-AA/196/1319
125°E	1983	STW-1	China, Peoples Republic of	FSS	6/4	SPA-AJ/239/1431
130°E	1983-1984	STATSIONAR-15	USSR	FSS	6/4	SPA-AJ/307/1469
135°E	Unknown	CSE	Japan (KATSURA)	BSS	6/2	SPA-AJ/19/1226
136°E	1983	CS-2b	Japan TCSJ	FSS	6,30/4,20	SPA-AJ/325/1490
140°E	Unknown	LOUTCH-4	USSR	FSS	14/11	SPA-AJ/87/1318
140°E	Unknown	STATSIONAR-7	USSR	FSS	6/4	SPA-AJ/31/1251
140°E	Unknown	VOLNA-6	USSR	MMSS	1.6/1.5	SPA-AA/174/1286

156°E	1985	AUSSAT I	Australia (OTC)	FSS	14/12	RES SPA2-3-AA/12/1456
160°E	1985	AUSSAT II	Australia (OTC)	FSS	14/12	RES SPA2-3-AA/13/1456
165°E	1985	AUSSAT III	Australia (OTC)	FSS	14/12	RES SPA2-3-AA/14/1456
190°E (170°W)	Unknown	LOUTCH-P4	USSR	FSS	14/11	SPA-AJ/124/1340
190°E (170°W)	Unknown	STATSIONAR-10	USSR	FSS	6/4	SPA-AJ/64/1280
190°E (170°W)	Unknown	VOLNA-7	USSR	MMSS	1.6/1.5	SPA-AA/175/1286
192°E (168°W)	1983	POTOK-3	USSR	FSS	6/4	SPA-AA/346/1485
214°E (146°W)	Unknown	AMIGO 2	Mexico	BSS	17/12	RES 33/A/1
221°E (139°W)	Mid-1980s	SATCOM IR	US-RCA Americom Communications	FSS	6/4	AR11/A/6/1524
224°E (136°W)	Unknown	AMIGO 1	Mexico	BSS	17/12	RES 33/A/2
237°E (123°W)	1983	WESTAR-V	US-Western Union	FSS	6/4	AR11/A/5/1524
241°E (119°W)	1984	SPACENET-I	US-Southern Pacific Sat. Co.	FSS	6,14/4,12	AR11/A/10/1525
243.5°E (116.5°W)	1985	ILHUICAHUA-2	Mexico	FSS	6/4	AR11/A/30/1540
244°E (116°W)	1983	ANIK-C2	Canada-Telesat	FSS	14/12	SPA-AJ/69/1302
245.5°E (114.5°W)	1985	ILHUICAHUA-1	Mexico	FSS	6/4	AR11/A/28/1539
246°E	1985	ANIK D2	Canada-Telesat	FSS	6/4	SPA-AA/358/1500

TABLE 2 (continued). PLANNED GEOSTATIONARY SATELLITES FOR FIXED, BROADCAST AND MARITIME MOBILE SERVICES

Subsatellite Longitude	Launch Date	Satellite Designation	Country or Organization	Function	Up/Down-Link Frequency (GHz)	IFRB Reference Circulars
254°E (106°W)	1985	GSTAR-1	US-GTE Satellite	FSS	14/12	AR11/A/14/1525
257°E (103°W)	1986	GSTAR-2	US-GTE Satellite	FSS	14/12	AR11/A/15/1525
264°E (96°W)	1983	USASAT 6C	US	FSS	14/12	AR11/A/35/1553
265°E (95°W)	1983	TELSTAR-3A	US-AT&T LL	FSS	6/4	AR11/A/8/1524
273°E (87°W)	1984	TELSTAR-3B	US	FSS	6/4	AR11/A/9/1524
284°E (75°W)	1986	SATCOL 1	Colombia	FSS	6/4	SPA-AJ/127/1343
284.6°E (75.4°W)	1986	SATCOL 2	Colombia	FSS	6/4	SPA-AJ/128/1343
286°E	1983	GALAXY 2	US	FSS	6/4	SPA-AA/312/1465
290°E (70°W)	Unknown	SBTS A-1	Brazil	FSS	6/4	AR11/A/16/1526
294°E	1985	USASAT 8A	US	FSS	6/4	AR11/A/36/1553
295°E (65°W)	1985	SBTS A-2	Brazil	FSS	6/4	AR11/A/17/1526
298°E	1986	USASAT 8B	US	FSS	6/4	AR11/A/37/1553
302°E	1987	USASAT 8C	US	FSS	6/4	AR11/A/38/1553
335°E (25°W)	Unknown	LOUTCH-P1	USSR	FSS	14/11	SPA-AA/177/1289
335°E (25°W)	Unknown	STATSIONAR-8	USSR	FSS	6/4	SPA-AJ/62/1280
335°E (25°W)	Unknown	VOLNA-1	USSR	MMSS	1.6/1.5	SPA-AA/169/1286
341°E (19°W)	1986	LUXSAT	Luxembourg	BSS	17/12	AR11/A/20/1529
341°E (19°W)	1985-1986	L-SAT	ESA	BSS	13,17,30/ 12,20	SPA-AA/308/1463 AR11/A/33/1544
341°E (19°W)	1986	HELVESAT-1	Switzerland	BSS	17/12	SPA-AA/365/1512
344°E (11°W)	1983-1984	STATSIONAR-11	USSR	FSS	6/4	SPA-AJ/303/1469
345.6°E (14.4°W)	1983	POTOK-1	USSR	FSS	6/4	SPA-AA/344/1485
346°E (14°W)	Unknown	LOUTCH 1	USSR	FSS	6/4	SPA-AJ/84/1318
346.5°E (13.5°W)	Unknown	VOLNA 2	USSR	MMSS	1.6/1.5	SPA-AA/170/1286
352°E (8°W)	1983	TELECOM I-A	France	FSS	6,14/4,12	SPA-AJ/299/1461
355°E (5°W)	1983	TELECOM I-B	France	FSS	6,14/4,12	SPA-AJ/300/1461

Note: The weekly IFRB Circular has special sections, some of which are related to the satellite services as follows:

AR11/A/---/Circ. No.
Contains advance publication of information on a planned satellite network.
AR11/C/---/Circ. No.
Contains requests for coordination under RR1060 of frequency assignments to a space station on a geostationary satellite.
RES/33/A---Contains information on a planned satellite in the Broadcasting Satellite Service.
SPA/AA/---/Circ. No., see AR11/A/---.
SPA/AJ/---/Circ. No., see AR11/C/---.

TABLE 3. FREQUENCY BAND KEY

ABBREVIATION	DESCRIPTION (GHz)
UHF	0.702 to 0.726 0.742 to 0.766
1.5	1.530 to 1.535, 1.535 to 1.544, MMSS[a]
1.6	1.6265 to 1.6455, MMSS
2.5	2.5 to 2.69 GHz, BSS[b]
4	3.400 to 3.900, FSS[c] 3.700 to 4.200, FSS
6	5.725 to 5.925, FSS 5.925 to 6.425, FSS
11	10.700 to 11.700, FSS
12	11.7 to 12.2[d], FSS, Region 2 11.7 to 12.5, BSS, Regions 1 and 3 12.2[d] to 12.7, BSS, Region 2 12.5 to 12.75, FSS, Regions 1 and 3 down
14	14.00 to 14.50, FSS
17	17.3 to 18.1, FSS–BSS Feeder
20	17.7 to 20, FSS, 20.2 to 21.2, FSS
30	29.5 to 30, FSS, 30 to 31, FSS

[a] MMSS: maritime mobile satellite service.
[b] BSS: broadcast satellite service.
[c] FSS: fixed satellite service.
[d] To be decided at RARC-83.

Translations of Abstracts

Mise au point d'un transmultiplexeur MRF-MRT à 60 voies

E. S. YAM ET M. D. REDMAN

Sommaire

Les auteurs présentent un transmultiplexeur MRF-MRT à groupe secondaire de 60 voies mis au point pour l'AMRT par satellite. Ils passent en revue les principes mathématiques de la modulation et de la démodulation numériques en bande latérale unique (BLU), et formulent des algorithmes de calcul rapide pour le traitement des signaux numériques dans les deux sens. Cette approche utilise un système de filtrage de bande passante entièrement réel à étage unique, ainsi que des transformations en cosinus distinctes rapides pour faciliter les calculs. Les algorithmes sont appliqués à la construction d'un équipement prototype de transmultiplexeur de groupe secondaire. La conception utilise une mémoire statique programmable (PROM) microcodable souple et opte pour la simplicité d'équipement. Le problème de conception posé par le prototype de filtre passe-bas à réponse d'impulsions finie (FIR) est esquissé, et les aspects de la conception applicables à l'AMRT par satellite y sont décrits. L'équipement de transmultiplexage de groupe secondaire a été mis au point et testé, et sa performance respecte les normes recommandées par le CCITT.

Limites de la tension en circuit ouvert et du rendement des cellules solaires

A. MEULENBERG, JR., ET R. A. ARNDT

Sommaire

Les tensions en circuit ouvert (V_{oc}) dans les cullules solaires au silicium à surface plane de 0,1 Ω cm, de type n^+/p, produites par les techniques de diffusion, sont actuellement égales ou inférieures à 654 mV, et leur rendement

Métodos eficaces para calcular la función de pérdida de Erlang

T. N. SHIMI Y Y. L. PARK

Abstracto

Se presenta un nuevo método para obtener una primera estimación de la intensidad máxima admisible de tráfico para una determinada calidad de servicio y capacidad de canales. La función de pérdida de Erlang, junto con otros medios matemáticos, se utiliza para diseñar un método más directo y rápido de obtener una estimación exacta de la intensidad del tráfico. Es de especial interés para situaciones en las que el tráfico interurbano es relativamente intenso.

Se emplea una representación integral de la función de pérdida de Erlang para fijar límites teóricos a la intensidad del tráfico, los cuales se toman como primeras estimaciones; luego se obtienen cálculos más refinados usando expansiones asintóticas y el método iterativo de Newton.

Author Index, CTR 1982

The following index gives the code numbers that are to be used for ordering reprints from Lab Records, COMSAT Laboratories, 22300 Comsat Drive, Clarksburg, Maryland 20871.

APPLE, J., see Assal, F. [CTR82/224].

ARNSTEIN, D., see Ghais, A. [CTR82/238].

ASSAL, F., Gupta, R., Apple, J. & Lopatin, A., "A Satellite Switching Center for SS-TDMA Communications," Spring, pp. 29–68 [CTR82/224].

BURWELL, C. & Gover, S.,* "Hardware Simulation Facility for 120-Mbit/s QPSK/TDMA System," Fall, pp. 335–369 [CTR82/235].

CHAKRABORTY, D. & Kappes, J., "Experimental Evaluation of Threshold Detection With Estimated Sequence Performance," Fall, pp. 371–397 [CTR82/236].

CHAKRABORTY, D., see Dobyns, T. [CTR82/226].

CHANG, C., see Chou, S. [CTR82/237].

CHOU, S. & Chang, C., "4-GHz High-Efficiency Broadband FET Power Amplifiers," Fall, pp. 399–411 [CTR82/237].

DiFONZO, D., see Krichevsky, V. [CTR82/231].

DOBYNS, T., Chakraborty, D., Suyderhoud, H. & Wolejsza, C. J., "60-Mbit/s QPSK-TDMA/DSI Field Test via Pacific Basin INTELSAT IV," Spring, pp. 93–119 [CTR82/226].

FANG, R. J. F., "A Demand-Assigned Mixed TDMA and FDMA/TDMA System," Spring, pp. 157–180 [CTR82/228].

GHAIS, A., Martin, J., Arnstein, D. & Lewis, M., "Summary of INTELSAT VI Communications Performance Specifications," Fall, pp. 413–429 [CTR82/238].

GOVER, S., see Burwell, C. [CTR82/235].

GUPTA, R., see Assal, F. [CTR82/224].

HORNA, O., "Cancellation of Acoustic Feedback," Fall, pp. 319–333 [CTR82/234].

HSING, J., "Digital Simulations of SBS Spacecraft Despin Operation," Spring, pp. 213–229 [CTR82/230].

KAISER, J., see Palmer, L. [CTR82/229].

KAPPES, J., see Chakraborty, D. [CTR82/236].

KRICHEVSKY, V. & DiFonzo, D. F., "Beam Scanning in the Offset Gregorian Antenna," Fall, pp. 251–269 [CTR82/231].

KUMAR, P. N., "Depolarization of 19-GHz Signals," Fall, pp. 271–293 [CTR82/232].

* Non-COMSAT author.

KUMAR, P. N., "Precipitation Fade Statistics for 19/29-GHz COMSTAR Beacon Signals and 12-GHz Radiometric Measurements," Spring, pp. 1–27 [CTR82/223].

LEWIS, M., see Ghais, A. [CTR82/238].

LOPATIN, A., see Assal, F. [CTR82/224].

MARTIN, J., see Ghais, A. [CTR82/238].

MILLS, D., see Palmer, L. [CTR82/229].

PALMER, L., Kaiser, J., Rothschild, S. & Mills, D., "SATNET Packet Data Transmission," Spring, pp. 181–212 [CTR82/229].

POKLEMBA, J., "An Approximation Technique for Realizing the Reciprocal Sin (x)/(x) Frequency Response," Spring, pp. 121–156 [CTR82/227].

PRICE, R., "RF Tests on the Etam Standard C Antenna," Spring, pp. 69–92 [CTR82/225].

ROTHSCHILD, S., see Palmer, L. [CTR82/229].

SINHA, A., "Optimum Orbital Location of a Communications Satellite," Fall, pp. 295–317 [CTR82/233].

SUYDERHOUD, H., see Dobyns, T. [CTR82/226].

WOLEJSZA, C. J., see Dobyns, T. [CTR82/226].

Index of 1982 Presentations and Publications by COMSAT Authors

The following is a cross-referenced index of technical publications and presentations by COMSAT authors in 1982, not including papers published in the *COMSAT Technical Review*. The code number at the end of an entry is the reprint number by which copies may be ordered from Lab Records at COMSAT Laboratories, 22300 Comsat Drive, Clarksburg, Maryland 20871.

ALLNUT, J. E.* & Rogers, D. V., "Novel Method for Predicting Site Diversity Gain on Satellite-to-Ground Radio Paths," *Electronics Letters*, March 1982, Vol. 18, No. 5, pp. 233–235 [82CLR38].

ASSAL, F., see Chou, S. [82CLR28]; Geller, B. [82CLR27].

BARGELLINI, P. L., "Domestic Satellite Communications Systems: Background and Projections," 22nd Int. Scientific Symp. on Space, Rome, Italy, March 1982, *PROC.*, pp. 123–133 [82CLR49].

BARGELLINI, P. L., "Communications Satellites: Spacecraft and System Architecture Evolution," 13th Int. Symp. on Space Technology and Science, Tokyo, Japan, June–July 1982, *PROC.*, pp. 811–817 [82CLR54].

BEARD, J. E., see Schnicke, W. R. [82CLR25].

BINCKES, J. B., see Schnicke, W. R. [82CLR25], [82CLR22].

BRADFIELD, D. E., "Simultaneous Transmission/Reflection Measurements Using the Hewlett-Packard 8410 B," *Microwave Journal*, Sept. 1982, Vol. 25, No. 9, pp. 154–155 [82CLR47].

BRISKMAN, R. D., see Edelson, B. I. [82CLR16].

CALVIT, T. O., see Fang, D. J. [82CLR01], [82CLR02]; Romero, D. D. [82CLR23].

CARLSON, H. E., see Fleming, P. L. [82CLR07].

CARPENTER, E., "An Optimized Dual Polarization Global Beam Antenna," AIAA 9th Comm. Satellite Systems Conf., March 1982, *PROC.*, pp. 736–740 [82CLR26].

CHAKRABORTY, D. & Kappes, J. M., "Some Aspects of Wideband HPA Linearizer Testing," Nat. Telesystems Conf., Nov. 1982, *CONF. REC.*, pp. E3.1.1–E3.1.6 [82CLR46].

CHANG, H.,* Alvarez, R.,* Lee, W.,* Nirva, K.* & Rieger, F. J., "FDM-FM Cochannel Interference Identification System," Int. Telemetering Conf., Sept. 1982, *PROC.*, Vol. XVIII, pp. 351–370 [82CLR17].

CHANG, P., see Rhodes, S. [82CLR43].

CHEN, C. H., see Fang, D. J. [82CLR05].

CHITRE, D. M., "A Selective-Repeat ARQ Scheme and Its Throughput Analysis," IEEE Int. Conf. on Comm., June 1982, *CONF. REC.*, Vol. 3, pp. 6G.4.1–6G.4.6 [82CLR32].

* Non-COMSAT author.

CHOU, S., Chang, C.,* & Assal, F., "High-Efficiency Broadband FET Power Amplifier for C-Band TWTA Replacement," IEEE Int. Conf. on Comm., June 1982, *CONF. REC.*, Vol. 1, pp. 1E.2.1–1E.2.4 [82CLR28].

COOK, W., see Kaul, A. [82CLR19].

CUDHEA, P. W.,* McNeill, D. A.* & Mills, D. L., "SATNET Operations," AIAA 9th Comm. Satellite Systems Conf., March 1982, *PROC.*, pp. 100–106 [82CLR18].

DAVIES, D. E.,* McNally, P. J., Lorenzo, J. P.* & Julian, M.,* "Incoherent Annealing of Implanted Layers in GaAs," *IEEE Electron Device Letters*, Apr. 1982, Vol. EDL-3, No. 4, pp. 102–103 [82CLR06].

DiFONZO, D. F., "The Evolution of Communications Satellite Antennas," IEEE Int. Symp. on Antennas and Propagation, May 1982, *Digest*, Vol. 1, pp. 358–361 [82CLR13].

DUNLOP, J. D. & Stockel, J. F., "Nickel-Hydrogen Battery Technology-Development and Status," *Journal of Energy*, Jan.–Feb. 1982, Vol. 6, No. 1, pp. 28–33 [82CLR03].

EAVES, R. E. & Kolba, D. P.,* "Multiple Beam EHF Antenna/Receiver Configuration for Unified Satellite Communications Up-Link Coverage," AIAA 9th Comm. Satellite Systems Conf., March 1982, *PROC.*, pp. 248–254 [82CLR21].

EDELSON, B. I. & Briskman, R. D., "The Satellite Communications Outlook," *Journal of the British Interplanetary Society*, Apr. 1982, Vol. 35, No. 4, pp. 147–155 [82CLR16].

EMMERT, C.,* Riginos, V. & Potukuchi, J., "In-Orbit Measurement of the SBS Satellite," AIAA 9th Satellite Systems Conf., March 1982, *PROC.*, pp. 167–173 [82CLR20].

FANG, D. J. & Chen, C. H., "Propagation of Centimeter/Millimeter Waves Along a Slant Path Through Precipitation," *Radio Science*, Sept.–Oct. 1982, Vol. 17, No. 5, pp. 989–1005 [82CLR05].

FANG, D. J. & Liu, C. H., "Fading Statistics of C-Band Satellite Signal During 1978–1980 Solar Maximum Years," *Propagation Aspects of Frequency Sharing, Interference and System Diversity*, AGARD-CPP-332, 1982, pp. 30-1 to 30-13 [82CLR50].

FANG, D. J., Tseng, F. T. & Calvit, T. O., "A Low Elevation Angle Propagation Measurement of 1.5-GHz Satellite Signals in the Gulf of Mexico," *IEEE Trans. on Antennas and Propagation*, Jan. 1982, Vol. AP-30, No. 1, pp. 10–15 [82CLR01].

FANG, D. J., Tseng, F. T. & Calvit, T. O., "A Measurement of the MARISAT L-Band Signals at Low Elevation Angles Onboard Mobil Aero," *IEEE Trans. on Comm.*, Feb. 1982, Vol. COM-30, No. 2, pp. 359–365 [82CLR02].

* Non-COMSAT author.

FANG, R. J. F. & Sandrin, W. A., "Data Collection Platform Services via K_u Sub U-Band Transponders," IEEE Global Telecom. Conf., Nov.–Dec. 1982, *CONF. REC.*, Vol. 3, pp. E5.1.1–E5.1.7 [82CLR40].

FANG, R. J. F., see Rhodes, S. [82CLR43].

FEIGENBAUM, I. A., "Reliability of the INTELSAT Communications System," 5th European Conf. on Electrotechnics-Eurocon '82, June 1982, *PROC.*, pp. 501–507 [82CLR51].

FLEMING, P. L., Meulenberg, A. & Carlson, H. E., "High-Performance GaAs Metal Insulator Semiconductor Transistor," *IEEE Electron Device Letters*, Apr. 1982, Vol. EDL-3, No. 4, pp. 104–105 [82CLR07].

GELLER, B. & Assal, F., "Impact of Monolithic Microwave Integrated Circuit Development on Communications Satellites," IEEE Int. Conf. on Comm., June 1982, *CONF. REC.*, Vol. 1, pp. 1E.1.1–1E.1.5 [82CLR27].

GETSINGER, W. J., "Measurement of the Characteristic Impedance of Microstrip Over a Wide Frequency Range," IEEE MTT-S Int. Microwave Symp., June 1982, *Digest*, pp. 342–344 [82CLR10].

GREENE, K. H., see Koepf, G. A. [82CLR37]; Paul, D. K. [UP092].

GUPTA, V. & Virupaksha, K., "Performance Evaluation of Adaptive Quantizers for a 16-kbit/s Sub-Band Coder," IEEE Int. Conf. on Acoustics, Speech, and Signal Processing, May 1982, *PROC.*, Vol. 3, pp. 1688–1691 [82CLR09].

HAGMANN, W., see Rhodes, S. [82CLR43].

HUNG, H. L., see Hyman, N. L. [82CLR08].

HYMAN, N. L. & Hung, H. L., "Thermal Design of a Thermoelectrically Cooled Low-Noise Amplifier," *Journal of Spacecraft and Rockets*, Sept.–Oct. 1982, Vol. 19, No. 5, pp. 387–388 [82CLR08].

INUKAI, T., "On-Board Clock Correction by Drift Prediction," IEEE Int. Conf. on Comm., June 1982, *CONF. REC.*, Vol. 3, pp. 5E.5.1–5E.5.7 [82CLR31].

KAISER, J., Dicks, J. R.,* Speziale, V.,* Wood, G.,* Bolingbroke, P.* & Sams, K.,* "A Full Duplex Video Teleconference via INTELSAT V F-2 and OTS-2 at 14/11 GHz," AIAA 9th Comm. Satellite Systems Conf., March 1982, *PROC.*, pp. 566–574 [82CLR24].

KAPPES, J. M., see Chakraborty, D. [82CLR46].

KAUL, A., Cook, W., Lang, H.* & Dodel, H.,* "An Experiment in High-Speed International Packet Switching," Satellite Systems Conf., March 1982, *PROC.*, pp. 130–134 [82CLR19].

KENNEDY, D. J.,* Jankowski, J. A.* & King, C. A., "TDMA Burst Scheduling within the INTELSAT System," IEEE Global Telecomm. Conf., Nov.–Dec. 1982, *CONF. REC.*, Vol. 3, pp. F5.2.1–F5.2.5 [82CLR44].

KING, C. A., see Kennedy, D. J. [82CLR44].

* Non-COMSAT author.

KOEPF, G. A., Kalen, D. M.* & Greene, K. H., "Raman Amplification at 1.118 μm in Single-Mode Fiber and its Limitation by Brillouin Scattering," *Electronics Letters*, Oct. 1982, Vol. 18, No. 22, pp. 942–943 [82CLR37].

KRICHEVSKY, V., "Beam Scanning in Offset Cassegrain Antenna," IEEE Int. Symp. on Antennas and Propagation, May 1982, *Digest*, Vol. 1, pp. 257–260 [82CLR11].

KROOP, D. C. & Prewitt, J. M. S.,* "Privacy in Medical Information Systems-Threats and Countermeasures," 1st Int. Conf. on Medical Computer Science/Computational Medicine, Sept. 1982, *Proc. MEDCOMP '82*, pp. 188–191 [82CLR35].

LIPKE, D. W., "A New Possibility for Aeronautical Satellite Communications," IEEE Global Telecomm. Conf., Nov.–Dec. 1982, *CONF. REC.*, Vol. 3, pp. E5.2.1–E5.2.4 [82CLR41].

LIU, C. H., see Fang, D. J. [82CLR50].

LYONS, J. W., "Comparison of Computer-Predicted and In-Orbit Solar Array Performance for Geosynchronous Communications Satellites," 17th Intersociety Energy Conversion Eng. Conf., Aug. 1982, *PROC.*, Vol. 3, pp. 1595–1600 [82CLR45].

MACKENTHUN, K. M., "An Easily Implementable Universal Code for the Binary Source," *IEEE Trans. on Information Theory*, July 1982, Vol. IT-28, No. 4, pp. 646–648 [82CLR04].

MARTIN, J. E., see Schnicke, W. R. [82CLR25], [82CLR22].

MEULENBERG, A., "Basis for Equivalent Fluence Concept in Space Solar Cells," Space Photovoltaic Research and Technology Conf., Apr. 1982, *PROC.*, NASA-CP-2256, pp. 185–194 [82CLR48].

MEULENBERG, A., see Fleming, P. L. [82CLR07].

McNALLY, P. J., see Davies, D. E. [82CLR06].

MILLS, D. L., see Cudhea, P. W. [82CLR18].

NOVOTNY, E. J., "Transborder Data Flow Regulation: Technical Issues of Legal Concern," *Computer/Law Journal*, Vol. 3, No. 2, Winter 1982, pp. 105–124 [82CLR52].

PALMER, L., "Modeling and Simulating the L-Band Maritime Channel," IEEE Global Telecomm. Conf., Nov.–Dec. 1982, *CONF. REC.*, Vol. 3, pp. E5.3.1–E5.3.8 [82CLR42].

PALMER, L., see Schnicke, W. R. [82CLR25].

PAUL, D. K., "Thickness and Refractive Index Measurements by Light Coupling: Design Guidelines of a Prism Coupler," Conf. on Integrated Circuit Metrology, May 1982, *Integrated Circuit Metrology*, D. Nyyssonen, editor, S.P.I.E. Vol. 342, pp. 100–108 [82CLR39].

PAUL, D. K. & Greene, K. H., "Reliability of 1.3 μm InGaAsP/InP Laser Diodes," Int. Conf. on Lasers, *Conf. Digest*, Dec. 1982 [UP092].

* Non-COMSAT author.

POTUKUCHI, J., see Emmert, C. [82CLR20].

RAPPAPORT, C. M., "The Offset Bifocal Reflector Antenna," IEEE Int. Symp. on Antennas and Propagation, May 1982, *Digest*, Vol. 1, pp. 265–268 [82CLR12].

REVESZ, A. G., "Bond Ordering in Noncrystalline Solids," 5th. Int. Conf. on the Physics of Noncrystalline Solids, Montpellier, France, July 1982 [UP093].

REVESZ, A. G. & Schaeffer, H. A.,* "The Mechanism of Oxygen Diffusion in Vitreous SiO_2," *Journal of the Electrochemical Society*, Feb. 1982, Vol. 129, No. 2, pp. 357–361 [82CLR34].

REVESZ, A. G. & Walrafen, G.,* "Structural Interpretations for Some Raman Lines from Vitreous Silica," 2nd Int. Conf. on the Structure of Noncrystalline Materials," Cambridge, England, July 1982 [UP094].

REVESZ, A. G., Walrafen, G.,* & Krichanan, P. N.,* "Gaussian Modeling of Raman Spectra from Fused Silica Under Extreme Conditions," American Ceramic Society Meeting, Cincinnati, Ohio, May 1982, abstract only.

REVESZ, A. G. & Wemple, S. H.,* "The Optical Properties of Noncrystalline Silicon and Sil-xHx Films," *Physica Status Solidi A*, 1982, Vol. 72, No. 2, pp. 721–729 [82CLR33].

RHODES, S., Hagmann, W., Chang, P. & Fang, R., "Signal Design for INMARSAT Standard-C Ship Earth Stations," IEEE Global Telecom. Conf., Nov.–Dec. 1982, *CONF. REC.*, Vol. 3, pp. E5.5.1–E5.5.10 [82CLR43].

RIEGER, F. J., see Chang, H. [82CLR17].

RIGINOS, V., see Emmert, C. [82CLR20].

ROGERS, D. V., see Allnut, J. E. [82CLR38].

ROMERO, D. D.* & Calvit, T. O., "SATCOL-A Domestic Satellite System for Colombia," AIAA 9th Comm. Satellite Systems Conf., March 1982, *PROC.*, pp. 429–435 [82CLR23].

SANDRIN, W. A., see Fang, R. J. F. [82CLR40].

SCHNICKE, W. R., Beard, J. E., Binckes, J. B., Palmer, L. C. & Martin, J. E., "Future Global Satellite Systems for INTELSAT," AIAA 9th Comm. Satellite Systems Conf., March 1982, *PROC.*, pp. 588–597 [82CLR25].

SCHNICKE, W. R., Binckes, J. B. & Martin, J. E., "Ten Year Life INTELSAT VI Spacecraft," AIAA 9th Comm. Satellite Systems Conf., March 1982, *PROC.*, pp. 421–428 [82CLR22].

STOCKEL, J. F., see Dunlop, J. D. [82CLR03].

SUYDERHOUD, H. G., see Yatsuzuka, Y. [82CLR15].

SZARVAS, G. G., "Impact of Speech Interpolation on FDM/FM Transmission," 7th Colloquium on Microwave Comm., Sept. 1982, pp. 95–99 [82CLR36].

TSENG, F. T., see Fang, D. J. [82CLR01], [82CLR02].

* Non-COMSAT author.

VIRUPAKSHA, Y., see Gupta, V. [82CLR09].

WELTI, G. R., "INTELSAT Architectures for the 1990's," IEEE Int. Conf. on Comm., June 1982, *CONF. REC.*, Vol. 2, pp. 3A.5.1–3A.5.7 [82CLR29].

WELTI, G. R., "Microwave Intersatellite Links for Communications Satellites," IEEE Int. Conf. on Comm., June 1982, *CONF. REC.*, Vol. 3, pp. 5E.4.1–5E.4.5 [82CLR30].

WELTI, G. R., "Technology Goals for High-Capacity Communications Satellites," IAF Congress, Paris, France, Sept. 1982 [82CLR53].

WILLIAMS, J. W., see Yadavalli, S. R. [82CLR14].

YADAVALLI, S. R.,* Westrom, J. L.* & Williams, J. W., "High Voltage Power Electronics Packaging on NASA's Space Telescope," 17th Intersociety Energy Conversion Engineering Conf., Aug. 1982, *PROC.*, Vol. 1, pp. 211–216 [82CLR14].

YATSUZUKA, Y.* & Suyderhoud, H. G., "A 32-kbps ADPCM Encoding with a Variable Initially Large Leakage and Adaptive Dual Loop Predictors," IEEE Int. Conf. on Acoustics, Speech and Signal Processing, May 1982, *PROC.*, Vol. 2, pp. 976–979 [82CLR15].

* Non-COMSAT author.